



**HAL**  
open science

## Ultrafast energy transients at the nanoscale

Michele Diego

► **To cite this version:**

Michele Diego. Ultrafast energy transients at the nanoscale. Physics [physics]. Université Claude Bernard - Lyon I, 2022. English. NNT : 2022LYO10185 . tel-04390206

**HAL Id: tel-04390206**

**<https://theses.hal.science/tel-04390206>**

Submitted on 12 Jan 2024

**HAL** is a multi-disciplinary open access archive for the deposit and dissemination of scientific research documents, whether they are published or not. The documents may come from teaching and research institutions in France or abroad, or from public or private research centers.

L'archive ouverte pluridisciplinaire **HAL**, est destinée au dépôt et à la diffusion de documents scientifiques de niveau recherche, publiés ou non, émanant des établissements d'enseignement et de recherche français ou étrangers, des laboratoires publics ou privés.



**THÈSE de DOCTORAT DE  
L'UNIVERSITÉ CLAUDE BERNARD LYON 1**

**École Doctorale n°52  
École Doctorale de Physique et Astrophysique de Lyon**

**Discipline : Physique**

Soutenue publiquement le 12/12/2022, par :

**Michele Diego**

---

**Ultrafast energy transients  
at the nanoscale**

---

Devant le jury composé de :

<b>Brevet, Pierre-François</b>	Professeur	Université Claude Bernard Lyon 1	Président
<b>Bossy, Emmanuel</b>	Professeur	Université Grenoble Alpes	Rapporteur
<b>Li Voti, Roberto</b>	Professeur	Sapienza-Università di Roma	Rapporteur
<b>Zardo, Ilaria</b>	Professeure	Universität Basel	Examinatrice
<b>Banfi, Francesco</b>	Professeur	Université Claude Bernard Lyon 1	Directeur de thèse
<b>Del Fatti, Natalia</b>	Professeure	Université Claude Bernard Lyon 1	Co-directrice de thèse
<b>Giordano, Stefano</b>	Directeur de Recherche	Université de Lille	Invité



# Acknowledgments

First of all, I would like to thank my thesis supervisors, Francesco Banfi and Natalia Del Fatti, who welcomed me into the team with open arms, always encouraged me to choose my direction in research, while also having the readiness and flexibility to help me rearrange plans when, due to personal or pandemic-related difficulties, new projects proved to be better solutions.

Next, many thanks are due to the rest of the FemtoNanoOptics group, Paolo Maioli, Fabien Vialla, Aurélien Crut, Fabrice Vallée, Noëlle Lascoux, Alessandro Casto and Clement Panais, for all the work done together, the fruitful discussions and the good times spent together at work, at conferences and also outside. Another *merci* certainly goes to a (former) member of the group, Romain Rouxel, with whom I shared the first part of my PhD, carrying out together experiments that later converged in both my thesis (Chapter 1) and his [1], as well as in two articles [2, 3]. My next *grazie* goes to Marco Gandolfi, who initiated me into numerical simulations with finite element method, which later became a fundamental pillar of my thesis work.

At this point, I would like to thank all the colleagues that I have not already mentioned, with whom I have collaborated on common studies/articles which constituted my thesis work during these three years:

- Fabio Medeghini and Francesco Rossella, for our work on ultrafast thermo-optical dynamics of individual nanodisks [2].
- Simone Peli, Stefano Danesi, Claudio Giannetti, Ivano Alessandri, Valentina Zannier, Valeria Demontis, Mirko Rocci, Fabio Beltram, Lucia Sorba and Stefano Roddaro, for the work on InAs nanowires mechanical properties, described in Chapter 2 and that made the object of a publication this year [4].
- Francesco Maria Bellussi and Matteo Fasano for our work on ultrafast photoacoustic effect in carbon nanotubes immersed in water, here described in Chapter 4 and that was published as my first author paper ever [5].
- Stefano Giordano, for our work on the photoacoustic of gold nano-transducers in water, which constitutes Chapter 3 and is the object of two papers under submission.

Finally, I would like to thank Fulvio Parmigiani, who was the person that helped orientating me in my doctoral choice and pointed me towards the FemtoNanoOptics team, correctly predicting that there would have been good affinity between us.

## Abstract

The opto-thermo-mechanical dynamics of different nano-systems is studied adopting both an experimental and theoretical approach. In particular, thermal and mechanical energy exchanges between nano-objects and their environments are analyzed in order to understand the underlying physics and provide predictive tools. Different ultrafast phenomena are addressed, such as the electron-electron interaction (fs timescale), electron-lattice thermalization (ps timescale), mechanical vibrations (ps-ns timescale) and thermal dynamics (ns timescale). The first investigated system consists in gold nanodisks on a sapphire substrate, studied individually by following their transient optical variation via ultrafast pump-probe spectroscopy. Their internal electron-electron and electron-lattice thermalization dynamics are addressed, as well as the thermal cooling by heat dissipation in the substrate. Then, we analyze the mechanical oscillations of semiconducting InAs nanowires, through ultrafast pump-probe time resolved measurements. Tailored numerical simulations are carried out to extract the nanowires elastic properties and to unveil the mechanisms responsible for the activation of the oscillations, demonstrating that they originate from the sudden substrate expansion. Subsequently, a purely theoretical study is performed, modelling the photoacoustic effect in water-immersed gold nanocylinders and nanofilms. Here the main focus is on the acoustic waves launching mechanisms and their competition. We demonstrate that the acoustic waves are not only launched by the expansion of water, the well known “thermophone effect”, but also by the expansion of the nano-object itself—we called this additional contribution the “mechanophone effect”. For this scope, both the thermal dynamics and the mechanical response are systematically addressed in a *gedanken* approach, i.e. freely varying the relevant physical parameters to understand their role in the thermophone vs mechanophone competition. Finally, we investigate the photoacoustic effect of water-immersed carbon nanotubes, combining microscopic atomistic simulations, analytical models and finite element methods. In this case, in addition to the thermophone vs mechanophone competition, we show how the activation of the mechanophone effect can trigger few nanometers wavelengths sound waves in water. Each system is described in the broader framework of the nanoparticle-environment relationship, with special attention on the direction in which energy exchanges take place.

## Résumé

La dynamique opto-thermique-mécanique de différents nano-systèmes est étudiée par une approche à la fois expérimentale et théorique. En particulier, les échanges d'énergie thermique et mécanique entre les nano-objets et leur environnement sont analysés afin de décrire, comprendre et prédire la physique qui sous-tend leur comportement. Différents phénomènes ultrarapides sont considérés, tels que l'interaction électron-électron (échelle de temps fs), la thermalisation électron-réseau (échelle de temps ps), les vibrations mécaniques (échelle de temps ps-ns) et la dynamique thermique (échelle de temps ns). Le premier système étudié consiste en des nanodisques d'or sur un substrat de saphir, étudiés individuellement en suivant leur variation optique transitoire grâce à la spectroscopie pompe-sonde ultrarapide. Leur dynamique de thermalisation interne électron-électron et électron-réseau est abordée, ainsi que le refroidissement thermique par dissipation de chaleur vers le substrat. Ensuite, nous analysons les oscillations mécaniques des nanofils semi-conducteurs de InAs, via des mesures résolues en temps de type pompe-sonde ultrarapide. Des simulations numériques sont effectuées pour extraire les propriétés élastiques de nanofils et pour dévoiler les mécanismes responsables de l'activation des oscillations, démontrant qu'elles proviennent de l'expansion soudaine du substrat. Ensuite, une étude purement théorique est réalisée, modélisant l'effet photoacoustique par un nanocylindre et un nanofilm d'or immergés dans l'eau. Ici, l'accent est mis sur les mécanismes possibles de lancement des ondes sonores et leur compétition. Nous démontrons que les ondes acoustiques ne sont pas seulement lancées par l'expansion de l'eau, le bien connu "effet thermophone", mais aussi par l'expansion de la nanoparticule elle-même — nous avons appelé cette contribution supplémentaire "effet mécanophone". Dans ce cadre, la dynamique thermique et la résultante réponse mécanique sont systématiquement abordées dans une approche *gedanken*, c'est-à-dire en faisant varier librement les paramètres physiques pour comprendre leur rôle dans la compétition thermophone vs mécanophone. Enfin, nous avons modélisé des nanotubes de carbone dans l'eau, en combinant des simulations atomistiques microscopiques, le calcul analytique des constantes élastiques et une modélisation continue par la méthode des éléments finis, afin de simuler l'effet photoacoustique généré par un tel système complexe et anisotrope. Dans ce cas, en plus de la compétition thermophone vs mécanophone, nous montrons comment l'activation de l'effet mécanophone peut déclencher des ondes sonores de quelques nanomètres de longueur d'onde dans l'eau. Chaque système est décrit dans le cadre plus large de la relation nanoparticule-environnement, avec une attention particulière sur la direction dans laquelle les échanges énergétiques ont lieu.

# Table of Contents

<b>General introduction</b>	<b>8</b>
<b>1 Ultrafast opto-thermal dynamics of individual gold nanodisks</b>	<b>12</b>
1.1 Introduction	12
1.2 Spatial Modulation Spectroscopy technique	13
1.2.1 Experimental set up	15
1.2.2 Gold Nanodisk SMS spectra	17
1.3 Cooling dynamics	22
1.3.1 Optical properties vs temperature evolution	24
1.3.2 Cooling dynamics of individual nanodisks	25
1.3.3 Cooling dynamics: ND morphology and TBR	30
1.4 Transient electrons and lattice dynamics	33
1.4.1 Experimental data	33
1.4.2 Modelling the transient optical response of gold NDs	35
1.4.3 Experimental data and theoretical model	38
1.5 Conclusions	41
<b>2 Ultrafast mechanical oscillations of InAs nanowires</b>	<b>44</b>
2.1 Introduction	44
2.2 InAs Nanowires Structure	46
2.2.1 Growth procedure	46
2.3 Ultrafast time-resolved measurements	48
2.3.1 ASOPS technique	48
2.3.2 Time-resolved measurements	50
2.4 Assessing NWs mechanical properties	52
2.4.1 Modeling the InAs NWs	52
2.4.2 InAs NWs mechanical properties	60
2.5 Origin of mechanical vibrations	63
2.6 Conclusions	71
<b>3 Photoacoustic effect: gold nano-transducers in water</b>	<b>74</b>
3.1 Introduction	74
3.2 Thermophone vs Mechanophone	76
3.3 Role of the TBR	77
3.4 Gold nanocylinder in water	78

3.4.1	Model equations . . . . .	80
3.4.2	Results . . . . .	84
3.4.3	Conclusions on the gold NC in water . . . . .	91
3.5	Gold nanofilm in water: a frequency sweep perspective . . . . .	92
3.5.1	Thermoacoustic model . . . . .	92
3.5.2	Thermal behaviour . . . . .	96
3.5.3	Acoustic behavior . . . . .	98
3.5.4	Mechanophone effect . . . . .	103
3.5.5	Thermophone effect . . . . .	104
3.5.6	Mechanophone vs thermophone: frequency sweep analysis . . . . .	107
3.6	Gold nanofilm in water: a time domain-perspective . . . . .	112
3.7	Conclusions on the gold nanofilm in water . . . . .	118
<b>4</b>	<b>Photoacoustic effect: carbon nanotubes in water . . . . .</b>	<b>120</b>
4.1	Introduction . . . . .	120
4.2	Theoretical model . . . . .	121
4.2.1	CNT modelling . . . . .	122
4.2.2	Optics . . . . .	124
4.2.3	Thermal dynamics . . . . .	126
4.2.4	Mechanical response . . . . .	128
4.2.5	CNT Mechanical properties . . . . .	131
4.3	Results . . . . .	133
4.3.1	Thermal dynamics . . . . .	133
4.3.2	Mechanical response . . . . .	136
4.4	Conclusions . . . . .	142
	<b>General Conclusion . . . . .</b>	<b>144</b>
	<b>Bibliography . . . . .</b>	<b>147</b>



## General Introduction

Approximately 60 years separate us from Richard Feynman's famous speech "Plenty of Room at the Bottom", held at the 1959 American Physical Society meeting at Caltech [6], where Feynman predicted that in the future we would have built machines at the atomic level. Around fifteen year later, Norio Taniguchi coined the word "nanotechnology". In 1986 Eric Drexler published his book "Engines of Creation: The Coming Era of Nanotechnology", merging Feynman's concepts and Taniguchi's word [7]. Today we still live in that era, where nanotechnology and nanoscience continue to push forward the research frontline in fields ranging from medicine [8, 9, 10, 11], environment [12, 13], climate change [14, 15], quantum devices [16] to nanoelectronics [17, 18].

Understanding nanoscale energy exchanges is fundamental in all the above mentioned sectors and others. In nanoelectronics, for instance, it is essential to manage the crucial problem of heat dissipation in nanocomponents [19]. In medicine and biology, controlling the thermo-acoustical properties of nanoparticle-based photothermal imaging/therapies can maximize their efficiency [20, 21].

Perhaps the most ancient example of application of the peculiar properties exhibited by matter at the nanoscale regards optical phenomena. Nanoparticles, indeed, are employed since centuries for decorating objects such as ceramics [22] or glasses [23], as in the famous case of the Roman Lycurgus cup [24], where a mix of metal nanoparticles is responsible for the object shining with different colours depending on how it is illuminated. Centuries later, Gustav Mie provided the first solution of Maxwell's equations describing optical scattering and absorption by spherical particles of arbitrary size [25], paving the way towards modern optical spectroscopy at the nanoscale [26, 27, 28, 29]. In a nutshell, the optical metallic nanoparticles properties are due to the confinement of the surface plasmons, i.e. the coherent oscillations of electrons at the surface of a metal. When the nanoparticle size is comparable to or smaller than the impinging light wavelength, the system translational invariance is lost, resulting in the so called localized surface plasmons (LSPs) [30]. In particular, the size, shape, and material of the nanoparticle, as well as the refractive index of its surroundings determine the LSP resonance (LSPR) [27, 31], i.e. the frequency at which the collective electronic oscillations are resonant with the incoming light. At such a frequency, the nanoparticle exhibits sharp spectral absorption and scattering peaks. For noble metal nanoparticles of adequate size, the resonance occurs at visible wavelengths [30], thus generating the brilliant colors in the metal colloidal solutions [32] mentioned above.

Nanoparticles unique features go far beyond optical properties alone. Regarding heat

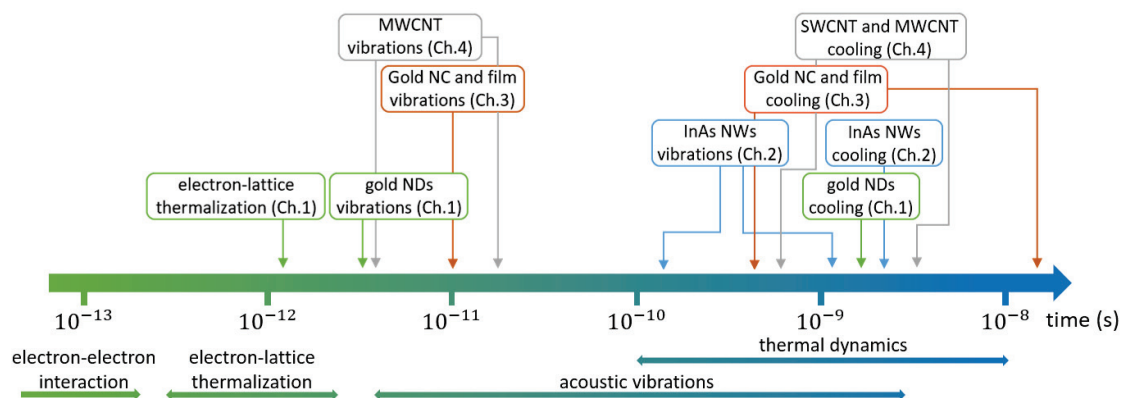


Figure 1. Timescale of the phenomena addressed in the thesis, with indications of the relevant chapters.

transfer phenomena in matter, two main differences occur when scaling from the macro- to the nano-scale. First, the thermal resistance at interfaces [33, 34] plays a much greater role in regulating the cooling rate of nanostructures [35, 36, 37, 38]. Second, Fourier's law of heat conduction is based on diffusive motion of heat carriers, thus it is not applicable to describe heat propagation over distances smaller than the heat carriers mean free paths (ballistic regime) [39, 40] and in structures wherein the causality relation between the temperature gradient and heat flux becomes manifest (hydrodynamic regime) [41, 42]. Concomitantly, also the mechanical properties of matter at the nanoscale stand as a key scientific issue. From a fundamental point of view, nanomechanics challenges the limits to which a continuum description of matter is reasonable. Nevertheless, despite what one might expect, continuum mechanics have so far demonstrated an impressive ability to predict experimental outcomes at the nanoscale [43, 44, 45]. For this very reason, the understanding of the mechanical properties and elastic constants of nano-objects is fundamental for any type of nano-application [46].

In this thesis, opto-thermo-mechanical phenomena, involving different nano-objects, are studied by following the energy exchanges between the nano-objects and the environment they are in contact with. These energy exchanges, at such a small scale, occur on times ranging from hundreds of femtoseconds (fs) to tens of nanoseconds (ns), depending on the particular nature of the process involved. Different typical phenomena, such as electron-electron interaction (hundreds of fs), electron-lattice thermalization (hundreds of fs to few picoseconds (ps)), nanoscale acoustic vibrations (tens of ps to few ns) and nanoscale thermal dynamics (hundreds of ps to tens of ns) are reported in Figure 1 (bottom part) with their characteristic timescales. Moreover, systems at the nanoscale, given their small dimensions, are intrinsically fragile, their manipulation is a difficult task and measuring their properties may induce a change in the system itself. Because of the ultrafast nature of the energy transfer at the nanoscale and the requirement for low perturbing, possibly non-contact probes, all-optical ultrafast techniques are an ideal tool to investigate

nano-objects transients phenomena [2, 47, 48, 49]. Exploiting the time-resolved and non-contact capabilities of pump and probe measurements, we can access the time evolution of phenomena at the nanoscale without excessively perturbing the system.

In this thesis work, two different ultrafast pump-probe techniques were employed. One, based on a mechanical delay line that controls the time delay between pump and probe pulses, was deployed in the context of a thermal dynamics study (Chapter 1). The other, exploiting two different lasers, which repetition rates are slightly detuned (asynchronous optical sampling - ASOPS), was deployed to investigate mechanical oscillations at the nanoscale (Chapter 2). Together with the experimental techniques, modeling is of crucial importance in this work, and is used to describe, understand and predict the physics behind the opto-thermo-mechanics of the specific systems under investigation. Specifically, finite element method (FEM) simulations are performed for all systems investigated in this thesis, aiming at rationalizing the experimental evidences (Chapters 1 and 2), or, combined with analytical methods, as a theoretical tool to predict new photoacoustic phenomena (Chapters 3 and 4).

Concerning the different nanoscale energy exchange phenomena, all the above mentioned ones are addressed throughout the chapters of the thesis, and summarized in Figure 1 together with their characteristic timescales. The *electron-electron interaction*, the *electron-lattice thermalization* and the *nanoparticle cooling dynamics* are the main topics of the time-resolved spectroscopy investigation of individual gold nanodisks (NDs) nanopatterned on a sapphire substrate, described in Chapter 1. In this case, the main focus is given to the optical and thermal phenomena, probing individual NDs and measuring their quantitative transient optical variations upon excitation via a pump pulse. We will see how the absolute temperature of individual NDs can be extracted experimentally from transient optical measurements, also allowing us to retrieve their individual thermal boundary resistance (TBR). In addition, the fast electron-electron interaction and electron-lattice thermalization are addressed, showing that, by selecting different probe wavelengths, we can access the electronic or the lattice thermal dynamics separately. In Chapter 2, instead, the focus is on *mechanical vibrations* of indium arsenide (InAs) nanowires (NWs). Also in this case we measure the transient optical response of the system, specifically on the signature of the mechanical oscillations in the time-resolved relative reflectivity changes. These time resolved measurements, together with a structural and morphological analysis of the samples via scanning/tunneling electron microscopes (SEM/TEM) and tailored numerical simulations, allow us to extract the InAs NWs elastic constants and unveil the origin of the mechanical oscillations. Chapter 3 is dedicated to a purely theoretical study on the photoacoustic launching mechanisms by a gold nanocylinder (NC) and a gold nanofilm immersed in water. Here the attention is placed on the *thermal dynamics* and the consequent *mechanical response* of the system, both through numerical simulations in the time domain and analytical calculations in the frequency domain. We demonstrate that,

at variance to what is typically found in the literature, where only the expansion of the liquid contributes to the photoacoustic launching mechanism —the so called “thermophone effect”—, also the expansion of the nanoparticle can play an important role, which we called “mechanophone effect”. In particular, the role of the TBR and of the excitation light pulse duration are systematically addressed in a *gedanken* approach, i.e. by freely varying these parameters to understand their role in the thermophone vs mechanophone competition. Finally, in Chapter 4, the knowledge acquired in the previous chapters is exploited to model two realistic and quite involved systems: a single-wall carbon nanotube (SWCNT) and a multi-walls carbon nanotube (MWCNT) immersed in water. The scope, here, is to simulate the photoacoustic effect generated by such systems. This is a multi-scale study, which merges atomistic simulations via molecular dynamics, carried out to extract thermal and morphological properties at the microscopic level, an analytical model, to extract the elastic constants of the SWCNT, and FEM simulations, describing the impulsive opto-thermo-mechanical dynamics of the system. Also in this case, the thermophone vs mechanophone competition is retrieved, this time including in the discussion also the size of the nanoparticle (SW vs MW). In addition, we show how the activation of the mechanophone effect can trigger few nanometers wavelengths sound waves in water, matching the CNT acoustic frequencies.

All the addressed systems are described in the broader framework of the nanoparticle-environment relationship in terms of their energy exchanges, with particular attention to the direction in which the energy is transferred. In the case of gold nanodisks on a sapphire substrate, only the nanodisks are responsible for the optical absorption and for their temperature rise. In this way, the heat is transferred from the nanoparticle to the substrate, which role is only to absorb the heat dissipated by the nanodisk and evacuate it. The opposite is true for the semiconducting nanowires. Here it is the substrate that absorbs most of the optical energy and it is its sudden expansion that activates the nanowires oscillations. The mechanical energy transfer, then, occurs predominately from the environment to the nano-object. In the case of the photoacoustic effect triggered by water-immersed nano-objects, it is the nano-object that absorbs the light pulse and heats up, but both the nano-object and the environment contribute to the total acoustic wave propagating in water, and a competition between the two is established.

# 1. Ultrafast opto-thermal dynamics of individual gold nanodisks

This chapter contains two studies carried out in parallel on the same sample —gold nanodisks on a sapphire substrate—, that resulted in two separate publications which I co-authored: *Ultrafast Thermo-Optical Dynamics of a Single Metal Nano-Object*, *The Journal of Physical Chemistry C* **124**, 15625 (2020) and *Electron and Lattice Heating Contributions to the Transient Optical Response of a Single Plasmonic Nano-Object*, *The Journal of Physical Chemistry C* **125**, 23275 (2021).

My contribution to this study was to carry out, together with Romain Rouxel (also a PhD student at the time), all the experimental activity, involving both the measurement of the spectra of the individual gold nanodisks and the time-resolved measurements on the ns and ps timescales. Numerical simulations, rationalising the experimental measurements, were carried out in our FemtoNanoOptics team.

This work allowed me to learn the use of the experimental set-up, both for SMS spectroscopy and pump-probe measurements. Furthermore, it allowed me to acquaint myself with the topic of ultrafast energy transients at the nanoscale.

## 1.1 Introduction

Ultrafast non-contact time-resolved experiments on absorbing nanostructures in contact with a non-absorbing substrate or matrix are particularly interesting to study nanoscale heat transfer. In these cases, the size of the heated spot on the sample coincides with the absorbing nanostructure (from tens of nanometers down to a few nanometers), rather than that of the pump beam, whose dimensions are larger and limited by diffraction (hundreds of nanometers). With this technique it is possible, for instance, to measure the thermal resistance at the nanoparticle/environment interfaces and eventually investigate its dependence on the composition of the nanoparticle, the environment and their interface. These kind of studies, however, are generally performed on ensembles of nanoparticles. This means that the measured signal is averaged over an unavoidable dispersion of shapes, sizes, orientations, defects and even thermal properties of each probed nanoparticle. Moreover, only by knowing the exact number of nanoparticles in the ensemble, one could analyse quantitatively the amplitude of time-resolved signals, not mentioning the possible difference in the efficiency with which heating is generated and affects different nanoparticles (due to their different position and the nonuniform pump and probe beams). In order to overcome this limitation, new techniques were invented to access single-particle

measurements, enabling a more precise (and often quantitative) comparison with theoretical models. Such techniques are used to study the linear optical response [27, 50], internal thermalization [51] and acoustic vibrations [52, 53, 54, 44] of metal nano-objects.

In this chapter, we will see the results of time-resolved spectroscopy on individual Au nanodisks (NDs) nanopatterned on a sapphire substrate. We will study two different timescales dynamics to unveil two different associated physics: the cooling dynamics of the ND, associated to few ns timescale, and the fast electron excitation followed by the electron-lattice thermalization, which occurs on a much faster timescale of few ps. First, we will introduce the principle of the spatial modulation spectroscopy (SMS) [55], a microscopy/spectroscopy technique invented in our laboratory, able to detect single nano-objects, measure their quantitative extinction spectra and characterize their morphologies. Then we will briefly discuss the pump and probe optical set-up involved in the time-resolved measurements and finally we will discuss the two different physics mentioned above with their relative analysis and results.

## 1.2 Spatial Modulation Spectroscopy technique

Spatial Modulation Spectroscopy (SMS) is a far-field optical spectroscopy technique able to probe individual nanoparticles [27, 55]. In our experiments, SMS enables us to locate the single gold NDs and measure their extinction cross-section for different wavelengths and polarizations of the incident light.

To understand its working principle, we consider a nanoparticle on a substrate and a laser beam directly impinging over it, as shown in Figure 2. Part of the incident beam power  $P_0$  (W) is absorbed by the nanoparticle, another part is scattered and another one is transmitted. If we place a photodetector along the direction of propagation of the light beam, we can measure the transmitted power  $P_t$ . The difference between the incident power and the transmitted one,  $\Delta P$  reads:

$$\Delta P = P_0 - P_t \approx P_{ext} = \sigma_{ext} I(x_0, y_0), \quad (1.1)$$

where  $P_{ext}$  is the power absorbed and scattered by the nanoparticle,  $I(x_0, y_0)$  is the light intensity (W/m<sup>2</sup>) of the incident beam at the  $(x_0, y_0)$  position of the nanoparticle (approximated as punctiform) and  $\sigma_{ext}$  (m<sup>2</sup>) is extinction cross section of the nanoparticle, i.e. the effective area that describes the absorption and scattering of light impinging on the nanoparticle. In general, however,  $P_0$  fluctuations are often large enough to cover the effect due to the presence of the nanoparticle. To increase the signal to noise ratio, it is necessary to make  $\Delta P$  oscillates in time at a specific frequency. Then, by eliminating all components at different frequencies, we can detect  $\Delta P$  at the selected frequency and thus enhance the signal to noise ratio. This can be achieved by modulating the light wavelength

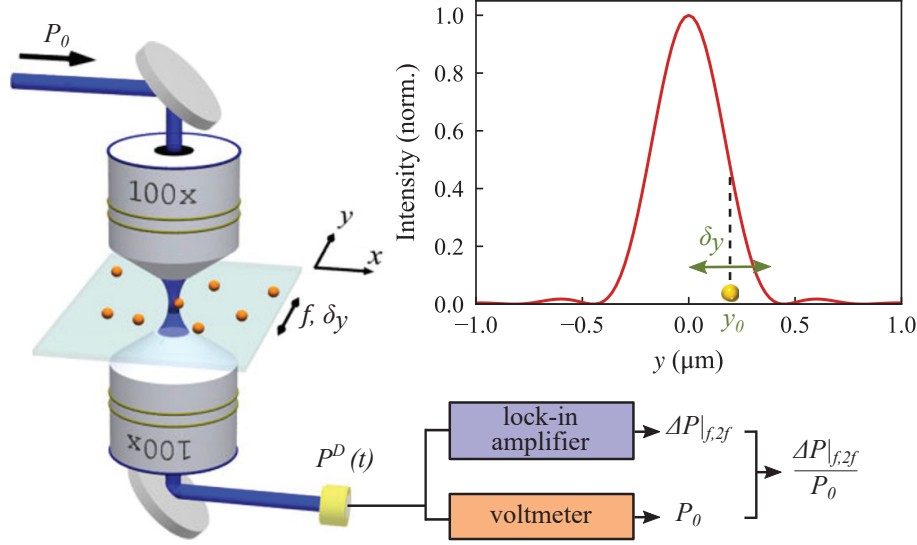


Figure 2. SMS scheme. Left side/bottom: the single nanoparticle is illuminated by a pulse of power  $P_0$ , while experiencing a periodic displacement along the  $y$  direction with frequency  $f$  and amplitude  $\delta y$ . The transmitted power  $P^D(t)$  is measured by a photodiode and its  $f$  and  $2f$  oscillating components are extracted with the use of a lock-in amplifier. The average signal  $P_0$  without the particle is measured by a voltmeter. Right/top: The intensity profile along  $y$  of the light beam (here represented as an Airy profile) is modulated by the displacement of the nanoparticle. Image taken from [1].

[56], polarization [57], or the position of the nanoparticle in respect to the beam [58, 59]. The latter case is the one used in this work: small periodic displacement along  $y$ -direction of the nanoparticle are assured by piezoelectric actuators on which the sample is mounted. If  $\delta_y$  is the amplitude and  $f$  the frequency at which the oscillation is performed, we have:

$$\Delta P(t) = \sigma_{ext} I(x_0, y_0 + \delta_y \sin(2\pi ft)). \quad (1.2)$$

A lock-in amplifier is used to extract Fourier components of the signal at frequencies  $nf$  (where  $n=1, 2, 3, \dots$ ). The components in phase with the modulation function  $\sin(2\pi ft)$  are given by:

$$\begin{cases} \Delta P|_{nf}(x_0, y_0) = \frac{2n}{T} \sigma_{ext} \int_{-T/2n}^{T/2n} I(x_0, y(t)) \sin(2\pi nft) dt & (n \text{ is odd}) \\ \Delta P|_{nf}(x_0, y_0) = \frac{2n}{T} \sigma_{ext} \int_{-T/2n}^{T/2n} I(x_0, y(t)) \cos(2\pi nft) dt & (n \text{ is even}), \end{cases} \quad (1.3)$$

where the period  $T$  is  $1/f$ . If we take  $\delta_y$  small in comparison to the beam spot, we can expand  $\Delta P(t)$  finding:

$$\Delta P(t) = \Delta P_0 + \Delta P|_f \sin(2\pi ft) + \Delta P|_{2f} \cos(4\pi ft) + o(\delta_y^2), \quad (1.4)$$

where

$$\Delta P_0(x_0, y_0) = \sigma_{ext} \left( I(x_0, y_0) + \frac{\delta_y^2}{4} \frac{\partial^2 I}{\partial y^2} \Big|_{x_0, y_0} \right) \quad (1.5)$$

$$\Delta P|_f(x_0, y_0) = \sigma_{ext} \delta_y \frac{\partial I}{\partial y} \Big|_{x_0, y_0} \quad (1.6)$$

$$\Delta P|_{2f}(x_0, y_0) = -\frac{\sigma_{ext} \delta_y^2}{4} \frac{\partial^2 I}{\partial y^2} \Big|_{x_0, y_0}. \quad (1.7)$$

In this way, we can deduce  $\sigma_{ext}$  directly by measuring  $\Delta P|_{nf}$  using the lock-in amplifier and knowing  $I(x, y)$ . Regarding  $I(x, y)$ , its profile is close to an Airy distribution, resulting from the diffraction of a quasi plane wave passing through the entrance pupil of the objective placed before the sample [60].

In order to obtain results independent from the incident laser power  $P_0$ , it is necessary to normalize  $\Delta P|_{nf}$  by  $P_0$ , measuring it after removing the nanoparticle from the beam path. Moreover, we need to take into account the frequency dependent response of the photodiode to obtain quantitative measurements. This is done comparing the signal of the photodiode for a stationary laser illumination with the signal modulated at a selected different frequency (the one used for SMS detection) using a mechanical chopper and then demodulated by the lock-in amplifier (see [1] for more details).

To visualize the procedure of extracting  $\sigma_{ext}$  from SMS measurements, Figure 3 shows the comparison between simulated signals  $\Delta P|_{f,2f}/P_0$  (panels a and c) generated using Equations 1.3 and first and second derivatives of  $I(x, y)$  as a function of the position  $(x, y)$  of a small individual nanoparticle (panels b and d). In this case,  $I(x, y)$  is an Airy light intensity profile centred in  $(x_0 = 0, y_0 = 0)$  and with full width half maximum (fwhm) of 380 nm, while  $\delta_y = 300$  nm (all values are realistic and close to the experimental ones). As can be seen, the signal  $\Delta P|_f/P_0$  and  $\partial I/\partial y$  present two lobes of opposite sign with a vanishing signal at the central position of the nanoparticle.  $\Delta P|_{2f}/P_0$  and  $\partial^2 I/\partial y^2$ , instead, exhibit a positive central peak and two negative lobes at its vertical sides. For this reason, signals at  $2f$  are generally more useful in the detection of the nanoparticle, the maximum signal corresponding exactly to its position.

## 1.2.1 Experimental set up

To obtain  $\Delta P|_{f,2f}$  images, as in Figure 3, it is necessary to change the nanoparticle position  $(x_0, y_0)$  in respect to the beam one. This is experimentally achieved with a piezo-electric stage that can move in the  $(x, y)$  plane and scan an area of  $100 \times 100 \mu\text{m}^2$  with a resolution of 0.3 nm in both directions. The spatial modulation of the sample, instead, is obtained through another piezoelectric actuator that can oscillates along the  $y$  axis with tunable frequency  $f$  and amplitude  $\delta_y$  (for our measurements  $f = 1500$  Hz and  $\delta_y \approx 300$

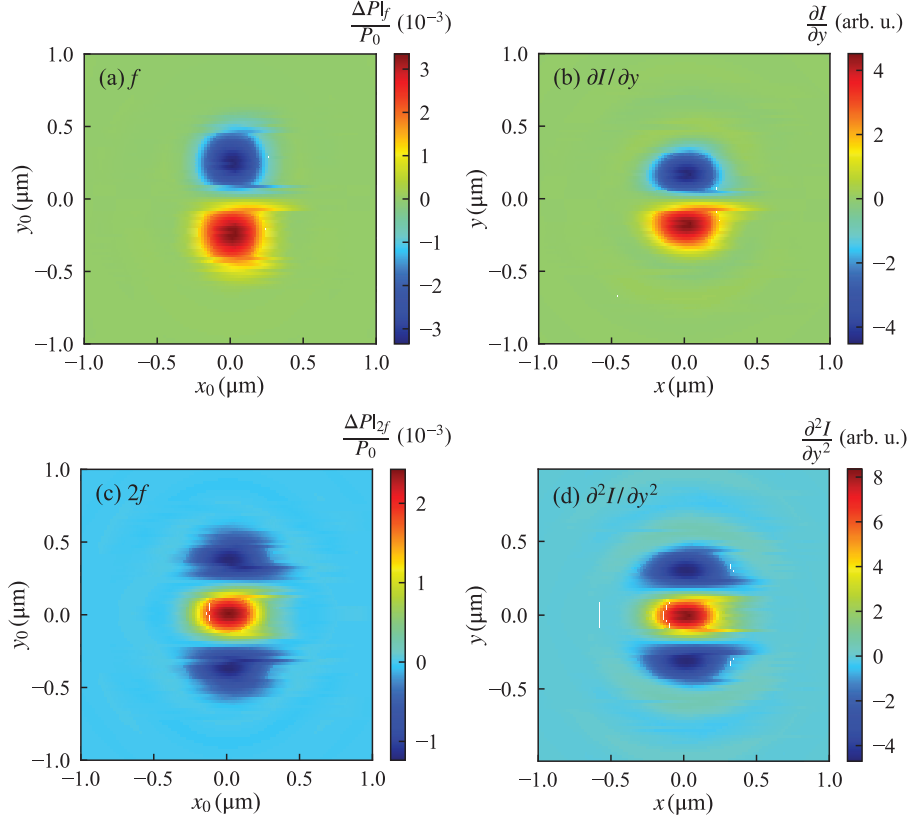


Figure 3. SMS theoretical images of  $\Delta P$  demodulated at  $f$  (panel a) or  $2f$  (panel c) as a function of the particle position  $(x_0, y_0)$ . First (panel b) and second (panel d)  $y$ -derivatives of the beam intensity profile  $I(x, y)$ . Image taken from [1].

nm). The laser beam is enlarged using a telescope, thus obtaining a quasi plane wave. Then it passes through a 100X apochromatic infinity-corrected objective with numerical aperture  $N.A. = 0.95$  and finally reaches the sample. In this way, the intensity profile  $I(x, y)$  in the focal plane is the Airy distribution, where the fwhm is close to the diffraction limit. After impinging on the sample, the transmitted beam passes through a second 100X objective with  $N.A. = 0.75$ , and then finally reaches the photodiode. The signal is demodulated by a lock-in amplifier at the desired frequency (typically  $2f$ ). In this way it is possible to display  $\Delta P|_{2f}/P_0$  in order to centre the nanoparticle, fit the signal (see [1] for details) and extract  $\sigma_{ext}$ .

Extinction spectra  $\sigma_{ext}(\lambda)$  are obtained by repeating this procedure for different wavelengths  $\lambda$ . In our set-up, it is possible to tune  $\lambda$  from the near ultraviolet to the near infrared range (375-1040 nm), thanks to different laser sources. The 690-1000 nm range is covered by a commercial mode-locked oscillator with an amplifying medium of sapphire ( $\text{Al}_2\text{O}_3$ ) crystal doped with trivalent titanium ions  $\text{Ti}^{3+}$  (Ti:Sapphire). The population inversion inside the titanium ions is generated by a continuous wave Nd:YVO<sub>4</sub> laser, which provides a 1064 nm wavelength that is subsequently frequency-doubled by a non linear lithium triborate crystal (LBO), obtaining a 532 nm wavelength, close to the absorption peak in

the Ti:Sapphire rod. The generation of short pulses ( $\approx 150$  fs) with a repetition rate of 80 MHz and an average power of 2 W (then strongly attenuated before impinging the sample) are provided by the longitudinal modes of the cavity. In order to obtain the UV-blue range of the spectrum (375-520 nm), the Ti:Sapphire output is frequency doubled by the second harmonic generation (SHG) of a barium beta borate crystal (BBO) with  $100 \mu\text{m}$  thickness. Finally, the missing intermediate range (500-750 nm) is assured by an automated optical parametric oscillator (OPO). In practice, OPO makes use of parametric amplifications and a birefringent crystal to convert, through non linear optics, the entry pump beam ( $\omega_p, \vec{k}_p$ ) (in our case the frequency doubled pulse from the Ti:Sapphire oscillator) into two beams: the signal ( $\omega_s, \vec{k}_s$ ) and the idler ( $\omega_i, \vec{k}_i$ ). The conservation of energy and momentum ensures that  $\omega_p = \omega_s + \omega_i$  and  $\vec{k}_p = \vec{k}_s + \vec{k}_i$ . We can select the frequency  $\omega_s$  of the signal beam by rotating the birefringent crystal and then amplifying it in the resonant cavity, thus generating coherent ultrashort light pulses with duration comparable to those of the pump pulses. Figure 4 shows a schematic summary of the different light sources. We state already that the same optical sources are used also for the ultrafast pump and probe measurements, described later.

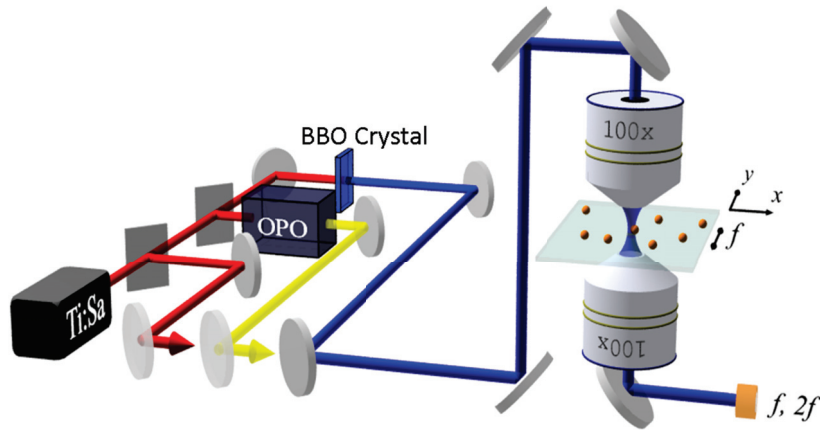


Figure 4. Light sources scheme for SMS experiments. Movable mirrors in the optical path are used to switch between the different sources. Image taken from [1].

## 1.2.2 Gold Nanodisk SMS spectra

In this section, we will discuss the results of linear spectroscopy measurements performed on single gold NDs. Before going into measurements, however, it is useful to briefly describe the investigated samples. Figure 5 shows the layout of these samples, with individual gold NDs placed along ordered lines and rows. We made use of two samples, S1 and S2, which differ in the height  $h$  of the nanodisks, being  $h = 18$  nm for S1 and  $h = 40$  nm for S2 (heights were measured by Atomic Force Microscopy (AFM)). In each sample, NDs are ordered by their diameter (from  $\approx 60$  to 180 nm), in order to study the

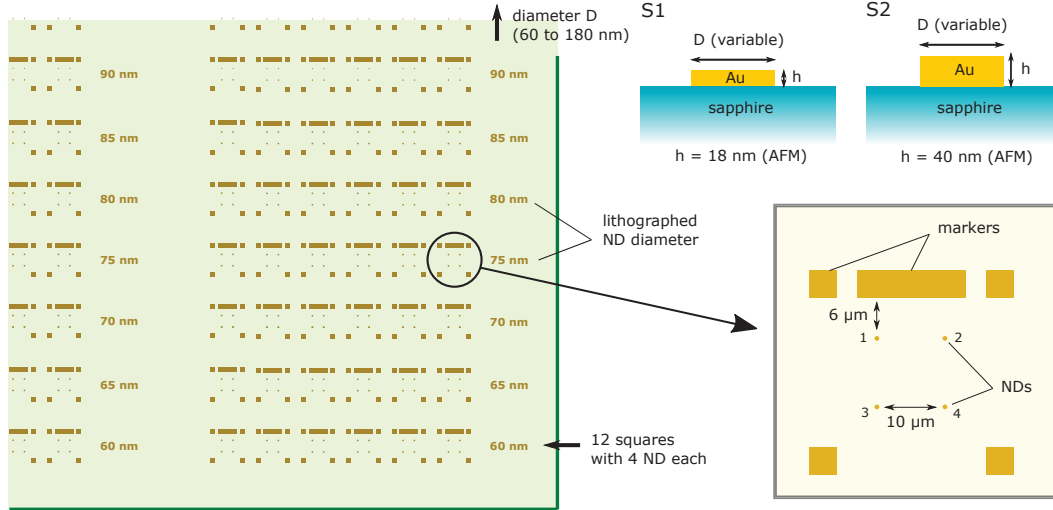


Figure 5. Scheme of gold NDs samples. A minimum distance of  $6 \mu\text{m}$  separates NDs from any other structure (markers or other NDs). Each horizontal line present 48 NDs with same diameters, ranging from 60 to 180 nm moving upward. Samples differ for the height of the NDs, being 18 nm in one case and 40 nm for the other (measured by AFM). Image taken from [1].

morphology dependence of thermal and mechanical NDs dynamics. The two samples were produced by electron beam lithography (EBL), Au thermal evaporation and lift-off techniques [61], in a collaboration with F. Rossella (Scuola Normale Superiore, Pisa). For each diameter, ranging from 60 to 180 nm, there are 48 identical NDs separated by at least  $6 \mu\text{m}$  from any other metallic structure, so to prevent optical, thermal or mechanical coupling. The substrate is composed by a 0.48 mm thick single sapphire ( $\alpha\text{-Al}_2\text{O}_3$ ) crystal cut along the (0001) plane.

During the fabrication process, however, NDs can be subjected to imperfections that might change their contact with the substrate or their structure. For this reason, in parallel with the  $\sigma_{ext}(\lambda)$  measurements, it is useful to assure the ND morphology and make sure it has the nominal cylindrical shape. In the opposite case, indeed, a comparison with the simulated system would be inconsistent and the analysis could be biased.

SMS measurements with different light polarization are a powerful instrument to achieve this goal. Let's say, for instance, that the nanoparticle, instead of being a perfectly circular ND, has an elongated shape with two main orthogonal axis. To each of the axis, we can associate a different localized surface plasmon resonance (LSPR) [62]. This give rise to two different extinction cross sections, namely  $\sigma_{\parallel}$  and  $\sigma_{\perp}$ , corresponding to the long and short axis respectively. By tuning with a wire-grid polarizer the direction of a linearly polarized light beam, we can excite one resonance or the other. For a generic polarization

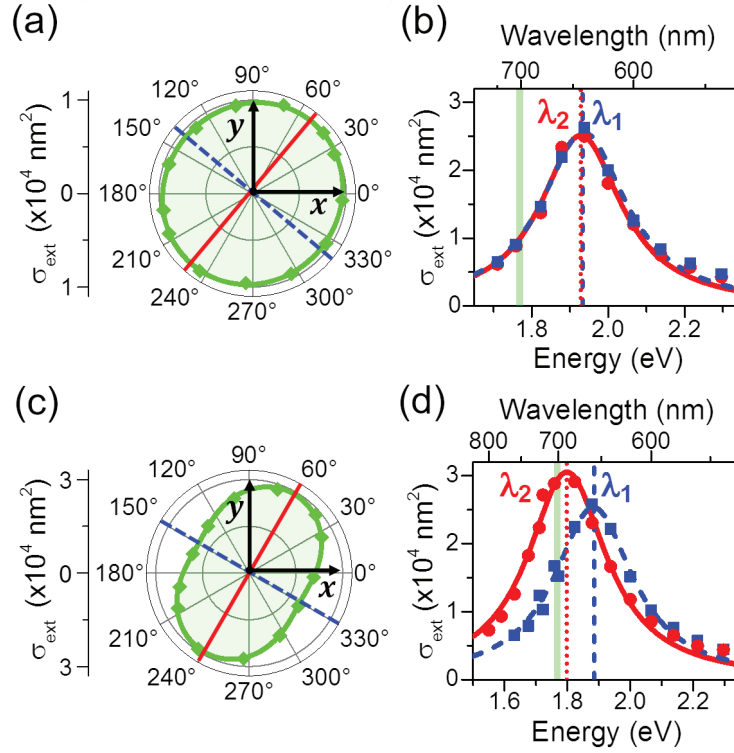


Figure 6. Morphology effects for a circular ND (panels a and b) and an elongated ND with two principal orthogonal axis (panels c and d). Polarization dependent extinction cross section  $\sigma_{ext}$  at  $\lambda = 700 \text{ nm}$  for the circular ND (panel a) and the elongated ND (panel c). Extinction spectra  $\sigma_{ext}(\lambda)$  with linear polarization along the two main axis (blue and red lines) for the circular ND (panel b) and the elongated ND (panel d). Adapted with permission from [61]. Copyright 2019 American Chemical Society.

of angle  $\theta$ , the extinction cross section reads:

$$\sigma_{ext}(\theta, \lambda) = \sigma_{\parallel}(\lambda) \cos^2(\theta - \theta_{max}) + \sigma_{\perp}(\lambda) \sin^2(\theta - \theta_{max}), \quad (1.8)$$

where  $\theta_{max}$  is the angle corresponding to the particle long axis. For elongated nanoparticles, the two LSPRs are spectrally separated and thus strongly dependent on the chosen angle. In this way, when performing SMS  $\sigma_{ext}(\theta, \lambda)$  measurements, we can also assure that gold NDs really possess their nominal circular symmetry, with no significant deviations due to fabrication imperfections.

Figure 6 reports  $\sigma_{ext}(\theta, \lambda)$  for a gold ND of nominal circular symmetry with equal perpendicular axis  $D_1 = D_2$  (panels a and b) and an elongated gold ND with different main axis  $D_1 \neq D_2$  (panels c and d). For the elongated gold ND, the extinction spectra with impinging light polarization along the two main axis are separated (panel d, red and blue curves), i.e. a spectral shift is present due to the two different LSPRs corresponding to the two axis. For the circular gold ND, instead, the two spectra are perfectly superimposed, since in this case  $\sigma_{\parallel}(\lambda) = \sigma_{\perp}(\lambda)$  (panel b, red and blue curves). This is even clearer from polar graphs, where we fix  $\lambda = 700 \text{ nm}$ , and then measure  $\sigma_{ext}$  as a function of  $\theta$ . For

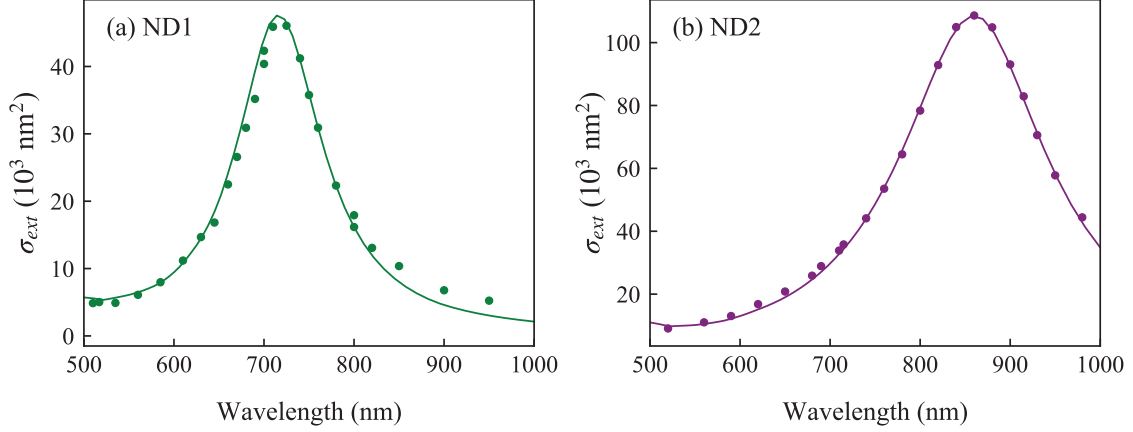


Figure 7. Extinction spectra of gold nanodisks ND1 (panel a) and ND2 (panel b). Dots represent experimental measurements, while continuous lines are the results of FEM simulations with the best parameters to fit the experimental spectra:  $h = 21$  nm and  $D = 101$  nm for ND1, while  $h = 22$  nm and  $D = 153$  nm for ND1. Image taken from [1].

the elongated gold ND (panel c),  $\sigma_{ext}(\theta)$  shows a clear  $\theta$  dependence, as expected from Equation 1.8. For the circular ND, instead,  $\sigma_{ext}$  is  $\theta$ -independent (panel a), confirming its rotational symmetry.

Once measured the extinction spectra of gold NDs, Finite Element Method (FEM) simulations are performed to reproduce experimental results and thus extract the NDs characteristics. For instance, the spectra of the elongated gold ND in Figure 6 is numerically reproduced assuming an elliptical shape with axis  $D_1$  and  $D_2$  differing by 14%. This demonstrates the high sensitivity of the SMS technique to small deviations from the nominal nanoparticles morphology, allowing us to select only quasi-circular gold NDs for the time-resolved thermal dynamics measurements that will be discussed further on. The non circular symmetry of elongated or deformed NDs, indeed, can introduce a degeneracy of vibrational modes with similar frequencies, thus complicating the fit of the time-resolved signals.

In this work we will focus on two gold NDs (referred to as ND1 and ND2), whose spectra are reported in Figure 7. Both their spectra are independent from light polarization, i.e. they have quasi circular shape. The LSPRs for the ND1 and ND2 are found at approximately 710 and 870 nm, respectively. Their spectra were taken before and after the time-resolved measurements, to ensure that the pump-probe technique didn't induce any significant change.

FEM simulations were performed in order to fit (continuous lines in Figure 7) the experimental data (dots) and extract key NDs properties, such as diameter  $D$ , height  $h$  and the scattering rate of electrons  $\gamma$  ( $\text{s}^{-1}$ ) in the Drude model (which is connected to photon absorption by electrons in the conduction band). In the case of a perfect cylinder, the aspect ratio  $D/h$  determines the resonance wavelength position, while the volume mostly determines the area spanned by the spectra in the energy domain. The LSPR linewidth,

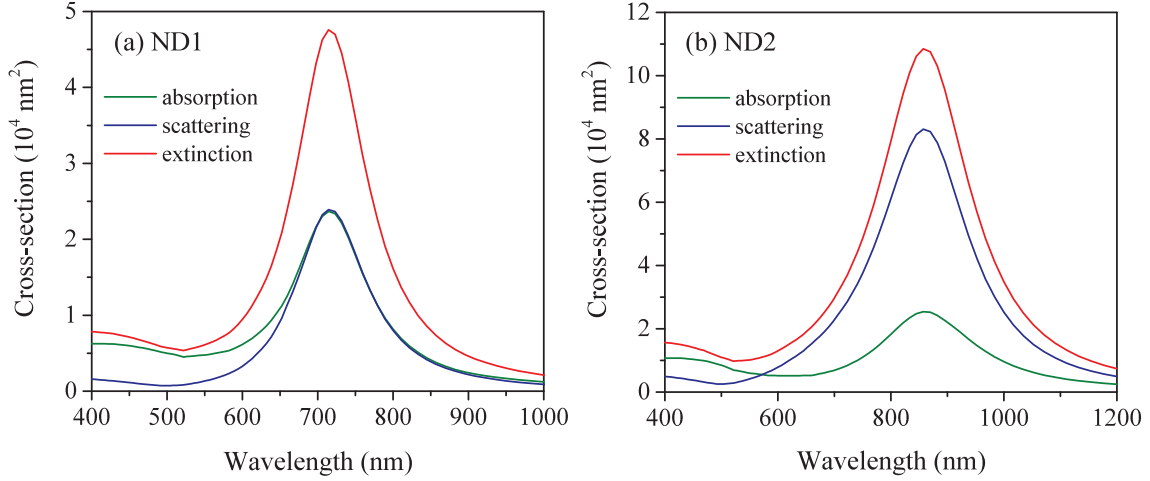


Figure 8. Extinction (red lines) cross section  $\sigma_{ext}$  spectra fitted from experimental data with FEM simulations for ND1 (panel a) and ND2 (panel b). Scattering (blue lines) and absorption (green lines) cross sections retrieved from the FEM simulations for ND1 (panel a) and ND2 (panel b). Image taken from [1].

instead, is correlated to  $\gamma$ , but its modeling is out of the scope of this study (it involves different electronic scattering mechanisms, including the ones with the ND surfaces), so it is let as a free parameter.

Experimental spectra were best reproduced by FEM simulations assuming  $D = 101$  nm,  $h = 21$  nm,  $\hbar\gamma = \hbar\gamma_0 + 100$  meV (where  $\gamma_0$  is the electron scattering rate for bulk Au,  $\hbar\gamma_0 \approx 50$  meV) for ND1, while  $D = 153$  nm,  $h = 22$  nm,  $\hbar\gamma = \hbar\gamma_0 + 45$  meV for ND2. The values for  $D$  and  $h$  are in reasonable agreement ( $\approx 10 - 20\%$  larger) with mean values found with atomic force and scanning electron microscope measurements for disks with same nominal dimensions (see [1] for more details). The ratio  $D/h$ , mostly determined by the position of the resonance, is less than 10% off than what measured with the other techniques mentioned above. The greatest magnitude of  $\gamma$  in respect to  $\gamma_0$  of Au bulk, instead, is an already known effect for NDs of similar sizes [61, 63].

Another useful ability of FEM simulations is to extract separate contributions to  $\sigma_{ext}$ , i.e. the absorption ( $\sigma_{abs}$ ) and the scattering ( $\sigma_{scat}$ ) cross sections. Figure 8 shows the different cross sections, where both  $\sigma_{abs}(\lambda)$  (green line) and  $\sigma_{scat}(\lambda)$  (blue line) contribute significantly to the extinction spectra (red line). The importance of this distinction is related to the time-resolved measurements analysis, where we investigate the cooling dynamics of the gold NDs, after excitation by a light pulse. To calculate the temperature of the excited NDs, indeed, we need to make use of the absorption cross section, rather than the extinction one.

Finally, from FEM simulations, we can predict the variation of NDs extinction spectra to changes in the Au dielectric function  $\epsilon$  and in particular in respect of its real,  $\epsilon_1$ , and imaginary,  $\epsilon_2$ , parts. This is done by varying slightly  $\epsilon_1$  and  $\epsilon_2$ , and then re-computing the spectra for each single ND. Figure 9 reports the derivatives  $\partial\sigma_{ext}/\partial\epsilon_1$  (black lines)

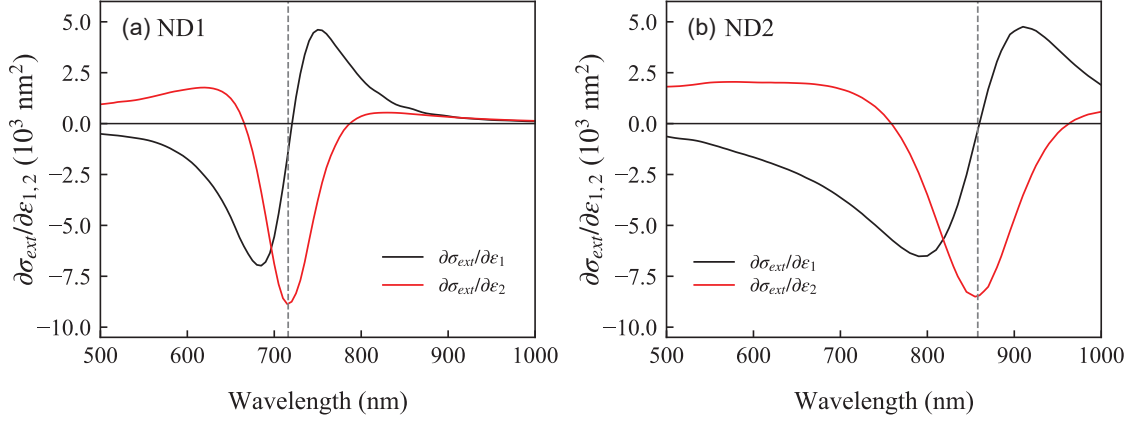


Figure 9. Calculated extinction cross section  $\sigma_{ext}$  derivatives in respect to dielectric function real  $\epsilon_1$  (black lines) and imaginary  $\epsilon_2$  (red lines) components for ND1 (panel a) and ND2 (panel b). These curves are calculated from the spectra in Figure 7. Vertical dashed lines correspond to the LSPR central position. Image taken from [1].

and  $\partial\sigma_{ext}/\partial\epsilon_2$  (red lines) for ND1 and ND2, respectively. These derivatives will be of fundamental importance when analyzing the optical response of NDs after the light excitation in time-resolved measurements.

### 1.3 Cooling dynamics

In this section we investigate the dynamics of individual gold NDs after a short laser pulse excitation. This is realized by exploiting the transient optical properties of gold NDs in pump-probe spectroscopy measurements. The key steps of this process are summarized in Figure 10 for a generic metallic nanoparticle in contact with a substrate. The initial state of the nanoparticle and the substrate is thermalized and at the equilibrium, with a common initial temperature  $T_0$ . Then the pump pulse is shined on the nanoparticle, the latter absorbs part of the energy light pulse through its absorption cross section  $\sigma_{abs}$ , and ends in an excited state. In a few hundreds of fs, the electrons reach a common electronic temperature  $T_{el}(t)$  through electron-electron scattering processes, with  $T_{el}(t)$  higher than the lattice temperature  $T_{lat}(t)$ . Electronic and lattice temperature thermalize in few ps, leaving the nanoparticle with a unique equilibrium temperature  $T_{eq}(t)$ . The electron-electron and electron-lattice thermalisation will be discussed in detail in the next section of this chapter. Here what is important to retain is that, after absorbing the pump pulse, the nanoparticle (in our case a gold ND) has a temperature  $T_{eq}(t) > T_0$  after a few ps.

The thermal rise in the nanoparticle causes a rapid thermal expansion, thus triggering mechanical oscillations, due to the excitation of its eigenmodes (typically of tens of ps periods for the investigated ND sizes). We will see, in the case of gold NDs, how to fit these oscillations, damped in a few hundreds ps. It is crucial to subtract the mechanical vibrations from the time-resolved signal, in order to appreciate solely the thermal dynamics.

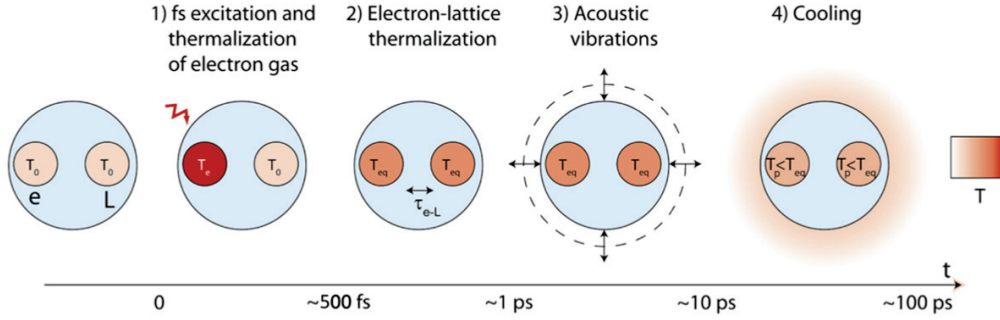


Figure 10. Ultrafast phenomena of a plasmonic nanoparticle triggered by a short (fs) light pulse. Indices ‘ $e$ ’ and ‘ $L$ ’ indicate the electron gas and the ionic lattice. On the right it is present the temperature scale color from cold (white) to hot (red). Image taken from [1].

The nanoparticle temperature cools down by dissipating heat into the substrate through the interface. Both the temperatures within the nanoparticle,  $T_{eq}(t)$ , and the substrate,  $T_{sub}(t)$ , are governed by the Fourier equation and the continuity equation:

$$\begin{aligned}\vec{q} &= -k\vec{\nabla}T_{eq/sub} \\ \rho c_p \frac{\partial T_{eq/sub}}{\partial t} &= -\vec{\nabla} \cdot \vec{q}\end{aligned}\quad (1.9)$$

where  $\vec{q}$  is the heat flux, while  $k$ ,  $\rho$  and  $c_p$  are the thermal conductivity (W/m K), the density ( $\text{kg/m}^3$ ) and the heat capacity (J/kg K) in the respective domains (in our case ND/substrate). At the interface between the nanoparticle and the substrate, however, the temperature is not continuous and the heat flux is regulated by the thermal boundary resistance (TBR) ( $\text{m}^2\text{K/W}$ ) [33]:

$$\vec{q} = \frac{1}{\mathcal{R}}(T_{eq}(t) - T_{sub}(t))\hat{u}\quad (1.10)$$

where  $\hat{u}$  is the versor perpendicular at the nanoparticle/substrate interface, and  $\mathcal{R}$  is the value of the TBR. Other sources of possible heat dissipation from the gold ND are neglected, as for instance the heat dissipation in air<sup>1</sup>.

It is worth to remark that the temperature within the gold ND,  $T_{eq}(t)$ , is almost uniform at each time  $t$ . To prove this, we need to compare the efficiency of thermal diffusion inside the ND to that of heat dissipation at the interface. This comparison is given by the ratio between the maximal temperature variation within the ND,  $T_{eq}(z=h) - T_{eq}(z=0)$  (i.e. the variation between the top ( $z=h$ ) and bottom ( $z=0$ ) ND basis) and the temperature jump at the ND/substrate interface,  $T_{eq}(z=0) - T_{sub}$ . Let’s write the conservation of heat flux at the interface:

$$|\vec{q}| = \frac{1}{\mathcal{R}}(T_{eq}(z=0) - T_{sub}) = |-k_{gnd}\vec{\nabla}T_{eq}(h=0)| \approx k_{gnd} \frac{T_{eq}(z=h) - T_{eq}(z=0)}{h},\quad (1.11)$$

<sup>1</sup>The Au/air TBR being much higher than the Au/sapphire one.

which allows us to calculate the degree of uniformity the temperature within the ND as:

$$\frac{T_{eq}(z = h) - T_{eq}(z = 0)}{T_{eq}(z = 0) - T_{sub}} = \frac{h}{k_{gnd}\mathcal{R}}. \quad (1.12)$$

$h/(k_{gnd}\mathcal{R})$  is exactly the Biot number  $Bi$  for the gold ND, whose purpose is indeed to determine if the temperature inside a body (with thermal conductivity  $k$  and characteristic length  $h$ ) is uniform or not, during a heat exchange process through a surface with a TBR of value  $\mathcal{R}$ . Taking a typical value for the TBR,  $\mathcal{R} \approx 2 \times 10^{-8} \text{ m}^2\text{K/W}$  [64, 65, 66],  $k_{gnd} = 317 \text{ W/(mK)}$  and  $h = 40 \text{ nm}$ , we obtain  $Bi \approx 6 \times 10^{-3} \ll 1$ . A  $Bi \ll 1$  implies that the temperature variation within the ND is negligible and we can consider the ND temperature as uniform at each time.

Finally, after several hundreds of ps or few ns, the entire heat accumulated in the ND is dissipated in the substrate and the ND returns to its initial equilibrium temperature.

### 1.3.1 Optical properties vs temperature evolution

The optical properties of the ND depend directly from the temperature. For this reason, the transient temperature inside the ND generates a time dependent variation of dielectric function real and imaginary components  $\Delta\epsilon_{1,2}(\lambda, t)$ . At the same time, since the heat dissipated from the ND is absorbed by the substrate, also a variation of the substrate dielectric function  $\Delta\epsilon_{sub}(\lambda, t)$  is present. In time-resolved spectroscopy, we measure the variation of the ND extinction cross section  $\Delta\sigma_{ext}(\lambda, t)$ , which depends on  $\Delta\epsilon_{1,2,sub}(\lambda, t)$  [67]. By doing a first order expansion, we can link the variation of the cross section to the variation of the dielectric constants:

$$\Delta\sigma_{ext}(\lambda, t) = \frac{\partial\sigma_{ext}}{\partial\epsilon_1}(\lambda)\Delta\epsilon_1(\lambda, t) + \frac{\partial\sigma_{ext}}{\partial\epsilon_2}(\lambda)\Delta\epsilon_2(\lambda, t) + \frac{\partial\sigma_{ext}}{\partial\epsilon_{sub}}(\lambda)\Delta\epsilon_{sub}(\lambda, t), \quad (1.13)$$

or, explicating the temperature dependence of the dielectric functions:

$$\Delta\sigma_{ext}(\lambda, t) = A_{gnd}(\lambda)\Delta T_{eq} + A_{sub}(\lambda)\Delta T_{sub}(t), \quad (1.14)$$

where

$$A_{gnd}(\lambda) = \frac{\partial\sigma_{ext}}{\partial\epsilon_1}(\lambda)\frac{d\epsilon_1}{dT_{eq}}(\lambda) + \frac{\partial\sigma_{ext}}{\partial\epsilon_2}(\lambda)\frac{d\epsilon_2}{dT_{eq}}(\lambda) \quad (1.15)$$

$$A_{sub}(\lambda) = \frac{\partial\sigma_{ext}}{\partial\epsilon_{sub}}(\lambda)\frac{d\epsilon_{sub}}{dT_{sub}}(\lambda). \quad (1.16)$$

We point out that a dependence on both the optical properties of the ND ( $\epsilon_{1,2}(\lambda, t)$ ) and of substrate ( $\epsilon_{sub}(\lambda, t)$ ) can lead to a not trivial temporal evolution of  $\Delta\sigma_{ext}$ . This is due to the fact that the temporal evolutions of the ND and of the substrate don't follow

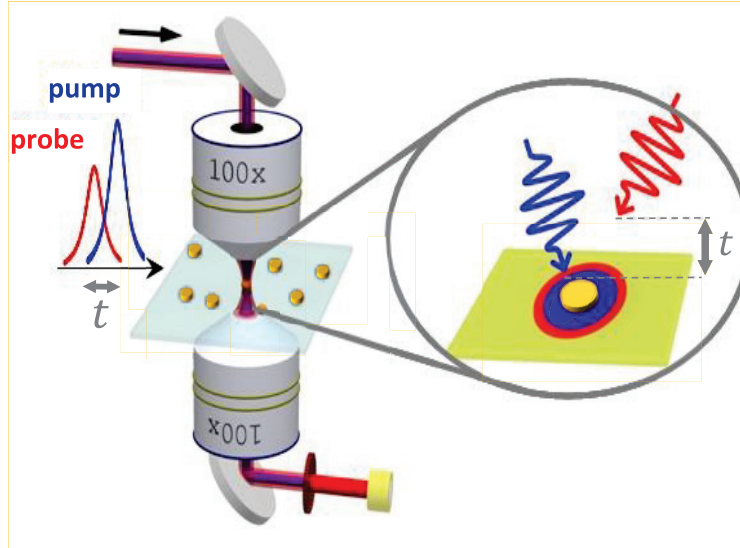


Figure 11. Scheme of pump-probe spectroscopy on single nanoparticle. Image taken from [1].

the same dynamics, with the first relaxing towards its initial value, while the second is still rising its temperature due to the incoming heat flux. Moreover, variations of the dielectric constants  $\Delta\epsilon_{1,2,sub}$  have different  $\lambda$  dependence. A complex temporal dynamics at different wavelength, then, may be expected for  $\Delta\sigma_{ext}$ . As we will see, however, in our investigations the sapphire substrate term won't contribute, and  $\Delta\sigma_{ext}$  will depend only on the optical properties of the gold ND.

### 1.3.2 Cooling dynamics of individual nanodisks

We have seen in Section 1.2 how the SMS technique allows us to align the selected gold ND in the center of the beams focal spot, assure its circular shape, extract its dimensions and linear properties  $\sigma_{ext}(\lambda)$ . After this procedure, the next step is to perform the time-resolved pump-probe measurements to unveil its cooling dynamics, i.e. measure  $\Delta\sigma_{ext}(\lambda, t)$ .

Figure 11 explains the principle of this pump-probe technique on a single nanoparticle. A pump pulse strikes the gold ND, exciting it and thus inducing a time dependent dynamics of its extinction cross section. The probe pulse, delayed in time by a motorized linear translation delay line of 15 cm with 3 round trips (corresponding to a maximal delay of 3 ns), impinges the ND and is transmitted through the substrate. By measuring the transmission of the probe pulse ( $T_{pr}$ ) with a photodiode as a function of the delay between pump and probe pulses, we are able to follow the time evolution of  $\Delta\sigma_{ext}(t)$  induced by the pump:

$$\frac{\Delta T_{pr}}{T_{pr}} = -\frac{\Delta\sigma_{ext}(\lambda_{pr})}{S_{pr}}, \quad (1.17)$$

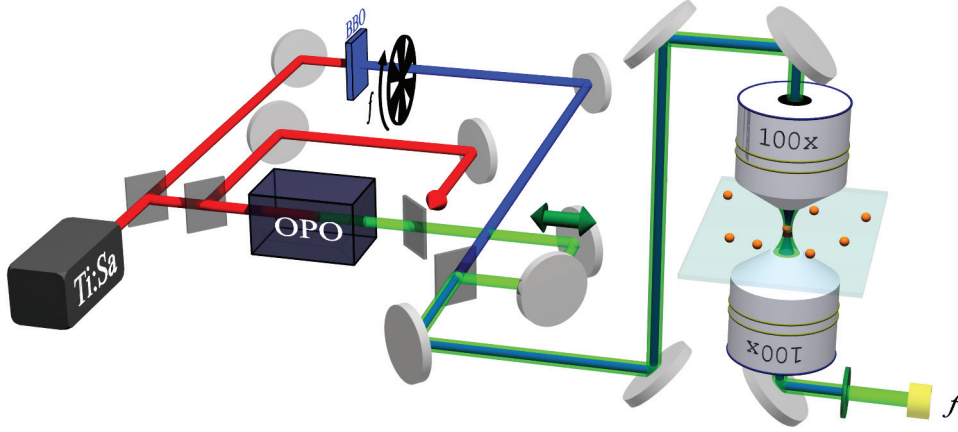


Figure 12. Laser sources schematics for the pump-probe experiments. The pump (blue beam) is the is frequency doubled output of the Ti:Sapphire oscillator (being then in the 375-520 nm range) and passes through the mechanical chopper of frequency  $f$ . The probe can be the direct output of the Ti:Sapphire (red beam, 750-1040 nm) or generated by the OPO (green beam, 500-750 nm). The delay between the pump and the probe beams is controlled by a delay line (dark green arrow). Image taken from [1].

where  $S_{pr}$  is the area of the probe beam (see [1] for more details). Note that these pump and probe experiments performed at single particle level provide a quantitative measurement of  $\Delta\sigma_{ext}$ , allowing for precise comparison with analytical or numerical models. The pump and probe pulses, in our configuration, are monochromatic beams with different wavelengths  $\lambda_{pp}$  and  $\lambda_{pr}$ . Figure 12 reports the scheme for the generation of the two beams. The output beam from the Ti:Sapphire oscillator is split in two different beams. One is frequency doubled by a second harmonic generator to produce the pump beam ( $\lambda_{pp} = 375 - 510$  nm). The probe beam is either the one from the Ti:Sapphire oscillator ( $\lambda_{pr} = 750 - 1040$  nm) or the one from the OPO ( $\lambda = 500 - 730$  nm). In order to detect weak variations  $\Delta\sigma_{ext}$ , we use a mechanical chopper with frequency 30 kHz in the pump beam path: in such a way we can enhance the signal to noise ratio by making use of a lock-in amplifier to demodulate the signal arriving at the photodiode and extracting only signals at that frequency (lock-in time constant is 100 ms in our measurements). Finally, to collect only the transmitted probe pulse, we use a edgepass filter, exploiting the different wavelength of the two beams and therefore cutting the pump. Pump-probe signals were acquired with 4 ps time step, while 12.5 ns are set between consecutive pump pulses (corresponding to a 80 MHz repetition rate), thus allowing the ND to returns to its equilibrium state before exciting it again.

### Cooling signal

Figure 13 (panel a) shows the cooling dynamics (black line) of a gold ND after excitation by the pump pulse. ND dimensions are  $h = 18$  nm and  $D = 100$  nm (measured

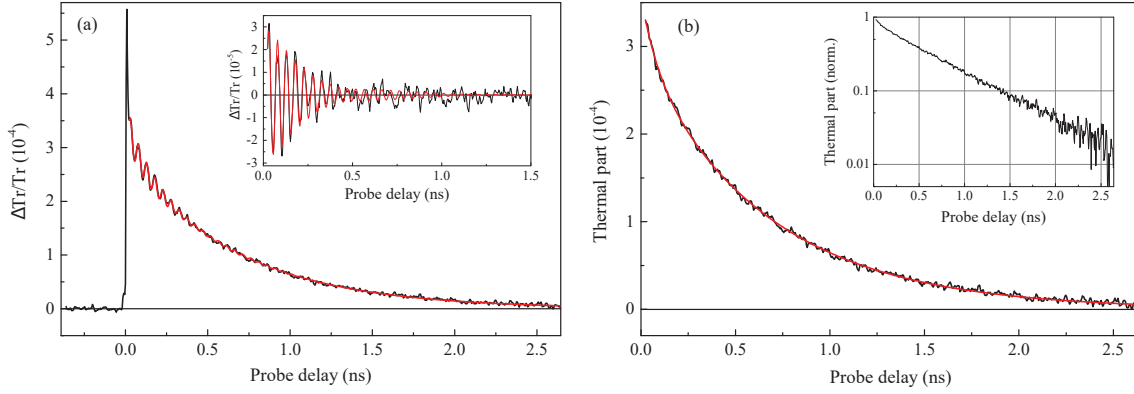


Figure 13. Complete  $\Delta Tr/Tr$  temporal evolution (panel a, black curve) and relative fit (red curve) with fit function from Equation 1.18 for a ND with  $h = 18$  nm and  $D = 100$  nm. Inset (panel a): experimental (black curve) and fit (red curve) oscillating mechanical part of the signal obtained by subtracting from the signal the two exponential terms corresponding to the thermal cooling. Panel b: same signal as in panel a but with the oscillatory part subtracted, thus isolating the ND cooling dynamics (black curve) and its biexponential fit (red curve). Inset (panel b): normalized thermal signal in semi-log scale. Image taken from [1].

by AFM). We can clearly see the different steps of the time evolution: the high electronic peak immediately after the pump absorption (at  $t=0$ , i.e. no delay between pump and probe), followed by the decay on a ns timescale linked to the ND cooling, while on a shorter timescale damped oscillations are the fingerprint of the vibrational modes presence. We can separate the different contributions by fitting the signal (red line in Figure 13) with a biexponential decay with characteristic times  $\tau_1$  and  $\tau_2$  (we set  $\tau_1 > \tau_2$ ), describing the ND thermal cooling, and damped sinusoidal oscillation functions, corresponding to the different vibrational modes of amplitude  $B_n$ , period  $T_n$ , phase  $\phi_n$ , characteristic damping time  $\tau_n^{osc}$ :

$$F_{fit}(t) = A_1 e^{-t/\tau_1} + A_2 e^{-t/\tau_2} + \sum_{n=1}^N B_n e^{-t/\tau_n^{osc}} \sin\left(\frac{2\pi t}{T_n} + \phi_n\right), \quad (1.18)$$

where  $N$  varies between 0 and 3 depending on the particular analyzed signal. In the inset of panel a (Figure 13), it is reported the oscillating part (black line) and its fit (red line), obtained by subtracting the double exponential decay (corresponding to the thermal part) from the total signal and its relative fit. In this case  $N = 2$  and the oscillation periods are found as 49 and 52 ps. Nevertheless, here we are mostly interested in the thermal dynamics of the system, i.e. the mechanical vibrations are an undesirable feature of the time-resolved signal, which we want to get rid off. For this purpose, we subtract from the signal the fit of the damped sinusoidal oscillations, remaining with solely the thermal cooling. Figure 13 (panel b) shows this thermal signal (black line) and its fit (red line) of the thermal cooling, while in the inset it is shown the thermal signal in normalized log-scale.

### Signal Dependence on the Probe Wavelength

Our optical set-up, as described at the beginning of this section, doesn't allow us to change fully independently the pump and probe wavelength  $\lambda_{pp}$  and  $\lambda_{pr}$ . When  $\lambda_{pr}$  is the direct output of the Ti:Sapphire oscillator (750-1040 nm), changing  $\lambda_{pr}$  leads to change also  $\lambda_{pp}$ , being equal to  $\lambda_{pr}/2$ . When instead  $\lambda_{pr}$  is generated by the OPO ( $\lambda_{pr} < 750$  nm), we can keep fixed  $\lambda_{pp} = 410$  nm. In order to bring out the effect of the pump—whose only purpose is to heat the ND—, we divide  $\sigma_{ext}$  by the estimated initial temperature rise  $\Delta T_{eq}$  ( $\Delta T_{eq} \approx 10$  K for a typical pump fluence  $\Phi$  of  $0.7$  J/m<sup>2</sup>). In this way, the quantity  $\Delta\sigma_{ext}(\lambda, t)/\Delta T_{eq}$  only contains the dependency on  $\lambda_{pr}$ . The time-resolved signals  $\Delta\sigma_{ext}(\lambda, t)/\Delta T_{eq}$  are shown in Figure 14 for the gold ND1 (panels a and c) and ND2 (panels b and d). We can clearly see the effect of  $\lambda_{pr}$  in panels a and b:  $\Delta\sigma_{ext}(\lambda, t)/\Delta T_{eq}$  changes significantly not only in the absolute amplitude, but also in the sign, having both positive (e.g.,  $\lambda_{pr} = 790$  nm (panel a) and 970 (panel b)) and negative (e.g.,  $\lambda_{pr} = 718$  nm (panel a) and 855 nm (panel b)) peaks.

In panels c and d, instead,  $\Delta\sigma_{ext}(\lambda, t)$  has been normalized and plotted in semi-log scale. From these plots, two features emerge: (i) the temporal dynamics is almost perfectly the same from all  $\lambda_{pr}$  and (ii) the temporal dynamics is a mono-exponential decay.

In Equation 1.13 we said that  $\Delta\sigma_{ext}(\lambda, t)$  depends on three different terms:  $\Delta\epsilon_{1,2}$  of the gold ND and  $\Delta\epsilon_{sub}$  of the substrate. Nevertheless, the  $\lambda_{pr}$ -independent time evolution of  $\Delta\sigma_{ext}(\lambda, t)$  and its mono-exponential behaviour are a strong proof that the substrate term  $\Delta\epsilon_{sub}$  has a negligible influence on the signals. A dependence on  $\Delta\epsilon_{sub}$ , indeed, would lead to a more complex temporal dynamics of  $\Delta\sigma_{ext}(\lambda, t)$ , with terms  $A_{sub}(\lambda)$  and  $\Delta T_{sub}(t)$  of Equation 1.14 playing a role in the signal dependence evolution, given their different behaviour in respect of  $A_{gnd}(\lambda)$  and  $\Delta T_{eq}(t)$  both regarding  $\lambda$  and  $t$ . This is at variance to what happens in other studies [67, 68], and can be rationalized in terms of the weak temperature dependence of the dielectric function of sapphire, resulting in a small  $A_{sub}(\lambda)$ , with  $d\epsilon_{sub}/dT \approx 10^{-5}$  K<sup>-1</sup> in the measured spectral range [69], in respect to  $d\epsilon_{1,2}/dT \approx 10^{-3}$  of gold [70]. Moreover, heat dissipation in the substrate is favored by sapphire high thermal conductivity (25 W/mK), meaning that the temperature rise in substrate close to the ND is minimal.

Having demonstrated that the substrate doesn't play a role in determining the time evolution of  $\Delta\sigma_{ext}$ , from equation 1.14 we obtain the direct proportionality between  $\Delta\sigma_{ext}$  and the gold ND temperature dynamics:

$$\Delta\sigma_{ext}(\lambda, t) = A_{gnd}(\lambda)\Delta T_{eq}(t). \quad (1.19)$$

We want to examine the wavelength dependent amplitude term  $A_{gnd}$ . This term can be extracted dividing the measured  $\Delta\sigma_{ext}$  at time  $t = 0$  (i.e. the peak of the time dependent signal) by the estimated temperature increase  $\Delta T(t = 0) = \Delta T_{eq}$ . Reformulating in

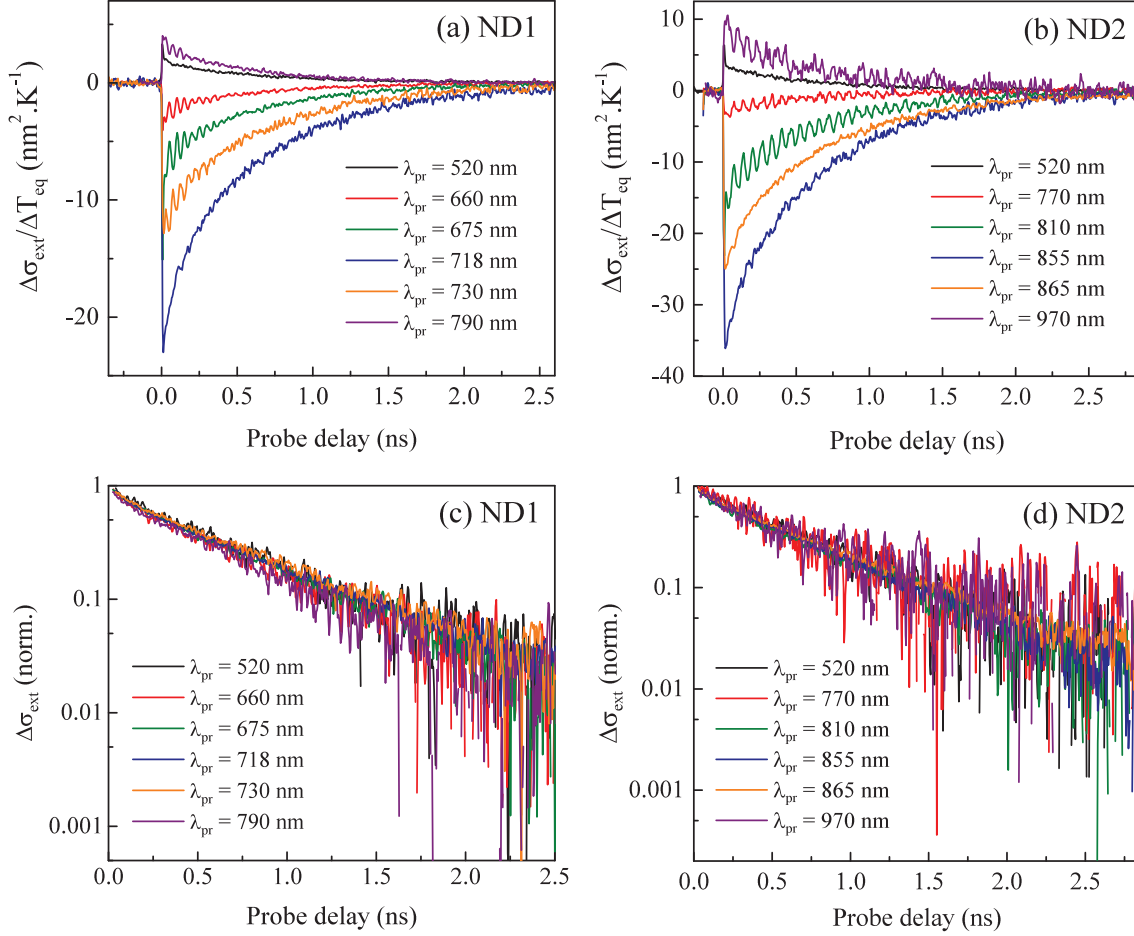


Figure 14. Experimental time-resolved signals  $\Delta\sigma_{ext}/\Delta T_{eq}$  measured on ND1 (panel a) and ND2 (panel b) with different probe wavelength  $\lambda_{pr}$  (colors in the legend). The pump wavelength  $\lambda_{pp}$  is 410 nm for signals with  $\lambda_{pr} < 750$  nm, while  $\lambda_{pp} = \lambda_{pr}/2$  for  $\lambda_{pr} > 750$  nm. Normalized thermal components of the same signals in semi-log scale (panels c and d). Image taken from [1].

a more operative way, we take the amplitudes  $A_1 + A_2$  of the bi-exponential decay fit function of Equation 1.18 and multiply by  $S_{pr}$  (see Equation 1.17). In this way we obtain:

$$A_{gnd} = \frac{\Delta\sigma_{ext}(t=0)}{\Delta T_{eq}} = \frac{-S_{pr}(A_1 + A_2)}{\Delta T_{eq}}. \quad (1.20)$$

Figure 15 shows the experimental  $A_{gnd}(\lambda)$  (black points) for the two investigated gold NDs (panels a and b). Error bars take into account the error on the dimension of the probe spot, as well as the pump power (influencing  $\Delta T_{eq}$ ) and the error on  $A_{1,2}$  (for more details consult [1]).

This experimental result can be compared to the  $A_{gnd}$  calculated with our model. In computing  $A_{gnd}$ , two terms have to be considered:  $\partial\sigma_{ext}/\partial\epsilon_{1,2}$ , which are evaluated by the FEM simulations spectra (see Figure 9) and  $d\epsilon_{1,2}/dT$ . Different values are found in the literature for the latter [71, 72, 73, 74, 75, 76]; thus we decided to use two different

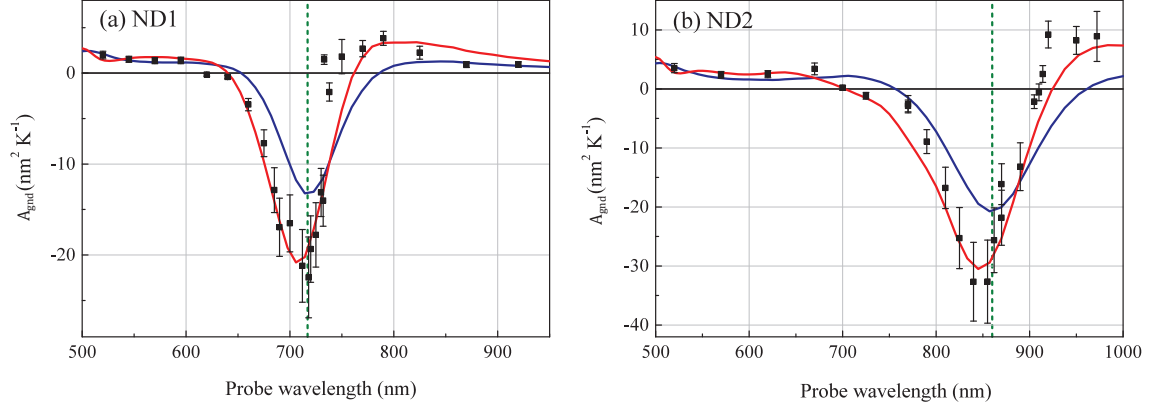


Figure 15.  $A_{gnd}$  coefficients at different wavelength obtained from the amplitude of the thermal components in experimental measures (black dots).  $A_{gnd}$  theoretical calculation based on Equation 1.15 using  $\partial\sigma_{ext}/\partial\epsilon_{1,2}$  obtained by FEM simulations (Figure 9) and  $d\epsilon_{1,2}/dT$  taken from references [70] (blue curves) and [71] (red curves). The dashed green vertical lines indicate the LSPR central position for the relative ND. Image taken from [1].

references: one experimental [70] (blue lines in Figure 15), the other theoretical [71] (red lines). In this way, for each gold ND we obtain two different theoretically calculated  $A_{gnd}$ . Nevertheless, both are in good agreement with our quantitative experimental results. As can be seen,  $A_{gnd}$  has a large amplitude of negative sign close to the LSPR (vertical dashed green lines), and smaller positive values on the LSPR sides, in agreement with amplitudes at time  $t = 0$  in Figure 14.

### 1.3.3 Cooling dynamics: ND morphology and TBR

The cooling dynamics of 60 NDs with different heights and diameters were measured exploiting the direct proportionality between the time-resolved signals and the NDs temperature. For all the measurements, the pump had  $\lambda_{pp} = 410$  nm with low fluence ( $< 1$  J/m<sup>2</sup>) in order to obtain a temperature rise of  $\approx 10$  K, small enough to avoid any ND modification during the measurement. The probe wavelength  $\lambda_{pr}$ , instead, was fixed at 510 nm, far from the LSPR of any ND in the chosen size range. Keeping  $\lambda_{pr}$  fixed for the entire experiment allows to measure several NDs with only small realignment of the pump and probe beams during the acquisition, reducing the intrinsic dispersion of data during the measurements with frequent realignments.

Acquired signals were fit with the function in Equations 1.18, then the mechanical oscillations were subtracted, remaining only with the thermal dynamics.

Figure 16 contains the normalized thermal signals of NDs with different heights ( $h = 18$  and 40 nm) and diameters ( $D$  ranging from 65 to 205 nm). The dynamics is strongly dependent on  $h$  and only weakly on  $D$ . All measurements shows a mono-exponential decay for times  $> 500$  ps, with a characteristic time decay  $\tau_1$  of  $\approx 0.7$  and 1.7 ns for  $h = 18$  and 40 nm, respectively. This kind of exponential behaviour strongly suggests a

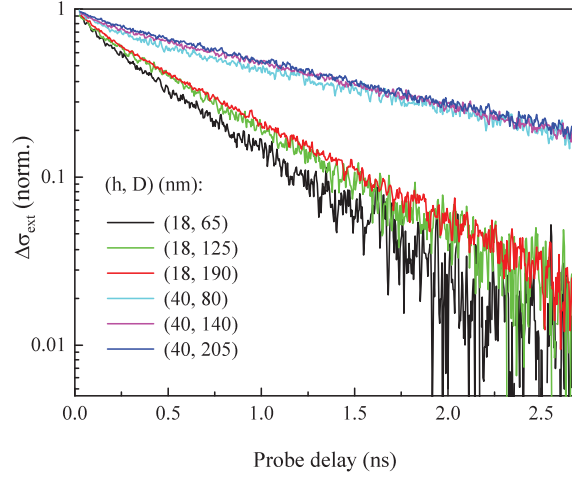


Figure 16. Normalized experimental thermal components of time-resolved signals for NDs with different height (18 and 40 nm) and diameters (ranging from 65 to 205 nm). Imaged taken from [1].

cooling dynamics limited by the interface heat transport [35, 36]. If the temperature within the ND is uniform at each given time (condition satisfied since, as we have seen, the Biot number is  $\ll 1$ ) and the substrate temperature is almost isothermal (justified by the high sapphire thermal conductivity) then the heat transfer is described only by Equation 1.10, where  $T_{sub}(t) = T_0$ :

$$|\vec{q}| = \frac{\rho_{gnd} c_{gnd} V}{S} \frac{dT_{eq}}{dt} = \frac{1}{\mathcal{R}} (T_{eq}(t) - T_0), \quad (1.21)$$

with  $V$  and  $S$  being the ND volume and surface in contact with the substrate. The solution of this differential equation is a mono-exponential decay of  $T_{eq}$  with characteristic time  $\tau = \rho_{gnd} c_{gnd} h \mathcal{R}$ . The proportionality between  $\tau$  and  $h$ , is in good agreement with the measurements:  $\tau_1(40\text{nm})/\tau_1(18\text{nm}) = 2.4 \approx 40/18$ . An estimation of  $\mathcal{R}$  from  $\mathcal{R} = \tau/(\rho_{gnd} c_{gnd} h)$ , gives a value of  $1.6 \times 10^{-8} \text{ m}^2\text{K/W}$ , in agreement with range for the gold/sapphire TBR ( $1 - 5 \times 10^{-8} \text{ m}^2\text{K/W}$ ) found in the literature for thin gold films [34, 64, 65, 66].

In addition to this simple analysis, we also performed FEM simulations, including Fourier's law with finite thermal conductivity in the sapphire substrate and the temperature gradient in the gold ND (non uniform temperature). Figure 17 shows results from these simulations for two NDs with  $h = 40 \text{ nm}$  and  $D = 80 \text{ nm}$  (orange curves) and  $D = 160 \text{ nm}$  (purple curves). The resulting dynamics, as expected, are slightly slower than the ideal case described by Equation 1.21 (blue dashed line), since the finite thermal conduction in the substrate slightly increase the local temperature in sapphire, close to the ND/substrate interface, thus reducing the heat flux from the ND. Moreover, the dynamics slightly deviates from a mono-exponential behaviour, but the non-exponential character is observable only at for times exceeding the experimental ones.

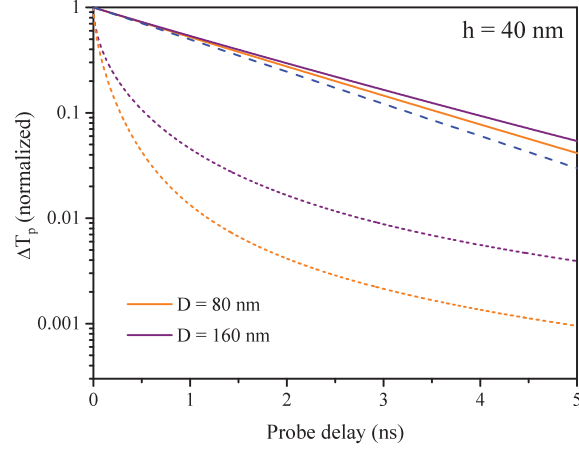


Figure 17. Normalized temperature dynamics calculated with FEM simulations for NDs with height  $h = 40$  nm and diameters  $D = 80$  nm (plain orange curve) and  $D = 160$  nm (plain purple curve) for a TBR value of  $\mathcal{R} = 1.4 \times 10^{-8}$  m<sup>2</sup>K/W. Same but with infinite substrate thermal conductivity (blue dashed line - note that in this case the two dynamics are equal). Cooling dynamics in the case of vanishing TBR  $\mathcal{R} \rightarrow 0$  (dotted lines). Image taken from [1].

The simulations confirm that the dynamics is mostly governed by the TBR at the interface. Numerically vanishing the TBR ( $\mathcal{R} \rightarrow 0$ ), indeed, drastically speeds up the heat dissipation, with a strong deviation from the measured dynamics (dotted lines in Figure 17).

The value of the TBR was then fitted using the FEM model that includes finite thermal conductivity in sapphire and non-uniform temperature in the ND. In this way, we can compare the characteristic time  $\tau$  of the simulated dynamics at different TBR values  $\mathcal{R}$ , with  $\tau_1$  measured from experimental data.

Figure 18 shows the extracted characteristic times as a function of the diameter for

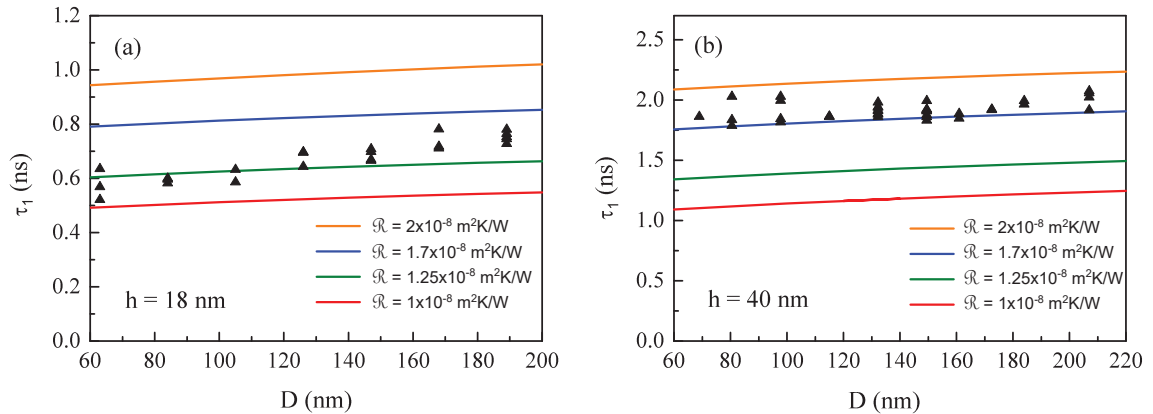


Figure 18. Experimental (black triangles) and simulated (colored lines) time constants  $\tau_1$  of the cooling dynamics for NDs with different diameters and different height (in panel a  $h = 18$  nm and in panel b  $h = 40$  nm). The different colors represents simulations with different TBR values (see legend). Image adapted from [1].

experimental data (black triangles) and FEM simulations (colored lines). This comparison between single particle experiments and modeling allows for a quantitative extraction of

the interface thermal property, which presets weak fluctuations from one nano-object to the other. In the  $h = 18$  nm case (panel a), the different  $\tau$  are well reproduced taking  $\mathcal{R} = 1.3 \pm 0.3 \times 10^{-8}$  m<sup>2</sup>K/W. For the  $h = 40$  nm NDs (panel b), experimental data are well fit by simulations for a slightly higher  $\mathcal{R} = 1.6 \pm 0.3 \times 10^{-8}$  m<sup>2</sup>K/W for the different investigated diameters. The difference in the TBR values for the two different samples could be due to different fabrication sessions that may have introduced small differences in the gold/sapphire interfaces.

## 1.4 Transient electrons and lattice dynamics

In Section 1.3 we described the cooling dynamics of gold NDs in contact with a sapphire substrate, after a short (fs) light pulse excitation. There, the focus was on phenomena occurring after few ps, when electrons and lattice have already reached a common temperature  $T_{eq}(t)$ , and we described the time evolution of the extinction cross section  $\sigma_{ext}$  always in terms of the common electron-lattice temperature  $T_{eq}(t)$ . This description explains thermal phenomena occurring in nanoparticles on a ns timescale. In the first  $\approx 10$  ps after the arrival of the pump pulse, however, the common temperature  $T_{eq}(t)$  is not yet established, electron-electron and electron-lattice thermalization still occurring<sup>2</sup>.

In this section we extend the description of the thermal phenomena to the ps timescale. In parallel with the ns timescale pump-probe measurements, indeed, we also performed measurements with a shorter time windows of 10 ps. We will see that, at such short timescale,  $\Delta\sigma_{ext}(t)$  strongly depends on the probe wavelength  $\lambda_{pr}$ , reflecting a complex dynamics during the electron-electron and electron-lattice thermalization. Finally, we will briefly introduce a theoretical model describing the influence on the Au dielectric function of the electron and the lattice heating, with which we are able to rationalize the phenomena occurring. We will see how these distinct dynamics can be selectively probed through the use of different  $\lambda_{pr}$ .

### 1.4.1 Experimental data

Experimental data were acquired on the same two gold NDs (ND1 and ND2) on which we performed the ns timescale measurements at different  $\lambda_{pr}$  (see Figure 14). In this way, we already possess the SMS  $\sigma_{ext}(\lambda)$  spectra for the two NDs (see Figures 7 and 9), which will be fundamental for modeling the  $\Delta\sigma_{ext}(\lambda, t)$  dynamics at the ps timescale. The optical set-up employed is the same as for the ns timescale measurements, the only different being the 10 ps time window and the time step, now reduced to 30 fs. Pump fluences were always kept low ( $< 1$  J/m<sup>2</sup>) to avoid any significant change in the NDs during

---

<sup>2</sup>Note that experimental data in Section 1.3.2 were taken with 4 ps time steps thus hiding faster processes.

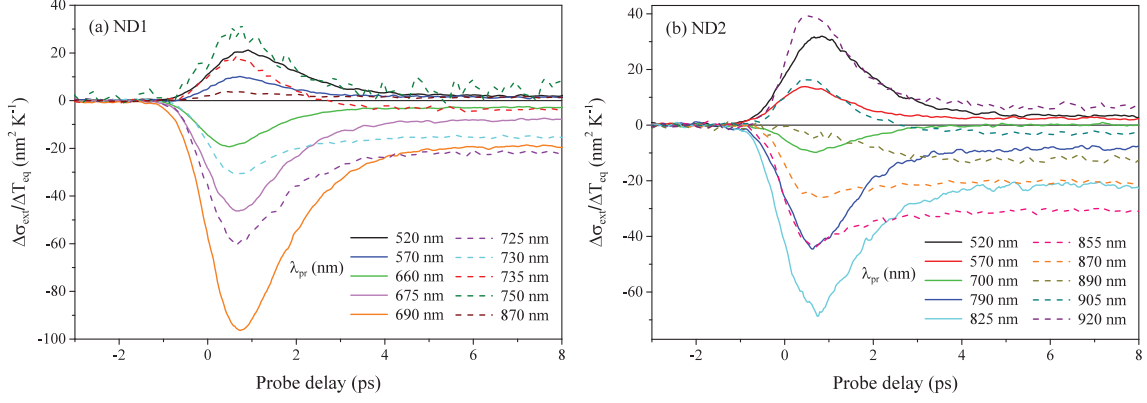


Figure 19.  $\Delta\sigma_{ext}/\Delta T_{eq}$  time evolution in the ps timescale at different probe wavelength  $\lambda_{pr}$  (different colors, see legend) measured on ND1 (panel a) and ND2 (panel b). Image taken from [1].

the measurements.

Particular attention to the pump power was necessary, since the electron-lattice energy exchange depends on the amount of energy absorbed by electrons from the light pulse. In other words, the characteristic time of the electron-lattice thermalization dynamics depends non trivially on the electron temperature  $T_e$ , due to the dependence of the electronic heat capacity on  $T_e$  (see [1] for more details). For this reason, all measurements should be performed keeping  $\Delta T_{eq}$  constant. Fixed  $\Delta T_{eq}$  is easily obtainable for probe pulses generated by the OPO, when  $\lambda_{pp}$  remains fixed at 410 nm for all measurements. On the contrary, pump generated by the Ti:Sapphire laser,  $\lambda_{pp} = \lambda_{pr}/2$ , which leads to intrinsic dispersion of the energy delivered by the pump and thus of  $\Delta T_{eq}$ .  $\Delta T_{eq}$  average values and standard deviations are  $10 \pm 3$  K for ND1 and  $6 \pm 2$  K for ND2. Still, as for the ns timescale analysis, we plot  $\Delta\sigma_{ext}/\Delta T_{eq}$ , but we need to keep in mind that the  $\Delta T_{eq}$  normalization could be only partially adequate to get rid of the  $T_{eq}$  dependence at the ps timescales.

Figure 19 shows the  $\Delta\sigma_{ext}/\Delta T_{eq}$  time evolution at the ps timescale for different  $\lambda_{pr}$  (see colors in the legends) in ND1 (panel a) and ND2 (panel b). As for signals in the ns timescale (see Figure 14), also in the ps timescale case signal amplitudes and peaks signs (positive/negative) change significantly at different  $\lambda_{pr}$ . However, at variance with the ns timescale case, here  $\Delta\sigma_{ext}/\Delta T_{eq}$  displays very different temporal dynamics at different  $\lambda_{pr}$ . This is even more evident in Figure 20, where the  $\Delta\sigma_{ext}$  time evolution is normalized by its peak value. Almost all signals display a fast rise around  $t = 0$  ps (zero delay between pump and probe pulses), followed by a decay dynamics with ps characteristic time. The normalized values of  $\Delta\sigma_{ext}$  at  $t = 8$  ps, however, change significantly at different  $\lambda_{pr}$ : there are negative values (e.g.,  $\lambda_{pr} = 735$  nm for ND1), values close to zero ( $\lambda_{pr} = 700$  nm for ND2) or close to one ( $\lambda_{pr} = 855$  nm for ND2). Moreover, ND2 presents, at  $\lambda_{pr} = 890$ , no peak close to  $t = 0$  ps, but a slow rise starting at  $t \approx 0$  and ending at  $t \approx 5$  ps, followed by a constant value.

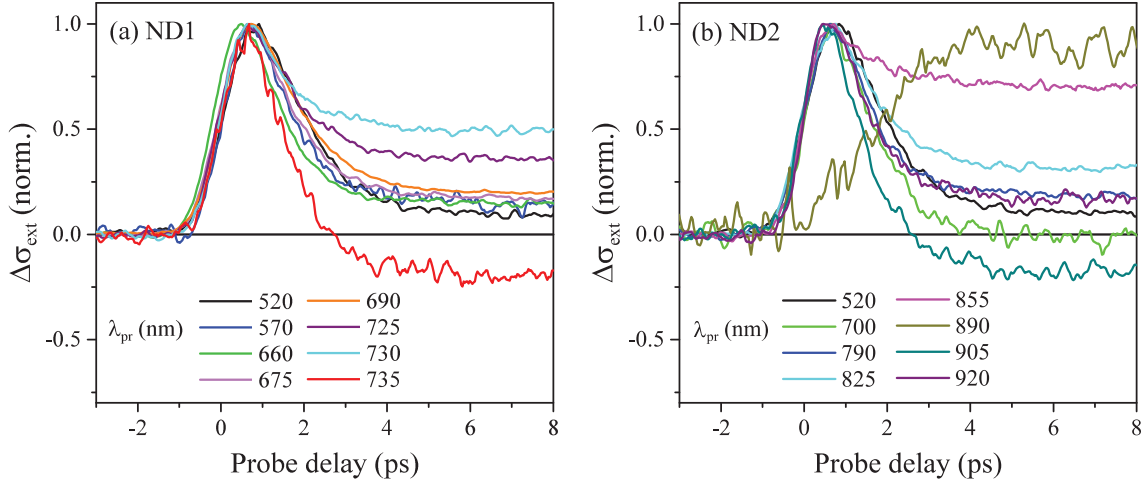


Figure 20. Normalized  $\Delta\sigma_{ext}$  time evolution in the ps timescale at different probe wavelength  $\lambda_{pr}$  (different colors, see legend) measured on ND1 (panel a) and ND2 (panel b). Image taken from [1].

## 1.4.2 Modelling the transient optical response of gold NDs

In the following, we introduce in steps the theoretical model which allows to describe the experimental measurements. The following description shows the main ingredients to explain the phenomena involved. A more detailed description of the model can be found in [1, 3].

- The distribution function of gold quasi-free electrons in the conduction band,  $f(E)$ , follows a time evolution after the injection of energy in the system by the pump pulse. This  $f(E, t)$  evolution is computed with a bulk-like approach by numerically solving Boltzmann equation [71, 77]. This approach includes three phases: the initial pulse excitation which leads to an athermal electron distribution, the thermalization of the electron gas by electron-electron scattering (hundreds of fs) and the electron-lattice energy transfer by electron-phonon scattering (few ps).

- The electronic energy excess density,  $\Delta u_e(t)$ , and corresponding temperature increase,  $\Delta T_e(t)$ , are deduced from  $\Delta f(E, t) = f(E, t) - f_0(E)$ , where  $f_0$  is the initial electronic Fermi-Dirac distribution at room temperature. In particular, the ND absorbs an energy density  $u_{abs}$ , which depends on the ND absorption cross section  $\sigma_{abs}$  and the power of the pump pulse (fluence  $\Phi \approx 0.6 \text{ J/m}^2$  in our experiments). An excitation temperature  $T_{exc}$ , i.e. the temperature electrons would achieve at the end of thermalization in absence of electron-phonon coupling, can be defined through the relation  $u_{abs} = \int_{T_0}^{T_{exc}} c_e(T_e) dT_e$ , with  $c_e = aT_e$  being the volumetric electronic heat capacity ( $a \approx 65 \text{ J/K}^2\text{m}^3$ ). From this integral, we obtain  $T_{exc} = (T_0^2 + 2u_{abs}/a)^{1/2}$ . In a similar way, we can define an equivalent temperature  $T_e(t)$  (i.e. associated with a Fermi-Dirac distribution with

same excess energy) from the time dependent excess energy density  $\Delta u_e(t)$ , resulting in  $T_e(t) = (T_0^2 + 2\Delta u_{abs}(t)/a)^{1/2}$ .

- The lattice excess energy density,  $\Delta u_L(t)$ , and corresponding lattice temperature increase,  $\Delta T_L(t)$ , are computed at each time step exploiting energy conservation for the electron-lattice system, i.e. assuming that the energy lost by the electrons is entirely transferred to the lattice. Finally,  $\Delta T_{eq}$  is the equilibrium temperature rise of the ND after its full internal electron-lattice thermalization.

- In a complete model, knowing  $\Delta f(E, t)$  and  $\Delta T_L(t)$ , we are able to determine the transient change of the ND dielectric function  $\Delta \epsilon(t)$  at each time step. The dielectric function  $\epsilon$  of Au bulk (with real  $\epsilon_1$  and imaginary  $\epsilon_2$  components) in the visible/near-infrared range can be written as the sum of two frequency dependent components, related to the interband and intraband (Drude-like) absorption mechanisms [27, 78, 79]:

$$\epsilon(\omega) = \epsilon^{ib}(\omega) + \epsilon^D(\omega) - 1 = \epsilon^{ib}(\omega) - \frac{\omega_p^2}{\omega(\omega + i\gamma)}, \quad (1.22)$$

where  $\omega_p$  is the plasma frequency ( $\hbar\omega_p \approx 9$  eV for bulk gold) and  $\gamma$  is the optical scattering rate of the conduction electrons ( $\hbar\gamma \approx 50$  meV for bulk gold). We use Johnson and Christy  $\epsilon_{JC}$  tables [80] as a reference for values of the bulk gold dielectric function. With that, we can deduce the interband component as  $\epsilon^{ib} = \epsilon_{JC} + \frac{\omega_p^2}{\omega(\omega + i\gamma)}$ , which we then theoretically reproduce knowing the gold band structure [71, 81] (see [3] for more details). This procedure, initially performed for a Fermi-Dirac electron distribution at room temperature, is reiterated for different electronic and lattice temperatures for non-thermal, i.e. non-Fermi-Dirac, electronic distributions, thus allowing to predict the temporal evolution of  $\epsilon^{ib}$  in time-resolved experiments.

- The dielectric function  $\epsilon$  in the NDs is a function of both the electronic distribution  $f(E)$  and the lattice temperature  $T_L$ . Given that typically  $\Delta T_L < 10$  K in our measurements, we can linearize the  $\epsilon$  dependence on  $T_L = T_0 + \Delta T_L$  as

$$\epsilon(f, T_L) \approx \epsilon(f, T_0) + \frac{\partial \epsilon}{\partial T_L}(f, T_0) \Delta T_L. \quad (1.23)$$

Numerical investigations shows that  $\frac{\partial \epsilon}{\partial T_L}(f, T_0)$  does not strongly depend on the electronic distribution [71], and thus we can approximate it as a constant  $\frac{\partial \epsilon}{\partial T_L}(f_0, T_0)$ . With this approximation, the modifications on  $\epsilon$  can be fully separated in an electronic and a lattice contributions, resulting from the modification of the electronic distribution,  $\Delta \epsilon_e(t)$  and from the increase in the lattice temperature  $\Delta T_L(t)$ :

$$\Delta \epsilon(t) = \Delta \epsilon_e(t) + \Delta \epsilon_L(t) \quad (1.24)$$

where

$$\Delta\epsilon_e(t) = \epsilon(f(t), T_0) - \epsilon(f_0, T_0) = \Delta\epsilon_e^{ib}(t) + \Delta\epsilon_e^D(t) \quad (1.25)$$

$$\Delta\epsilon_L(t) = \frac{\partial\epsilon}{\partial T_L}(f_0, T_0) \Delta T_L(t), \quad (1.26)$$

where we expressed explicitly the interband and Drude components of the electronic dielectric part. Note that  $\Delta\epsilon_L(t)$  is proportional to  $\Delta T_L(t)$ , while the dependence of  $\Delta\epsilon_e(t)$  on the electronic temperature is more complex.

The two components in the electronic contribution  $\Delta\epsilon_e(t)$  were calculated separately.  $\Delta\epsilon_e^{ib}(t)$ , associated with the variation in the probability of interband transitions between the conduction and the valence band caused by the evolution of the electron distribution  $f(E, t)$ , was calculated by reproducing the calculation explained above with  $f(E, t)$  obtained at multiple times  $t$  by solving Boltzmann equation. Moreover, the modification of  $f(E, t)$  generates a  $\Delta\epsilon_e^D(t)$  change of the Drude component, dominated by the modification of the electron-electron scattering rate  $\gamma_{e-e}$  which contributes to the total scattering rate in the Drude component of  $\epsilon$ . The variation of  $\gamma_{e-e}$  has been predicted to be quadratic with the electron temperature  $T_e$  [71, 82] (see [3] for more details on the equation for  $\Delta\gamma_{e-e}$ ).

The temperature rise in the lattice is responsible for modification of the probability of interband electronic transitions (by lattice dilatation), the scattering rate of electrons (change in the electron-phonon scattering rate) and the plasma frequency  $\omega_p$  (change in the electron density). However, since in our measurements we are in a small  $\Delta T_L$  regime, the optical consequences of lattice heating can be summarized by a single  $d\epsilon/dT_L$  term, calculated in the literature from a theoretical model accounting for all the effects mentioned above [71].

- Combining  $\Delta\epsilon(t)$  with the computed optical derivatives  $\partial\sigma_{ext}/\partial\epsilon_1$  and  $\partial\sigma_{ext}/\partial\epsilon_2$ , we are able to predict the cross section variations  $\Delta\sigma_{ext}(\lambda_{pr}, t)$  of gold NDs, which we can compare to the experimental data. We already described the SMS spectra of the two NDs (Figure 7 in Section 1.2.2). Then, we said that with tailored FEM simulations we can extract the NDs size as well as their absorption and scattering cross-sections contributions to the total extinction cross section  $\sigma_{ext}$  (Figure 8) and its derivatives  $\partial\sigma_{ext}/\partial\epsilon_{1,2}$  (Figure 9). In this way, and by making explicit use of the two components in the variation of the dielectric function  $\Delta\epsilon_{1,2}(\lambda_{pr}, t)$ , we can deduce the variation of the extinction cross section:

$$\Delta\sigma_{ext}(\lambda_{pr}, t) = \frac{\partial\sigma_{ext}}{\partial\epsilon_1}(\lambda_{pr})\Delta\epsilon_1(\lambda_{pr}, t) + \frac{\partial\sigma_{ext}}{\partial\epsilon_2}(\lambda_{pr})\Delta\epsilon_2(\lambda_{pr}, t), \quad (1.27)$$

(at these short timescales the environment heating is negligible). From this equation and using the simplified model, it follows that we can decompose  $\Delta\sigma_{ext}(\lambda_{pr}, t)$  in the sum of

two components, associated to the electronic and lattice heating:

$$\Delta\sigma_{ext}(\lambda_{pr}, t) = \Delta\sigma_{ext,e}(\lambda_{pr}, t) + \Delta\sigma_{ext,L}(\lambda_{pr}, t). \quad (1.28)$$

### 1.4.3 Experimental data and theoretical model

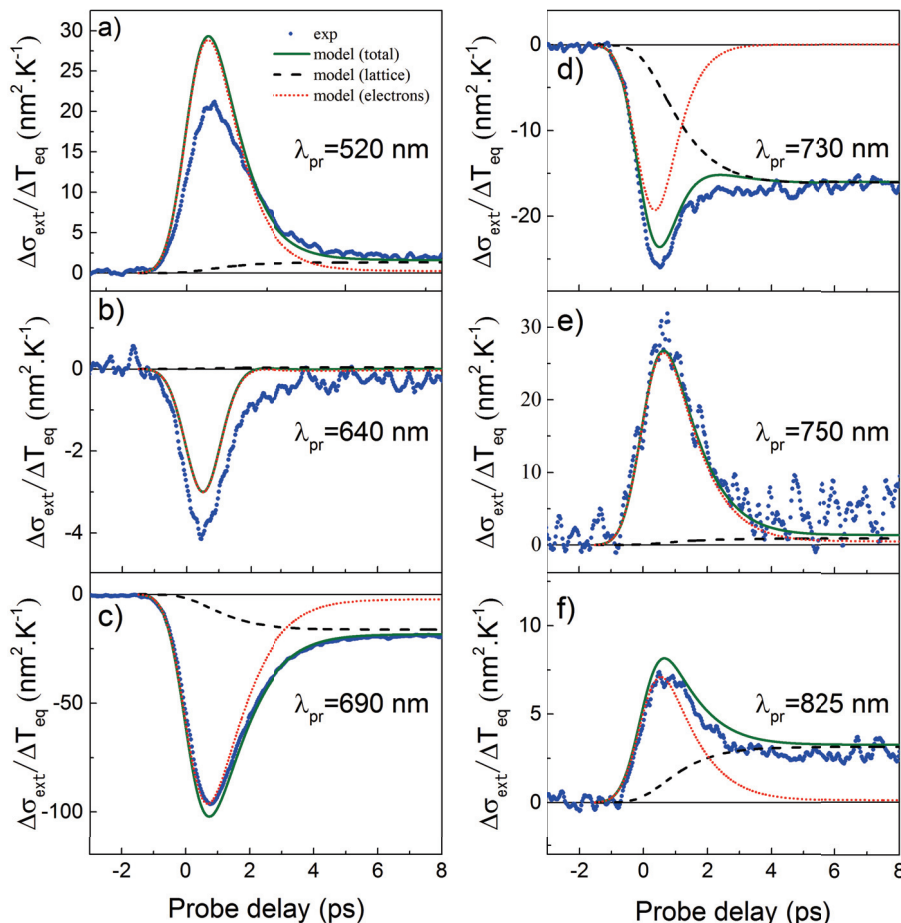


Figure 21. Comparison between experimental data (blue dots) and the theoretical calculation (green lines) at different  $\lambda_{pr}$  (different panels) performed on ND1. The theoretical calculation is given by the sum of electron contribution,  $\Delta\sigma_{ext,e}$  (red dotted lines), and the lattice contribution,  $\Delta\sigma_{ext,L}$  (black dashed lines). Reprinted with permission from [3]. Copyright 2021 American Chemical Society.

Measured signals were quantitatively compared with calculations carried out by the model described above. The agreement between experimental and simulated signals was found to be optimized by a characteristic time of the electron-lattice energy transfer  $\tau_{e-L} \approx 800$  fs, a value slightly smaller than the one measured on large diameter colloidal gold nanoparticles [83]. Figure 21 and Figure 22 shows the comparison between the experimental data (blue dots) and the theoretical calculation (green line) at different  $\lambda_{pr}$  for ND1 and ND2, respectively. Overall simulations are in good agreement with experimental data in terms of amplitude and dynamics for almost all  $\lambda_{pr}$ , with just some discrepancy

in the amplitude for certain  $\lambda_{pr}$  (520 nm for ND1 and 915 nm for ND2). The possibility to distinguish the components associated to the electron,  $\Delta\sigma_{ext,e}$  (red dotted lines), and the lattice,  $\Delta\sigma_{ext,L}$  (black dashed lines), allows us to clarify the origins of the measured transient signals and explain their temporal profiles. Signals decreasing to almost zero at the end of the ND internal thermalization, such as  $\lambda_{pr} = 640$  nm for ND1 (panel b in Figure 21) and  $\lambda_{pr} = 725$  and 915 nm for ND2 (panels a and f in Figure 22), correspond to cases in which the lattice heat doesn't contribute significantly to  $\Delta\sigma_{ext}$ . Such signals thus reflect the heating and cooling dynamics of the electrons in the NDs.

On the other hand, the signal at  $\lambda_{pr} = 890$  nm for ND2 (panel d in Figure 22) presents a slow increase (in absolute value) of the signal with no fast peak close to  $t = 0$ . This corresponds to the case in which electron heating have a negligible impact on the transient extinction signal.

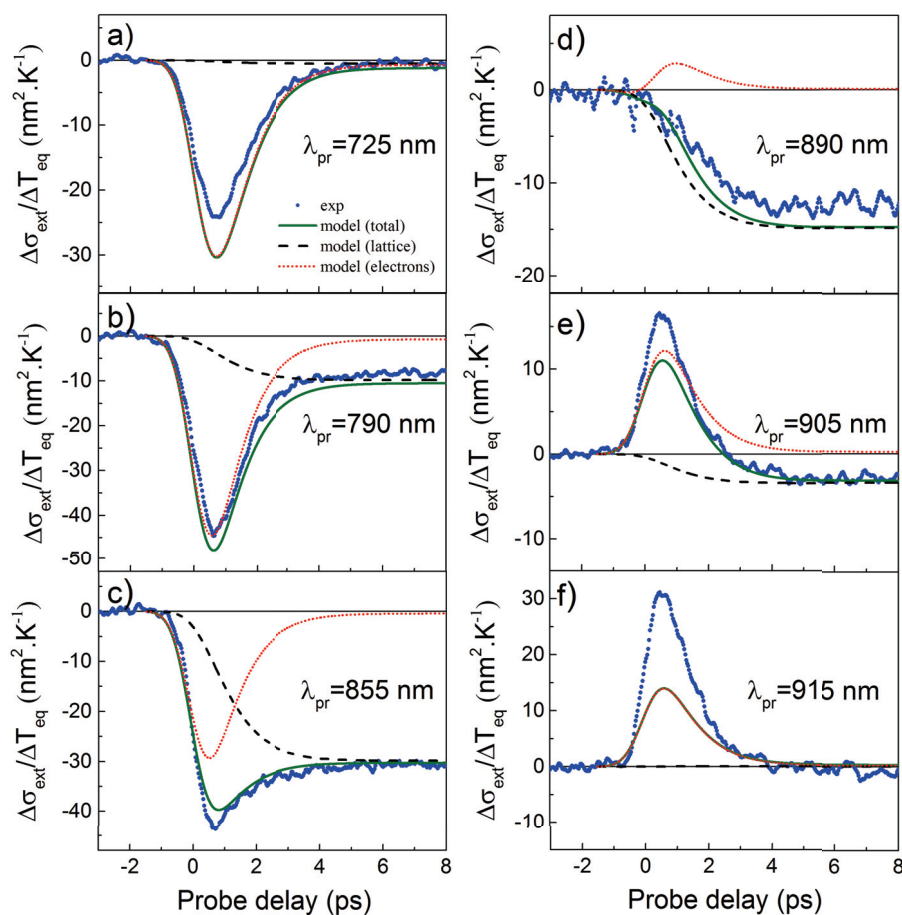


Figure 22. Comparison between experimental data (blue dots) and the theoretical calculation (green lines) at different  $\lambda_{pr}$  (different panels) performed on ND2. The theoretical calculation is given by the sum of electron contribution,  $\Delta\sigma_{ext,e}$  (red dotted lines), and the lattice contribution,  $\Delta\sigma_{ext,L}$  (black dashed lines). Reprinted with permission from [3]. Copyright 2021 American Chemical Society.

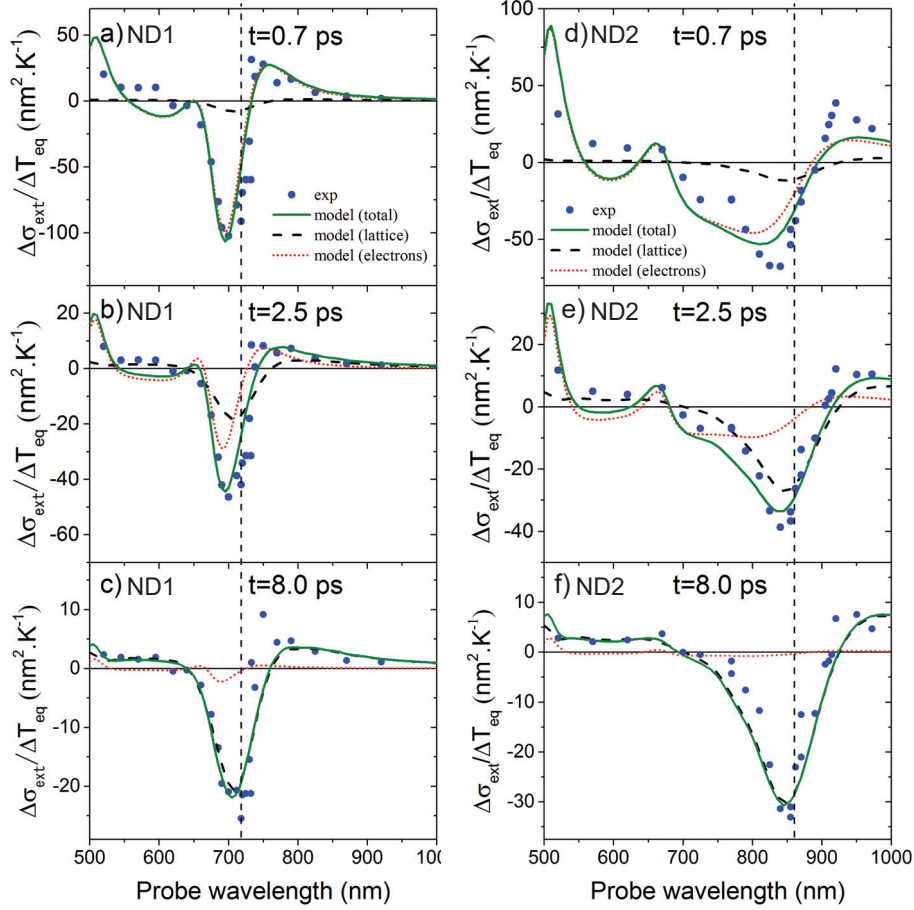


Figure 23. Experimental (blue dots) and theoretical (green lines) transient extinction spectra at specific delays for ND1 (left) and ND2 (right). Pump-probe delays are fixed at 0.7 ps (panels a and d), 2.5 ps (panels b and e) and 8 ps (panels c and f). The simulated transient extinction spectra are the results of the electron (red dots) and the lattice (black dashed lines) contributions. Vertical dashed lines indicate the central position of the SPR. Reprinted with permission from [3]. Copyright 2021 American Chemical Society.

A third particular case is that of signals presenting a constant  $\Delta\sigma_{ext}$  background value after the end of the ND excitation and electron thermalization (after  $\approx 2$  ps) and a peak prior to the full ND internal thermalization, such as  $\lambda_{pr} = 730$  nm for ND1 (panel d in Figure 21) and  $\lambda_{pr} = 855$  nm for ND2 (panel c in Figure 22). In such cases, the temporal variations of  $\Delta\sigma_{ext,e}$  and  $\Delta\sigma_{ext,L}$ , induced by electron-phonon energy exchanges, compensate each other so that their sum  $\Delta\sigma_{ext}$  remains constant.

All other signals present a less specific dynamics, resulting from both electron and lattice time dependent contributions have to be taken into account to describe the observed dynamics.

An alternative way to observe the electron and lattice contributions to  $\sigma_{ext}$  dependence on the pump-probe delay time and on  $\lambda_{pr}$ , is to plot the transient extinction spectra at fixed pump-probe delays. Figure 23 shows  $\Delta\sigma_{ext}/\Delta T_{eq}(\lambda_{pr})$  for ND1 (left) and ND2 (right), at fixed delays time of 0.7 ps (panels a and d), 2.5 ps (panels b and e) and 8 ps

(panels c and f). The color code is the same as for Figures 21 and 22. The agreement between measurements and simulations is overall good, both in terms of amplitudes and shapes, and gets better with increasing time delays. At short delay (0.7 ps) the transient spectra is dominated by the electron contribution  $\Delta\sigma_{ext,e}$ , since the electron-lattice heat transfer has a longer characteristic time. After the electronic thermalization (2.5 ps), the transient spectra is the results of both the electronic and lattice contributions, being the electron temperature still higher than the lattice one, which however started to rise. When the internal thermalization is complete (8 ps), instead, the lattice contribution is the dominant one for all  $\lambda_{pr}$ . In this case, then, the dominant term is  $\Delta\sigma_{ext,L}$ , which from Equations 1.25, 1.26 and 1.27 is  $\propto \Delta T_L$ . Since the thermalization is complete,  $\Delta T_L = \Delta T_{eq}$ , we are therefore plotting what we called  $A_{gnd}$  in Section 1.3.2 for the ns timescale measurements. Indeed panels c and f of Figure 23 present the same shape as  $A_{gnd}$  in Figure 15, showing the intersection from the ps and the ns timescales.

## 1.5 Conclusions

In this chapter, we have seen the results of time-resolved spectroscopy on individual gold NDs nanopatterned on a sapphire substrate. We described how the spatial modulation spectroscopy technique allows to quantitatively retrieve the optical properties of individual nanoparticles and, in combination with numerical simulations, also the shape and the size of the individual nanoparticles. Then, we have seen the time-resolved pump-probe measurements at two different timescales: the ns timescale, associated to the thermal cooling of the gold NDs, and the ps timescale, associated to the faster dynamics of the electron-electron interactions and electron-lattice thermalization within the NDs.

The cooling dynamics of individual nanodisks was quantitatively investigated to obtain the absolute amplitudes of the transient extinction cross section changes induced by the nanodisks heating. The amplitude of the cooling dynamics strongly depends on the probe wavelength, in agreement with results from numerical simulations. The kinetics of the process, however, is independent on the probe wavelength, implying the negligible contribution of the substrate on the nanoparticle optical changes. Then, we discussed measurements performed on nanodisks with different diameters, comparing them to tailored simulations. The cooling dynamics is mostly limited by the TBR at gold/sapphire interface, whose value we derived for individual NDs.

Subsequently, the electron excitation and the electron-lattice thermalization were experimentally measured with a shorter time window and time step. In this case, the time-resolved optical response depends on the selected probe wavelength, influencing both the amplitude and the kinetics of the process. A theoretical model was introduced, capable to rationalize the experimental results in terms of electronic and lattice contributions to the modifications of the interband and intraband components of the Au dielectric function.

The good agreement between experiments and numerical simulations, based on our model, confirm the wavelength dependence of time-resolved signals on electron-lattice heating. At certain specific probe wavelengths, the electronic (lattice) contribution is negligible, offering the possibility to selectively probe the lattice (electronic) heating dynamics.

This work shows that the transient optical response induced by optical excitation, internal thermalization and cooling dynamics of metal nanoparticles can be measured at the individual level and rationalized in terms of a theoretical model implemented in numerical simulations. These measurements may be extended to other compositions and geometries of different nano-objects and their supporting materials, paving the way to direct investigations of different nanoscale thermal transport regimes for individual nanoparticles.

In the next chapter, we will see another example of time-resolved transient optical measurements on nanoparticles in contact with a substrate. However, a few significant differences distinguish the two studies, both from an experimental point of view and concerning the investigated system. Experimentally, we will work with reflected rather than transmitted light, and the probed sample will be an ensemble of nanoparticles rather than a single one. Regarding the system, the nanoparticles involved are Indium Arsenide nanowires, i.e. a semiconductor material, as opposed to the plasmonic NDs. Also the main physical focus will be shifted, from the thermal dynamics to the mechanical one, the vibrational response of the nanowires being the main object of interest. In particular, we will see how to extract a mechanical parameter of the system, i.e. the Young modulus of the Indium Arsenide nanowires. Then, the genesis of the nanowires vibrations will be unveiled, showing that the mechanical oscillations are for the most part originated by the sudden expansion of the substrate.



## 2. Ultrafast mechanical oscillations of InAs nanowires

This work is the result of a collaboration with colleagues at Università Cattolica and Università di Brescia (Brescia, Italy), where the optical set-up and pump-probe measurements were performed, and at NEST Lab Scuola Normale Superiore and Istituto Nanoscienze-CNR (Pisa, Italy), where sample synthesis and characterisation was performed.

The results are published in the article *Ultrafast Photoacoustic Nanometrology of InAs Nanowires Mechanical Properties*, *The Journal of Physical Chemistry C* **126**, 6361 (2022), of which I'm co-author and to which redaction I contributed.

This part of the thesis work allowed me to get acquainted with the modelling of ultrafast mechanical transients in nanoscale systems triggered by a short laser pulse. Furthermore, although I was not involved in first person in the experimental part, it did allow me to become aware of the synthesis, characterisation and experimental subtleties involved, a key aspect to properly rationalise the underlying physics and implement a realistic modelling. This work was then accessory, in the frame of the thesis, to undertake the theoretical work illustrated in the following chapters.

### 2.1 Introduction

The focus of this chapter is on the opto-thermo-mechanical dynamics of semiconductor nanowires (NWs) made of Indium Arsenide (InAs) with a Wurtzite (WZ) structure, synthesized by gold-catalyzed chemical beam epitaxy on a InAs substrate. Primary importance will be given to the mechanical properties of such NWs and the activation mechanism of their longitudinal mechanical modes. This choice is part of a broader perspective: NWs have been, indeed, at the forefront of nanoscience research for more than two decades thanks to their applications [84, 85, 86, 87, 88, 89, 90] and novel optoelectronic configurations [91, 92]. In this context, mechanical properties play a central role [93, 94] in view of any device development. Great effort was devoted to this issue [95, 96] exploiting methodologies ranging from bending and resonance measurements to nanoindentation, mainly exploiting AFM, in-situ electron microscopies and optical microscopies [97]. Recently, ultrafast spectroscopy arose as a valid addition yielding access to the NWs high frequency mechanical response in a contactless mode [98, 99, 100, 101, 102, 103, 104, 105]. Nevertheless, a clear understanding of NWs mechanics is still missing [97]. Manipulation of NWs is a difficult task and, in this process, errors can be introduced biasing

the measured mechanical data. Sample morphology variations, introduced in the growth process, also contribute to wide dispersion in the measured data, requiring, in order to make further progress, the assessment of the NWs morphological features through a systematic statistical characterization. The assessment of InAs NWs mechanical properties faces the same criticalities mentioned above, as shown by the widely varying reported values of their Young modulus and its dependence with NW dimensions [106, 107, 108]. Nevertheless, the use of InAs NW structures is growing in a variety of applications, as in optoelectronics [87, 109, 110] and nanoelectronics [111, 112].

In this chapter, we will describe the experimental set-up used for the acquisition of the relaxation dynamics after a sudden excitation, the structural and morphological analysis of the NWs via electronic microscopy measurements and the modelling of the NWs mechanics and its excitation mechanism. This multitechnique approach allows to understand the thermo-mechanical time evolution of the system, with particular attention to the different mechanical phenomena involved, ultimately extracting the InAs NWs Young modulus.

From a technical point of view, there are two main differences with respect to the experiment performed on gold NDs and described in Chapter 1. First, in the present case we investigate ensembles of nano-objects rather than a single one. For this reason, analyzing the morphological differences between NWs of the same sample is fundamental to comprehend how the statistical dispersion of the NW morphological parameters affects the acquired data. Secondly, the pump-probe optical set up, exploited for the present investigation, is based on a different working principle from the one described in Section 1.3. Instead of using a mechanical delay line to control the time interval between pump and probe pulses, here we exploit the asynchronous optical sampling (ASOPS) technique, where the pump and probe pulses are provided by two different femtosecond laser sources which repetition rate is slightly detuned by a small frequency  $\Delta f_{lasers}$ . ASOPS thus allows performing pump and probe measurements avoiding any mechanical movement (no motorized delay line). This fact, together with a laser repetition rate of 100 MHz, allows to achieve delay times of 10 ns. Third, regarding the investigated sample, we move from gold NDs to InAs NWs, i.e. from metallic to semiconducting nano-systems. This fact adds a new mechanism responsible for the expansion of the nano-object upon short laser excitation, i.e. the deformation potential, due to the creation of transient electron-hole pairs. Moreover, InAs NWs are characterized by a highly anisotropic lattice structure, which we will have to take into account to access the mechanical constants of the system. Retrieval of the NW Young modulus in the NWs axial direction, in particular, is the first scope of this study. Secondly, the mechanism triggering the mechanical oscillations will be unveiled. Contrary to the case of metallic NDs so far investigated, NWs oscillations are not launched by their direct expansion. Oscillations arise indeed from a sudden expansion of the supporting InAs substrate. This mechanism constitutes an interesting phenomenon,

being at variance with respect to the excitation mechanisms so far identified in ultrafast experiments on nanowires [99] and on a plethora of nanosystems. This launching mechanism bears generality beyond the specific case, potentially encompassing a variety of systems serving as nano-optomechanical resonators.

## 2.2 InAs Nanowires Structure

### 2.2.1 Growth procedure

Samples growth and characterization were carried out by colleagues at NEST LABS@NEST, Istituto Nanoscienze-CNR and Scuola Normale Superiore, Pisa, Italy. Here we will give a short overview of the NW synthesis method and then we will focus on their structure and morphology.

Five assemblies of vertical WZ InAs NWs forests, each characterized by a different length (in the nominal range of 250-1250 nm), were synthesized by Au-assisted Vapour-Liquid-Solid (VLS) growth [113] in a Chemical Beam Epitaxy (CBE) system on InAs (111) substrates.

Before mounting the sample in the CBE chamber, a thin gold film of effective thickness  $\approx 0.1 - 0.5$  nm was deposited at room temperature on the substrate in a thermal evaporator equipped with quartz crystal thickness monitor for evaporation rate and film thickness feedback. The substrates were then introduced in the UHV chamber of a Riber C-21 CBE system. A thermal treatment prior to growth was carried out, keeping the substrate at the annealing temperature ( $460 \pm 10$  °C) for 20 minutes under As flux, in order to trigger the gold film dewetting and the formation of metallic seed nanoparticles. To obtain different nanoparticles density and diameter distributions, the Au film thickness and the annealing temperature were varied [114]. In this way, the 0.5 nm thick film (effective thickness) yields NPs with a larger mean diameter than that of NPs obtained with a nominal Au thickness of 0.1 nm. After annealing, the temperature was lowered to  $370 \pm 10$  °C and the InAs NW growth was carried out for different time durations, in order to obtain NWs of different lengths. This yields InAs NWs with Au semi-spheres on top of their tip whose diameters match that of the supporting NWs. In four samples the NWs average diameter is around 45 nm, whereas in one case the diameter was reduced to 20 nm for benchmarking purposes.

As we shall see further on, the assessment of the NWs morphological and structural features is crucial for the retrieval of the InAs NWs mechanical properties. For this reason, a systematic statistical analysis of electron microscopy data was performed. SEM images of the NWs were acquired with a Zeiss Merlin Zeiss field-emission SEM. Diameter ( $D$ ) and length ( $L$ ) distributions of the NWs were measured using the procedure and image

analysis software package described in [114]. TEM analysis was performed using a JEOL TEM-2200FS microscope, equipped with an in-column  $\Omega$  filter, operated at 200 kV. For TEM observation, the NWs were transferred to carbon-coated Cu grids by gentle rubbing.

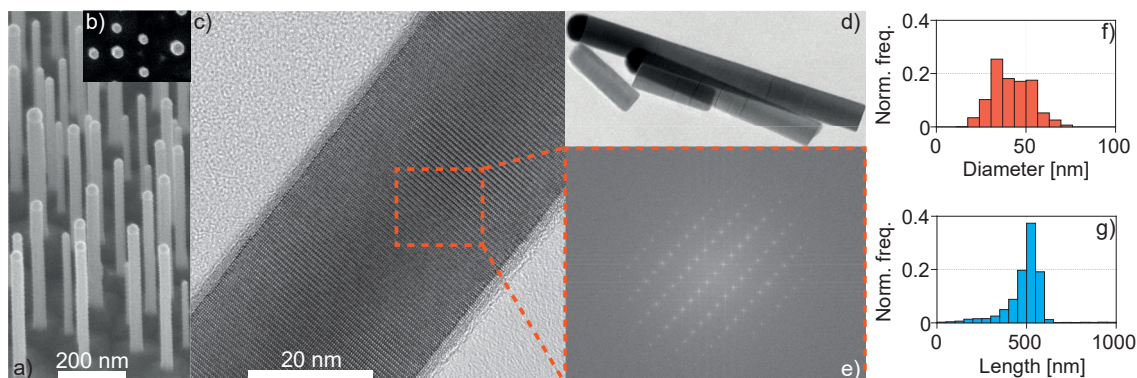


Figure 24. Morphological and structural characterization of the InAs nanowires samples. 45°-tilted (panel a) and top view (panel b) SEM images of InAs NWs grown on InAs (111) substrate. HRTEM images (panel c) and corresponding FT pattern (panel e) of the NW body taken along  $[2, -1, -1, 0]$  zone axis. TEM image (panel d). Nanowires diameter (panel f) and length (panel g) distribution (normalized against the total number of inspected NWs) for sample S2 obtained from SEM images analysis. The length does not include the Au tip. The average diameter and length are  $\bar{D} = 43$  nm and  $\bar{L} = 475$  nm, respectively. Reprinted with permission from [4]. Copyright 2022 American Chemical Society.

Figure 24 reports the morphological and structural characterization of a representative sample (S2). The NWs geometrical parameters were assessed from SEM images that are shown at 45°-tilted view (panel a) and from top view (panel b), in the figure. Despite the presence of the gold nanoparticle on top of the NW, clearly observable in panel a, the SEM top view suggests a hexagonal cross-section for the NWs, typical of the WZ InAs structure. Both images reveal the presence of some degree of dispersion in the geometrical parameters (diameter and length).

High resolution HRTEM, acquired on individual NWs, showed the high crystallographic quality of the NWs (panel c), with almost no sign of stacking faults. The NWs crystal structure is pure WZ, as arises from the analysis of the Fourier transform (FT) (panel e) taken on the data reported in panel c - square area delimited by red dashed line. Structural data are in agreement with existing literature, reporting a pure WZ structure for diameters below 50 nm [115]. The same holds true on all five sample batches.

As already stated, a detailed knowledge of the NWs morphological features is fundamental to correctly access their mechanical properties. To this end, a systematic analysis of SEM data [114] was carried out to statistically characterize the NWs size distribution for each sample. Panels f and g report the distribution of NWs diameter,  $D$ , and length,  $L$ , obtained from the analysis of a set of 2000 NWs from the same sample (S2) (the reported length  $L$  value does not include the Au tip). For S2, the average values are  $\bar{D} = 43$  nm and  $\bar{L} = 475$

nm. The same analysis was carried out on all five samples. Results are summarized in Table 1.

Sample	$\bar{L}$ (nm)	$\sigma_L$ (nm)	$\bar{D}$ (nm)	$\sigma_D$ (nm)
S1	265	40	43	10
S2	475	100	43	10
S3	625	150	20	5
S4	1138	100	45	15
S5	1240	70	48	15

Table 1. Sample number, average length ( $\bar{L}$ ) and diameter ( $\bar{D}$ ), with the corresponding standard deviations ( $\sigma_L$  and  $\sigma_D$ ).  $\bar{L}$  does not include the Au tip. The statistics has been performed sampling 2000 NWs on each sample.

## 2.3 Ultrafast time-resolved measurements

### 2.3.1 ASOPS technique

Pump-probe measurements were performed to access the NWs mechanical oscillations for different NWs lengths and diameters. Despite the experimental similarity to the pump-probe technique described in 1.3, the set-up here involved differs from the one used for the investigation of gold NDs. The Asynchronous Optical Sampling (ASOPS) technique was here implemented via a MENLO C-Fiber 780 High Power ASOPS system. Such a system consists of two lasers delivering synchronized trains of pulses with pulse duration of  $\approx 100$  fs. One train of pulses serves as pump and the other as probe. The core

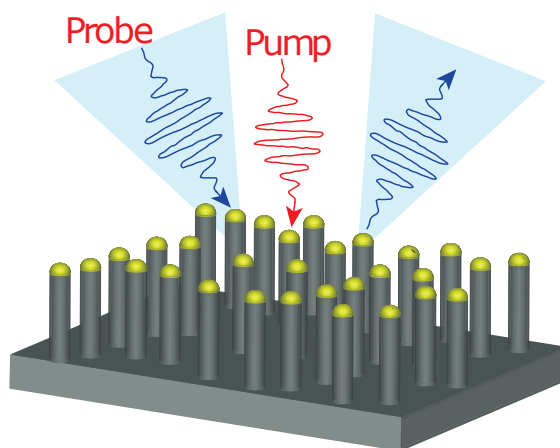


Figure 25. Sketch of the pump-probe (reflection) experiment performed on InAs NWs on InAs substrate. Reprinted with permission from [4]. Copyright 2022 American Chemical Society.

of the ASOPS technique resides in the pump and probe beam having slightly different re-

tation rates,  $f_{pp}$  and  $f_{pr}$ , respectively, with  $\Delta f_{lasers} = f_{pp} - f_{pr}$  and  $\Delta f_{lasers} \ll f_{pr} \sim f_{pp}$ . To illustrate the ASOPS technique, let's assume that the pump and probe are spatially and temporally overlapped at time  $t_0$ . Their next strike, here addressed as first strike, will occur respectively at  $t_1 = t_0 + 1/f_{pp}$  and  $t_0 + 1/f_{pr} = t_1 + \Delta t$ . The accumulated delay time between the two pulses at the first strike ( $i = 1$ ) is then  $\Delta t = |1/f_{pp} - 1/f_{pr}| \approx \Delta f_{lasers}/f_{pp}^2$ . The time delay between the two pulses at the second strike ( $i = 2$ ) will be  $2\Delta t$ . In this way the time delay will continue to increase, gaining a factor  $\Delta t$  at each strike, until the  $n$ -th strike, with  $n$  such that  $n\Delta t = 1/f_{pp}$ , i.e. when the pump and the probe are again temporally overlapped. This occurs after a time span of  $1/\Delta f_{lasers}$  and the sampled time windows delay is  $1/f_{pp}$ . In the actual experiment, if we set  $f_{pp} = 100$  MHz and  $\Delta f_{lasers} = 1$  kHz, we obtain a time resolved window measurement of 10 ns, with time-delay steps of  $\Delta t = 100$  fs, in a laboratory time span of 1 ms. In order to improve the signal-to-noise ratio, the time-resolved scan is typically repeated  $10^5$  times, yielding to an overall acquisition time within the few minutes range.

Overall, the ASOPS technique has several advantages with respect to the standard technique based on moving delay-line and lock-in detection. First, the signal-to-noise ratio achievable with the ASOPS exceeds the one in standard pump-probe techniques based on a mechanical delay line. In the ASOPS system, the pump-probe time delay is managed electronically, avoiding any moving mechanical parts [116]. This fact, together with a typical laser repetition rate  $f_{pp} \approx 100$  MHz makes it possible to detect relative reflectivity variation of  $\approx 10^{-7}$ . Secondly, the ASOPS technique is particularly suited for acquiring signals extending up to long delay-times. For the present case, the delay-time extended up to 10 ns, which in a mechanical delay line set-up would correspond to a hardly manageable delay line length of  $\approx 3$  m. Finally, the ASOPS and the mechanical delay line techniques differ in the way data are acquired. In the mechanical delay line set-up, to decrease the signal-to-noise ratio, the signal is recorded many times via lock-in detection (e.g.,  $N$  times), at a fixed time delay  $t_i$ , before moving to the following time delay  $t_{i+1}$  and so on. In this way, between the data at time  $t = 0$  and the ones at the maximum delay  $t = t_{max}$ , several minutes could have passed. Contrarily, in the ASOPS set-up, signals at different  $t_i$  are acquired consecutively. Then, after the acquisition of a complete trace, i.e. covering all delay times from  $t = 0$  to  $t_{max} = 10$  ns, which takes a few minutes, another complete time-resolved trace is acquired. In other words, in the mechanical delay time, the signal is acquired  $N$  times for each  $t_i$  before passing to  $t_{i+1}$ ; in the ASOPS technique, instead, the signal is recorded only once for each  $t_i$  from  $t = 0$  to  $t_{max}$  and then this cycle is repeated  $N$  times. In this way, through ASOPS technique one can compare the entire time-evolution of the system taken in different moments, thus understanding if there is a change in time of the acquired data.

Another difference from the experiment on gold NDs of Chapter 1 is that, in the case of the InAs NWs, we measure the light reflected by the sample, as sketched in Figure

25, rather than acquiring the transmitted signal. This is because, in this case, the substrate is not transparent at our working wavelengths; actually, as we will see further on, in this system is the substrate the main responsible for light absorption. The reflectivity variation is recorded sending the probe and its reference beam to a Fixed Gain Balanced Differential Si Photodiode with 350 MHz bandwidth. The differential photodiode analog output signal is digitized via a 16 bit, 105 MS/s acquisition board. Despite the high repetition rate, the low fluence renders the pump cumulative effect negligible [117].

### 2.3.2 Time-resolved measurements

In the excitation step, the pump pulse is provided by a laser with wavelength  $\lambda_p=1560$  nm, 100 fs pulse duration, 30  $\mu\text{m}$  beam diameter at full width half maximum (fwhm), impinging on the sample at normal incidence, operating at a repetition rate of 100 MHz and delivering an average power of  $\approx 100$  mW. The single pump pulse fluence is fixed at  $\approx 1$  J/m<sup>2</sup>. The 0.8 eV pump photon energy excites electrons both within the Au tips and the exposed InAs portion of the sample, the InAs energy gap being  $\approx 0.4$  eV. This triggers a cascade of events, as already described in Section 1.3, plus the one peculiar to semiconductors that will be addressed further on, ultimately resulting in the excitation of the system mechanical modes. The genesis of the latter will be discussed in Section 2.5, for the time being it suffices to recognize they are excited. As time evolves, the system relaxes back to equilibrium via different pathways (thermal and mechanical channels) and, given the semiconductor nature of InAs Nws, also through electron-hole recombination. In this way, as for the gold NDs, this leads to a time and space varying dielectric constant, resulting in a time-varying sample optical reflectivity. This dynamics, and in particular the time-periodic modulations, can be revealed following the time evolution of the relative reflectivity variation,  $\Delta R/R_0(t)$ , where  $\Delta R(t)$  is the optical reflectivity variation with respect to its equilibrium value  $R_0$ .  $\Delta R/R_0(t)$  is measured via the laser probe pulse, characterized by a  $\lambda = 780$  nm, 100 fs pulse duration, 15  $\mu\text{m}$  beam diameter at fwhm and impinging at quasi-normal incidence (incidence angle  $\approx 8^\circ$ ).

The trace  $\Delta R/R_0$  versus delay time, acquired on sample S2, is reported in Figure 26 (panel a, black curve). Note that here we reported a time window of 4.5 ns, rather than the full pump-probe delay time span of 10 ns. The fast peak, due to electron excitation, is followed by slower dynamics, encoding the previously-mentioned relaxation pathways. The oscillations, due to the mechanical vibrations, are superposed on the relaxation background. For the sake of extracting the oscillating signals, the non-oscillating background is fitted with a sum of three exponential functions, this fit being reported as a yellow line. The fit is only intended to extract the oscillating signal, we do not dwell here on its physical meaning. The non-oscillating background (panel a, yellow curve) is then subtracted from the total signal (black line) to obtain the residue, clearly revealing oscillations on the ns

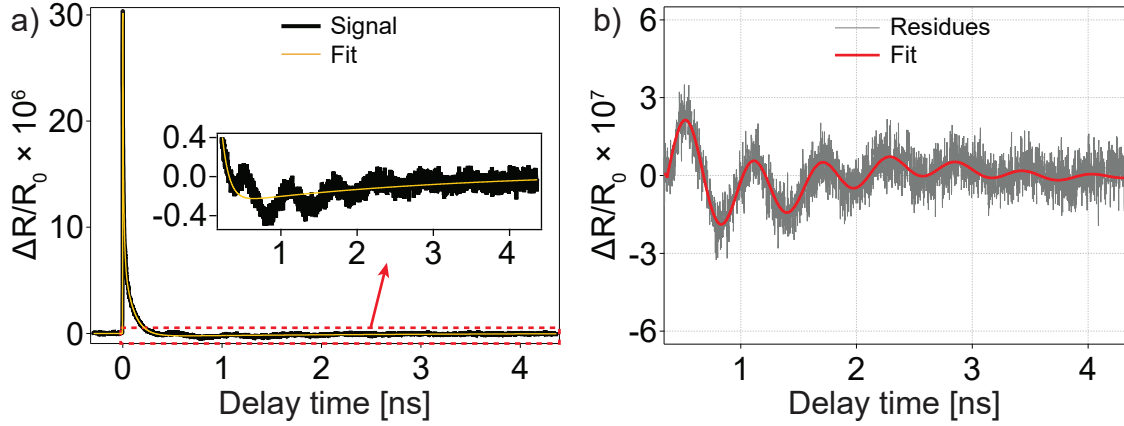


Figure 26. Time-resolved measurements.  $\Delta R/R_0$  vs delay time between pump and probe pulses (black curve) and three-exponentials fit (yellow curve) (panel a). Inset: expanded view emphasizing the temporal window where mechanical oscillations are visible. Residues (gray trace) vs delay time and two-damped oscillators fit (red trace) (panel b). The residues are obtained as the difference between the black and yellow curves of the inset in panel a. Data are reported for sample number 2:  $\bar{D} = 43$  nm and  $\bar{L} = 475$  nm. The horizontal axis was limited to the region where mechanical oscillations are visible. Reprinted with permission from [4]. Copyright 2022 American Chemical Society.

timescale, as reported in Figure 26 (panel b).

The residue (gray line) is well fitted by the sum of two damped oscillators (red line). The longer oscillation period exceeds the extension of the temporal window and does not display the same features in all samples. Speculating on it would thus be rather hazardous. Furthermore, although the long period oscillation grants an optimal fit quality, its relative weight is exiguous with respect to that of the shorter period oscillator:

$$f(t) = f_0 + \sum_{i=1}^2 A_i \sin(\omega_i(t - t_0) + \phi_i) e^{-\frac{t-t_0}{\tau_i}}, \quad (2.1)$$

where  $f_0$  is the background of the signal and  $t_0$  is a temporal offset.  $A_i$ ,  $\omega_i$ ,  $\phi_i$ ,  $\tau_i$  are the amplitude, the angular frequency, the phase and the lifetime of the oscillators, respectively. For the fitting parameters we obtained the values reported in Table 2. The oscillator labelled with the pedex ‘2’ is the one corresponding to the extensional modes. As can be appreciated, the other oscillator has a smaller amplitude and the oscillation periods is comparable with the extension of the signal time window ( $\omega_1 \approx 2.31 \times 10^9$  (rad/s) corresponds to a period of  $\approx 2.7$  ns). For this reason we do not speculate on it. We concentrate, instead, on the well developed shorter oscillation period,  $\tau_2$ , which from now on we will referred as  $\tau$  (without the pedex) for simplicity. For S2, reported in Figure 26 (panel b),  $\tau = 582$  ps.

The rationalization of the system mechanical modes requires investigating its oscillation periods against the relevant system dimension [118, 119, 116, 120, 121]. In

Fitting parameter	Value	Standard deviation
$f_0 \times 10^9$	5.5	0.6
$t_0$ (ps)	427	3
$A_1 \times 10^7$	1.17	0.04
$\omega_1$ (Grad/s)	2.31	0.02
$\phi_1$ (rad)	2.60	0.02
$\tau_1$ (ns)	1.51	0.06
$A_2 \times 10^7$	2.21	0.03
$\omega_2$ (Grad/s)	10.79	0.02
$\phi_2$ (rad)	5.94	0.03
$\tau_2$ (ns)	1.19	0.02

Table 2. Parameters obtained by fitting the residue curve reported in Figure 26 (panel b).

this sense, Figure 27 (black circles) displays the oscillation period  $\tau$  (left axis) and the corresponding oscillation frequency  $\nu = \tau^{-1}$  (right axis) versus the NWs average length  $\bar{L}$ . The periods were obtained fitting the measurements acquired on each sample according to the above-mentioned procedure. The period (vertical) error bars arise from the fitting procedure and fall within the markers size (black circles) and hence are not displayed. The horizontal black error bars correspond to the NWs length distribution's standard deviation for each sample.

The period scales linearly with the NWs average length, regardless of the NWs diameter, for instance sample 3 ( $\bar{L} = 625$  nm) follows the same trend despite a halved diameter of  $\bar{D} = 20$  nm. The oscillations are thus attributed to the NW extensional modes, characterized by a displacement predominantly along the NW axial direction.

## 2.4 Assessing NWs mechanical properties

### 2.4.1 Modeling the InAs NWs

In this section we present the model that allowed rationalizing the oscillations observed experimentally and introduced in the previews section. The model is inherently multiphysics and relies on input data from the morphological characterization described in Section 2.2. Numerical simulations were implemented and solved via finite element method (FEM) in the frame of a continuum mechanics model.

InAs NWs are modeled individually, the scope of the simulations being the understanding of the behaviour of each NW and its interaction with the substrate, negligible interaction between NWs being assumed. The NW geometry is modeled as a cylinder anchored to a semi-sphere far exceeding the NW diameter that represents the InAs substrate (calculations were also performed for a hexagonal InAs geometry, yielding the same

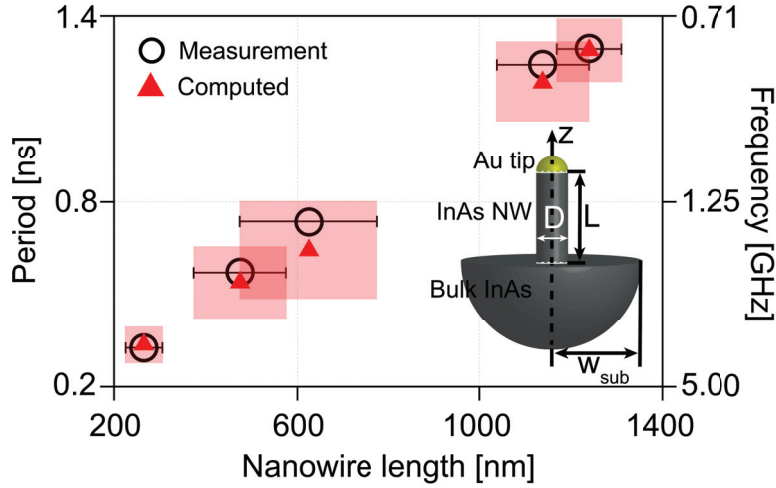


Figure 27. Experimental vs theoretical oscillation periods. Black circles: measured extensional mode periods (left axis) and corresponding frequencies (right axis) vs NW average lengths (horizontal axis). Full red triangles: theoretical oscillation periods of the fundamental extensional mode. Pink rectangles: uncertainty box. The rectangles horizontal widths (and the horizontal black error bars) represent the NWs length distribution standard deviation for each sample, as obtained from SEM measurements and summarized in Table 1. The corresponding computed extensional modes periods make up each rectangle vertical side. Inset: sketch of the geometry adopted for the finite elements mechanical simulations. Adapted with permission from [4]. Copyright 2022 American Chemical Society.

results but with a higher computational cost, see Section 2.4.2). A Au semi-sphere rests on the top of the NW, with a diameter matching the NW one. The geometry is depicted in the inset of Figure 27, the  $z$  coordinate being parallel to the cylinder axis. The cylinder diameter and length are chosen as the average NW diameter,  $\bar{D}$ , and length,  $\bar{L}$ , for each sample. The computed oscillation periods of Figure 27, result from a full mechanical model, comprising the presence of the gold tip and the substrate. This is at variance with simplified approaches of common use in the literature [122, 123, 124, 125, 126].

The equations governing the mechanics are [127]:

$$\rho \frac{\partial^2 \vec{u}}{\partial t^2} = \nabla \cdot \boldsymbol{\sigma} \quad (2.2)$$

$$\boldsymbol{\sigma} = \mathbf{C} \cdot \boldsymbol{\varepsilon} + \boldsymbol{\sigma}_{ext}, \quad (2.3)$$

where  $\boldsymbol{\sigma}$  and  $\boldsymbol{\varepsilon}$  are the stress (Pa) and strain (adimensional) tensors respectively,  $\rho$  is the material density ( $\text{kg/m}^3$ ),  $\mathbf{C}$  is the elastic matrix (Pa) and  $\vec{u}$  the displacement field (m). The external stress term,  $\boldsymbol{\sigma}_{ext}$  (Pa), is added to account for the external excitation source. Equations 2.2 and 2.3 show the crucial role of knowing the elastic constants of the system. It will now be shown which elastic constants can be assigned to the different domains composing the system so as to successfully simulate the observed oscillation vs NW lengths dispersion.

### InAs substrate

The substrate is made of bulk InAs (111)B, that is grown along the [111] direction. Note that (111)B refers to the atoms exposed on the surface, As atoms in this case, as opposed to (111)A which exposes In atoms. For density, we take the bulk InAs value  $\rho_{InAs} = 5670 \text{ kg/m}^3$  [128]. The orientation of the crystal structure in our case requires, for the present case, particular care. Bulk InAs has a Zincblend (ZB) structure with a cubic unit cell. The elastic matrix of a ZB crystal is standardly reported for a spatial reference frame with axes parallel to the crystallographic directions [128], i.e. [100], [010], [001]. The three independent elastic constants for bulk ZB InAs are summarized in Table 3. In the case of InAs (111)B, however, the z axis of the spatial reference frame lays

	elastic constant	ZB InAs	Polycrystal Au
$C_{11}$ (GPa)		83.29	207.00
$C_{44}$ (GPa)		39.59	28.50
$C_{12}$ (GPa)		45.26	$C_{11} - 2C_{44}$

Table 3. elastic matrix elements of ZB InAs and polycrystal (isotropic) gold (taken from [128]). For ZB InAs, the elastic matrix elements are reported for the standard case of the coordinate system axes parallel to the crystallographic axes, i.e. [100], [010], [001].

along the diagonal of the cubic crystal, i.e [111] direction, rather than along a standard crystallographic axis. In other words, the InAs (111)B structure has a rotated axis reference frame with respect to the ZB InAs crystallography axis. Thus, we need to rotate the “standard” elastic matrix to comply with our reference system.

Before entering the specific InAs case, we describe in general how the elastic matrix changes when we rotate the reference frame from the coordinates  $(x_1, x_2, x_3)$  to  $(x'_1, x'_2, x'_3)$ . Note that we use the coordinates  $(x_1, x_2, x_3)$  instead of  $(x, y, z)$ , for the sake of simplicity in notation. The rotation matrix can be written as:

$$\mathbf{R} = \begin{pmatrix} l_1 & l_2 & l_3 \\ m_1 & m_2 & m_3 \\ n_1 & n_2 & n_3 \end{pmatrix}, \quad (2.4)$$

with  $\mathbf{R}$  having the property  $\mathbf{R}^{-1} = \mathbf{R}^T$ .

The displacement field  $\vec{u}$  rotates together with the frame, becoming  $\vec{u}' = \mathbf{R}\vec{u}$ . The strain tensor  $\boldsymbol{\varepsilon}'$  is obtained by deriving  $\vec{u}'$  with respect to  $x'$ . If we want to write  $\boldsymbol{\varepsilon}'$  as a function of  $\boldsymbol{\varepsilon}$ , we have to express the derivatives  $\partial u'_j / \partial x'_k$  as functions of  $\partial u_q / \partial x_s$  (where

$j, k, q, s = 1, 2, 3$ ). This reads:

$$\varepsilon'_{jk} = \frac{\partial u'_j}{\partial x'_k} = \frac{\partial(\mathbf{R}\vec{u})_j}{\partial x'_k} = \sum_{q=1}^3 R_{jq} \frac{\partial u_q}{\partial x'_k} = \sum_{q=1}^3 \sum_{s=1}^3 R_{jq} \frac{\partial u_q}{\partial x_s} \frac{\partial x_s}{\partial x'_k} = \sum_{q=1}^3 \sum_{s=1}^3 R_{jq} R_{ks} \frac{\partial u_q}{\partial x_s}. \quad (2.5)$$

By writing relation 2.5 for all  $j, k$  and combining the terms entering in the expressions for the strain in Voigt notation, we obtain the following transformation for the strain:

$$\boldsymbol{\varepsilon}' = \mathbf{W}\boldsymbol{\varepsilon} = \begin{pmatrix} W^{(1)} & W^{(2)} \\ 2W^{(3)} & W^{(4)} \end{pmatrix} \boldsymbol{\varepsilon}, \quad (2.6)$$

where

$$\mathbf{W}^{(1)} = \begin{pmatrix} l_1^2 & l_2^2 & l_3^2 \\ m_1^2 & m_2^2 & m_3^2 \\ n_1^2 & n_2^2 & n_3^2 \end{pmatrix},$$

$$\mathbf{W}^{(2)} = \begin{pmatrix} l_2 l_3 & l_1 l_3 & l_1 l_2 \\ m_2 m_3 & m_1 m_3 & m_1 m_2 \\ n_2 n_3 & n_1 n_3 & n_1 n_2 \end{pmatrix},$$

$$\mathbf{W}^{(3)} = \begin{pmatrix} n_1 m_1 & n_2 m_2 & n_3 m_3 \\ l_1 n_1 & l_2 n_2 & l_3 n_3 \\ l_1 m_1 & l_2 m_2 & l_3 m_3 \end{pmatrix},$$

$$\mathbf{W}^{(4)} = \begin{pmatrix} n_2 m_3 + n_3 m_2 & n_1 m_3 + n_3 m_1 & n_1 m_2 + n_2 m_1 \\ n_2 l_3 + n_3 l_2 & n_1 l_3 + n_3 l_1 & n_1 l_2 + n_2 l_1 \\ m_2 l_3 + m_3 l_2 & m_1 l_3 + m_3 l_1 & m_1 l_2 + m_2 l_1 \end{pmatrix}.$$

From energetic considerations, the work done by the system,  $W_{done}$ , in the starting reference frame  $(x_1, x_2, x_3)$ , reads:

$$W_{done} = (\delta\boldsymbol{\varepsilon})^T \boldsymbol{\sigma}, \quad (2.7)$$

has to be equal to the work also in the rotated reference frame  $(x'_1, x'_2, x'_3)$

$$W_{done} = (\delta\boldsymbol{\varepsilon}')^T \boldsymbol{\sigma}'. \quad (2.8)$$

By definition, we know that

$$(\delta\boldsymbol{\varepsilon}')^T \boldsymbol{\sigma}' = (\mathbf{W}\delta\boldsymbol{\varepsilon})^T \boldsymbol{\sigma}' = (\delta\boldsymbol{\varepsilon})^T (\mathbf{W}^T \boldsymbol{\sigma}'). \quad (2.9)$$

So, given the arbitrariness of the infinitesimal strain  $\delta\varepsilon$ , using Equations 2.7, 2.8 and 2.9, one finds that the stress in the rotated frame satisfies the relation  $\boldsymbol{\sigma}' = \mathbf{W}^{-T} \boldsymbol{\sigma}$ .

Again, just applying definition of  $\varepsilon'$ , we get:

$$\boldsymbol{\sigma}' = \mathbf{C}' \boldsymbol{\varepsilon}' = \mathbf{C}' (\mathbf{W} \boldsymbol{\varepsilon}), \quad (2.10)$$

but we shown that  $\boldsymbol{\sigma}' = \mathbf{W}^{-T} \boldsymbol{\sigma}$ , so

$$\mathbf{C}' (\mathbf{W} \boldsymbol{\varepsilon}) = \mathbf{W}^{-T} \boldsymbol{\sigma} = \mathbf{W}^{-T} \mathbf{C} \boldsymbol{\varepsilon}. \quad (2.11)$$

Equation 2.11 holds for any strain, so finally we have  $\mathbf{C}' \mathbf{W} = \mathbf{W}^{-T} \mathbf{C}$ , implying:

$$\mathbf{C}' = \mathbf{W}^{-T} \mathbf{C} \mathbf{W}^{-1}, \quad (2.12)$$

where it can be demonstrated that:

$$\mathbf{W}^{-T} = \begin{pmatrix} W^{(1)} & 2W^{(2)} \\ W^{(3)} & W^{(4)} \end{pmatrix}. \quad (2.13)$$

With this knowledge at hand, we can now compute the rotation of a cubic crystal elastic matrix from  $x_3$  parallel to [001] (i.e. the standard system from which constants in Table 3 have been elaborated) to  $x_3$  parallel to [111] (i.e. our (111)B substrate). The starting reference system has the three axes parallel to the sides of the cubic unit cell of the ZB InAs crystal. The transformation we want to apply can be decomposed in two subsequent rotations: a frame rotation of an angle  $\alpha_{rot} = 45^\circ$  around the  $x_1$  axis, with a new reference system with axis  $(\tilde{x}_1, \tilde{x}_2, \tilde{x}_3)$ ; and a second rotation of an angle  $\beta_{rot} = -\arctan(1/\sqrt{2})$  around  $\tilde{x}_2$ . The final coordinate frame axis  $(x'_1, x'_2, x'_3)$  after the two rotations has, as desired, the  $x'_3$  axis along the cube diagonal.

The matrix  $\mathbf{R}$  of the two combined rotations reads:

$$\mathbf{R} = \begin{pmatrix} \cos(\beta_{rot}) & 0 & \sin(\beta_{rot}) \\ 0 & 1 & 0 \\ -\sin(\beta_{rot}) & 0 & \cos(\beta_{rot}) \end{pmatrix} \begin{pmatrix} 1 & 0 & 0 \\ 0 & \cos(\alpha_{rot}) & -\sin(\alpha_{rot}) \\ 0 & \sin(\alpha_{rot}) & \cos(\alpha_{rot}) \end{pmatrix}, \quad (2.14)$$

from which we can calculate:

$$\mathbf{W}^{-T} = \begin{pmatrix} 2/3 & 1/6 & 1/6 & 1/3 & -2/3 & -2/3 \\ 0 & 1/2 & 1/2 & -1 & 0 & 0 \\ 1/3 & 1/3 & 1/3 & 2/3 & 2/3 & 2/3 \\ 0 & 1/\sqrt{6} & -1/\sqrt{6} & 0 & -1/\sqrt{6} & 1/\sqrt{6} \\ 2/\sqrt{18} & -1/\sqrt{18} & -1/\sqrt{18} & -2/\sqrt{18} & 1/\sqrt{18} & 1/\sqrt{18} \\ 0 & -1/\sqrt{12} & 1/\sqrt{12} & 0 & -1/\sqrt{3} & 1/\sqrt{3} \end{pmatrix}. \quad (2.15)$$

The elastic matrix of a generic cubic crystal in the standard form (i.e. with the reference frame axes parallel to the sides of the cubic unit cell) reads [128]:

$$\mathbf{C} = \begin{pmatrix} C_{11} & C_{12} & C_{12} & 0 & 0 & 0 \\ C_{12} & C_{11} & C_{12} & 0 & 0 & 0 \\ C_{12} & C_{12} & C_{11} & 0 & 0 & 0 \\ 0 & 0 & 0 & C_{44} & 0 & 0 \\ 0 & 0 & 0 & 0 & C_{44} & 0 \\ 0 & 0 & 0 & 0 & 0 & C_{44} \end{pmatrix}. \quad (2.16)$$

After applying the rotation  $\mathbf{C}' = \mathbf{W}^{-T} \mathbf{C} \mathbf{W}^{-1}$  (Equation 2.11), the elastic matrix becomes

$$\mathbf{C}' = \begin{pmatrix} C'_{11} & C'_{12} & C'_{13} & 0 & -C'_{25} & 0 \\ C'_{12} & C'_{11} & C'_{13} & 0 & C'_{25} & 0 \\ C'_{13} & C'_{13} & C'_{33} & 0 & 0 & 0 \\ 0 & 0 & 0 & C'_{44} & 0 & C'_{25} \\ -C'_{25} & C'_{25} & 0 & 0 & C'_{44} & 0 \\ 0 & 0 & 0 & C'_{25} & 0 & C'_{66} \end{pmatrix}, \quad (2.17)$$

where we can express the  $C'_{jk}$  components in terms of the elastic constants  $C_{11}$ ,  $C_{12}$  and  $C_{44}$ :

$$\left\{ \begin{array}{l} C'_{11} = \frac{1}{2}C_{11} + \frac{1}{2}C_{12} + C_{44} \\ C'_{12} = \frac{1}{6}C_{11} + \frac{5}{6}C_{12} - \frac{1}{3}C_{44} \\ C'_{13} = \frac{1}{3}C_{11} + \frac{2}{3}C_{12} - \frac{2}{3}C_{44} \\ C'_{33} = \frac{1}{3}C_{11} + \frac{2}{3}C_{12} + \frac{4}{3}C_{44} \\ C'_{44} = \frac{1}{3}(C_{11} - C_{12} + C_{44}) \\ C'_{25} = -\frac{1}{\sqrt{18}}(C_{11} - C_{12} - 2C_{44}) \\ C'_{66} = \frac{1}{6}C_{11} - \frac{1}{6}C_{12} + \frac{2}{3}C_{44}. \end{array} \right. \quad (2.18)$$

We remark that the elastic matrix constant corresponding to the cube diagonal is  $C'_{33}$ . In this way, by inserting the elastic constants of Table 3 in the rotated matrix 2.17, we finally

obtain the InAs elastic matrix for the case of the actual sample's substrate:

$$\mathbf{C}' \text{ (GPa)} = \begin{pmatrix} 103.9 & 38.6 & 31.7 & 0 & -9.7 & 0 \\ 38.6 & 103.9 & 31.7 & 0 & 9.7 & 0 \\ 31.7 & 31.7 & 110.7 & 0 & 0 & 0 \\ 0 & 0 & 0 & 25.8 & 0 & 9.7 \\ -9.7 & 9.7 & 0 & 0 & 25.8 & 0 \\ 0 & 0 & 0 & 9.7 & 0 & 32.7 \end{pmatrix}. \quad (2.19)$$

### InAs NWs

Here we face one of the crucial issues for modeling our system: the choice of the mechanical properties to be assigned to the InAs NWs. As we have seen in Section 2.2, the NWs studied in this work have a WZ structure. For this reason the choice of their elastic properties is not trivial. WZ InAs, indeed, does not exist in nature as a bulk crystal. Nevertheless, the ZB InAs crystal in the spatial reference system with an axis parallel to the cube diagonal (as for case of the InAs (111)B substrate), is quite similar to the unit cell of WZ InAs [129]. To visualize this similarity, Figure 28 reports InAs WZ (panel a) and ZB (panel b) structures. In panel a, the WZ structure is shown from the top (left panel), exhibiting the (001) plane (perpendicular to the NW vertical  $z$ -axis) and with a certain tilt (right panel), the latter is intended to better visualize also the vertical atomic arrangement. Atoms are labeled with letters (In atoms, in violet) or with numbers (As atoms, in green) for an easier identification in the two perspectives. As can be seen, for each hexagon of As atoms, made of six atoms at the corners (atoms numbered from 1 to 6) and one at the center (atom number 7), there are three In atoms (atoms labeled A,B,C) accommodated inside the hexagon in horizontal projection, while they are immediately underneath the hexagon in the  $z$  direction. This is also schematized in the sketch (panel c), with all atoms having now the same size and being distinguished only by their color. On the other hand, in panel b) the ZB structure is shown, with the (111) plane highlighted in orange (In and As atoms have the same colors as in panel a). As can be seen, in such a plane, the As atoms form the same hexagonal structure as in the WZ (001) plane. Moreover, also in this case we find three In atoms accommodated inside the As hexagon from a planar projection perspective, while being slightly distanced along the direction perpendicular to the (111) plane. Again this is schematized in the sketch (panel c), where all atoms have now the same size and are distinguished only by their color. Therefore we chose to attribute the rotated bulk ZB InAs elastic matrix not only to the (111)B substrate, but also to the InAs NWs.

We can calculate the density of WZ InAs from the unit cell dimension and number of atoms. The unit cell of WZ InAs contains indeed two atoms of In and two atoms of As [130]. The mass of the unit cell amounts then to  $2 \times (114.8 \text{ g/mol} + 74.9 \text{ g/mol})/N_A \approx 6.3 \times 10^{-25}$

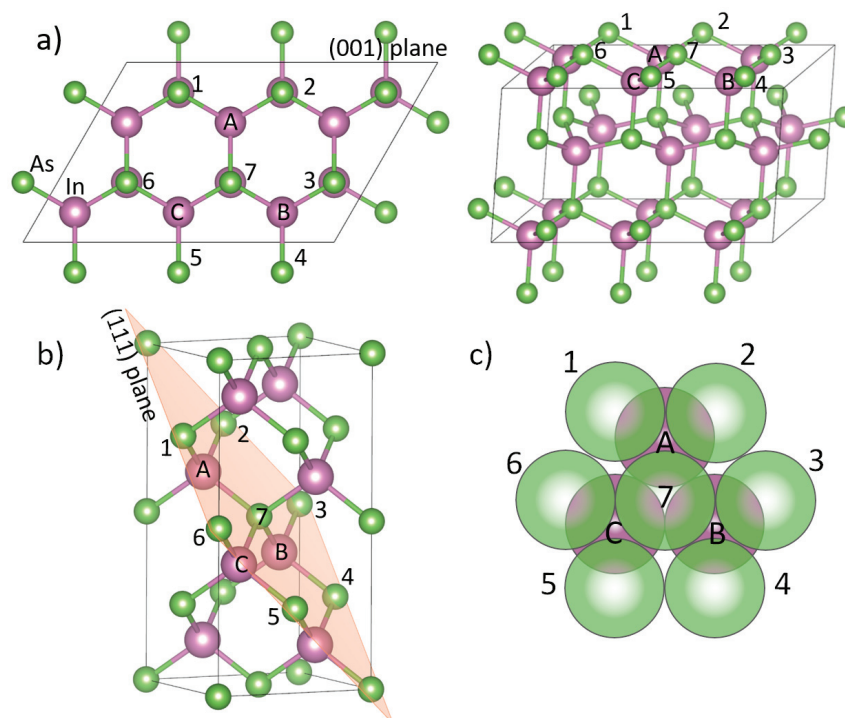


Figure 28. InAs NW lattice WZ structure (panel a) and InAs substrate ZB structure (panel b). The (111) plane is highlighted in the InAs substrate structure. Atoms are labeled with letters (In atoms, in violet) or with numbers (As atoms, in green). For each hexagons made of six As atoms at the corners (atoms numbered from 1 to 6) and one at the center (atom number 7), there are three In atoms (atoms labeled A,B,C) accommodated inside the hexagon in horizontal projection, while they are immediately underneath the hexagon in the  $z$  direction. A sketch of one As hexagon with the three In atoms underneath (panel c), valid both for the (001) WZ plane and the (111) ZB plane. Images created with [131].

kg, where  $N_A$  is the Avogadro's number. The unit cell height is  $c \approx 7 \text{ \AA}$ , and its base is one third of an hexagon, whose side is  $a \approx 4.3 \text{ \AA}$ . Thus, the unit cell volume is  $2.598 \times a^2 c / 3 \approx 1.1 \times 10^{-28} \text{ m}^3$ . From it, we can obtain the WZ InAs density, as the ratio between mass and volume of the unit cell:  $5670 \text{ kg/m}^3$ , a value very close to the InAs bulk one.

### Gold semi-sphere tip

The metal nanoparticle on the tip of each NWs is approximated with a Au semi-sphere with diameter equal to the corresponding NW diameter. We assign to it polycrystalline gold elastic constants (reported in Table 3, right column) and density  $19.3 \times 10^3 \text{ kg/m}^3$  [128].

### 2.4.2 InAs NWs mechanical properties

The simulation cell is taken radial symmetric both for the sample geometry and for laser excitation. The laser pulse, taken as infinitely extended in the radial dimension, strikes the sample propagating along the  $z$ -axis (i.e. the NW longitudinal axis). A 2D-axisymmetric ( $z$ -axis being the axis of symmetry) frequency-sweep analysis was performed. This means that the entire NW was forced to oscillate via a time-harmonic, spatially homogeneous, isotropic external stress  $\sigma_{ext}$  (see Equations 2.2 and 2.3) of frequency  $\nu$ :

$$\sigma_{ext} = A \mathbf{I}_d \exp(i2\pi\nu t), \quad (2.20)$$

with  $\mathbf{I}_d$  the  $3 \times 3$  identity matrix and  $A$  (Pa) an arbitrary constant amplitude. The problem is then solved in the frequency domain. The frequency-analysis is computationally time-efficient and very useful to spot out the excitation modes, nevertheless it does not shed light on the physics of the actual excitation mechanism encountered in experiments. The time resolved simulations, describing the dynamics of the system following the pump excitation, will be addressed in the last part of this chapter. The mechanical energy stored

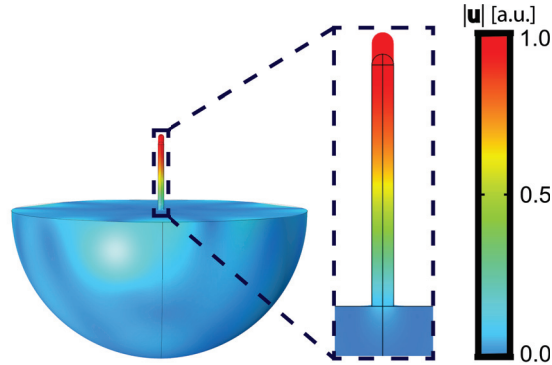


Figure 29. Displacement field of the fundamental extensional eigenmode (color scale and deformed geometry) and zoom on the NW (dashed box). The black contour represents the undeformed geometry of the NW. The color scale shows the modulus of the eigenmode displacement normalized against its maximum. Adapted with permission from [4]. Copyright 2022 American Chemical Society.

within the entire NW was computed as a function of the frequency  $\nu$ . The latter curve has a resonant line-shape and correspond to a NW mode. Fitting the line-shape with a Lorentzian function yields the frequency of the resonance maximum [132, 133].

Selecting the first resonance and inspecting its corresponding displacement profile, we recognize the NW fundamental axial extensional mode, as reported in Figure 29. This procedure is iterated for NWs with diameter and length corresponding to the mean value sizes for each sample, yielding the frequency of the fundamental extensional mode and the corresponding oscillation period for each NW, displayed in Figure 27 (red triangles).

In the same figure, we also report the effect of the NW sizes distributions (see Section 2.2) on the theoretically calculated periods. This is realized attributing to every NW mode a corresponding uncertainty box (pink semi-transparent rectangles in Figure 27). For each sample, the horizontal box side extends over the length range  $[\bar{L} - \sigma_L, \bar{L} + \sigma_L]$ , the values being taken from Table 1. The vertical side reports the fundamental extensional mode periods calculated for NWs with lengths in the previous range and diameters in the  $[\bar{D} - \sigma_D, \bar{D} + \sigma_D]$  interval.

The agreement between the experimental and computed oscillation periods is very good, the experimental results always being included in the theoretically uncertainty boxes. We stress that the agreement is obtained only on the basis of the physical model, that is no physical variable in the simulations is set as a free parameter to fit the experimental data. We thus conclude that the WZ InAs NW elastic matrix is well approximated by the bulk ZB InAs matrix rotated so as to have the  $z$ -axis of the spatial reference frame parallel to the crystal diagonal  $[111]$ .

The elastic matrix is key to access the InAs NW mechanical properties. In the case of the axial extensional mode, for instance, the oscillations depend on the axial Young modulus, i.e along the  $[111]$  direction. To calculate its value, we start by its definition:

$$E_{[111]} = \frac{\sigma'_3}{\varepsilon'_3}$$

Exerting an external stress along the  $x'_3$  direction (i.e.  $\boldsymbol{\sigma}' = [0, 0, \sigma'_3, 0, 0, 0]^T$  in Voigt notation) yields:

$$E_{[111]} = \frac{\sigma'_3}{\varepsilon'_3} = \frac{\sigma'_3}{(\mathbf{S}\boldsymbol{\sigma}')_3} = \frac{\sigma'_3}{S_{33}\sigma'_3} = \frac{1}{S_{33}}, \quad (2.21)$$

where  $\mathbf{S} = \mathbf{C}'^{-1}$  is the compliance matrix with components  $S_{ij}$  ( $i, j = 1, \dots, 6$ ). The stiffness and the compliance matrices have the same shape. In particular, they both have vanishing elements in the same positions. Inversion of matrix  $\mathbf{C}$  (see Equation 2.17) yields to

$$E_{[111]} = C'_{33} - \frac{2C'^2_{13}}{C'_{11} + C'_{12}} = 3C_{44} \frac{C_{11} + 2C_{12}}{C_{11} + 2C_{12} + C_{44}}, \quad (2.22)$$

where the expression on the right-hand side was obtained upon substitutions of Equations 2.18. Such a Young modulus along the axial direction results in a sound velocity  $[122]$   $v_{[111]} = \sqrt{E_{[111]}/\rho_{InAs}} = 4130$  m/s along the same direction.

### Complete vs simplified models

A legitimate question to be addressed is to what extent the full computational machinery is actually necessary to correctly access the mechanical problem. This aspect is important, on the one side, to distinguish among the key elements responsible for the mechanical response and the ones that play a minor role, on the other to provide in which

circumstances simplified models may be safely used. To this end, we here inspect to what extent reducing the model complexity affects the correct fundamental extensional mode period. In Figure 30, we report the sketches of three simplified models, specifically (i) the

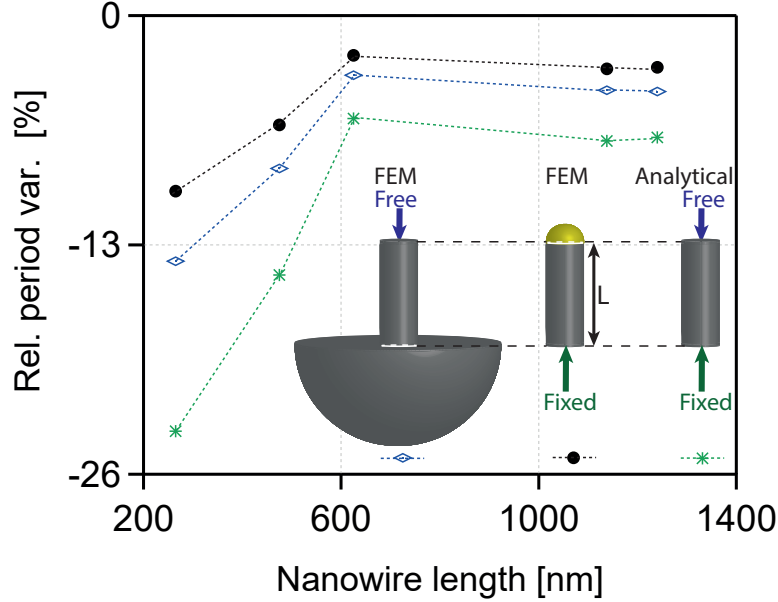


Figure 30. Comparison between the complete model and the simplified ones. Relative difference variation between the oscillation periods of the simplified models and the one of the complete numerical model vs NW length. The blue rhombuses, black circles and green stars correspond to (i) FEM model neglecting the gold tip, (ii) FEM model with fixed boundary condition (BC) at the NW-substrate interface and (iii) analytical formula for a NW without gold tip under free-fixed BCs, respectively, as schematized in the inset. Reprinted with permission from [4]. Copyright 2022 American Chemical Society.

FEM model neglecting the gold tip, (ii) FEM model with fixed BC - i.e. zero-displacement - at the NW-substrate interface and (iii) the commonly adopted analytical model for a NW without gold tip under free-fixed BCs, yielding  $4\sqrt{\rho_{InAs}/E_{[111]}}L$  for the fundamental longitudinal oscillation period. In all cases we adopt the elastic matrix for the WZ InAs NWs, as previously discussed.

The full mechanical model, which best reproduces experimental results, is taken as the benchmark. Figure 30 reports the relative period variation  $(\tau_{simp} - \tau)/\tau_{simp}$  for the investigated NWs, where the period  $\tau_{simp}$  is calculated adopting the specific simplified model among the three mentioned ones, and the period  $\tau$  results from the complete model. Neglecting the Au tip only (blue rhombuses) results in a shorter simulated pillar thus yielding a comparatively lower oscillation period. Qualitatively, the effect of the Au tip may be recovered encapsulating it in a NW effective length,  $\tilde{L}$ , exceeding the NW nominal length  $L$ . Interestingly, the same reasoning holds true also for the substitution of the substrate with a fixed BC at the bottom end of the InAs NW (black circles and green asterisks in Figure 30). When the substrate is present (as in the case of the complete model), the

material portion lying just under the NW base is not rigid and, during the NW oscillation, it deforms to some extent. The oscillation period is hence longer when the deformation is allowed to take place also in the substrate. When removing the substrate, this effect may be qualitatively accounted for introducing an effective  $\tilde{L} > L$ .

The commonly used analytical model (green asterisks) encompasses both simplifications, thus significantly underestimating the correct oscillation periods. In all cases, the underestimate worsen for shorter NW lengths, the relative weight of the Au tip and/or of the proximal substrate to  $\tilde{L}$  being higher. For instance, for the case of S1 (265 nm NW length) the underestimate of the actual oscillation period amounts to 25%.

The NW diameter also plays a role in the models comparison, even though to a much lesser extent. The relative period variations reported for the 625 nm NW case, which have been calculated for S3 (the only sample with  $\bar{D} \approx 20$  nm, half of that of the other NWs), are slightly longer than would result taking  $\bar{D} \approx 40$  nm (as for the other samples). This is the reason for the relative maximum occurring for this specific NW length in Figure 30.

Recapping, adoption of the full model is necessary, the approximate models leading to a systematic underestimate of the oscillation period, potentially biasing the correct assessment of the NW mechanical properties.

One last point is worth to be discussed, i.e. the circular rather than hexagonal geometry of the NWs. As already mentioned at the beginning of this chapter, in this work we assumed a circular, as opposed to hexagonal (as suggested by the SEM images in Figure 24), NW cross section. We did test the viability of the approximation computing the extensional modes of the NWs with hexagonal cross-section. The periods, for the case of the hexagonal NW, lay very close to the ones obtained with the cylindrical NW. Indeed, the extensional modes feature motion mainly along the NW axial direction. As a consequence, the NW shape in the radial direction does not significantly alter the longitudinal modes. This result allows to greatly reduce the computational burden, an hexagonal cross-section requiring a full 3D simulation (because of the loss of radial symmetry) at variance with the case of a cylindrical NW.

## 2.5 Origin of mechanical vibrations

In this section we focus on the origin of the mechanical vibrations triggered by the pump pulse. This is a crucial issue in view of applications in ultrafast opto-mechanics. The quest arises since, as will be proved shortly, negligible electromagnetic energy is absorbed in the NW where the longitudinal modes are confined. This is true both in the case where the gold semi-sphere is placed above the NW and in the absence of the Au nanoparticle. These results were obtained from tailored electromagnetic energy absorption calculation with and without the gold tip. The energy is mostly absorbed in the uncovered portion of the InAs substrate only. The pump photon energy,  $E_p = hc/\lambda_p \approx 0.8$  eV, exceeds the InAs

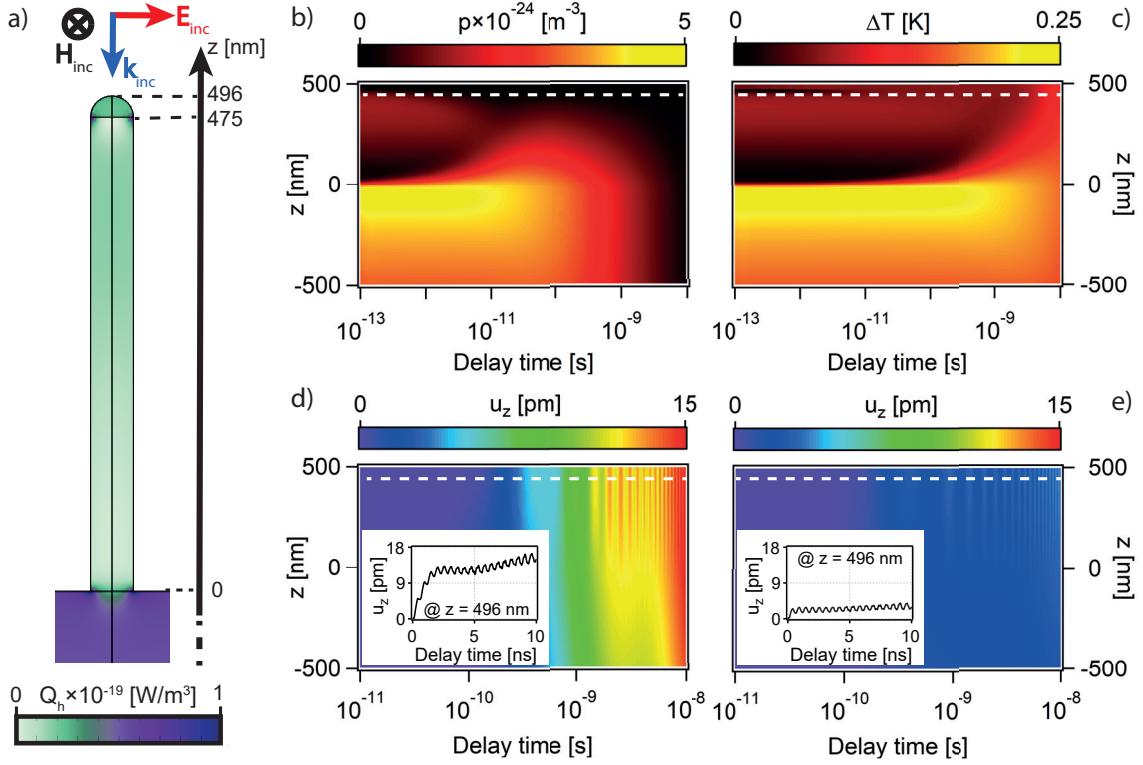


Figure 31. Absorbed power density in the sample (panel a) upon absorption of the pump pulse:  $Q_h$  is displayed in the cross-sectional plane perpendicular to the magnetic field,  $H_{inc}$ , of the incident radiation of wave vector  $k_{inc}$ . Holes density (panel b) and temperature variation (panel c) color maps calculated along the NW symmetry axis vs  $z$ -coordinate (vertical axis) and delay time (horizontal axis, log scale).  $z$ -component of the displacement field (colour scale) calculated along the NW symmetry axis vs  $z$ -coordinate (vertical axis) and delay time (horizontal axis, log scale) as triggered by only the deformation potential (panel d) or only the thermal expansion (panel e). Insets panels d and e:  $z$ -component of the displacement field at the top of the Au tip (left axis) vs delay time (horizontal axis, linear scale). White dashed line in panels b and e: interface between the InAs NW and the Au tip ( $z=475$  nm). Note that the time axis in panels b-c differs from the one in panels d and e. Simulations refer to sample S2:  $\bar{D} = 43$  nm and  $\bar{L} = 475$  nm. Reprinted with permission from [4]. Copyright 2022 American Chemical Society.

energy gap,  $E_g$ , ranging from  $\approx 0.35$  eV for ZB InAs [134] to  $\approx 0.50$  eV for WZ InAs [135]. Electronic transitions from the valance to the conduction band are hence activated, with electron-hole pairs generation. This leads to an external mechanical stress  $\sigma_{ext}$  via two concurrent mechanisms [136]: (i) deformation potential, which is proportional to the electron-hole pair density and (ii) lattice thermal expansion, which arises from the temperature increase due to the phonon-mediated intraband electrons (holes) relaxation to the bottom (top) of the conduction (valence) band.

The natural question that then arises is the following: which of the different physical mechanisms is the one responsible for exciting the NW extensional modes? Specifically, are the modes launched (i) via the diffusion of either electron-hole pairs and heat in the

NWs and the resulting external stress therein generated or (ii) via a substrate-mediated “hammer effect”, in which the initial impulsive stress generated in the substrate triggers a displacement field that propagates in a wave-like motion from the substrate to the NWs? To answer this question, we first need to solve the time-dependent displacement field triggered by the laser pulse. To this end we outline the strategy which will be detailed further on. We address the electromagnetic excitation, calculating the spatio-temporal profile of the absorbed power density [137, 138],  $Q_h(\mathbf{r}, t)$  ( $\text{W}/\text{m}^3$ ), delivered to the sample by the pump pulse (step 1). Once we know  $Q_h(\mathbf{r}, t)$ , we are able to retrieve both the spatio-temporal electron-hole pair density,  $p(\mathbf{r}, t)$  ( $1/\text{m}^3$ ), and temperature,  $T(\mathbf{r}, t)$ , distributions (steps 2a and 2b, respectively). These quantities are the fundamental ingredients to calculate the stress source term  $\sigma_{ext}(\mathbf{r}, t)$  entering Equation 2.3 via the deformation potential and/or thermal expansion (steps 3a and 3b respectively). Ultimately, we are interested in the displacement field,  $\vec{u}(\mathbf{r}, t)$ , associated to the stress tensor  $\sigma$ , either by the deformation potential or thermal expansion (steps 4a and 4b, respectively).

$$\begin{array}{c}
 \text{step 1} \\
 \boxed{Q_h(\mathbf{r}, t)} \Rightarrow \left\{ \begin{array}{l}
 \begin{array}{c}
 \text{step 2a} \\
 \frac{\partial p}{\partial t} - D_p \nabla^2 p + \frac{1}{\tau_p} p = \frac{Q_h(\mathbf{r}, t)}{E_p} \Rightarrow \boxed{\sigma_{ext}(\mathbf{r}, t)} = -d_{e-h} p(\mathbf{r}, t) \mathbf{I}_d \Rightarrow \begin{array}{c}
 \text{step 4a} \\
 \rho \frac{\partial^2 \vec{u}}{\partial t^2} = \nabla \cdot \sigma \\
 \sigma = \mathbf{C} \cdot \varepsilon + \boxed{\sigma_{ext}}
 \end{array} \\
 \text{step 3a}
 \end{array} \\
 \\
 \begin{array}{c}
 \text{step 2b} \\
 \rho C_p \frac{\partial T}{\partial t} - \kappa_T \nabla^2 T = \boxed{Q_h(\mathbf{r}, t)} \left(1 - \frac{E_g}{E_p}\right) \Rightarrow \boxed{\sigma_{ext}(\mathbf{r}, t)} = -\mathbf{C} \cdot \alpha \Delta T(\mathbf{r}, t) \Rightarrow \begin{array}{c}
 \text{step 4b} \\
 \rho \frac{\partial^2 \vec{u}}{\partial t^2} = \nabla \cdot \sigma \\
 \sigma = \mathbf{C} \cdot \varepsilon + \boxed{\sigma_{ext}}
 \end{array} \\
 \text{step 3b}
 \end{array}
 \end{array} \right.
 \end{array}$$

Figure 32. Outline of the theoretical frame adopted to access the time dependent displacement field. Deformed potential (scenario (a)) and thermal expansion (scenario (b)) contributions. The color code for the frames allows following the role played by the pertinent quantity in the calculation chain.

- *Step 1.* We calculate the electromagnetic field distribution within the system. In this way, we gain access to the absorbed power density  $Q_h = \Re(\tilde{\mathbf{J}} \cdot \tilde{\mathbf{E}})/2$ , where  $\tilde{\mathbf{J}}$  and  $\tilde{\mathbf{E}}$  are the complex-valued current density and electric field, respectively ( $\Re$  stands for real part).

Figure 31 (panel a) reports the spatial distribution of  $Q_h$  in the system (gold tip, NW and substrate), obtained at the peak intensity of the pulse and represented in a cross-sectional plane containing the wave vector  $\mathbf{k}_{inc}$  and the electric field  $\mathbf{E}_{inc}$  of the pump beam. As can be appreciated in the figure, light is predominantly absorbed in the substrate ( $z \leq 0$  nm). Note the difference with respect to the gold NDs on sapphire substrate system described in Chapter 1, where the light was only absorbed by the plasmonic nanoparticle. The energy dissipation in the NW is comparatively exiguous, limited to the Au tip ( $475 \text{ nm} \leq z \leq 496 \text{ nm}$ ) and to the top half of the NW ( $240 \text{ nm} \leq z \leq 460 \text{ nm}$ ).

In order to determine which is the dominant effect causing the vibrations in the NW,

we address the two above mentioned scenarios separately, the actual situation being the superposition of the two.

We now focus on scenario (a): the NW mechanical response contribution which is triggered only by the deformation potential due to electron-hole pairs formation.

• *Step 2a.* We first calculate the transient distribution of the electron-hole pairs. We assume that every absorbed photon generates an electron-hole pair. The number of electron-hole pairs per unit volume generated per unit time is then given by  $Q_h(\mathbf{r}, t)/E_p$ , serving as the source term in the diffusion equation. The electron and hole densities remain anchored throughout the dynamics, space charge neutrality being achieved within few ps [139]; the hole density is thus representative of that of the electron-hole pairs. The diffusion equation for the hole density,  $p(\mathbf{r}, t)$ , is then given by the equation

$$\frac{\partial p}{\partial t} - D_p \nabla^2 p + \frac{1}{\tau_p} p = \frac{Q_h(\mathbf{r}, t)}{E_p}, \quad (2.23)$$

where  $D_p=10^{-3}$  m<sup>2</sup>/s and  $\tau_p=10$  ns are respectively the diffusivity and recombination time for holes in InAs [140]. The recombination term does not play significantly here,  $\tau_p$  matching the time-scale of our experiment.

Regarding BCs, the substrate dimensions are  $\approx 0.1$  mm, far exceeding the carriers diffusion distance, which can be estimated by  $\approx \sqrt{D_p t_{max}} \approx 3$   $\mu$ m, occurring on the experiment time-scale,  $t_{max}=10$  ns. This means that the substrate lateral and bottom boundaries do not affect the solution. On the InAs external surfaces (both of the NW and the substrate) we assign a recombination velocity  $S_p = 30$  m/s [141]. Inside the gold semi-sphere and at its boundary with the NW ( $z=475$  nm) the hole density is fixed to zero, electron-hole separation being quenched in metals. We assume that before the pump pulse strikes, no electron-hole pairs are present, the initial condition thus being  $p_0 = 0$  throughout the simulation domain.

Figure 31 (panel b) reports the computed hole density  $p$  along the NW symmetry axis ( $z$  coordinate, vertical axis) as a function of the delay time (in log-scale), taken with respect to the instant maximizing the pump pulse intensity. The vertical axis was extended to negative  $z$  values in order to show the hole density also in the substrate portion proximal to the NW. At short delay times ( $10^{-13}$  s),  $p$  matches the  $Q_h$  distribution (Figure 31, panel a), with the exception of the Au tip ( $z \geq 475$  nm:  $z$  values above the white dashed-line), where absorption is present but  $p$  is fixed to zero. The density  $p$  is higher in the NW proximal substrate ( $-150$  nm  $\leq z \leq 0$  nm) with a maximum value of  $5 \times 10^{24}$  1/m<sup>3</sup>, while it drops inside the InAs NW. As time evolves, the hole concentration in the proximal substrate diffuses both inside the NW and into the deep portions of the substrate. When  $t \approx 7$  ns,  $p$  is reduced by an order of magnitude or more along the entire range of shown  $z$ -coordinates.

• *Step 3a.* Assuming an isotropic stress, the electron-hole pairs generate an external

stress [136] given by

$$\boldsymbol{\sigma}_{ext}(\mathbf{r}, t) = -d_{e-h}p(\mathbf{r}, t)\mathbf{I}_d, \quad (2.24)$$

where  $\mathbf{I}_d$  is the  $3 \times 3$  identity matrix and  $d_{e-h}$  the deformation potential (eV):

$$d_{e-h} = B \frac{\partial E_g}{\partial P} = B \frac{\partial E_c}{\partial P} - B \frac{\partial E_v}{\partial P} = a_c - a_v, \quad (2.25)$$

where  $B$  is the bulk modulus (Pa),  $P$  the pressure (Pa),  $E_c$  ( $E_v$ ) the minimum (maximum) of the conduction (valence) band (eV) and  $E_g = E_c - E_v$  the energy gap. For InAs,  $a_c = 5.22$  eV and  $a_v = -0.48$  eV [142], leading to  $d_{e-h} = 5.68$  eV.

Equation 2.25 assumes that each electron promoted to the conduction band contributes equally to the deformation potential, independently from its final energy in the conduction band. The same is assumed also for the holes in the valence band. This simplification allows for a manageable computational time while yielding reasonably good estimations [136].

- *Step 4a.* Now that we have calculated  $\boldsymbol{\sigma}_{ext}$  generated by the electron-hole pairs, we are able to insert it in the generalized Hooke's law in Equation 2.3. Since we want to access the mechanical response due to solely the electron-hole pairs, we insert  $\boldsymbol{\sigma}_{ext}$  calculated in the previous step 3a, as the sole external stress term perturbing the system initially at rest. Free BCs are assigned on all the external boundaries and the elastic constants are the those adopted for the frequency-sweep analysis (Section 2.4).

Figure 31 (panel d) reports the  $z$ -component of the displacement field along the NW axis,  $u_z$  as a function of  $z$  and of the delay time (log-scale). The system is appreciably deformed,  $u_z \approx 0.2$ - $0.8$  pm, after a delay time of  $\approx 100$  ps. For all the reported quota,  $u_z$  increases rather smoothly. Most importantly, in the NW and Au tip only (i.e. for any cut at a coordinate  $z \geq 0$  nm), well defined oscillations are clearly visible on the 1 to 10 ns time-scale, superposed on the developing displacement background. This is well appreciated from the inset, where  $u_z$ , calculated at the top of the Au tip ( $z=496$  nm), is reported as a function of the delay time (in linear scale). The oscillation frequency, 1.8 GHz, matches the experimental value ascribed to the NW fundamental extensional mode, see Figure 29.

We now address scenario (b): the NW mechanical response contribution which is triggered only by the temperature rise in the system.

- *Step 2b.* Using the calculated absorbed power density from electromagnetic absorption by the system (*Step 1*), we can derive the transient temperature distribution throughout the system. The electrons (holes) photoexcited in the conduction (valence) band relax to the bottom (top) of the conduction (valence) band via phonon-emission, raising the non-equilibrium lattice temperature  $T$ . As for the (a) scenario we assume that every absorbed photon generates a electron-hole pair, and that fast (on a ps timescale) non-radiative scattering is the only intraband relaxation process. Each absorbed photon then

contributes with an energy  $E_p - E_g$  to lattice heating, band-filling effects being disregarded in this estimate (a meaningful approximation provided the photo-excited carrier density is low enough).

The fraction of the absorbed electromagnetic power density converted to heat then reads  $Q_h(\mathbf{r}, t) \left(1 - \frac{E_g}{E_p}\right)$ . This is the source term which we can use in the diffusion equation for  $T$ :

$$\rho C_p \frac{\partial T}{\partial t} - \kappa_T \nabla^2 T = Q_h(\mathbf{r}, t) \left(1 - \frac{E_g}{E_p}\right), \quad (2.26)$$

where  $\rho$  (kg/m<sup>3</sup>),  $\kappa_T$  (W/(m·K)) and  $C_p$  (J/(kg·K)) are the mass density, the thermal conductivity and the heat capacity, respectively. Their values are reported in Table 4. The substrate dimensions exceed the temperature diffusion distance, estimated as  $\sqrt{D_T t_{max}} \approx 0.5 \mu\text{m}$ , covered on the experimental time-scale ( $t_{max}=10$  ns). The substrate lateral and bottom boundaries hence do not play a role in the present thermal problem. On the InAs and Au surfaces we assign radiative BCs. The system initial temperature is set as the room temperature ( $T_0=293$  K).

Thermal parameter	InAs substrate	InAs NW	Au tip
$\kappa_T$ (W/m K)	27 [143]	16 [144]	318 [145]
$C_p$ (J/kg K)	250 [146]	250 [146]	129 [145]
$\rho$ (kg/m <sup>3</sup> )	5670	5670	19300
$D_T$ (10 <sup>-5</sup> m <sup>2</sup> /s)	1.9	1.9	12.8
$\alpha$ (10 <sup>-6</sup> 1/K)	4.45	4.45	14.2 [147]

Table 4. Thermal parameters adopted for the simulation.

The temperature increase,  $\Delta T=T - T_0$ , is reported in Figure 31 (panel c), the axis being the same as for panel d of the same figure. Under many aspects the same considerations we made for  $p$  are also valid for  $\Delta T$ , both quantities satisfying a diffusion equation. The color map for  $\Delta T$  (panel c) resembles, up to  $\approx 1$  ns, the color map for  $p$  (panel b) up to  $\approx 20$  ps. This is intuitively rationalized exploiting the rule of thumb estimate for the diffusion time over a generic distance  $x$ , with  $t_{D,i} = x^2/D_i$ , where the pendex  $i=\{p, T\}$ , yielding to  $t_{D,T}/t_{D,p}=D_T/D_p = 50$ , which indeed matches the timescale stretch arising between the two color maps.

- *Step 3b.* Temperature variations are responsible for an external thermal stress  $\sigma_{ext}(\mathbf{r}, t) = -\mathbf{C} \cdot \alpha \Delta T(\mathbf{r}, t)$ , where  $\alpha$  (1/K) is the thermal expansion tensor of the material. Assuming, for simplicity, that all the materials in the system have an isotropic thermal expansion, we can write  $\alpha = \alpha \mathbf{I}_d$ , with  $\alpha$  being the linear thermal expansion coefficient, with values reported in Table 4 for the InAs and gold.

- *Step 4b.* In a similar way to what happens in the scenario (a), the new calculated  $\sigma_{ext}$ , this time generated only by the temperature increase, is inserted in the generalized Hooke's law (Equation 2.3) as the sole external stress term perturbing the system. In this

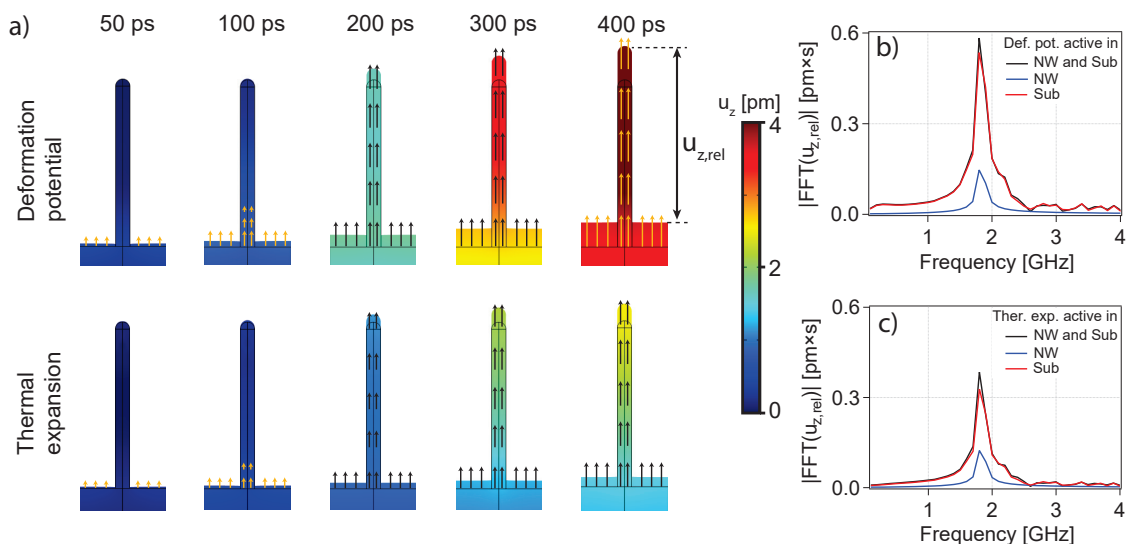


Figure 33. Displacement profiles: deformation potential vs thermal expansion. Profile deformation snapshots at different times (panel a), arrows and color scale refer to the the  $z$ -component of the displacement field,  $u_z$ , triggered by the deformation potential (top row) and thermal expansion (bottom row). Double-pointed arrow: definition of relative displacement,  $u_{z,rel} = u_z(496 \text{ nm}) - u_z(0 \text{ nm})$ . Modulus of the relative displacement FT for the case of displacement triggered by the deformation potential (panel b). The black line indicates the deformation potential active both in the NW and substrate. The blue and red lines, instead, indicate the deformation potential active only in the NW and substrate, respectively. Panel c reports the same information as panel b, but for the case of displacement triggered by thermal expansion. Simulations refer to sample S2:  $\bar{D} = 43 \text{ nm}$  and  $\bar{L} = 475 \text{ nm}$ . Reprinted with permission from [4]. Copyright 2022 American Chemical Society.

way, we can solve Equations 2.2 and 2.3 to obtain the displacement field for the scenario (b).

Figure 31 (panel e) reports  $u_z$ , with the axis being the same as for panel d. Also in the present scenario, oscillations are visible in the NW on the same timescale and superposed on a slowly increasing background. The oscillation frequency is again 1.8 GHz, in agreement with experimental value corresponding to the NW fundamental extensional mode. The main differences between the two scenarios are a lower magnitude of the displacement and of the peak-to-peak oscillation amplitude in the thermal expansion case as compared to the deformation potential one.

With the knowledge acquired differentiating the deformation potential and the thermal contributions in the mechanical response of the system after the pump excitation, we are now in a position to address the origin of the NW mechanical vibrations, namely to answer whether the NW longitudinal modes are launched (i) via a diffusion process or (ii) via a “hammer effect” arising from the substrate.

In Figure 33 (panel a) we report snapshots of the mechanical deformation within the

NW and its proximal substrate at different time instants, chosen around the inception of the mechanical dynamics for both scenarios: deformation potential (top row), and thermal expansion (bottom row). The horizontal black lines indicate the undeformed geometry, while the arrows indicate the displacement, their length being proportional to the  $z$ -component of the displacement field modulus. The time frames sequence suggests that deformation originates in the substrate, pushing the NW upwards and triggering the mechanical vibrations inside the NW.

Since we are mostly interested in the NW mechanical vibrations, we get rid of the slower substrate displacement by considering the relative displacement  $u_{z,rel}$ , defined as the difference between  $u_z$  at the NW tip and base, (its visualisation can be found at the 400 ps time-frame in top row in panel a of Figure 33).

To inspect accurately where the oscillation originates, we calculated  $u_{z,rel}$  after selectively switching off the deformation potential (scenario (a)), or thermal expansion (scenario (b)), within the NW and the substrate, respectively. In this way, we can selectively see the contributions for the substrate and from the NW of the different scenarios. In all cases, a resonance appears at the NW longitudinal mode frequency of 1.8 GHz, as shown in panels b of Figure 33. Here, we report the absolute value of the FT of  $u_{z,rel}$  for the case of the deformation potential active both in the substrate and NW (black curve), in the substrate only (red curve), and in the NW only (blue curve). As can be seen, the black and red curves are almost overlapped, i.e. the contribution of the blue curve to the black one being minimal.

Selectively switching on and off the contributions from the different domains of the system, allows unveiling the physics behind the mechanical response of the system. When only the NW domain is active, the blue curve accounts for the main mechanism responsible for the genesis of the NW longitudinal oscillation. In this case, only the e-h pairs in the NW act as a source term for  $\sigma_{ext}$  and their presence predominantly derives from diffusion from the substrate, see discussion of panel b in Figure 31. Since the blue curve weakly contributes to the black curve, we can exclude e-h diffusion as responsible for launching the NW modes. On the other hand, the red curve, which is the main contribution to the NW oscillation spectral weight, implies that the displacement and external stress within the NW originate from the wave-like propagation of the displacement and external stress originally generated in the substrate. This means that, when we take into account the deformation potential only, the origin of the NW oscillations is ascribed to a “hammer effect”, deriving from the substrate.

Similarly, panel c of Figure 33 reports the absolute value of the FT of  $u_{z,rel}$  calculated for the case of thermal expansion active both in the substrate and the NW (black curve), in the substrate only (red curve), and in the NW only (blue curve). The discussion parallels that for panel b of the same figure, with thermal expansion and temperature replacing deformation potential and e-h pair, respectively. We then conclude that, also for the

case of thermal expansion, the origin of the NW oscillations arises from this “hammer effect” acting in the substrate. In terms of displacement amplitude, the thermal expansion contribution to the NW vibrations is half of that by the deformation potential, as can be seen comparing panels b and c in Figure 33.

This mechanism, although always present for photon energies in the InAs absorption spectrum, may not be the only important one for some specific wavelengths of the pump beam. For instance, at 530 nm, i.e. surface plasmon resonance of the gold nanoparticle,  $Q_h$  within the NW becomes relevant and the direct NW excitation contributes significantly. Moreover, the relative contribution of the deformation potential and thermal expansion also depends on the photon energy. Specifically, for a photon energy tuned at exactly  $E_g$ , only the deformation potential plays a role, whereas for higher photon energies thermal expansion contributes as well.

The origin of the oscillation via a substrate-mediated “hammer effect” bears great generality, and can be potentially important in any other semiconductor NW system [148, 149, 150, 151, 152]. Nevertheless, it is at variance with respect to direct excitation mechanisms, as commonly encountered in time-resolved opto-acoustic experiments on nanowires [153, 53] and on a plethora of nanosystems [154, 155, 156, 118, 157, 116, 158], or to propagating modes launched via NW metal capping serving as transducer [99].

## 2.6 Conclusions

In this chapter, we reported on the mechanical nanometrology of vertically aligned gold-catalyzed InAs NWs forests of varying lengths on a InAs substrate. The study was performed via a multi-technique approach, encompassing electron microscopies, ultrafast pump-probe measurements and finite element simulations.

We addressed the long standing issue of InAs NWs mechanical properties, and we were able to provide a reliable, experimentally benchmarked, elastic matrix implying a Young modulus of 97 GPa.

We then investigated the genesis of the NWs mechanical oscillations. Through FEM simulations, we were able to show that the NW oscillations originate from an impulsive “hammer-like” excitation triggered in the substrate and propagating in a wave-like motion into the NW, rather than from an expansion of the NW itself. This is a radically different process with respect to the ones reported so far and, in particular, at variance with the gold NDs on a sapphire substrate system, described in Chapter 1. In that case, indeed, it was only the ND to absorb the light pulse, rise its temperature and starts vibrating. The transparent sapphire substrate had only an indirect role in the dynamics, both from a thermal point of view, by absorbing heat from the ND and evacuating it, and from a mechanical point of view, by absorbing and attenuating the vibrations of the ND (this part, however, being of secondary importance in our study). In the case of InAs NWs excited by a pump pulse with  $\lambda_p=1560$

nm, the opposite happens. It is the InAs substrate the main responsible for the light absorption and also for the generation of the mechanical stress, which then propagates in the NW. Additional excitation mechanisms can set-in when operating with different wavelengths. Figure 34, for instance, shows the absorbed power density in the case of  $\lambda_p=530$  nm. At variance with respect to  $\lambda_p=1560$  nm (see Figure 31), in this case the absorption is significant also in the gold semi-sphere and in the InAs nanowire, the oscillation potentially originating within the NW.

The present findings are of interest for any device engineering based on InAs NWs, considered the crucial role of the mechanical properties. Moreover, the genesis of the mechanical oscillations can have an impact in ultrafast opto-mechanical applications. Finally, it provides new insight on the working principle of pump-probe techniques as a mechanical nanometrology tool.

In the next chapter, we will return to study metallic nano-objects, this time in contact with a liquid environment rather than a solid substrate. As for this chapter, great importance will be given to the different competing physics behind the mechanical response of the system after an optical excitation. In particular, the total mechanical response will be separated in the contributions from the nanoparticle and from its surrounding liquid. Varying the system thermal properties largely affect the relative nanoparticle and liquid contributions, thus resulting in different acoustic waves launching mechanisms.

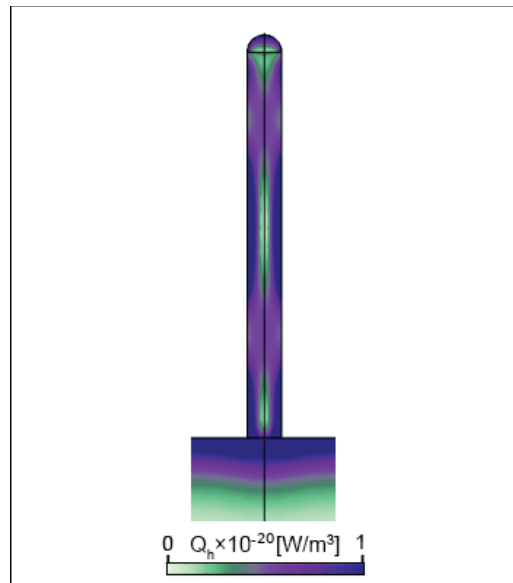


Figure 34. Absorbed power density in the sample upon absorption of a pump pulse with wavelength  $\lambda_p = 530$  nm:  $Q_h$  is displayed in the cross-sectional plane perpendicular to the magnetic field,  $H_{inc}$ , of the incident radiation of wave vector  $k_{inc}$ .



### 3. Photoacoustic effect: gold nano-transducers in water

This chapter theoretically focuses on the photoacoustic effect of metal-nano-transducers in contact with a liquid. In particular, the different mechanisms by which the acoustic wave is launched are investigated. The chapter is structured in two sections, whose results will make the object of two articles to be submitted shortly, one to *Applied Phys. Lett.*, the other to *Phys Rev. E*.

The entire work stems from a collaboration with Dr. Stefano Giordano at the Institute of Electronics, Microelectronics and Nanotechnology (IEMN) and Université de Lille, France.

The first section focuses on water immersed gold nanocylinders. I contributed from the idea conception, to the system modelling, all the way to the manuscript draft redaction. This was the second article I redacted in first person.

The second section deepens the physical understanding of the phenomena addressed in the first section. The investigated systems is now a gold nanofilm in contact with water. The section consists of a purely analytical part, investigating the photoacoustic response under a time periodic laser beam excitation, and in a numerical one, investigating the photoacoustic response under short laser pulse excitation. My main contribution concerned the second part, although I was fully involved in discussing the model and the physics object of the analytic part too.

#### 3.1 Introduction

The main focus of this chapter is dedicated to the ultrafast thermo-acoustic energy exchange between single metal nanotransducers and a liquid environment. In respect to the previous two chapters, the roles between the nanoparticle and its environment change. In Chapter 1, only the gold nanoparticle absorbs the light pulse, rises its temperature and activates its vibrational modes. The role of the transparent substrate is to allow for the cooling of the nanodisk, mediated by the TBR, and evacuate it. In Chapter 2, the opposite is true. It is the substrate that absorbs the pump pulse, expands and “hammers” the InAs nanowires, activating their vibrational mode. In this chapter, we will see how the acoustic response of the system will be launched both by the nanotransducer, addressed as nanoparticle in the present context, and its environment, depending on the optical and thermal parameters which may be varied in an experiment, namely the laser pulse length and the TBR.

Another difference, as compared to Chapters 1 and 2, consists in shifting the focus from the nanoparticle to the environment, with respect to the media from which information on the system is extracted. In the previous chapters, we have seen pump-probe experiments performed on nanoparticles in contact with a solid substrate, probing the nanoparticle to reveal the thermo-acoustical evolution of the optically excited system. Then, by comparing the measured dynamics with tailored simulations, we were able to extract properties of the system, as the gold/sapphire TBR of individual nanodisks or the Young modulus of InAs nanowires. Here, to understand the opto-thermo-mechanical dynamics of the system we will instead mostly rely on changes within the liquid environment that surrounds the nanoparticle. This is realized by performing simulations on the outcome of different photoacoustic launching mechanisms in liquids by individual metal nanoparticles. We will be able to extract the key parameters that may serve as tuning knob to regulate the nanoparticle/liquid environment photoacoustic interaction.

Before discussing these mechanisms and the role of the different parameters involved in the phenomenon, we introduce the photoacoustic effect by means of a brief historical review. For an exhaustive review we address the reader to the works of Manohar *et al.* [159] and Bertolotti *et al.* [160]. This will help to contextualize the present results in a broader perspective.

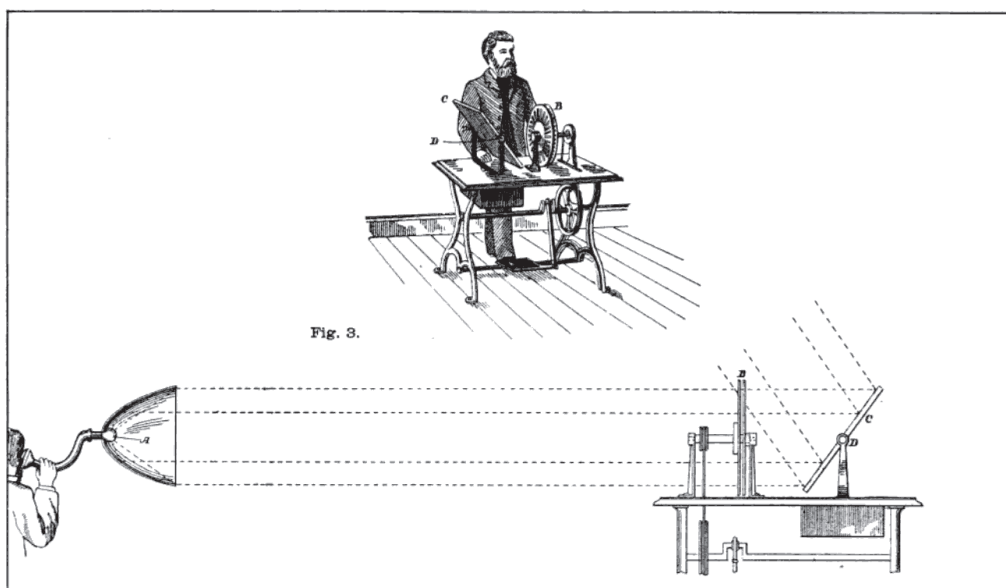


Figure 35. Original drawing of a photoacoustic device taken from [161]. A mirror (c) is tilted at a chosen angle by fine tuning its rotation around its axis (d). Light is reflected by the mirror and passes through a rotating slotted disk (b) which lets through an intermittent light beam. Light arrives then at the receiver (left), consisting in a parabolic reflector, in the focus of which there is the photoacoustic medium (a) generating sound waves, that can be listened through the hearing-tube.

Discovered in 1880 by Alexander Graham Bell [161], the photoacoustic effect is a phenomenon in which a material converts absorbed light in sound waves. An original sketch

of a Bell's photoacoustic device is reported in Figure 35. In his work, Bell succeeded in recognizing the importance of different parameters on the photoacoustic outcome such as a modulated light source (using a rotating slotted wheel to switch on and off the visible light), light nature (visible, infra-red or ultra-violet) and the material itself.

The discovery of the photoacoustic effect, at first triggered excitement in the scientific community, with other scientists joining the field. New experimental and theoretical steps were taken, aimed at the understanding the photoacoustic generation mechanisms [162, 163] and extending the investigation to absorbing gasses [164, 165]. That said, the interest on the topic rapidly faded due to the difficulties involved in implementing applications. Soon the phenomenon was perceived more as a curious effect rather than a serious technological opportunity [159]. It was only after five decades that the photoacoustic effect reappeared in a scientific report [166] and was then exploited for gas detection and analysis [167, 168, 169, 170]. Finally in the 1970s, studies on the photoacoustic effect in solids came back to the scene [171, 172].

Today the photoacoustic effect makes the object of a renewed interest in the scientific community thanks to its potential in imaging and therapeutic applications [173, 174, 175, 176, 177]. In this context, a particular effort is dedicated to the study of metal nanoparticles, which have proven to be efficient photoacoustic generators, exploiting their high and tunable optical absorption properties [178, 179], high contrast imaging features [180] and biocompatibility [181, 182].

In describing the photoacoustic effect generated by metal nanoparticles immersed in liquids, we can identify three main concatenated physical steps: (i) the nanoparticle absorbs the light pulse and rises its temperature by converting the light energy in heat, (ii) a heat flow is established between the nanoparticle and the surrounding liquid, thus rising the liquid temperature and (iii) a mechanical response of the system is triggered, generating a propagating sound wave in the liquid.

Here, we will see the results of simulations based on a continuous model that takes into account different sound waves launching mechanisms. The absorber will be either gold nanoparticles or nanofilms immersed in an aqueous medium. We will study systematically the role of the TBR and of the light pulse duration in the photoacoustic outcome and in particular in the competition between the different launching mechanisms.

### **3.2 Thermophone vs Mechanophone**

As we said, the photoacoustic effect from metal nanoparticles immersed in water can be divided in three steps involving the optics, the thermal dynamics and the mechanical response finally resulting in sound waves generation. The emitted sound wave, however, is the combined results of the different launching mechanisms, notably the *thermophone effect* and the *mechanophone effect*. In the thermophone effect it is the thermal expansion

of the liquid which triggers the emission of the acoustic wave. In this case, the role of the nanoparticle is purely thermal: it works as a nanoheater and its role is to absorb the light pulse energy and convert it in heat that then flows in the surrounding liquid. On the contrary, in the mechanophone effect it is the thermal expansion of the nanoparticle which launches the sound wave. The expansion of the nanoparticle, indeed, generates a mechanical boost against the liquid, thus launching a sound wave in it. Despite the fact that in a real physical scenario both these two launching mechanisms are in principle always present, most of the investigations so far focused on the thermophone effect [183, 184, 185, 186], being the mechanophone one negligible. We can mention thermophones made out of aluminum wires [187], gold wires [188], silver wires [189], graphene [190, 191, 192, 193, 194] and boron nitride foams [195, 196]. In particular, most of the studies were carried out on metallic nanoparticles, either single [145, 147, 197, 198, 199, 200, 201, 202] or agglomerates [199], using ns light pulses, ns lasers being the standard for photoacoustic generation in bio-medical applications. The implications of the laser pulse duration on the photoacoustic generation by a single gold nanosphere was only touched in the seminal work of Prost *et al.* [147], the main focus though being on the long pulsed-regime [147, 202]. In all cases, with the exception of Prost *et al.* [147], only the thermophone effect was active.

Here we will access also the ps laser excitation, where, we shall see, the mechanophone effect plays a fundamental role. We will analyze the parameters role in the thermophone vs mechanophone competition. We will understand how the mechanophone contribution can become the prevailing launching mechanism contributing to the total acoustic wave and the advantages of such scenario. As we will see, the key parameters in the thermophone vs mechanophone competition are the size of the nanoparticle, the TBR at the nanoparticle/liquid interface and the light pulse duration. In this chapter we focus systematically on the TBR and the light pulse duration, while in Chapter 4 we will see also the effect of the nanoparticle size.

### 3.3 Role of the TBR

Throughout the entire work of this thesis, the TBR is a crucial parameter regulating the thermal energy exchange at the nanoscale. This chapter makes no exception and, before entering in the description of the simulations, it is worth introducing intuitively the role of the TBR in the competition between the thermophone and the mechanophone effects.

In the thermophone effect, we said that is the thermal expansion of the liquid which generates the sound wave. Thus, the more efficiently the liquid absorbs heat from the nanoparticle, the higher its acoustic response. From this simple consideration, it naturally follows that the lower is the TBR, the higher is the thermophone effect. On the contrary, the mechanophone effect is given by the nanoparticle thermal expansion. To maximize the

mechanophone contribution, the nanoparticle temperature should be the highest possible, thus the heat dissipation towards the surrounding liquid should be limited as much as possible. In other words, the higher the TBR, the greater will be the mechanophone contribution.

A study of the photoacoustic dependence on different parameters, including the TBR, was brought out by Cavigli *et al.* [203]. In Cavigli's work, however, only the thermophone effect is considered, without accounting for the mechanophone effect contribution. This leads to an almost zero acoustic wave at high TBR values, when in reality the mechanophone effect would generate a substantial sound wave.

In the following, we will see the results of a model implemented to understand the thermophone vs mechanophone competition as a function of the TBR, while exciting the system with light pulses of duration ranging from ns down to ps. The TBR will be allowed to vary freely, in order to gain a theoretical understanding of its role in the photoacoustic effect.

The solid/liquid TBR manipulation is a wide research field by its own, which makes use of different techniques as pressure [204, 205], temperature [206, 207, 208, 209], presence of surfactants [210], wettability [206, 211, 212, 213, 214, 215], nano-engineering of the solid interface [216, 217] and thin layer deposition [218, 219]. Regarding this last technique, C. Herrero *et al.* recently predicted a ultra-high TBR value for the gold/water interface when depositing a few graphene layers on the gold surface [220], two order of magnitude larger than the typical gold/water TBR. Taking for the gold/water TBR  $\approx 10^{-8}$  m<sup>2</sup>K/W) [67, 221, 222, 223], we thus obtain the graphene-functionalized gold water TBR to be  $\approx 10^{-6}$  m<sup>2</sup>K/W. With such a value we will see how, in our system, the mechanophone effect predominates over the thermophone one both for ns and ps light pulses duration.

### 3.4 Gold nanocylinder in water

The first system that we will study is a polycrystalline gold nanocylinder (NC) immersed in water. Methodologically, we adopt a multi-physics approach combining optics, thermal dynamics and mechanics in the frame of a continuum model solved via Finite Element Methods (FEM). We will describe the opto-thermo-acoustic dynamics of the system after an initial excitation by a laser pulse of variable duration:  $\tau_L = 1$  ns, 100 ps, 10 ps.

The system is modeled with two co-axial cylinders of same height  $H$ , internal radius  $R_{gnc}$  and external radius  $R_w$ , see Figure 36. The internal cylinder, with  $R_{gnc} = 10$  nm, represents the gold NC. The external one represents the surrounding water and its radius  $R_w$  is chosen long enough to avoid any heat accumulation or acoustic wave reflection at the boundary of the system during the simulations timescale. The height  $H$  of the system

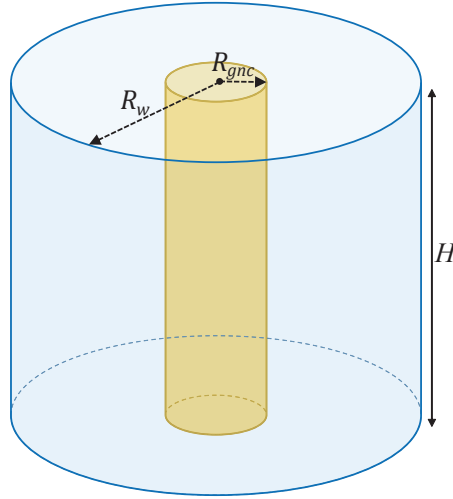


Figure 36. Scheme of the gold NC immersed in water.

Material property	Gold	Water
Thermal conductivity (W/(m K))	318	0.6
Heat capacity (J/(kg K))	129	$4.2 \times 10^3$
Density (kg/m <sup>3</sup> )	$19.3 \times 10^3$	$1 \times 10^3$
First Lamé coefficient (GPa)	147	2.25
Second Lamé coefficient (GPa)	27.8	0
Linear thermal expansion coefficient (K <sup>-1</sup> )	$1.43 \times 10^{-5}$	$\alpha_w(T)$ , with $\alpha_w(293 \text{ K}) = 7 \times 10^{-5}$

Table 5. Materials properties of gold and water.

is taken large enough to suppress any border effect close to the gold NC top/bottom basis<sup>1</sup>, thus allowing us to apply a zero *vertical* displacement condition at the basis. In other words, the problem is only *r*-dependent.

We assume the system can be described in the linear elastic regime, that there is no thermoacoustic feedback (the thermal dynamics induces the acoustic response, but the opposite effect is negligible) and that viscoelasticity is negligible in both Au and water, i.e. no intrinsic damping is present.

Regarding the materials properties of gold and water, such as the thermal conductivity  $k$  (W/(mK)), the heat capacity  $c_p$  (J/(kgK)), the density  $\rho$  (kg/m<sup>3</sup>), the first and second Lamé coefficients  $\lambda$  and  $\mu$  (Pa) and the linear thermal expansion coefficient  $\alpha$  (1/K), they are taken from the literature [145, 147, 68] and summarized in Table 5. In the temperature range spanned by simulations, the only coefficient that has a non-negligible temperature dependence is the water thermal expansion coefficient. To include this dependency, we used in our model a third order polynomial function  $\alpha_w(T)$  which fit the temperature dependent water thermal expansion coefficient [147].

<sup>1</sup>Periodic boundary conditions may be equally applied.

### 3.4.1 Model equations

Here we will describe in more detail the equations governing the three physical steps behind the photoacoustic effect triggered in an individual metal NC immersed in water by a laser pulse.

#### Optics

At the initial time  $t = 0$  the system is at equilibrium. The gold NC is thermalised with the surrounding water and the displacement field is zero (as well as all its temporal derivatives). Then, a single light pulse of intensity  $I(t)$  ( $\text{W}/\text{m}^2$ ) is delivered. Here, given the small size of the NC, we assume spatial homogeneity of the light pulse over the gold NC. The light pulse is taken with gaussian temporal dependence:

$$I(t) = 2\sqrt{\frac{\ln(2)}{\pi}} \frac{\Phi}{\tau_L} \exp\left(-4\ln(2)\frac{(t-t_0)^2}{\tau_L^2}\right), \quad (3.1)$$

where  $\tau_L$  is the pulse temporal full width half maximum (fwhm),  $t_0$  is the pulse temporal peak and  $\Phi$  is the light fluence ( $\text{J}/\text{m}^2$ ). In our simulations we will use three durations of  $\tau_L$  ( $=10$  ps,  $100$  ps,  $1$  ns), while  $\Phi$  will always be kept constant ( $\approx 10$   $\text{J}/\text{m}^2$ , a typical value used in experiments). We do not consider here the fs regime, where the metal electrons and lattice are out of the equilibrium upon laser absorption [3, 224, 58]. We therefore limit our analysis to a situation where the gold NC is always internally thermalized at a common temperature.

The light wavelength is chosen in the visible range, so we can assume the water absorption to be negligible and only absorption by the NC plays a role. In the one-dimensional geometry, the NC absorption cross section  $\sigma^{abs}$  ( $\text{m}^2$ ) is linearly dependent on the NC height  $H$  and depends on the light polarization [225, 226]. In the present case, choosing a light pulse wavelength  $\lambda \approx 530$  nm and polarization along the NC radius, we obtain  $\sigma^{abs}/H = 6.8$   $\text{nm}^2/\text{nm}$ , the calculation being performed for an infinite cylinder [227] and using room temperature values for gold dielectric constants [80].

In this way, we are able to calculate the power density  $Q(t)$  ( $\text{W}/\text{m}^3$ ) absorbed by the NC as:

$$Q(t) = \frac{\sigma^{abs} I(t)}{\pi R_{gnc}^2 H} = \frac{6.8(\text{nm}) I(t)}{\pi R_{gnc}^2} \quad (3.2)$$

#### Thermal dynamics

Once we know the power density absorbed by the system, we can move one step forward in our description. Indeed,  $Q(t)$  will be introduced as the heat source in the thermal diffusion equation governing the thermal dynamics of the system. To describe heat

diffusion, both in the NC and in water, we use Fourier's law and the continuity equation:

$$\vec{q} = -k\vec{\nabla}T \quad (3.3)$$

$$\rho c_p \frac{\partial T}{\partial t} = -\vec{\nabla} \cdot \vec{q} + Q(t), \quad (3.4)$$

where  $T$  is the temperature (K),  $\vec{q}$  is the heat flux (W/m<sup>2</sup>) and the heat source term  $Q(t)$  is non-zero only within the NC. The other materials properties ( $k$ ,  $\rho$ ,  $c_p$ ) for the respective domains are reported in Table 5. Equations 3.3 and 3.4 are cast in cylindrical coordinates. The only not null components are the radial ones:

$$q_r = -k \frac{\partial T}{\partial r} \quad (3.5)$$

$$\rho c_p \frac{\partial T}{\partial t} = -\frac{1}{r} q_r - \frac{\partial q_r}{\partial r} + Q(t). \quad (3.6)$$

At  $t = 0$  the system is thermalized with an uniform temperature  $T(t = 0) = T_0 = 293$  K. When the light pulse strikes, the NC absorbs part of its energy and converts into in heat, rising in temperature. It thus starts to dissipate heat in the surrounding water, through the interface at  $r = R_{gnc}$ . This process is regulated by the TBR [33, 215], and formally accounted by the continuity of the heat flux and the TBR-type boundary condition at the interface:

$$q(R_{gnc}^-) = q(R_{gnc}^+) = q(R_{gnc}) \quad (3.7)$$

$$q(R_{gnc}) = \frac{1}{\mathcal{R}} (T(R_{gnc}^-) - T(R_{gnc}^+)), \quad (3.8)$$

where  $\mathcal{R}$  is the TBR,  $R_{gnc}^+$  and  $R_{gnc}^-$  indicate the outer and inner sides of the surface  $r = R_{gnc}$ . At the water external boundary ( $r = R_w$ ), instead, a thermal insulation condition ( $q_r = 0$ ) is set. The value of  $R_w$  is chosen so as to that, in the simulations timescale of interest, the heat flux does not reach the water boundary. At  $r = 0$ , instead, the heat flux must vanish due to the radial symmetry.

### Acoustic response

By inserting the spatio-temporal temperature evolution  $T(r, t)$  in the equations governing the mechanical dynamics, we can finally calculate the acoustic response of the system and, in particular, the pressure wave launched in water. Both in the metal NC and in water these equations can be cast in the form [127]:

$$\rho \frac{\partial^2 \vec{u}}{\partial t^2} = \nabla \cdot \boldsymbol{\sigma} \quad (3.9)$$

$$\boldsymbol{\sigma} = \mathbf{C} \cdot (\nabla_s \vec{u} - \alpha \Delta T), \quad (3.10)$$

where  $\vec{u}$  is the displacement field (m),  $\boldsymbol{\sigma}$  the stress tensor (Pa) and  $\nabla_S \vec{u}$  the symmetric part of the displacement gradient tensor. Materials properties, such as the stiffness tensor  $\mathbf{C}$  (Pa) and the thermal expansion tensor  $\boldsymbol{\alpha}$  ( $\text{K}^{-1}$ ), have to be properly selected in the respective domains (NC/water). Note that Equations 3.9 and 3.10 are exactly the same as Equations 2.2 and 2.3 of Chapter 2, since  $\boldsymbol{\varepsilon} = \frac{1}{2}(\partial u_i / \partial x_j + \partial u_j / \partial x_i)$  (where  $i, j = x, y, z$  and  $x_1 = x, x_2 = y, x_3 = z$ ); and  $\boldsymbol{\sigma}_{ext} = -\mathbf{C} \cdot \boldsymbol{\alpha} \Delta T$  (as in *Step 3b* of Section 2.5).

As we did for the thermal dynamics section, also here we can cast the equations in cylindrical coordinates. In so doing, it is also useful to exploit the homogeneity and isotropy of both the polycrystalline gold NC and water. With this hypothesis,  $\mathbf{C}$  can be expressed in terms of the Lamé parameters<sup>2</sup>  $\lambda$  and  $\mu$  (taking the form reported below), and  $\boldsymbol{\alpha} = \alpha \mathbf{I}_d$ , with  $\mathbf{I}_d$  being the identity matrix. The Lamé parameters  $\lambda, \mu$  and the linear thermal expansion coefficient  $\alpha$  can be found in Table 5 for both water and gold. Thus, in cylindrical coordinates  $(r, \phi, z)$  and Voigt notation, the terms appearing in Equations 3.9 and 3.9 read:

$$\nabla \cdot \boldsymbol{\sigma} = \begin{pmatrix} \partial/\partial r + 1/r & -1/r & 0 & 0 & \partial/\partial z & \frac{1}{r} \partial/\partial \phi \\ 0 & \frac{1}{r} \partial/\partial \phi & 0 & \partial/\partial z & 0 & \partial/\partial r + 2/r \\ 0 & 0 & \partial/\partial z & \frac{1}{r} \partial/\partial \phi & \partial/\partial r + 1/r & 0 \end{pmatrix} \begin{pmatrix} \sigma_{rr} \\ \sigma_{\phi\phi} \\ \sigma_{zz} \\ 0 \\ 0 \\ 0 \end{pmatrix}; \quad (3.11)$$

$$\nabla_S \vec{u} = \begin{pmatrix} \partial/\partial r & 0 & 0 \\ 1/r & \frac{1}{r} \partial/\partial \phi & 0 \\ 0 & 0 & \partial/\partial z \\ 0 & \partial/\partial z & 1/r \partial/\partial \phi \\ \partial/\partial z & 0 & \partial/\partial r \\ \frac{1}{r} \partial/\partial \phi & \partial/\partial r - 1/r & 0 \end{pmatrix} \begin{pmatrix} u_r \\ u_\phi \\ u_z \end{pmatrix}; \quad (3.12)$$

$$\mathbf{C} = \begin{pmatrix} \lambda + 2\mu & \lambda & \lambda & 0 & 0 & 0 \\ \lambda & \lambda + 2\mu & \lambda & 0 & 0 & 0 \\ \lambda & \lambda & \lambda + 2\mu & 0 & 0 & 0 \\ 0 & 0 & 0 & \mu & 0 & 0 \\ 0 & 0 & 0 & 0 & \mu & 0 \\ 0 & 0 & 0 & 0 & 0 & \mu \end{pmatrix}; \quad \boldsymbol{\alpha} \Delta T = \begin{pmatrix} \alpha \Delta T \\ \alpha \Delta T \\ \alpha \Delta T \\ 0 \\ 0 \\ 0 \end{pmatrix}. \quad (3.13)$$

The symmetry of the problem implies that: (a)  $u_\phi = u_z = 0$ , (b) the  $\partial/\partial \phi$  and  $\partial/\partial z$  derivatives of any quantity are null. Exploiting these evidencies, after some straightforward

<sup>2</sup>Note that these coefficients can be used both for solids and for liquids.

calculation we obtain from Equations 3.9 and 3.10:

$$\begin{aligned}
 \rho \frac{\partial^2 u_r}{\partial t^2} &= \frac{\partial \sigma_{rr}}{\partial r} + \frac{1}{r}(\sigma_{rr} - \sigma_{\phi\phi}) \\
 \sigma_{rr} &= (\lambda + 2\mu) \frac{\partial u_r}{\partial r} + \lambda \frac{u_r}{r} - \alpha(3\lambda + 2\mu) \Delta T \\
 \sigma_{\phi\phi} &= \lambda \frac{\partial u_r}{\partial r} + (\lambda + 2\mu) \frac{u_r}{r} - \alpha(3\lambda + 2\mu) \Delta T \\
 \sigma_{zz} &= \lambda \left( \frac{\partial u_r}{\partial r} + \frac{u_r}{r} \right) - \alpha(3\lambda + 2\mu) \Delta T,
 \end{aligned} \tag{3.14}$$

and finally, by deriving in time the last three equations, we end with:

$$\begin{aligned}
 \rho \frac{\partial v_r}{\partial t} &= \frac{\partial \sigma_{rr}}{\partial r} + \frac{1}{r}(\sigma_{rr} - \sigma_{\phi\phi}) \\
 \frac{\partial \sigma_{rr}}{\partial t} &= (\lambda + 2\mu) \frac{\partial v_r}{\partial r} + \lambda \frac{v_r}{r} - \alpha(3\lambda + 2\mu) \frac{\partial T}{\partial t} \\
 \frac{\partial \sigma_{\phi\phi}}{\partial t} &= \lambda \frac{\partial v_r}{\partial r} + (\lambda + 2\mu) \frac{v_r}{r} - \alpha(3\lambda + 2\mu) \frac{\partial T}{\partial t} \\
 \frac{\partial \sigma_{zz}}{\partial t} &= \lambda \left( \frac{\partial v_r}{\partial r} + \frac{v_r}{r} \right) - \alpha(3\lambda + 2\mu) \frac{\partial T}{\partial t},
 \end{aligned} \tag{3.15}$$

where  $v_r = \partial u_r / \partial t$ . Note that we could have avoided reporting  $\sigma_{zz}$  in the set of equations since we are only interested in the radial direction, and  $\sigma_{zz}$  doesn't play a role in determining neither  $\sigma_{rr}$  or  $v_r$ . Moreover we notice that, when  $\mu = 0$ , as for water, we have  $\sigma_{rr} = \sigma_{\phi\phi} = \sigma_{zz}$ .

The initial conditions are zero-displacement field in the entire system ( $u_r(t = 0) = 0$ ), as well as its temporal derivative ( $v_r(t = 0) = 0$ ) and the stress tensor ( $\boldsymbol{\sigma}(t = 0) = 0$ ). As for the boundary conditions at the NC/water interface ( $r = R_{gnc}$ ), we set:

$$v_r(R_{gnc}^-) = v_r(R_{gnc}^+) \tag{3.16}$$

$$\sigma_{rr}(R_{gnc}^-) = \sigma_{rr}(R_{gnc}^+), \tag{3.17}$$

while a stress free boundary condition ( $\boldsymbol{\sigma} = 0$ ) is taken at the boundary of the external water domain ( $r = R_w$ ).

### Poynting vector and acoustic energy

The final outcome of the equations governing the acoustic response is the pressure wave in water  $p = -\sigma_{rr} = -\sigma_{\phi\phi}$ . Knowing  $p$  is both important *per se* and to calculate the mechanical energy transported by the sound wave while propagating in water. For the latter purpose, we introduce the acoustic Poynting vector  $\vec{P}$  (W/m<sup>2</sup>) [127].

To understand what  $\vec{P}$  means, let's take a closed surface  $S$ . The total mechanical energy  $U$

passing through a Gaussian surface  $S$  per unit time is given by [127]

$$\frac{dU}{dt} = \oint_S -(\vec{v} \cdot \boldsymbol{\sigma}) \cdot \hat{n} dS = \oint_S \vec{P} \cdot \hat{n} dS, \quad (3.18)$$

where  $\hat{n}$  is the  $S$  surface versor (outgoing). The integral of  $\vec{P}$ , then, gives the mechanical power passing through the closed surface  $S$ . In order to calculate the mechanical energy transported through a closed surface by a pressure wave generated by the photoacoustic effect, we then need to integrate  $\vec{P}$ , first over the chosen surface  $S$ , containing the metal NC, and, subsequently in time. This is:

$$U = \int \oint_S -[(v_r \sigma_{rr} + v_\phi \sigma_{\phi r} + v_z \sigma_{zr})\hat{r} + (v_r \sigma_{r\phi} + v_\phi \sigma_{\phi\phi} + v_z \sigma_{z\phi})\hat{\phi} + (v_r \sigma_{rz} + v_\phi \sigma_{\phi z} + v_z \sigma_{zz})\hat{z}] \cdot \hat{n} dS dt. \quad (3.19)$$

However, since for the present case  $v_\phi = v_z = 0$  and  $\sigma_{r\phi} = \sigma_{rz} = 0$ , the mechanical energy produced by the photoacoustic effect, and travelling in water, reads:

$$\int \oint_S -v_r \sigma_{rr} \hat{r} \cdot \hat{n} dS dt. \quad (3.20)$$

We take  $S$  as a cylindrical surface in water, co-axial with and containing the NC. The surface  $S$  has radius  $R_S$ , then  $\hat{n} \cdot \hat{r} = 1$  along its lateral surface, while  $\hat{n} \cdot \hat{r} = 0$  on the top/bottom basis. With this choice, the mechanical energy transported in water by the propagating sound wave crossing  $S$  simply reads:

$$U = 2\pi R_S H \int -v_r \sigma_{rr} dt, \quad (3.21)$$

where, we recall,  $H$  is the height of the NC and  $R_S$  the radius of the surface cylindrical surface  $S$ .

One could think that, because of the conservation of energy, the energy  $U$  transported by the propagating acoustic wave should be the same for any choice of the surface  $S$  as long as  $R_S > R_{gnc}$ . In reality, close to the NC surface there is an accumulation of mechanical energy due to the propagation of heat in water, which results in a maximum of  $U$ . In order to have a well defined energy value to compare for the different launching mechanisms, we must take  $R_S$  large enough to attain an asymptotic value for  $U$ .

### 3.4.2 Results

This section reports simulations results of the photoacoustic effect generated in a gold NC-immersed-in-water system, for varying TBR and  $\tau_L$  ( $= 1$  ns, 100 ps, 10 ps) values.

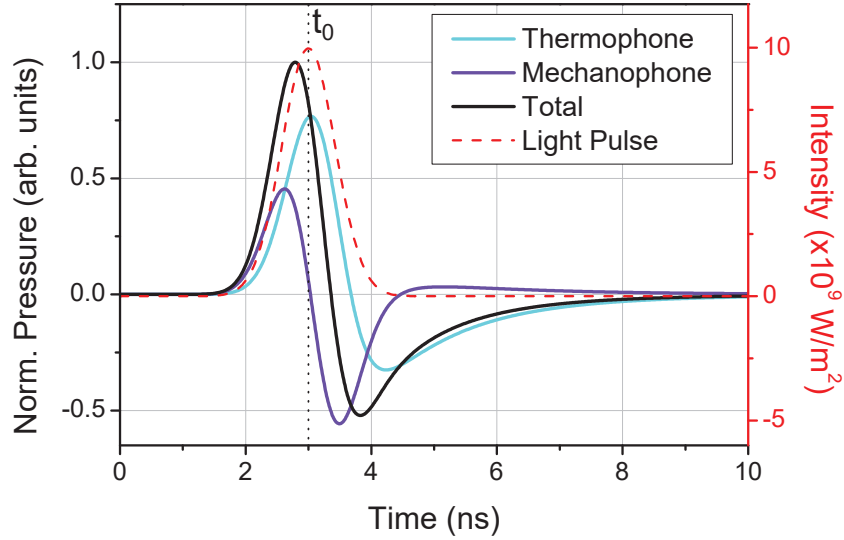


Figure 37. Time evolution of the pressure in water ( $r = R_{gnc} + 5$  nm) in the  $\tau_L = 1$  ns case and with  $\mathcal{R} = 1 \times 10^{-7}$  m<sup>2</sup>K/W. Left-axis: thermophone contribution (light blue), mechanophone contribution (violet) and total pressure (black). Curves are normalized to the total pressure peak. Right-axis: light pulse intensity time evolution (red dashed curve).

The first step is to demonstrate that both the thermophone and the mechanophone contributions have to be considered to correctly describe the launching of the acoustic wave in water. To do so we selectively activate the sole thermophone or mechanophone effect setting to zero the thermal expansion coefficient  $\alpha$  in the gold NC or external water domain, respectively. Indeed, the total pressure wave is obtained taking into account both values of the thermal expansion throughout the entire system. Figure 37 shows the results for the nanoscale excitation regime, reporting the water pressure time evolution at  $r = R_{gnc} + 5$  nm. The pressure is normalized to the total pressure peak. We see that, for  $\mathcal{R} = 1 \times 10^{-7}$  m<sup>2</sup>K/W, chosen between the realistic gold/water value and the graphene-functionalized gold water interface value, and  $\tau_L = 1$  ns, the thermophone (light blue curve) and the mechanophone (violet curve) contributions have comparable amplitudes. This means that both contributions have to be taken into account in order to correctly predict the amplitude of the total pressure (black curve).

We will see that, only for certain values of the TBR and  $\tau_L$ , one effect or the other will be negligible. As already mentioned, most literature cases of photoacoustic effect generated by metal nanoparticles immersed in liquids [145, 199, 200] belong to particular situations in which the mechanophone contribution is negligible, however this is not the general case.

We now move to investigating the thermophone vs mechanophone competition for different values of the TBR and  $\tau_L$ . We start considering two extreme cases. When  $\mathcal{R} \rightarrow \infty$ , the gold NC is thermally isolated from the surrounding water, thus only the gold NC rises its temperature. The only sound wave launching mechanisms is the mechanophone, triggered by the gold NC dilatation. On the contrary, when  $\mathcal{R} \rightarrow 0$ , the efficiency of heat dissipation from the gold NC to water is maximized. The thermophone

contribution should thus be maximum, while the mechanophone minimum.

We want, however, to give a more quantitative description of the competition between the two launching mechanisms while changing the TBR and  $\tau_L$ , the only quantities which may be experimentally varied. The TBR can be tuned engineering the Au/water interface,  $\tau_L$  intervening on the laser source or laser pulse. For this scope, we introduce the dimensionless ratio  $\tau_{Th}/\tau_L$ , where  $\tau_{Th}$  is given by

$$\tau_{Th} = \mathcal{R}R_{gnc}c_p\rho/2. \quad (3.22)$$

With such definition,  $\tau_{Th}$  represent the characteristic time of the gold NC thermal decay only when the TBR is the system's prevailing thermal impedance, the Biot number  $Bi \ll 1$  and for isothermal water<sup>3</sup>, similarly to what we have seen in see Section 1.3 of Chapter 1. In a complete description, the timescale of this thermal decay is not ruled only by the TBR, but also by the gold NC and proximal water thermal impedances through their thermal conductivities and thermal inertia, as will be detailed for the case of a simpler, in terms of mathematics, case in Sections 3.5 and 3.6. Due to the intricate relaxation dynamics, a formal definition of the characteristic time for the thermal dynamics doesn't exist. Nevertheless, in our case, the TBR is the *only* material parameter that can be tuned, the thermal properties of the gold NC and water being fixed. For this reason,  $\tau_{Th}$  has the merit of providing a rule-of-thumb estimate of the heat dissipation phenomenon, while also linking it, in a handy analytical form, to the TBR. With such definition, indeed, we can re-write the two extreme scenario reported above (vanishing and infinite TBR) in terms of  $\tau_{Th}/\tau_L$  as

$$\tau_{Th}/\tau_L \gg 1 \quad (\Leftrightarrow \mathcal{R} \rightarrow \infty) \Rightarrow \text{maximize mechanophone and zero thermophone}$$

$$\tau_{Th}/\tau_L \ll 1 \quad (\Leftrightarrow \mathcal{R} \rightarrow 0) \Rightarrow \text{minimize mechanophone and maximize thermophone.}$$

The usefulness of  $\tau_{Th}/\tau_L$  is proven in Figure 38. Panels a and b show the temperature time evolution in water ( $r = R_{gnc} + 5$  nm) and in the gold NC ( $r = 0$  nm), respectively, for a fixed value of  $\tau_L = 1$  ns, while varying the TBR across five decades, from  $10^{-5}$  to  $10^{-9}$  m<sup>2</sup>K/W, so as to cover the range of  $\tau_{Th}/\tau_L$  from  $\approx 0.01$  to  $\approx 100$ . For small values of  $\tau_{Th}/\tau_L$  ( $\approx 0.01$ , orange curve), the heat exchange between the gold NC and water is most efficient, bringing water temperature to its highest peak ( $T \approx 300$  K) and the corresponding gold NC temperature peak to its lowest value ( $T \approx 305$  K). The opposite is true for the largest  $\tau_{Th}/\tau_L$  case ( $\approx 100$ , black curve), where the heat exchange efficiency is minimized, water temperature shows its lowest peak ( $T \approx 293.5$  K) and the corresponding gold NC temperature reaches its highest peak ( $T \approx 378$  K). Intermediate values of  $\tau_{Th}/\tau_L$  (green, blue, magenta curves) confirm the described trend.

<sup>3</sup>This hypothesis does not strictly hold in several instances.

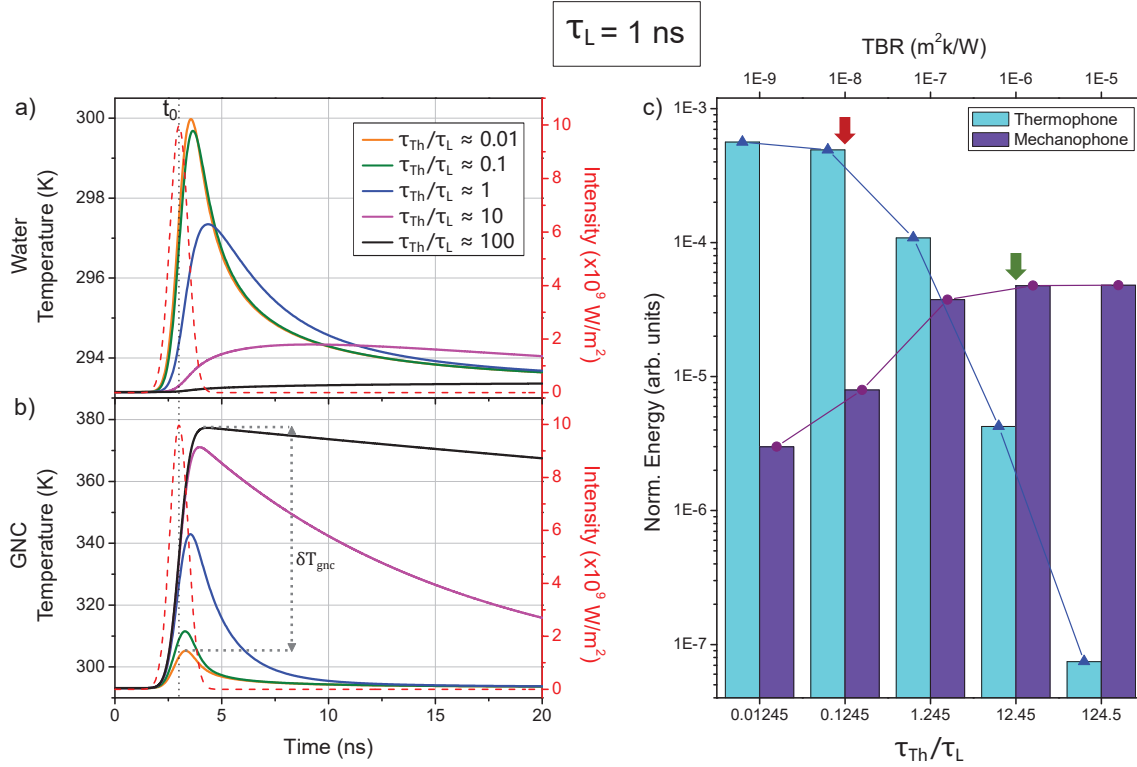


Figure 38. Temperature time evolution in the  $\tau_L = 1 \text{ ns}$  case for different  $\tau_{Th}/\tau_L$  in water ( $r = R_{gnc} + 5 \text{ nm}$ ) (panel a) and in the gold NC ( $r = 0 \text{ nm}$ ) (panel b). The light pulse intensity time evolution is also plotted in the (right axis, panels a and b). Panel c: normalized mechanical energy in water generated by the thermophone (light blue) and the mechanophone (violet) contributions at different  $\tau_{Th}/\tau_L$  (bottom axis) or different TBRs (top axis). A realistic value for the gold/water TBR is pointed by the red arrow, that of the graphene-functionalized gold water interface by the green arrow.

The different thermal dynamics are reflected in the competition between the thermophone and the mechanophone launching mechanisms. Panel c of Figure 38 shows the mechanical energy in water (calculated with the acoustic Poynting vector) generated by solely the thermophone (light blue) and solely mechanophone (violet) effects, as a function of  $\tau_{Th}/\tau_L$  (bottom axis) or the TBR (top axis). Energies are normalized to a fixed value, corresponding to the maximal mechanical energy found in our simulations for this system, i.e. the thermophone energy for the  $\tau_L = 10 \text{ ps}$  and  $\tau_{Th}/\tau_L \approx 0.01$  case (that will be describe later). It is clearly visible that, while varying  $\tau_{Th}/\tau_L$  from low to high values (in other words increasing the TBR), the thermophone contribution decreases and the mechanophone one increases. We notice that, in this case, it is possible to almost suppress the mechanophone contribution ( $\tau_{Th}/\tau_L \approx 0.01$  case) or the thermophone contribution ( $\tau_{Th}/\tau_L \approx 100$  case). For a realistic value of the gold/water TBR value ( $\mathcal{R} \approx 1 \times 10^{-8} \text{ m}^2\text{K/W}$ ), pointed by a red arrow in panel c), the thermophone contribution prevails on the mechanophone one, which is almost two order of magnitude smaller. This scenario is the most commonly studied in the literature [145, 147, 197, 198, 199, 200], ns laser pulses being the standard for photoacoustic bio-medical applications. However, we point out that

for a TBR value of  $\mathcal{R} \approx 1 \times 10^{-6} \text{ m}^2\text{K/W}$ , i.e. two order of magnitude higher than the realistic gold/water interface, achievable adhering a graphene sheet on the gold surface [220], the mechanophone prevails even for  $\tau_L = 1 \text{ ns}$ . The latter case is pointed by the green arrow in panel c.

We now investigate the effect of the pulse duration of the thermophone vs mechanophone competition. Figure 39 follows the same scheme as Figure 38 but for  $\tau_L = 100 \text{ ps}$ : panels a and b show the temperature time evolution of, respectively, water ( $r = R_{gnc} + 5 \text{ nm}$ ) and the gold NC ( $r = 0 \text{ nm}$ ), for different  $\tau_{Th}/\tau_L$ ; panel c shows the normalized mechanical energy generated by the thermophone (light blue) and the mechanophone (violet) effects as a function of  $\tau_{Th}/\tau_L$  (bottom axis) or the TBR (top axis). The range of TBR values has been down-shifted of one decade (now from  $10^{-6}$  to  $10^{-10} \text{ m}^2\text{K/W}$ ), in order to span the same  $\tau_{Th}/\tau_L$  range (0.01 – 100) as in the  $\tau_L = 1 \text{ ns}$  case. The general rule discussed before applies also in this case: when  $\tau_{Th}/\tau_L$  is small ( $\approx 0.01$ , orange curve) the gold NC/water heat exchange is efficient, thus giving the highest temperature peak in water ( $T \approx 304 \text{ K}$ , panel a) and the lowest one for the gold NC ( $T \approx 323 \text{ K}$ ,

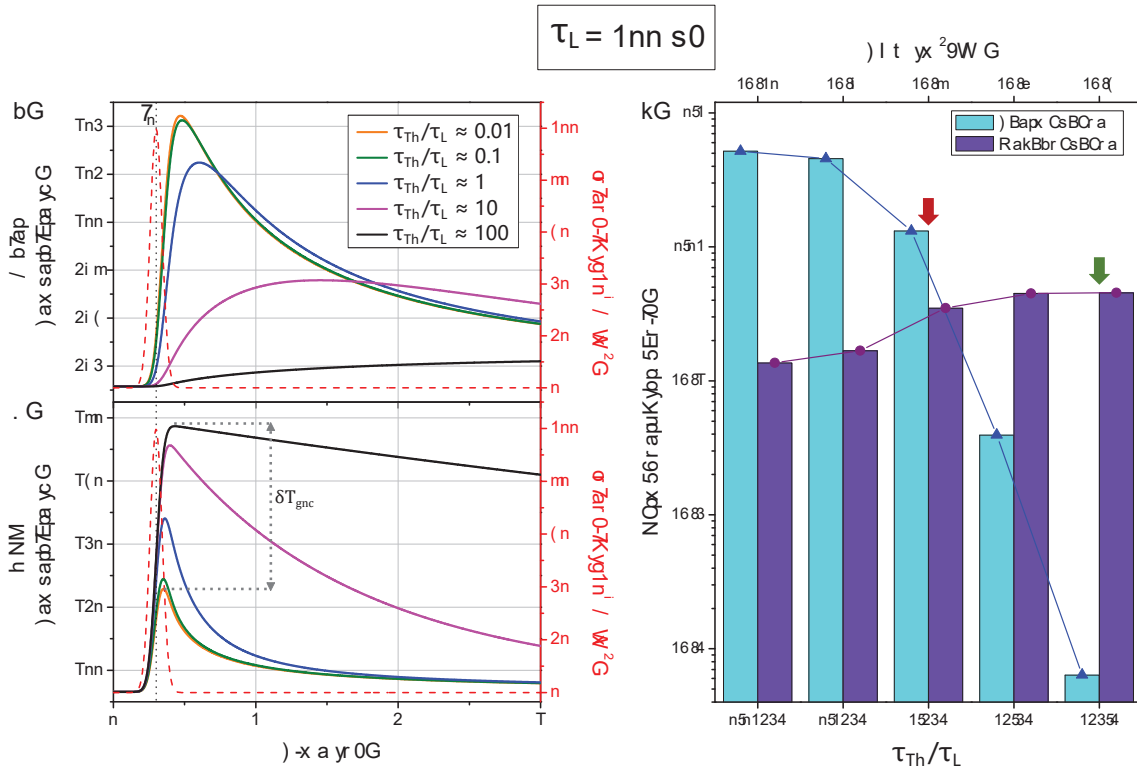


Figure 39. Temperature time evolution in the  $\tau_L = 100 \text{ ps}$  case for different  $\tau_{Th}/\tau_L$  in water ( $r = R_{gnc} + 5 \text{ nm}$ ) (panel a) and in the gold NC ( $r = 0 \text{ nm}$ ) (panel b). The light pulse intensity time evolution is also plotted in the (right axis, panels a and b). Panel c: normalized mechanical energy in water generated by the thermophone (light blue) and the mechanophone (violet) contributions at different  $\tau_{Th}/\tau_L$  (bottom axis) or different TBRs (top axis). A realistic value for the gold/water TBR is pointed by the red arrow, that of the graphene-functionalized gold water interface by the green arrow.

panel b). The opposite happens for large values of  $\tau_{Th}/\tau_L$  ( $\approx 100$ , black curve), where the heat exchange is inefficient and thus the water temperature peak is small ( $T \approx 294$  K, panel a), while the corresponding gold NC's one is high ( $T \approx 378$  K, panel b). However, the histogram of the energy generated by the thermophone and the mechanophone effects (panel c) shows two differences from the one in Figure 38. The first difference is that, for a realistic value of the gold/water TBR value (pointed by the red arrow), the thermophone and the mechanophone contributions are much closer than in the  $\tau_L = 1$  ns case. This means that, for the  $\tau_L = 100$  ps case, neglecting the mechanophone effect would bring to a substantial underestimate of the real sound wave generated. Clearly, for the high TBR value ( $10^{-6}$  m<sup>2</sup>K/W), corresponding to the graphene-functionalized Au/water interface and pointed by the green arrow, the mechanophone effect is even more predominant than in the ns light pulse case. The second difference is that the mechanophone contribution is much less dependent on  $\tau_{Th}/\tau_L$  than in Figure 38. In the  $\tau_L = 1$  ns case, indeed, the mechanophone energy contribution changes by more than one order of magnitude between the  $\tau_{Th}/\tau_L \approx 0.01$  case and  $\tau_{Th}/\tau_L \approx 100$  one. In Figure 39, instead, the mechanophone effect energy contribution remains within the same order of magnitude for all the  $\tau_{Th}/\tau_L$ . Among the physical reasons behind this trend, is that reducing  $\tau_L$  for a fixed value of  $\tau_{TBR}/\tau_L = 10^{-2}$  implies reducing the TBR, eventually to a point where the gold NC and the proximal water thermal impedances remain as the only factors ruling the thermal dynamic. Using a shorter  $\tau_L$  brings to a higher temperature peak in the gold NC, since the energy is delivered faster, even for a situation of negligible TBR (small  $\tau_{Th}/\tau_L$ ), where thermal cooling is only limited by the gold NC and proximal water thermal impedances. We can understand this by comparing the gold NC temperatures for different  $\tau_{Th}/\tau_L$  (panels b in Figure 38 and Figure 39). For this scope, it is useful to define  $\delta T_{gnc}$  as the difference between the NC peak temperatures in the case of  $\tau_{Th}/\tau_L \approx 100$  and  $\tau_{Th}/\tau_L \approx 0.01$  (see panels b). For  $\tau_L = 100$  ps, we obtain  $\delta T_{gnc} \approx 55$  K, a value substantially smaller than in the  $\tau_L = 1$  ns case, where  $\delta T_{gnc} \approx 73$  K. When shortening  $\tau_L$ , the range  $\delta T_{gnc}$  shrinks, due to the increase of the low temperature peaks. The smaller is  $\delta T_{gnc}$ , the more similar are the gold NC thermal expansions, resulting in similar mechanophone contributions while varying  $\tau_{Th}/\tau_L$ .

This trend results even clearer in the  $\tau_L = 10$  ps case, shown in Figure 40. The figure scheme is the same as for Figure 38 and Figure 39. As expected, in panel b the different temperature peaks of the gold NC are even closer than in the  $\tau_L = 100$  ps case, confirming the trend we described above. In this case, for  $\tau_{Th}/\tau_L \approx 0.01$  (orange curve), the gold NC temperature peak is at  $T \approx 350$  K, while for  $\tau_{Th}/\tau_L \approx 100$  (black curve) the peak is  $T \approx 378$  K, resulting in  $\delta T_{gnc} \approx 28$  K. Given such a small  $\delta T_{gnc}$ , the mechanophone contribution is almost constant and results in a flat energy contribution in the histogram of panel c. A similar behaviour is not observable for the thermophone effect, which always drastically decreases for high values of  $\tau_{Th}/\tau_L$  ( $\approx 100$ ). For high values of

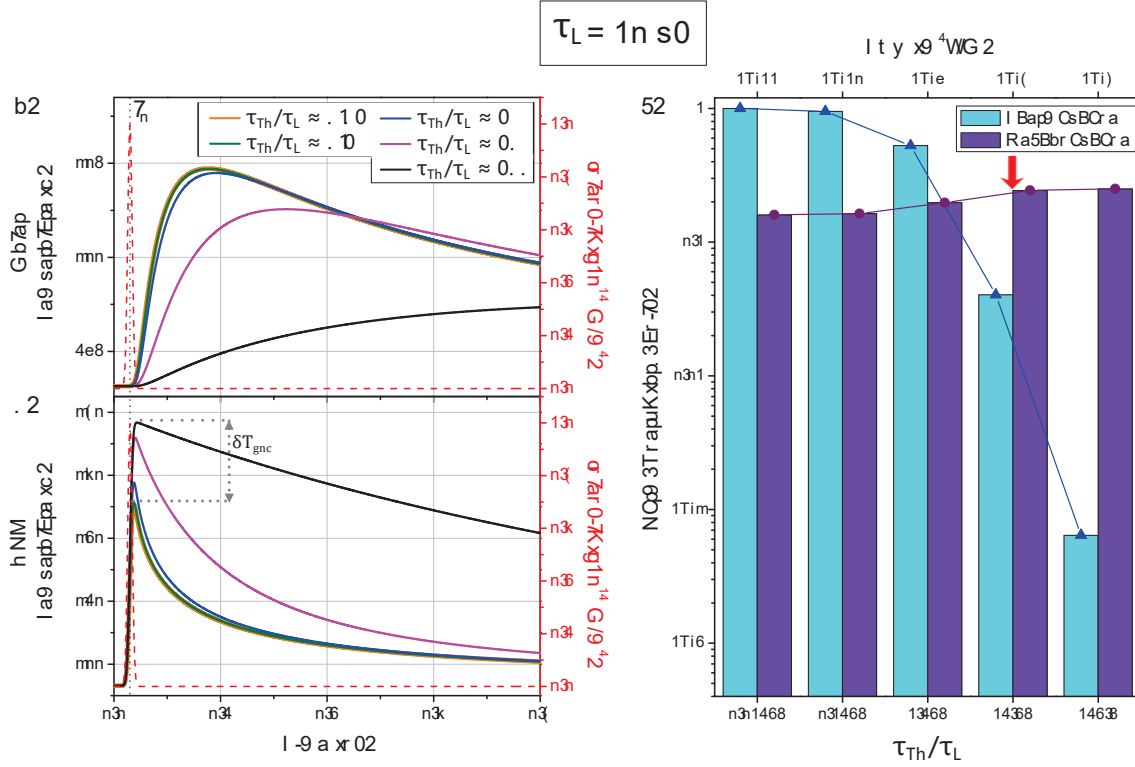


Figure 40. Temperature time evolution in the  $\tau_L = 10$  ps case for different  $\tau_{Th}/\tau_L$  in water ( $r = R_{gnc} + 5$  nm) (panel a) and in the gold NC ( $r = 0$  nm) (panel b). The light pulse intensity time evolution is also plotted in the (right axis, panels a and b). Panel c: normalized mechanical energy in water generated by the thermophone (light blue) and the mechanophone (violet) contributions at different  $\tau_{Th}/\tau_L$  (bottom axis) or different TBRs (top axis). A realistic value for the gold/water TBR is pointed by the red arrow.

the TBR, indeed, the heat flux from the NC to water is reduced, no matter how short  $\tau_L$  is. Moreover, in the  $\tau_L = 10$  ps case, we notice that a realistic gold/water TBR value (pointed by the red arrow in panel c) results in a mechanophone energy contribution larger than the thermophone one, as opposed to what is found for  $\tau_L = 1$  ns.

A last feature is worth to be discussed. Note that, even in the 10 ps light pulse case, the energy generated from the mechanophone effect for  $\tau_{Th}/\tau_L \approx 100$  is lower than the one generated from the thermophone for  $\tau_{Th}/\tau_L \approx 0.01$ . This is due to the thermal expansion coefficient of water and gold. The water thermal expansion coefficient is  $\approx 5$  times higher than the gold one at room temperature. Water expansion is then more efficient than the gold one and thus the maximum of the thermophone effect is higher than the maximum of the mechanophone effect. To prove this, we performed a simulation in which the water thermal expansion coefficient at room temperature is artificially inserted also in the NC domain. The result (not reported) showed that in this way the maximum mechanophone contribution (at  $\tau_{Th}/\tau_L \approx 100$ ) is higher than the maximum thermophone contribution ( $\tau_{Th}/\tau_L \approx 0.01$ ) by a factor  $\approx 5$ .

### 3.4.3 Conclusions on the gold NC in water

In this section we reported different launching mechanisms of acoustic waves triggered by the photoacoustic effect generated by a gold NC immersed in water. Our main focus was to understand the role of the TBR and the light pulse duration in the different launching mechanisms. For this scope, we built a continuous opto-thermo-acoustic model. With our simulations we showed that the total acoustic wave is the result of the combination of two different mechanisms: the thermophone effect, due to the thermal expansion of water, and the mechanophone effect, due to the thermal expansion of the gold NC. First we demonstrated that both of them can contribute significantly to the total emitted sound wave. The competition between the thermophone and the mechanophone effects was analyzed for different values of the TBR and different light pulses duration ranging from the ns to the ps regime. This was realised by calculating the mechanical energy propagating in water due to only the thermophone contribution or only the mechanophone. We saw that a low TBR value maximizes the thermophone effect while minimising the mechanophone one. On the contrary, a high TBR value maximizes the mechanophone effect while zeroing the thermophone one. Moreover, we recognized that the light pulse duration plays an important role in the dependence of the mechanophone effect on the TBR. For the ns pulse, indeed, the mechanophone effect changes by orders of magnitude when varying the TBR value. This is not true for 100 to 10 ps light pulses. In this case, the mechanophone contribution remains almost constants for all explored TBR value. The thermophone effect, instead, is TBR-dependent for all duration of the light pulse. We rationalized these phenomena in terms of the temperature time evolution in the NC and water domains. We then discussed a realistic gold/water TBR case, showing that the thermophone effect prevails for the ns light pulse, and the mechanophone effect prevails for the ps light pulse. On the contrary, we have seen that using the TBR for a graphene-functionalized Au/water interface, results in the predominance of the mechanophone effect for the ns light pulse, and thus even more so for the 100 to 10 ps ones.

These results bear generality beyond the particular geometry and material here investigated. The system can be easily generalized to any other liquid-immersed metal nanoparticle. The present results show the importance of the mechanophone effect, which is often not taken into account. They also suggest the possibility of creating efficient photoacoustic systems by using metals and liquids with high TBR. This is an unconventional approach with respect to what is usually found in the literature. In most studies of this type, it is suggested to lower the TBR as much as possible in order to increase the photoacoustic signal, implicitly suggesting to increase the thermophone effect at the expense of mechanophone one. This high-TBR perspective has the advantage of leading to a photoacoustic effect with a predominant mechanophone contribution, thus keeping the liquid at almost constant temperature, see panels a of Figures 39 and 40 for the case

$$\tau_{Th}/\tau_L = 100.$$

In the next section, we will present a study on this photoacoustic effect for the case of a gold nanofilm in contact with water. This choice has the merit of simplifying the formalism, given the simpler geometry of the nanofilm, allowing us to conduct an analytical study of the thermophone vs mechanophone competition in the frequency domain, that is for the case of a time-harmonic spatially homogeneous light excitation. Then we will perform FEM simulations on the same system, for the case of a pulsed laser excitation, that is in the time domain. We will then make a direct comparison between results in the frequency and time domains.

### 3.5 Gold nanofilm in water: a frequency sweep perspective

In this section, we report on the photoacoustic effect in the case of a 20 nm thick gold nanofilm under time harmonic light excitation. One side of the film is in contact with water, the other is either free or clamped. We adopt this simpler geometry and excitation scheme, so as to perform an analytical investigation in the frequency domain of the thermophone vs mechanophone competition. This approach allows to formally retrieve the interplay of the parameters ruling photoacoustic generation in a clear, explicit form.

We will see that the thermophone dominates at low frequency, while at high frequency the mechanophone regime is the predominant one. We will provide a simple formula for the threshold frequency at which the mechanophone contribution becomes more effective than the thermophone one. As for the previous section, the TBR will play a central role, affecting the threshold frequency at which the mechanophone becomes predominant. In particular, three paradigmatic TBR values will be taken into account:  $\mathcal{R}=0$ , to inspect perfect thermal contact;  $3 \times 10^{-8} \text{ m}^2\text{K/W}$ , a realistic value for the gold/water TBR; and  $3 \times 10^{-7} \text{ m}^2\text{K/W}$ , a higher TBR value, achievable, as we have seen, through different nano-engineering approaches (see. Section 3.3). Finally, we will link the frequency domain study to time-resolved numerical simulations on the same system. This is realized by performing FEM simulations of the thermo-mechanical dynamics of the system upon light pulse excitation of four different times duration:  $\tau_L = 1 \text{ ps}$ ,  $50 \text{ ps}$ ,  $500 \text{ ps}$  and  $10 \text{ ns}$ . The different  $\tau_L$  allow spanning different ranges of the frequency domains, thus allowing for a direct comparison between the results found in the frequency domain and in the temporal one.

#### 3.5.1 Thermoacoustic model

We start by writing out the balance equations in a fluid. We assume the nanofilm to have lateral extension much larger than its thickness, i.e. the system is one-dimensional

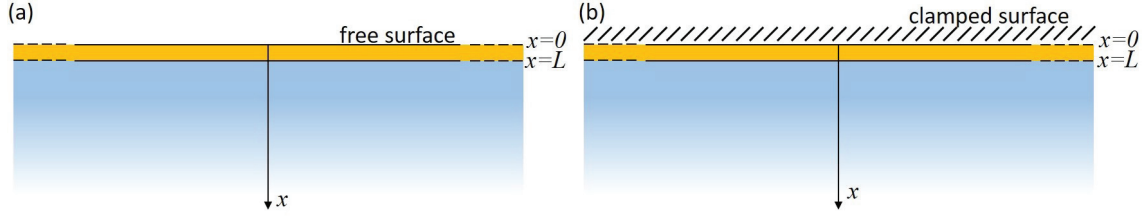


Figure 41. Scheme of the gold nanofilm ( $x \in [0, L]$ ) with one side in contact with water ( $x \in [L, +\infty)$ ). Boundary conditions for the other side can be: free (zero stress, panel a) or clamped (zero displacement, panel b).

and is described by the  $x$ -coordinate perpendicular to the nanofilm surface. The  $x$ -axis originates at the film surface and is oriented towards water, as sketched in Figure 41. Thus, in one-dimensional geometry we have in the liquid medium [184, 228]:

$$\begin{aligned}
 \frac{1}{B_0} \frac{\partial p}{\partial t} &= \alpha_0 \frac{\partial T}{\partial t} - \frac{\partial v}{\partial x}, \\
 \rho_0 \frac{\partial v}{\partial t} &= -\frac{\partial p}{\partial x} + (\lambda_0 + 2\mu_0) \frac{\partial^2 v}{\partial x^2}, \\
 \rho_0 c_{p0} \frac{\partial T}{\partial t} &= k_0 \frac{\partial^2 T}{\partial x^2} + \alpha_0 T_0 \frac{\partial p}{\partial t}.
 \end{aligned} \tag{3.23}$$

where the temperature variation  $T$  (K), the mechanical pressure  $p$  (Pa), and the velocity  $v$  (m/s) are the pertinent variables to describe the spatio-temporal evolution of the system. Moreover,  $\rho_0$  is the density ( $\text{kg/m}^3$ ),  $B_0$  the bulk modulus (Pa),  $\alpha_0$  the coefficient of volumetric expansion ( $1/\text{K}$ ),  $\lambda_0$  and  $\mu_0$  the first and second viscosity coefficients<sup>4</sup> (Pa s),  $c_{p0}$  the specific heat at constant pressure ( $\text{J}/(\text{kg K})$ ),  $T_0$  the ambient temperature (K) and, finally,  $k_0$  the thermal conductivity ( $\text{W}/(\text{m K})$ ) in the liquid. All these parameters will be considered as constants, in order to allow for an analytical approach. Generalizations to non-constant parameters are possible, but would complicate both the formal solution and the straightforward physical comprehension. It is important to remark that the balance equations given in Equation 3.23 represent the combination of the linearized classical conservation laws of mass, momentum and energy with the linearized constitutive equations of the material. This linearization finds an easy justification in our context, since thermoacoustic waves are usually represented by small variations of the relevant quantities around given equilibrium values.

For the solid layer, i.e. the gold film, the balance equations can be written exactly in the

<sup>4</sup>We underline that no confusion should be made in between  $\lambda_0, \mu_0$  and  $\lambda_1, \mu_1$ , which are the viscosity coefficients (Pa s), and  $\lambda_s, \mu_s$ , which are the elastic Lamé coefficients (Pa), which pertain to the mechanics. In water, the elastic coefficients are written in terms of the bulk modulus  $B_0$ .

same mathematical form as [184, 229]

$$\begin{aligned}\frac{1}{B_1} \frac{\partial p}{\partial t} &= \alpha_1 \frac{\partial T}{\partial t} - \frac{\partial v}{\partial x}, \\ \rho_1 \frac{\partial v}{\partial t} &= -\frac{\partial p}{\partial x} + (\lambda_1 + 2\mu_1) \frac{\partial^2 v}{\partial x^2}, \\ \rho_1 c_{p1} \frac{\partial T}{\partial t} &= k_1 \frac{\partial^2 T}{\partial x^2} + \alpha_1 T_0 \frac{\partial p}{\partial t} + Q(t),\end{aligned}\tag{3.24}$$

where we have to introduce the following quantities

$$B_1 = \frac{B_s}{1 - \frac{4}{3} \frac{v_T^2}{v_L^2}},\tag{3.25}$$

$$\alpha_1 = \alpha_s \left( 1 - \frac{4}{3} \frac{v_T^2}{v_L^2} \right),\tag{3.26}$$

$$c_{p1} = c_{ps} \left( 1 - \frac{4}{3} \frac{v_T^2}{v_L^2} \frac{c_{ps} - c_{vs}}{c_{ps}} \right),\tag{3.27}$$

$$\rho_1 = \rho_s,\tag{3.28}$$

$$k_1 = k_s,\tag{3.29}$$

with

$$v_T = \sqrt{\frac{\mu_s}{\rho_s}},\tag{3.30}$$

$$v_L = \sqrt{\frac{\lambda_s + 2\mu_s}{\rho_s}},\tag{3.31}$$

$$B_s = \lambda_s + \frac{2}{3}\mu_s.\tag{3.32}$$

Here, for the solid,  $\rho_s$  is the density (kg/m<sup>3</sup>),  $B_s$  the bulk modulus (Pa),  $\alpha_s$  the coefficient of volumetric expansion (1/K),  $\lambda_1$  and  $\mu_1$  the first and second viscosity coefficients (Pa s),  $\lambda_s$  and  $\mu_s$  the elastic Lamé coefficients (Pa),  $c_{ps}$  and  $c_{vs}$  the specific heats at constant pressure and volume respectively (J/(kg K)) and, finally,  $k_s$  the thermal conductivity (W/(m K)). In addition,  $Q(t)$  represents the power density (W/m<sup>3</sup>), absorbed by the solid material from the excitation source. In the present section  $Q(t)$  is assumed spatially homogeneous. This fact will be important further on and duly reminded.

We make the following assumptions: (i) the viscous behavior of both the fluid and the solid is neglected, (ii) the effect of motion or deformation on the thermal problem is neglected within both the fluid and the solid regions (no feedback effect), (iii) in the solid layer it is assumed that  $c_{ps} = c_{vs}$  and therefore, from Equations 3.27,  $c_{p1} = c_{ps}$ . Hence,

the equations for the fluid can be simplified to

$$\begin{aligned}\frac{1}{B_0} \frac{\partial p}{\partial t} &= \alpha_0 \frac{\partial T}{\partial t} - \frac{\partial v}{\partial x}, \\ \rho_0 \frac{\partial v}{\partial t} &= -\frac{\partial p}{\partial x}, \\ \rho_0 c_{p0} \frac{\partial T}{\partial t} &= k_0 \frac{\partial^2 T}{\partial x^2}.\end{aligned}\tag{3.33}$$

while those of the solid become

$$\begin{aligned}\frac{1}{B_1} \frac{\partial p}{\partial t} &= \alpha_1 \frac{\partial T}{\partial t} - \frac{\partial v}{\partial x}, \\ \rho_1 \frac{\partial v}{\partial t} &= -\frac{\partial p}{\partial x}, \\ \rho_1 c_{p1} \frac{\partial T}{\partial t} &= k_1 \frac{\partial^2 T}{\partial x^2} + Q(t).\end{aligned}\tag{3.34}$$

These equations are the starting point of our analytical model and correspond to the Cartesian one-dimensional version of Equations 3.3, 3.4 and 3.15, which were calculated for a three dimensional system with cylindrical coordinates.

It is important to say a few words about the assumption of neglecting fluid viscosities. We emphasize that, as the frequency of the acoustic wave increases, the attenuation phenomena in the fluid become more prominent [230], therefore at certain frequencies  $\omega$  (rad/s) of interest in this work, dissipative effects may not be negligible. Let us assume for instance that the acoustic penetration length scales as  $\omega^{-2}$  [184]. All results concerning the relevant acoustic in the fluid region are thus correct only in a layer near the solid-fluid interface. Further away from this layer, the acoustic motion decreases exponentially with the penetration length, the latter depending on the viscosity coefficients. Nevertheless, the analysis of the acoustic wave, and in particular of the mechanophone launching mechanism, in the high frequency regime, where the attenuation is quite large, is not only important from the theoretical point of view but also relevant for a better understanding of nanoparticle-fluid interactions at ultrahigh acoustic vibration frequencies [231]. In particular, it is crucial to investigate the dependence of the energy dissipation on the fluid properties in order to develop high-quality-factor mechanical resonators operating in fluids [232, 233, 234, 52, 235]. Moreover, simple liquids interacting with high-frequency resonators have recently exhibited a sort of solid-like viscoelastic behavior [236, 237, 238, 239, 240]. The high-frequency generation by means of the mechanophone mechanism can be therefore useful to accurately study these systems and phenomena.

### 3.5.2 Thermal behaviour

We take the solid layer in the region  $x \in [0, L]$  and a fluid medium (e.g., water) for  $x \in [L, +\infty)$ , see Figure 41. The equations discussed so far are described in the time domain. Here, we will switch to the frequency domain, where we can solve analytically the equations describing our system. To do so, we assume that the power density is delivered to the solid layer with a sinusoidal time-varying behavior, having a fixed angular frequency  $\omega$ :  $Q(t) = Q_w e^{i\omega t}$ . For ease of notation, from now on we will address  $Q_w$  as simply  $Q$ . Therefore, we can substitute all physical quantities with the corresponding complex valued phasors by applying the Fourier transform (FT). In this way, we get

$$i\omega\rho_1c_{p1}T = k_1\frac{\partial^2T}{\partial x^2} + Q, \quad x \in [0, L], \quad (3.35)$$

$$i\omega\rho_0c_{p0}T = k_0\frac{\partial^2T}{\partial x^2}, \quad x \in [L, +\infty). \quad (3.36)$$

Here, we used the standard substitution  $\partial/\partial t \rightarrow i\omega$ , based on the assumed time behavior  $e^{i\omega t}$ .

The thermal behavior of the system is uncoupled from the mechanical one, which means that we can first solve Equations 3.35 and 3.36, by taking into account the following boundary conditions [241, 242, 243, 244]:

$$q(L) = \frac{1}{\mathcal{R}}(T(L^-) - T(L^+)) \quad (3.37)$$

$$-k_1\frac{\partial T}{\partial x}(L^-) = -k_0\frac{\partial T}{\partial x}(L^+) = q(L), \quad (3.38)$$

the first equation describes the heat flux at the solid/liquid interface  $L$ , which is ruled by the presence of the TBR,  $\mathcal{R}$ . The second equation describes the continuity of the heat flux, defined as  $q(x) = -k_1\frac{\partial T}{\partial x}$  in the solid and  $q(x) = -k_0\frac{\partial T}{\partial x}$  in the fluid. At the other surface, i.e. the solid/vacuum interface at  $x = 0$ , we assume an adiabatic condition:

$$-k_1\frac{\partial T}{\partial x}(0) = q(0) = 0. \quad (3.39)$$

The general solution of Equation 3.35 for  $x \in [0, L]$  can be written as

$$T(x) = Ae^{\vartheta_1x} + Be^{-\vartheta_1x} + \frac{Q}{i\omega\rho_1c_{p1}}, \quad (3.40)$$

where  $A$  and  $B$  are unknown coefficients and  $\vartheta_1$  is given by

$$\vartheta_1 = \frac{\sqrt{2}}{2} \sqrt{\frac{\omega\rho_1c_{p1}}{k_1}}(1 + i). \quad (3.41)$$

We also assumed that the absorbed power density  $Q$  is homogeneously distributed for  $x \in [0, L]$ .

On the other hand, in the liquid, the general solution of Equation 3.36 for  $x \in [L, +\infty)$  is given by

$$T(x) = Ce^{\vartheta_0 x} + De^{-\vartheta_0 x}, \quad (3.42)$$

where  $C$  and  $D$  are unknown coefficients and  $\vartheta_0$  can be written as

$$\vartheta_0 = \frac{\sqrt{2}}{2} \sqrt{\frac{\omega \rho_0 c_{p0}}{k_0}} (1 + i). \quad (3.43)$$

Since the temperature must remain finite for large values of  $x$ , this implies  $C = 0$ . The imaginary part of  $\vartheta_0$  corresponds to the propagation constant of the thermal wave, while its real part defines the thermal length given by  $\mathcal{L}_{th} = 1/\Re\{\vartheta_0\} = \sqrt{\frac{2k_0}{\omega \rho_0 c_{p0}}}$  [184], which identifies the penetration length of the thermal wave into the liquid domain. The application of the boundary conditions stated in Equations 3.37, 3.38 and 3.39 leads to

$$A = B = -\frac{Q}{2i\omega \rho_1 c_{p1}} \left( \frac{k_0 \vartheta_0}{k_0 \vartheta_0 \cosh(\vartheta_1 L) + (1 + \mathcal{R}k_0 \vartheta_0) k_1 \vartheta_1 \sinh(\vartheta_1 L)} \right), \quad (3.44)$$

$$D = \frac{Q}{i\omega \rho_1 c_{p1}} \left( \frac{k_1 \vartheta_1 \sinh(\vartheta_1 L) e^{\vartheta_0 L}}{k_0 \vartheta_0 \cosh(\vartheta_1 L) + (1 + \mathcal{R}k_0 \vartheta_0) k_1 \vartheta_1 \sinh(\vartheta_1 L)} \right). \quad (3.45)$$

We can now write the solutions for the temperature in both the solid and liquid domains. For  $x \in [0, L]$ , i.e. in the solid domain, we have

$$T(x) = \frac{Q}{i\omega \rho_1 c_{p1}} \left( 1 - \frac{k_0 \vartheta_0 \cosh(\vartheta_1 x)}{k_0 \vartheta_0 \cosh(\vartheta_1 L) + (1 + \mathcal{R}k_0 \vartheta_0) k_1 \vartheta_1 \sinh(\vartheta_1 L)} \right), \quad (3.46)$$

while for  $x \in [L, +\infty)$ , we obtain

$$T(x) = \frac{Q}{i\omega \rho_1 c_{p1}} \left( \frac{k_1 \vartheta_1 \sinh(\vartheta_1 L) e^{-\vartheta_0(x-L)}}{k_0 \vartheta_0 \cosh(\vartheta_1 L) + (1 + \mathcal{R}k_0 \vartheta_0) k_1 \vartheta_1 \sinh(\vartheta_1 L)} \right). \quad (3.47)$$

To reconstruct the spatio-temporal behavior of a function  $f(x, t)$ , we must use the phasor  $f(x)$  and apply the relation  $f(x, t) = \Re\{f(x)e^{i\omega t}\}$ . In our case, this procedure can be applied to both the temperature  $T$  and the heat flux  $q$ .

### 3.5.3 Acoustic behavior

In both solid and fluid regions, the equations for pressure and velocity (Equations 3.33 and 3.34) can be rewritten as follows for the sinusoidal time behavior

$$\frac{i\omega}{B_{0,1}}p = i\omega\alpha_{0,1}T - \frac{\partial v}{\partial x}, \quad (3.48)$$

$$i\omega\rho_{0,1}v = -\frac{\partial p}{\partial x}, \quad (3.49)$$

where again we use the indexes zero and one for the liquid and the solid domains, respectively. This system of equations can be easily rearranged in the more useful form

$$\frac{\omega^2\rho_{0,1}}{B_{0,1}}p + \frac{\partial^2 p}{\partial x^2} = \omega^2\rho_{0,1}\alpha_{0,1}T, \quad (3.50)$$

$$v = -\frac{1}{i\omega\rho_{0,1}}\frac{\partial p}{\partial x}. \quad (3.51)$$

This means that, once the first equation is solved for the pressure  $p$ , the velocity field  $v$  can be directly obtained from the second one. Of course, in order to solve the first equation we must consider the temperature profile pertinent to the each domain, as obtained in the previous section. First, we search for the general solution of Equation 3.50, valid for any profile  $T(x)$ . To do so, we start by the homogeneous counterpart of Equation 3.50:

$$\frac{\omega^2\rho_{0,1}}{B_{0,1}}p_h + \frac{\partial^2 p_h}{\partial x^2} = 0, \quad (3.52)$$

from which we directly obtain the solution  $p_h$  as

$$p_h(x) = Ee^{-\delta_{0,1}x} + Fe^{\delta_{0,1}x}, \quad (3.53)$$

where

$$\delta_{0,1} = i\omega\sqrt{\frac{\rho_{0,1}}{B_{0,1}}}. \quad (3.54)$$

The constants  $E$  and  $F$  will be determined at a later stage through the pertinent boundary conditions. These two terms represent the progressive and regressive pressure waves.

Regarding the nonhomogeneous equation,

$$\frac{\omega^2\rho_{0,1}}{B_{0,1}}p_{nh} + \frac{\partial^2 p_{nh}}{\partial x^2} = \omega^2\rho_{0,1}\alpha_{0,1}T, \quad (3.55)$$

by adopting the method of variation of parameters (Lagrange's method) we can write a particular solution  $p_{nh}$  in the form

$$p_{nh}(x) = e(x)p_e(x) + f(x)p_f(x), \quad (3.56)$$

where  $p_e(x) = e^{-\delta_{0,1}x}$  and  $p_f(x) = e^{\delta_{0,1}x}$ . We underline that Equation 3.56 simply represents a generalization of Equation 3.53, where, however, the coefficients  $e$  and  $f$  depend on  $x$ . Therefore, following Lagrange theory, the first derivatives of  $e$  and  $f$  fulfill the following algebraic system

$$e'(x)p_e(x) + f'(x)p_f(x) = 0, \quad (3.57)$$

$$e'(x)p_e'(x) + f'(x)p_f'(x) = \omega^2 \rho_{0,1} \alpha_{0,1} T(x), \quad (3.58)$$

where we used the compact notation  $g'(x) = \partial g / \partial x$  for the spatial derivative. This system always has only one solution since the Wronskian determinant  $W(x) = p_e(x)p_f'(x) - p_f(x)p_e'(x)$  is different from zero, being given by the explicit relation  $W(x) = 2i\omega \sqrt{\rho_{0,1}/B_{0,1}}$ . The solutions can be easily obtained and read

$$e'(x) = -\frac{1}{2i} \omega \alpha_{0,1} T(x) \sqrt{\rho_{0,1} B_{0,1}} p_f(x), \quad (3.59)$$

$$f'(x) = \frac{1}{2i} \omega \alpha_{0,1} T(x) \sqrt{\rho_{0,1} B_{0,1}} p_e(x), \quad (3.60)$$

from which we obtain

$$e(x) = -\frac{1}{2i} \omega \alpha_{0,1} \sqrt{\rho_{0,1} B_{0,1}} \int T(x) e^{\delta_{0,1}x} dx, \quad (3.61)$$

$$f(x) = \frac{1}{2i} \omega \alpha_{0,1} \sqrt{\rho_{0,1} B_{0,1}} \int T(x) e^{-\delta_{0,1}x} dx. \quad (3.62)$$

Finally, we obtain the general solution of Equation 3.50, holding for any temperature profile  $T(x)$ , as the sum of Equations 3.53 and 3.56:

$$\begin{aligned} p(x) &= p_h(x) + p_{nh}(x) \\ &= [E + e(x)] e^{-\delta_{0,1}x} + [F + f(x)] e^{\delta_{0,1}x}, \end{aligned} \quad (3.63)$$

where  $e(x)$  and  $f(x)$  can be found calculating the integrals in Equations 3.61 and 3.62. We can now specify this general solution for the solid and fluid regions. In the solid region ( $x \in [0, L]$ ), we use the temperature profile given in Equation 3.46 and, after some

straightforward calculations, we obtain

$$p(x) = Ee^{-\delta_1 x} + Fe^{\delta_1 x} + \sqrt{\frac{B_1}{\rho_1}} \frac{\delta_1}{\delta_1^2 - \vartheta_1^2} \frac{\alpha_1 Q}{c_{p1}} \left[ \frac{\delta_1^2 - \vartheta_1^2}{\delta_1^2} - \frac{k_0 \vartheta_0 \cosh(\vartheta_1 x)}{k_0 \vartheta_0 \cosh(\vartheta_1 L) + (1 + \mathcal{R} k_0 \vartheta_0) k_1 \vartheta_1 \sinh(\vartheta_1 L)} \right], \quad (3.64)$$

$$v(x) = \frac{\delta_1}{i\omega \rho_1} Ee^{-\delta_1 x} - \frac{\delta_1}{i\omega \rho_1} Fe^{\delta_1 x} + \sqrt{\frac{B_1}{\rho_1}} \frac{\delta_1}{\delta_1^2 - \vartheta_1^2} \frac{\alpha_1 Q}{i\omega \rho_1 c_{p1}} \times \frac{k_0 \vartheta_0 \vartheta_1 \sinh(\vartheta_1 x)}{k_0 \vartheta_0 \cosh(\vartheta_1 L) + (1 + \mathcal{R} k_0 \vartheta_0) k_1 \vartheta_1 \sinh(\vartheta_1 L)}. \quad (3.65)$$

In the fluid region with  $x \in [L, +\infty)$ , instead, we substitute the temperature profile given in Equation 3.47, and we obtain

$$p(x) = Ge^{-\delta_0 x} + He^{\delta_0 x} + \frac{\rho_0}{\rho_1} \sqrt{\frac{B_0}{\rho_0}} \frac{\delta_0}{\delta_0^2 - \vartheta_0^2} \frac{\alpha_0 Q}{c_{p1}} e^{-\vartheta_0(x-L)} \times \frac{k_1 \vartheta_1 \sinh(\vartheta_1 L)}{k_0 \vartheta_0 \cosh(\vartheta_1 L) + (1 + \mathcal{R} k_0 \vartheta_0) k_1 \vartheta_1 \sinh(\vartheta_1 L)}, \quad (3.66)$$

$$v(x) = \frac{\delta_0}{i\omega \rho_0} Ge^{-\delta_0 x} - \frac{\delta_0}{i\omega \rho_0} He^{\delta_0 x} + \frac{1}{i\omega \rho_1} \sqrt{\frac{B_0}{\rho_0}} \frac{\delta_0}{\delta_0^2 - \vartheta_0^2} \frac{\alpha_0 Q}{c_{p1}} e^{-\vartheta_0(x-L)} \times \frac{k_1 \vartheta_1 \vartheta_0 \sinh(\vartheta_1 L)}{k_0 \vartheta_0 \cosh(\vartheta_1 L) + (1 + \mathcal{R} k_0 \vartheta_0) k_1 \vartheta_1 \sinh(\vartheta_1 L)}, \quad (3.67)$$

where we substituted the coefficients  $E$  and  $F$  with two new symbols  $G$  and  $H$  to properly distinguish the different regions. We further observe that we must impose  $H = 0$  since we do not consider regressive waves in the fluid (the acoustic wave in liquid is generated at small  $x$  and propagates in the direction of growing  $x$  values). The other coefficients ( $E$ ,  $F$ ,  $G$ ) are fixed upon imposing the mechanical boundary conditions. First, we impose the continuity of pressure and velocity at the interface between solid and fluid [184, 228, 229]

$$p(L^-) = p(L^+), \quad (3.68)$$

$$v(L^-) = v(L^+). \quad (3.69)$$

These relations are equivalent to the continuity of normal mechanical stress and displacement, describing the ideal interface behavior in continuum mechanics. Then we have to impose the mechanical condition on the side of the solid film not in contact with water, for  $x = 0$ . To do this, we have two possibilities describing either the free surface (zero-stress) condition:

$$p(0) = 0, \quad (3.70)$$

or the clamped surface (zero-displacement) condition:

$$v(0) = 0. \quad (3.71)$$

In more explicit form, the two continuity conditions stated in Equations 3.68 and 3.69 deliver

$$\begin{aligned} & Ee^{-\delta_1 L} + Fe^{\delta_1 L} + \sqrt{\frac{B_1}{\rho_1}} \frac{\delta_1}{\delta_1^2 - \vartheta_1^2} \frac{\alpha_1 Q}{c_{p1}} \left[ \frac{\delta_1^2 - \vartheta_1^2}{\delta_1^2} - \frac{k_0 \vartheta_0 \cosh(\vartheta_1 L)}{S} \right] \\ &= Ge^{-\delta_0 L} + \frac{\rho_0}{\rho_1} \sqrt{\frac{B_0}{\rho_0}} \frac{\delta_0}{\delta_0^2 - \vartheta_0^2} \frac{\alpha_0 Q}{c_{p1}} \frac{k_1 \vartheta_1 \sinh(\vartheta_1 L)}{S}, \end{aligned} \quad (3.72)$$

$$\begin{aligned} & \frac{\delta_1}{i\omega\rho_1} Ee^{-\delta_1 L} - \frac{\delta_1}{i\omega\rho_1} Fe^{\delta_1 L} + \sqrt{\frac{B_1}{\rho_1}} \frac{\delta_1}{\delta_1^2 - \vartheta_1^2} \alpha_1 Q \frac{k_0 \vartheta_0 \vartheta_1 \sinh(\vartheta_1 L)}{i\omega\rho_1 c_{p1} S} \\ &= \frac{\delta_0}{i\omega\rho_0} Ge^{-\delta_0 L} + \sqrt{\frac{B_0}{\rho_0}} \frac{\delta_0 \alpha_0 Q}{\delta_0^2 - \vartheta_0^2} \frac{k_1 \vartheta_1 \vartheta_0 \sinh(\vartheta_1 L)}{i\omega\rho_1 c_{p1} S}, \end{aligned} \quad (3.73)$$

where

$$S = k_0 \vartheta_0 \cosh(\vartheta_1 L) + (1 + \mathcal{R} k_0 \vartheta_0) k_1 \vartheta_1 \sinh(\vartheta_1 L). \quad (3.74)$$

The free surface condition for  $x = 0$  leads to

$$E + F + \sqrt{\frac{B_1}{\rho_1}} \frac{\delta_1}{\delta_1^2 - \vartheta_1^2} \frac{\alpha_1 Q}{c_{p1}} \left[ \frac{\delta_1^2 - \vartheta_1^2}{\delta_1^2} - \frac{k_0 \vartheta_0}{S} \right] = 0, \quad (3.75)$$

whereas the clamped surface condition to

$$E - F = 0. \quad (3.76)$$

To make the notation more compact, we introduce a binary parameter  $b$  such that  $b = +1$  implies the free surface condition at  $x = 0$ , while  $b = -1$  implies the clamped surface condition at  $x = 0$ . With such notation, the three boundary conditions (two continuity equations for  $x = L$  and one free/clamped boundary at  $x = 0$ ) can be cast as follows:

$$Ee^{-\delta_1 L} + Fe^{\delta_1 L} = Ge^{-\delta_0 L} + \xi, \quad (3.77)$$

$$Ee^{-\delta_1 L} - Fe^{\delta_1 L} = \frac{\delta_0 \rho_1}{\delta_1 \rho_0} Ge^{-\delta_0 L} + \eta, \quad (3.78)$$

$$E + bF + \frac{1+b}{2} \varphi = 0, \quad (3.79)$$

where

$$\xi = \frac{\rho_0}{\rho_1} \sqrt{\frac{B_0}{\rho_0}} \frac{\delta_0}{\delta_0^2 - \vartheta_0^2} \frac{\alpha_0 Q}{c_{p1}} \frac{k_1 \vartheta_1 \sinh(\vartheta_1 L)}{S} \quad (3.80)$$

$$- \sqrt{\frac{B_1}{\rho_1}} \frac{\delta_1}{\delta_1^2 - \vartheta_1^2} \frac{\alpha_1 Q}{c_{p1}} \left[ \frac{\delta_1^2 - \vartheta_1^2}{\delta_1^2} - \frac{k_0 \vartheta_0 \cosh(\vartheta_1 L)}{S} \right],$$

$$\eta = \sqrt{\frac{B_0}{\rho_0}} \frac{\delta_0}{\delta_0^2 - \vartheta_0^2} \alpha_0 Q \frac{k_1 \vartheta_1 \vartheta_0 \sinh(\vartheta_1 L)}{\delta_1 c_{p1} S} \quad (3.81)$$

$$- \sqrt{\frac{B_1}{\rho_1}} \frac{\alpha_1 Q}{\delta_1^2 - \vartheta_1^2} \frac{k_0 \vartheta_0 \vartheta_1 \sinh(\vartheta_1 L)}{c_{p1} S},$$

$$\varphi = \sqrt{\frac{B_1}{\rho_1}} \frac{\delta_1}{\delta_1^2 - \vartheta_1^2} \frac{\alpha_1 Q}{c_{p1}} \left[ \frac{\delta_1^2 - \vartheta_1^2}{\delta_1^2} - \frac{k_0 \vartheta_0}{S} \right]. \quad (3.82)$$

The solution for  $F$  can be obtained straightforwardly

$$F = \frac{\frac{\delta_0 \rho_1}{\delta_1 \rho_0} \xi - \eta + \left( \frac{\delta_0 \rho_1}{\delta_1 \rho_0} - 1 \right) \frac{1+b}{2} \varphi e^{-\delta_1 L}}{\frac{\delta_0 \rho_1}{\delta_1 \rho_0} (e^{\delta_1 L} - b e^{-\delta_1 L}) + (e^{\delta_1 L} + b e^{-\delta_1 L})}, \quad (3.83)$$

and the other coefficients can be directly calculated through the relations

$$E = -bF - \frac{1+b}{2} \varphi, \quad (3.84)$$

$$G = e^{\delta_0 L} \left[ F (e^{\delta_1 L} - b e^{-\delta_1 L}) - \xi - \frac{1+b}{2} \varphi e^{-\delta_1 L} \right]. \quad (3.85)$$

This concludes the solution of the acoustic response of the system with both stress-free ( $b = +1$ ) and displacement-free ( $b = -1$ ) conditions for the film surface not in contact with the liquid ( $x = 0$ ).

With the developed model, we can now investigate the thermophone vs mechanophone competition for the nanofilm/water system in the frequency domain. From one hand, the heat that flows from the solid to the fluid creates periodic compressions and dilatations in the fluid at the same frequency as the absorbed power density and therefore produces an acoustic wave propagating in the fluid region, this is the thermophone effect. On the other hand, the energy applied to the system also generates an oscillatory strain and stress within the nanofilm, which finally generates an acoustic wave in water through the mechanophone mechanism. To clarify the interplay and magnitude of the competition between these two launching mechanisms across the entire suitable frequency spectrum, let us calculate the acoustic pressure in the two cases by first turning off the sole thermophone effect and then the sole mechanophone effect. As for the gold nanocylinder (see Section 3.4), in order to turn off the thermophone, we set  $\alpha_0 = 0$ , and conversely, to turn off the mechanophone,

we set  $\alpha_1 = 0$ . We pinpoint that the total response of the system is given by the sum of the partial response with  $\alpha_0 = 0$  and that with  $\alpha_1 = 0$ . This is well seen from the mathematical form of the three coefficients in Equations 3.80, 3.81 and 3.82.

### 3.5.4 Mechanophone effect

We start by considering solely the mechanophone contribution. This is done by canceling the thermophone effect, imposing  $\alpha_0 = 0$ , i.e. eliminating the thermal expansion of the liquid. Only the compression and dilatation processes in the nanofilm can mechanically generate an acoustic wave in the fluid via means of the piston effect. Under this assumption, the coefficients of Equations 3.80, 3.81 and 3.82 reduce to

$$\xi = -\sqrt{\frac{B_1}{\rho_1}} \frac{\delta_1}{\delta_1^2 - \vartheta_1^2} \frac{\alpha_1 Q}{c_{p1}} \left[ \frac{\delta_1^2 - \vartheta_1^2}{\delta_1^2} - \frac{k_0 \vartheta_0 \cosh(\vartheta_1 L)}{S} \right], \quad (3.86)$$

$$\eta = -\sqrt{\frac{B_1}{\rho_1}} \frac{\alpha_1 Q}{\delta_1^2 - \vartheta_1^2} \frac{k_0 \vartheta_0 \vartheta_1 \sinh(\vartheta_1 L)}{c_{p1} S}, \quad (3.87)$$

$$\varphi = \sqrt{\frac{B_1}{\rho_1}} \frac{\delta_1}{\delta_1^2 - \vartheta_1^2} \frac{\alpha_1 Q}{c_{p1}} \left[ \frac{\delta_1^2 - \vartheta_1^2}{\delta_1^2} - \frac{k_0 \vartheta_0}{S} \right]. \quad (3.88)$$

With these coefficients, we can elaborate the expression for the pressure of the acoustic wave in liquid ( $x > L$ ), thus obtaining

$$p(x) = -\frac{\eta (e^{\delta_1 L} - b e^{-\delta_1 L}) + (1 + b)\varphi + \xi (e^{\delta_1 L} + b e^{-\delta_1 L})}{\sqrt{\frac{\rho_1 B_1}{\rho_0 B_0}} (e^{\delta_1 L} - b e^{-\delta_1 L}) + (e^{\delta_1 L} + b e^{-\delta_1 L})} e^{-\delta_0(x-L)}. \quad (3.89)$$

We now address both the case of a free surface at  $x = 0$  ( $b = +1$ ) and that of a clamped surface at  $x = 0$  ( $b = -1$ ). For  $b = +1$ , we easily get the following expression for the pressure intensity (we call pressure intensity the modulus of the pressure):

$$\begin{aligned} |p| &= \left| \frac{\eta \sinh(\delta_1 L) + \varphi + \xi \cosh(\delta_1 L)}{\sqrt{\frac{\rho_1 B_1}{\rho_0 B_0}} \sinh(\delta_1 L) + \cosh(\delta_1 L)} \right| \\ &= \left| \frac{\eta i \sin\left(\omega \sqrt{\frac{\rho_1}{B_1}} L\right) + \phi + \xi \cos\left(\omega \sqrt{\frac{\rho_1}{B_1}} L\right)}{\sqrt{\frac{\rho_1 B_1}{\rho_0 B_0}} i \sin\left(\omega \sqrt{\frac{\rho_1}{B_1}} L\right) + \cos\left(\omega \sqrt{\frac{\rho_1}{B_1}} L\right)} \right|, \end{aligned} \quad (3.90)$$

where we considered the fact that  $\delta_0$  is a purely imaginary number. On the other hand, for  $b = -1$ , we obtain

$$\begin{aligned}
 |p| &= \left| \frac{\eta \cosh(\delta_1 L) + \xi \sinh(\delta_1 L)}{\sqrt{\frac{\rho_1 B_1}{\rho_0 B_0}} \cosh(\delta_1 L) + \sinh(\delta_1 L)} \right| \\
 &= \left| \frac{\eta \cos\left(\omega \sqrt{\frac{\rho_1}{B_1}} L\right) + \xi i \sin\left(\omega \sqrt{\frac{\rho_1}{B_1}} L\right)}{\sqrt{\frac{\rho_1 B_1}{\rho_0 B_0}} \cos\left(\omega \sqrt{\frac{\rho_1}{B_1}} L\right) + i \sin\left(\omega \sqrt{\frac{\rho_1}{B_1}} L\right)} \right|. \tag{3.91}
 \end{aligned}$$

We point out that the one-dimensional geometry of this system implies a non-decaying pressure in the fluid for large  $x$ , as opposed to the nanocylinder case, where the cylindrical pressure wave asymptotically decays as  $1/\sqrt{r}$  due to energy conservation.

For small values of the frequency  $\omega$ , the expression for  $|p|$  can be simplified by adopting a second-order approximation for trigonometric and hyperbolic functions, including those appearing in  $S$ , (see Equation 3.74). After a tedious but straightforward calculation, we obtain the following behavior for the free surface case ( $b = +1$ ):

$$|p| \simeq \frac{Q \alpha_1 \rho_1 L^3}{2 \sqrt{\rho_0 k_0 c_{p0}}} \omega^{3/2}, \quad \omega \ll \frac{1}{L} \sqrt{\frac{B_1}{\rho_1}}, \tag{3.92}$$

and the expression below for the clamped surface ( $b = -1$ ):

$$|p| \simeq Q \alpha_1 L^2 \sqrt{\frac{\omega B_0}{k_0 c_{p0}}}, \quad \omega \ll \frac{1}{L} \sqrt{\frac{B_1}{\rho_1}}. \tag{3.93}$$

This means that, for small values of the frequency, the free surface case implies a pressure in the liquid scaling as  $\sim \omega^{3/2}$ , whereas the clamped surface case implies scaling  $\sim \omega^{1/2}$ . Although the exact pressure response of the system is dependent on the TBR ( $S$  depends on  $\mathcal{R}$  in previous solutions, see Equation 3.74), note that for low frequencies this dependence does not appear in Equations 3.92 and 3.93. These approximations, for both free and clamped generating layer, will prove very useful further on to quantitatively compare the two mechanisms of acoustic generation.

### 3.5.5 Thermophone effect

We now move to the pure thermophone case. We cancel the mechanophone effect by imposing  $\alpha_1 = 0$ , which is tantamount to eliminate the thermal expansion of the solid. In this way, only the compression and dilatation processes triggered by the thermal expansion of the fluid can generate an acoustic wave in it. Under this working conditions,

the coefficients of Equations 3.80, 3.81 and 3.82 reduce to

$$\xi = \frac{\rho_0}{\rho_1} \sqrt{\frac{B_0}{\rho_0}} \frac{\delta_0}{\delta_0^2 - \vartheta_0^2} \frac{\alpha_0 Q k_1 \vartheta_1 \sinh(\vartheta_1 L)}{c_{p1} S}, \quad (3.94)$$

$$\eta = \sqrt{\frac{B_0}{\rho_0}} \frac{\delta_0}{\delta_0^2 - \vartheta_0^2} \alpha_0 Q \frac{k_1 \vartheta_1 \vartheta_0 \sinh(\vartheta_1 L)}{\delta_1 c_{p1} S}, \quad (3.95)$$

$$\varphi = 0. \quad (3.96)$$

With these expressions at hand, we can obtain the expression for the pressure of the acoustic wave launched in the liquid ( $x > L$ ) as

$$p(x) = -e^{-\delta_0(x-L)} \sqrt{\frac{B_0}{\rho_0}} \frac{\delta_0}{\delta_0^2 - \vartheta_0^2} \frac{\alpha_0 Q k_1 \vartheta_1 \sinh(\vartheta_1 L)}{c_{p1} S} \times \frac{\frac{\theta_0 B_1}{i\omega \rho_1} (e^{\delta_1 L} - b e^{-\delta_1 L}) + \frac{\rho_0}{\rho_1} (e^{\delta_1 L} + b e^{-\delta_1 L})}{\sqrt{\frac{\rho_1 B_1}{\rho_0 B_0} (e^{\delta_1 L} - b e^{-\delta_1 L}) + (e^{\delta_1 L} + b e^{-\delta_1 L})}}, \quad (3.97)$$

which is exact provided  $\alpha_1 = 0$  and contains no other approximations. In order to further simplify this expression, since for the thermophone mechanism the solid deformation is not relevant, we can add the additional assumption that  $B_1 \rightarrow \infty$ , which cancels wave propagation in the solid and thus all resonance phenomena. This leads to

$$p(x) = -e^{-\delta_0(x-L)} \frac{B_0 \delta_0}{\delta_0^2 - \vartheta_0^2} \frac{\alpha_0 \vartheta_0 Q k_1 \vartheta_1 \sinh(\vartheta_1 L)}{i\omega \rho_1 c_{p1} S}, \quad (3.98)$$

where the parameter  $b$  has obviously disappeared since the boundary condition for  $x = 0$  no longer has any effect on the undeformable solid. Again, Equation 3.98 is exact under the hypotheses  $\alpha_1 = 0$  and  $B_1 \rightarrow \infty$ . The intensity of the pressure of the acoustic wave then reads

$$|p| = \frac{\alpha_0 \rho_0 Q}{\rho_1 c_{p1}} \sqrt{\frac{\omega c_{p0} B_0}{k_0}} \left| \frac{1}{\delta_0^2 - \vartheta_0^2} \frac{k_1 \vartheta_1 \sinh(\vartheta_1 L)}{S} \right|. \quad (3.99)$$

We now focus on the absolute value in Equation 3.99. Previously we provided, for the case of the sole mechanophone effect, an approximation of the pressure generated for low frequencies since, as will be later discussed, this mechanism is less effective in that region of the frequency spectrum. Assuming that, conversely, the thermophone mechanism is less effective for high frequencies, we now develop a valid approximation of Equation 3.99 for intermediate and/or high frequencies. In this way, we will see how the two approximations allow us to identify a threshold frequency, or cross-over, above which the mechanophone mechanism becomes more effective than the thermophone one.

For large enough frequencies, the fraction  $k_1\vartheta_1 \sinh(\vartheta_1 L)/S$  can be approximated by  $k_1\vartheta_1/[k_0\vartheta_0 + (1 + \mathcal{R}k_0\vartheta_0)k_1\vartheta_1]$  since  $2 \sinh(\vartheta_1 L) \simeq 2 \cosh(\vartheta_1 L) \simeq \exp(\vartheta_1 L)$  for  $|\vartheta_1 L| \gg 1$ . Moreover, if  $\Re\{\mathcal{R}k_0\vartheta_0\} \gg 1$  and  $\Re\{\mathcal{R}k_1\vartheta_1\} \gg 1$ , we obtain the simpler relation  $k_1\vartheta_1 \sinh(\vartheta_1 L)/S \simeq 1/(\mathcal{R}k_0\vartheta_0)$ . These two further assumptions correspond to  $\omega \gg 2/(\mathcal{R}^2 \rho_0 k_0 c_{p0})$  and  $\omega \gg 2/(\mathcal{R}^2 \rho_1 k_1 c_{p1})$ , where typically  $2/(\mathcal{R}^2 \rho_1 k_1 c_{p1}) < 2/(\mathcal{R}^2 \rho_0 k_0 c_{p0})$  and therefore only the first condition is sufficient to justify the approximation. This is especially true in our case, where we take the nanofilm as made of gold and the liquid as water, at least at the frequency domain of our interest (see next Section for numerical examples). In addition, it is easy to prove that  $|1/(\delta_0^2 - \vartheta_0^2)| \simeq k_0/(\omega \rho_0 c_{p0})$  for  $\omega \ll B_0 c_{p0}/k_0$ . These approximations can be applied to Equation 3.99, thus obtaining

$$|p| = \frac{\sqrt{B_0 \rho_0}}{\rho_0 c_{p0} \rho_1 c_{p1}} \frac{\alpha_0 Q}{\omega \mathcal{R}}, \quad \frac{2}{\mathcal{R}^2 \rho_0 k_0 c_{p0}} \ll \omega \ll \frac{B_0 c_{p0}}{k_0}. \quad (3.100)$$

This result shows the degradation of the thermophone effect for increasing  $\omega$  within the central frequency range, described by a scaling of the pressure intensity  $\sim 1/\omega$ . For even larger values of frequency it is easily seen that the scaling shifts to a faster  $1/\omega^2$  law, but this is not relevant to our analysis.

It is interesting to remark that if the thermal boundary resistance  $\mathcal{R}$  is very small, the fraction  $k_1\vartheta_1 \sinh(\vartheta_1 L)/S$  can still be approximated by  $k_1\vartheta_1/[k_0\vartheta_0 + (1 + \mathcal{R}k_0\vartheta_0)k_1\vartheta_1]$  (valid for  $|\vartheta_1 L| \gg 1$ ), but we can not further make the assumptions  $\Re\{\mathcal{R}k_0\vartheta_0\} \gg 1$  and  $\Re\{\mathcal{R}k_1\vartheta_1\} \gg 1$ . Then, from Equation 3.99, the pressure intensity can be approximated by

$$|p| = \frac{\alpha_0 Q}{\rho_1 c_{p1}} \sqrt{\frac{k_0 B_0}{\omega c_{p0}}} \frac{\sqrt{\rho_1 c_{p1} k_1}}{|\sqrt{\rho_0 c_{p0} k_0} + \sqrt{\rho_1 c_{p1} k_1 (1 + \mathcal{R} k_0 \vartheta_0)}|},$$

where the singularity for  $\mathcal{R} \rightarrow 0$  exhibited in Equation 3.100 is no longer present. In particular, for  $\mathcal{R} \rightarrow 0$  (perfect thermophone condition), the approximation reads

$$|p| = \frac{\alpha_0 Q}{\rho_1 c_{p1}} \sqrt{\frac{k_0 B_0}{\omega c_{p0}}} \frac{\sqrt{\rho_1 c_{p1} k_1}}{\sqrt{\rho_0 c_{p0} k_0} + \sqrt{\rho_1 c_{p1} k_1}}, \quad (3.101)$$

which will be used to prove that, also for  $\mathcal{R} = 0$ , the mechanophone effect can still prevail over the thermophone for high enough frequencies. We remark that, when  $\mathcal{R} = 0$ , the pressure intensity  $\sim 1/\sqrt{\omega}$  (see Equation 3.101), whereas it scales as  $1/\omega$  law for sufficiently large values of  $\mathcal{R}$  and for ‘‘intermediate’’ frequencies (see Equation 3.100). We can thus conclude that, increasing the TBR from zero to a sufficiently high value, not only decreases the thermoacoustic performance but also changes the shape pressure frequency dependence in water.

### 3.5.6 Mechanophone vs thermophone: frequency sweep analysis

We consider here the paradigmatic system in which the solid nanofilm is made of gold and water is the liquid. This choice is the one-dimension Cartesian analogue of the water-immersed nanocylinder, addressed in Section 3.4. We set the film thickness to  $L = 20$  nm. The materials parameters are summarized in Table 5 (with the exception of the thermal expansion coefficient of water, which here is assumed independent of temperature and its volumetric value is set at  $3 \times 10^{-4}$ ). Regarding the TBR, we assume  $\mathcal{R} = 3 \times 10^{-8}$  m<sup>2</sup>K/W, a realistic value for the gold/water interface.

Figures 42 and 43 report the frequency spectrum of the pressure generated in water for the case of the free gold film surface (i.e.  $b = +1$ ) and for that of a clamped surface (i.e.  $b = -1$ ), respectively. The curves are normalized with respect to the power density  $Q$  absorbed by the gold film. These spectra show that the thermophone is predominant at low frequencies, while the mechanophone prevails at high frequencies. Indeed, in these figures, we compare the complete solution for the total pressure ( $\alpha_0 \neq 0$  and  $\alpha_1 \neq 0$ , black line) given by Equation 3.66 (with the relevant coefficients) with the purely mechanophone solution ( $\alpha_0 = 0$ , blue line) given in Equation 3.90 (with  $b = +1$ ) or Equation 3.91 (with  $b = -1$ ) and the purely thermophone solution ( $\alpha_1 = 0$ , red line) given in Equation 3.97 (with  $b = \pm 1$ ). It is clearly visible that the thermophone contribution overlaps the total pressure for low values of  $\omega$ , while for large  $\omega$  values the mechanophone becomes the only significant contribution, overlapping the total pressure. In both figures, in the high frequency range, the mechanophone effect and, as a consequence, the total pressure, present very prominent upward and downward peaks. These are due to the activation of the film's vibrational modes, resulting in resonances (upward peaks) and anti-resonances (downward peaks). The peaks correspond to the acoustic eigenfrequencies of a free-standing Au film:  $\omega_n = \pi v_s n / L$ , with  $n=1,2,3,..etc.$  Specifically, the resonances (upward peaks) frequencies correspond to the eigenmodes with odd  $n$ , whereas antiresonances (downward peaks) correspond to the eigenmodes with even  $n$ . The physical reason for this behaviour is the following. The source term  $Q$  in the last line of Equation 3.24 is *spatially homogeneous*, ultimately resulting in a *spatially homogeneous* mechanical excitation of the film. The latter cannot excite the  $n$  even eigenmodes for symmetry reasons<sup>5</sup>, therefore resulting in antiresonances. Also the thermophone effect presents downward peaks at the same frequencies, despite the nanofilm thermal expansion being zero in this case. This is due to the expansion and compression of water which, in the thermophone effect, pushes against the nanofilm activating its quasi-eigenfrequencies, specularly to what happens in reverse during the mechanophone effect. On the contrary, the formula of the high frequency thermophone approximation (Equation 3.100) doesn't show any peak, this is due to the gold bulk modulus approximation  $B_1 \rightarrow \infty$  we made for extracting Equation 3.100, which

<sup>5</sup>These reasons are evident looking at the displacement profile across a free standing film for even  $n$ .

implies an incompressible nanofilm. Finally, notice that the pressure presents different resonance frequencies in the case of a free film surface and in that of the film clamped surface. This is consistent with the free-free and free-clamped films breathing modes<sup>6</sup>. We won't go any further in discussing the activation of the vibrational modes, since this is not the central interest of this chapter and will be extensively discussed in Chapter 4 for another system.

Returning to the thermophone and mechanophone contributions, it can be seen that the curves corresponding to these two effects intersect for a given frequency, corresponding to the threshold for the predominance of one of the two effects. Nonetheless, from the mathematical point of view, it is particularly difficult to find such a threshold frequency by looking for intersections between the two curves related to mechanophone (blue curve) and thermophone (red curve) effects. However, it turns out to be rather easy to find the intersection between the approximated pressure curves, plotted in Figures 42 and 43 for both the mechanophone (blue dashed curve) and thermophone (red dashed curve) mechanisms, respectively.

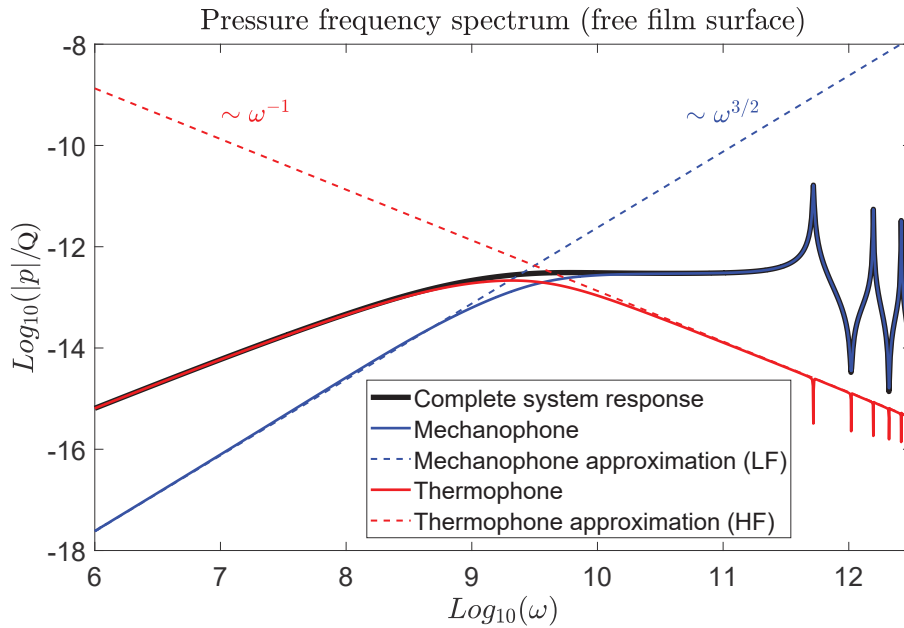


Figure 42. Water pressure intensity frequency spectrum for the case of gold free film surface at  $x = 0$  ( $b = +1$ ) and  $\mathcal{R} = 3 \times 10^{-8} \text{ m}^2\text{K}/\text{W}$ . The total pressure (Equation 3.66, black curve) is compared to the sole mechanophone contribution (Equation 3.90, blue curve) and sole thermophone contribution (Equation 3.97, red curve). Moreover, the low frequency approximation of the sole mechanophone response (Equation 3.92, blue dashed line) and the high frequency approximation of the sole thermophone response (Equation 3.100, red dashed line) are reported. The intersection of the two curves from the approximations identifies the threshold frequency beyond which the mechanophone mechanism becomes predominant.

<sup>6</sup>The resonance frequencies for a free-free film of thickness  $L$  are given by  $\omega_n = \pi v_s n / L$ , with  $v_s$  the sound velocity in the solid; while for a free-clamped film are given by  $\omega_n = \pi v_s (1 + 2n) / (2L)$ .

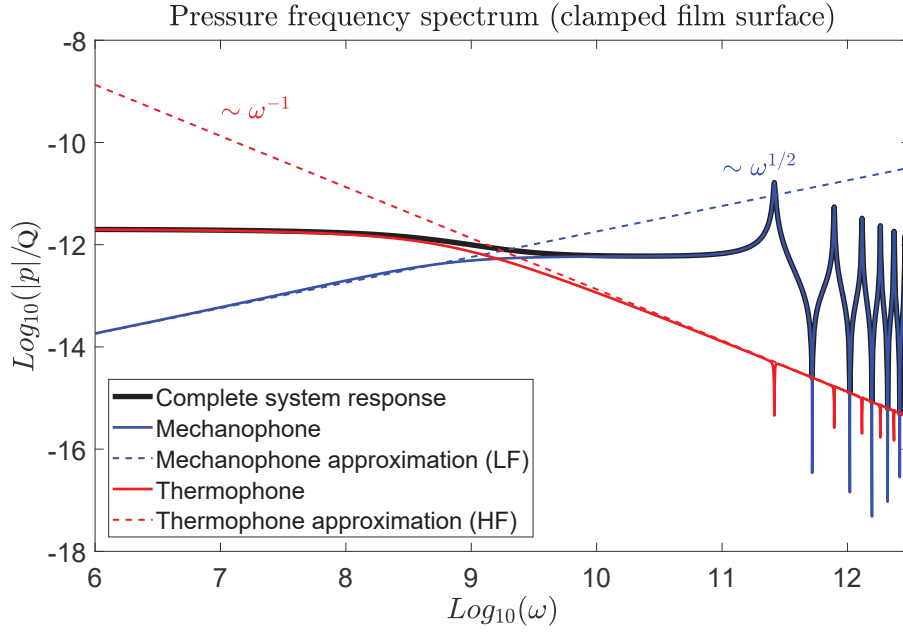


Figure 43. Water pressure intensity frequency spectrum for the case of gold clamped film surface at  $x = 0$  ( $b = -1$ ) and  $\mathcal{R} = 3 \times 10^{-8} \text{ m}^2\text{K/W}$ . The total pressure (Equation 3.66, black curve) is compared to the sole mechanophone contribution (Equation 3.91, blue curve) and sole thermophone contribution (Equation 3.97, red curve). Moreover, the low frequency approximation of the sole mechanophone response (Equation 3.93, blue dashed line) and the high frequency approximation of the sole thermophone response (Equation 3.100, red dashed line) are reported. The intersection of the two curves from the approximations identifies the threshold frequency beyond which the mechanophone mechanism becomes predominant.

To this end, for the free surface case ( $b = +1$ , Figure 42), we calculate the intersection point between the low frequency (LF) approximation of the mechanophone, given in Equation 3.92, and the high frequency (HF) approximation of the thermophone, in Equation 3.100. The frequency threshold turns out to be

$$\omega^*(b = +1) = \left[ 2 \frac{\alpha_0}{\alpha_1} \frac{1}{\mathcal{R} \rho_1^2 c_{p1} L^3} \sqrt{\frac{B_0 k_0}{c_{p0}}} \right]^{2/5}. \quad (3.102)$$

For the clamped surface case ( $b = -1$ , Figure 43), we follow the same reasoning, intersecting the curves pertaining to the low frequency (LF) approximation of the mechanophone response (Equation 3.93) with that of high frequency (HF) approximation of the thermophone response (Equation 3.100). For the frequency threshold we obtain:

$$\omega^*(b = -1) = \left[ \frac{\alpha_0}{\alpha_1} \frac{1}{L^2 \rho_1 c_{p1} \mathcal{R}} \sqrt{\frac{k_0}{\rho_0 c_{p0}}} \right]^{2/3}, \quad (3.103)$$

that represents the frequency beyond which the mechanophone prevails for the clamped surface at  $x = 0$ , as one can see in Figure 43.

### Thermophone vs mechanophone: the role of the TBR in the frequency domain

We recall that, Equations 3.102 and 3.103, for the threshold frequencies, are valid only for finite values of the TBR. In the case of  $\mathcal{R} \rightarrow 0$ , the threshold values are obtained substituting Equation 3.101 instead of 3.100. In particular, it is interesting to remark that a threshold frequency, beyond which the mechanophone is more efficient than the thermophone, exists even for the limiting case of  $\mathcal{R} = 0$ . Also for this case, we consider both the cases  $b = +1$  and  $b = -1$ . When  $b = +1$  (free surface at  $x = 0$ ), we intersect the curves given by Equation 3.101 and Equation 3.92, obtaining

$$\omega^*(b = +1, \mathcal{R} = 0) = \left[ \frac{2\alpha_0 k_0}{\alpha_1 \rho_1^2 L^3 c_{p1}} \sqrt{B_0 \rho_0} \frac{\sqrt{\rho_1 c_{p1} k_1}}{\sqrt{\rho_0 c_{p0} k_0} + \sqrt{\rho_1 c_{p1} k_1}} \right]^{1/2}. \quad (3.104)$$

On the other hand, when  $b = -1$  (clamped surface at  $x = 0$ ), we intersect the curves given by Equation 3.101 and Equation 3.93, this time yielding

$$\omega^*(b = -1, \mathcal{R} = 0) = \frac{\alpha_0 k_0}{\alpha_1 L^2 \rho_1 c_{p1}} \frac{\sqrt{\rho_1 c_{p1} k_1}}{\sqrt{\rho_0 c_{p0} k_0} + \sqrt{\rho_1 c_{p1} k_1}}. \quad (3.105)$$

These results show that at, even in the most unfavorable conditions, i.e. where TBR is negligible, there still exists a threshold frequency, beyond which the mechanophone mechanism turns out to be predominant over the thermophone. This adds a new piece of information to what already obtained in Section 3.4, in the frame of excitation with a pulsed source. There we found the predominance of the mechanophone only for relatively high values of  $\mathcal{R}$ . The reason we couldn't see the mechanophone predominance for small value of the TBR, can be explained taking into account the intrinsic relationship between the frequency and the time domain. In the time domain, indeed, exciting the system with a light pulse of temporal duration  $\tau_L$ , involves harmonic excitations up to  $\approx \tau_L^{-1}$ . Otherwise stated, in our time resolved simulations, we don't access the pressure at a specifically selected  $\omega$ , but we rather obtain the pressure integrated over all angular frequencies up to  $\approx \tau_L^{-1}$ . In this way, once fixed a very small (eventually null) TBR, even if the mechanophone is predominant beyond a certain threshold frequency, the sum of the thermophone contributions from all the excited frequencies can still be higher than the mechanophone one. For the case addressed in Section 3.4, we discuss a minimum  $\tau_L = 10$  ps (see Figure 40), which implies an excitation frequency bandwidth up to  $\approx 10^{11}$  rad/s. This value is very close to the one found as the frequency threshold for

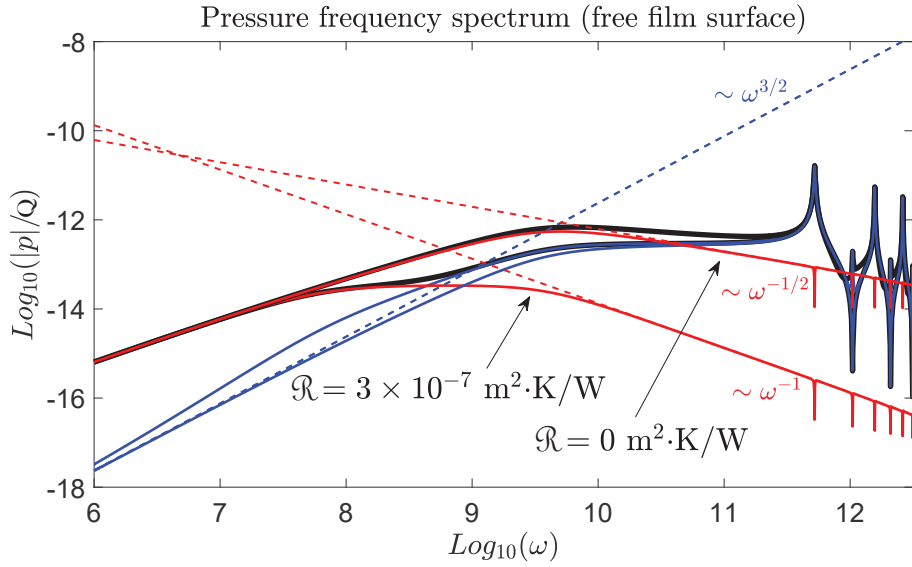


Figure 44. Effect of the TBR on the pressure intensity frequency spectrum with film surface free at  $x = 0$  ( $b = +1$ ). The physical parameters and color codes are the same as for the curves in Figures 42 and 43, except the values of  $\mathcal{R}$ , which are shown in the figure. The approximated high frequency response of the thermophone with  $\mathcal{R} = 0$  is obtained from Equation 3.101. The thermophone response scales as  $\sim 1/\omega$  for  $\mathcal{R} > 0$ , and as  $1/\sqrt{\omega}$  for  $\mathcal{R} = 0$ .

the nanofilm at  $\mathcal{R} = 0$  (see Figure 44). The comparison between the nanofilm and the nanocylinder is not formally correct, but given the similar size of the two nano-objects, it can be used at least as a hint on the physics behind the obtained results. Indeed, if we excite even higher frequencies, by decreasing  $\tau_L$  down to 1 ps, the nanocylinder exhibits the mechanophone predominance at very small  $\mathcal{R}$ <sup>7</sup>. However, a compelling demonstration of the mechanophone prevalence, at  $\mathcal{R} = 0$  and in the time domain, will be provided at the end of this section, when we will discuss photoacoustics of the nanofilm-water system under pulsed excitation (see Figure 48).

A comparison of different TBR values in the thermophone vs mechanophone competition in the frequency domain is reported in Figures 44 and 45, where we show the pressure vs frequency curve (same colors as for Figures 42 and 43) for  $\mathcal{R} = 0$  and  $3 \times 10^{-7} \text{ m}^2\text{K/W}$ . Figures 44 and 45 show results for the free ( $b = +1$ ) and clamped ( $b = -1$ ) surfaces, respectively. In both cases, as the TBR decreases, the thermophone contribution is effective over a broader frequency range, with the threshold frequency, above which the mechanophone prevails, shifting towards higher frequency. From the point of view of applications, therefore, the mechanophone effect at high frequencies is particularly important in systems where the TBR is sufficiently high. In addition, in

<sup>7</sup>We didn't present this data in Section 3.4 because, although the clear mechanophone predominance on the thermophone, the pressure time-evolution for  $\tau_L = 1$  ps was computationally too demanding, leaving the time evolution incomplete and thus preventing us from calculating the energies associated with thermophone and mechanophone.

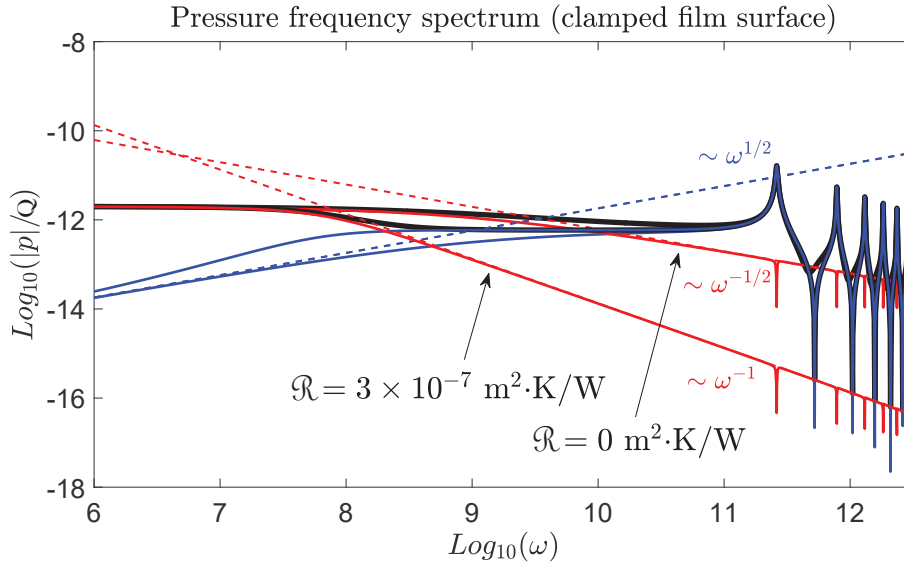


Figure 45. Effect of the TBR on the pressure intensity frequency spectrum with film surface clamped at  $x = 0$  ( $b = -1$ ). The physical parameters and color codes are the same as for the curves in Figures 42 and 43, except the values of  $\mathcal{R}$ , which are shown in the figure. The approximated high frequency response of the thermophone with  $\mathcal{R} = 0$  is obtained from Equation 3.101. The thermophone response scales as  $\sim 1/\omega$  for  $\mathcal{R} > 0$ , and as  $1/\sqrt{\omega}$  for  $\mathcal{R} = 0$ .

Figures 44 and 45, we can appreciate that the degradation in frequency of the efficiency of the thermophone mechanism follows a  $1/\omega$  law when the TBR is sufficiently high, in accordance with Equation 3.100, and instead follows a  $1/\sqrt{\omega}$  law when  $\mathcal{R}$  is exactly zero, as predicted from Equation 3.101. However, despite the higher slope of degradation of the thermophone mechanism in the case of  $\mathcal{R} > 0$ , mechanophone compensation extends the efficiency of the total pressure to a significantly wider frequency range.

### 3.6 Gold nanofilm in water: a time domain-perspective

The frequency sweep analysis, performed in the previous section, is very instructive under a fundamental stand point. It yields plain and rather handy formulas (at least in limiting cases), allowing to inspect how the interplay of the thermal parameters and excitation frequency affects the photoacoustic generation mechanism.

Excitation with a time-harmonic source, covering the frequency range so far explored, is though unrealistic in a true experimental scenario, where the exploited source would rather be a pulsed laser delivering gaussian laser pulses of duration  $\tau_L$ .

The question then arises as whether the handy and insightful frequency-sweep analysis remains a good predictive tool also for the photoacoustic problem triggered by a pulsed laser source. With this aim in mind, we here investigate the same gold film/water systems addressed in Section 3.5.6, but under impulsive excitation.

On an intuitive base, the answer should be somehow positive. As a matter of fact, a pulsed laser excitation may be seen in Fourier space as a sum of time-harmonic sources, covering the frequency range from 0 Hz to  $\sim \tau_L^{-1}$ . The question remains though as to the effect on the water pressure of exciting the system with a single frequency  $\omega$  rather than will all frequencies *up to* the frequency  $\omega$ . Let's therefore proceed illustrating the time-domain perspective.

For the sake of simplicity, we only address the case of a Au film of thickness 20 nm with free boundary condition at  $x = 0$  ( $b = +1$ ). By the way, this system closely resembles the Au nanoplate-on-water sample experimentally addressed in Ref. [231] under pulsed laser excitation.

The opto-thermo-acoustic dynamics of the system follows the same steps as for the gold nanocylinder making the object of Section 3.4: (i) the system is at equilibrium with a uniform temperature  $T_0$ ; (ii) a light pulse strikes the system and delivers energy to the gold nanofilm; (iii) the nanofilm converts the absorbed energy in heat, rising its temperature and exchanging heat with the water region through the TBR; (iv) both the nanofilm and water expand, launching acoustic waves in water via the mechanophone and the thermophone effects. We won't repeat the entire detailed description of these steps, but we rather briefly review them, stressing the difference between the nanofilm and the nanocylinder systems. The first difference, of course, is the reference frame, which, in the present case, is taken in Cartesian coordinates rather than cylindrical, thus changing the form of the thermo-acoustic equations. The thermal dynamics remains described by the general Equations 3.5 and 3.6, which in Cartesian coordinates take the form of Equation 3.33 (last line) for the nanofilm and Equation 3.34 (last line) for water. A second difference is that we assume a temperature-independent water thermal expansion coefficients, adopting the same value used in the analytical treatment. Regarding the acoustic response of the system, also in this case the general Equations 3.9 and 3.10 are valid, but, in Cartesian coordinates, take the form of Equations 3.33 for the nanofilm, and 3.34 for water (first and second lines), respectively. The boundary conditions at the nanofilm/water interface are, for the thermal dynamics, cast in the form of a TBR-like boundary condition (Equation 3.37) together with the continuity of the heat flux (Equation 3.38). For the mechanical response we assume the continuity of stress and velocity (Equations 3.68 and 3.69). The main difference, with respect to the nanocylinder, concerns the optics, although, as will be explained shortly, in the present case, it is more of a speculation, relevant in view of generalization to thicker films. We take the power density delivered to the film in the form<sup>8</sup>

$$Q(x, t) = I(t) \frac{(1 - R)}{\lambda_{pen}} \exp\left(-\frac{L - x}{\lambda_{pen}}\right), \quad (3.106)$$

---

<sup>8</sup>This simplified approach proved valid in similar systems [37]. A more precise estimate can be obtained solving Fresnel equations for the Au film/water domain, the difference being exiguous and not biasing the physics [245].

where  $I(t)$  is the intensity of the light pulse with gaussian temporal dependence and fluence  $\Phi \approx 10 \text{ J/m}^2$  (see Equation 3.1),  $R$  is the optical reflection coefficient and  $\lambda_{pen}$  (m) the optical penetration depth. The last two quantities can be easily calculated assuming light is impinging on the nanofilm free surface ( $x = 0$ ) at normal incidence:

$$R = \frac{(n_1 - n_2)^2 + (\kappa_1 - \kappa_2)^2}{(n_1 + n_2)^2 + (\kappa_1 + \kappa_2)^2} \quad (3.107)$$

$$\lambda_{pen} = \frac{\lambda_p}{4\pi\kappa_2}, \quad (3.108)$$

where  $n_{1,2}$  represents the real part and  $\kappa_{1,2}$  the imaginary part of the complex refraction index in air (index 1) and gold (index 2). Setting the light pulse wavelength  $\lambda_p = 550 \text{ nm}$ , we use for air  $n_1 = 1$  and  $\kappa_1 = 0$ , while for gold  $n_2 = 0.39$  and  $\kappa_2 = 2.48$  [246].  $Q(x, t)$  is spatially non-homogeneous, at variance with the source term adopted in the frequency-domain analysis (Equation 3.24). That said,  $\lambda_{pen}$  is only slightly inferior to  $L$ , resulting in a weak spatial inhomogeneity of  $Q(x, t)$ . Furthermore, given the exiguous film thickness, also ballistic electrons contribute homogenizing  $Q(x, t)$  on a timescale shorter than the mechanical and thermal dynamic timescales. In summary, for the present purposes,  $Q(x, t)$  could be here assumed substantially-spatially homogeneous, as was the case for the gold NC and for the same reasons. Nevertheless, in the present context we opted to introduce a realistic laser absorption profile for the sake of future generalization. As a matter of fact, when analyzing films of sufficient thicknesses, the above-mentioned mechanisms either do not hold anymore or do not suffice to spatially smooth out  $Q(x, t)$  on the relevant timescale.

The set of equations were then solved numerically via FEM.

### From the frequency to the time domain

We now discuss simulation results for the impulsive excitation scheme. First of all, we need to identify the values of  $\tau_L$  to be adopted for a meaningful comparison with the frequency-domain study. With reference to Figure 42, for  $\mathcal{R} = 3 \times 10^{-8} \text{ m}^2\text{K/W}$ , the frequency domain is suitably partitioned in four spectral regions: (1) low frequency range ( $\omega \leq 10^8 \text{ rad/s}$ ), where the thermophone contribution prevails; (2) close to the threshold frequency range ( $\omega \approx 3 \times 10^9 \text{ rad/s}$ ), where the thermophone and mechanophone contribute similarly; (3) high frequency range ( $\omega \approx 3 \times 10^{10} \text{ rad/s}$ ), where the mechanophone is predominant; and (4) very high frequency range ( $\omega \geq 5 \times 10^{11} \text{ rad/s}$ ), where the mechanophone is predominant and the nanofilm oscillations are activated. To access these spectral regions, we need to excite the system with a light pulse of duration  $\tau_L \approx 1/\omega$ , with  $\omega = \{10^8, 3 \times 10^9, 3 \times 10^{10}, 5 \times 10^{11}\} \text{ rad/s}$ . This approximately corresponds to  $\tau_L = 10 \text{ ns}$ ,  $500 \text{ ps}$ ,  $50 \text{ ps}$  and  $1 \text{ ps}$ . We underline that the laser pulse potentially excites all frequencies up to  $1/\tau_L$ , that is within its bandwidth (BW).

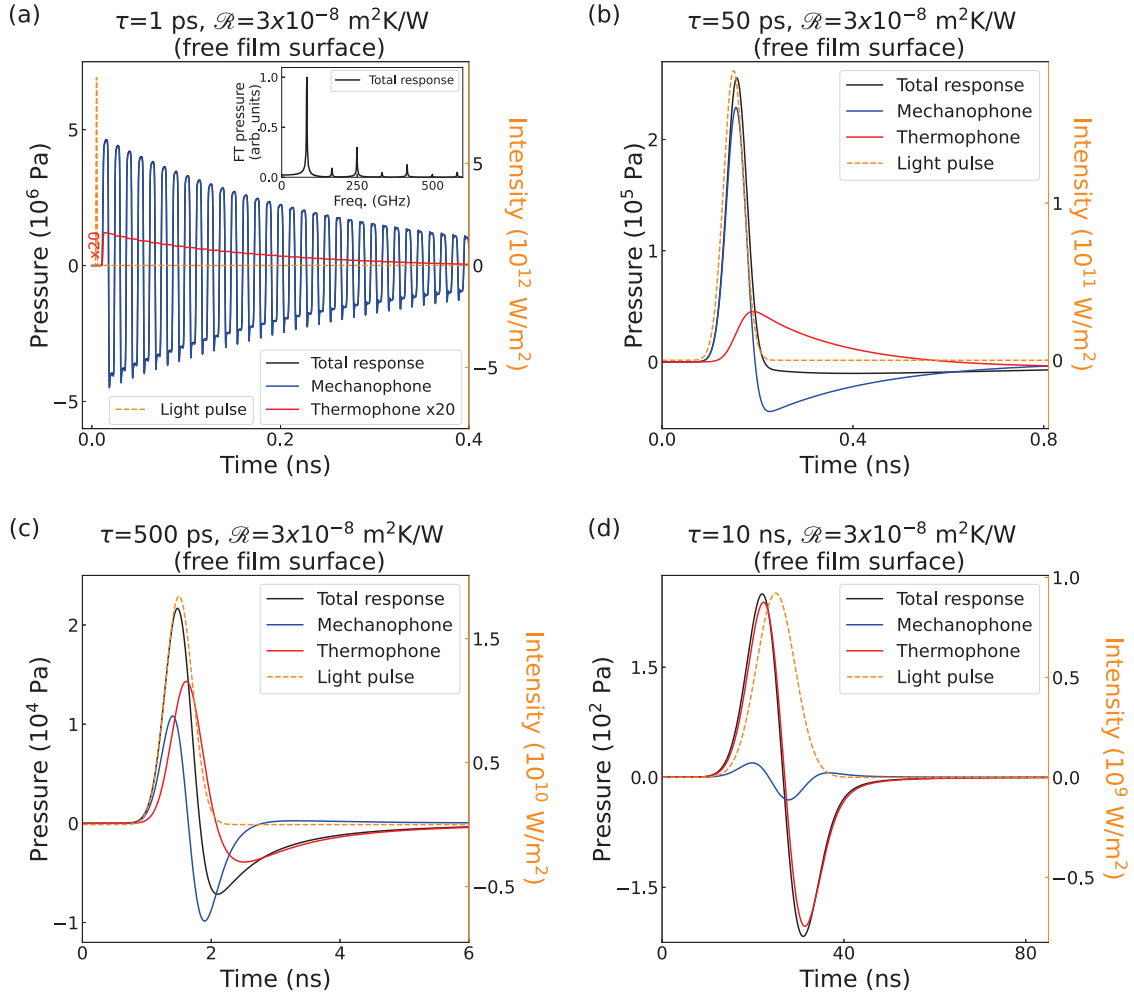


Figure 46. Case of a film with a free surface at  $x = 0$ ;  $\mathcal{R} = 3 \times 10^{-8} \text{ m}^2\text{K/W}$  and different light pulse durations:  $\tau_L = 1 \text{ ps}$  (panel a),  $50 \text{ ps}$  (panel b),  $500 \text{ ps}$  (panel c),  $10 \text{ ns}$  (panel d). Left-axis: time evolution of the pressure in water at  $10 \text{ nm}$  from the nanofilm/water interface: total pressure (black curves), thermophone pressure contribution (red curves) and mechanophone pressure contribution (blue curves). The thermophone is multiplied by a factor 20 in panel a for sake of visualization. Inset of panel a: modulus of FT of the total pressure. Right-axis: light pulse intensity (orange dashed line) as a function of time. The time and pressure scale differs in each panel.

Figure 46 shows the time evolution of the pressure in water ( $10 \text{ nm}$  from the interface) for  $\mathcal{R} = 3 \times 10^{-8} \text{ m}^2\text{K/W}$  and for the above mentioned  $\tau_L$  values. The total pressure (black curves) is reported together with the thermophone (red curves) and the mechanophone (blue curves) contributions. Panel a corresponds to  $\tau_L = 1 \text{ ps}$ , which BW includes all frequencies up to the “very high frequency” range. The mechanophone effect outperforms the thermophone. Moreover, such a short light pulse triggers oscillations of the nanofilm, thus resulting in water pressure oscillations, as appreciated from the inset of panel a, where the magnitude of the FT of the total pressure is reported. We note that, because of the spatial non-homogeneity of  $Q(x, t)$ , the symmetry considerations that prevented exciting the even  $n$  eigenmodes of the film, when adopting a spatial homogeneous  $Q(t)$  (see section

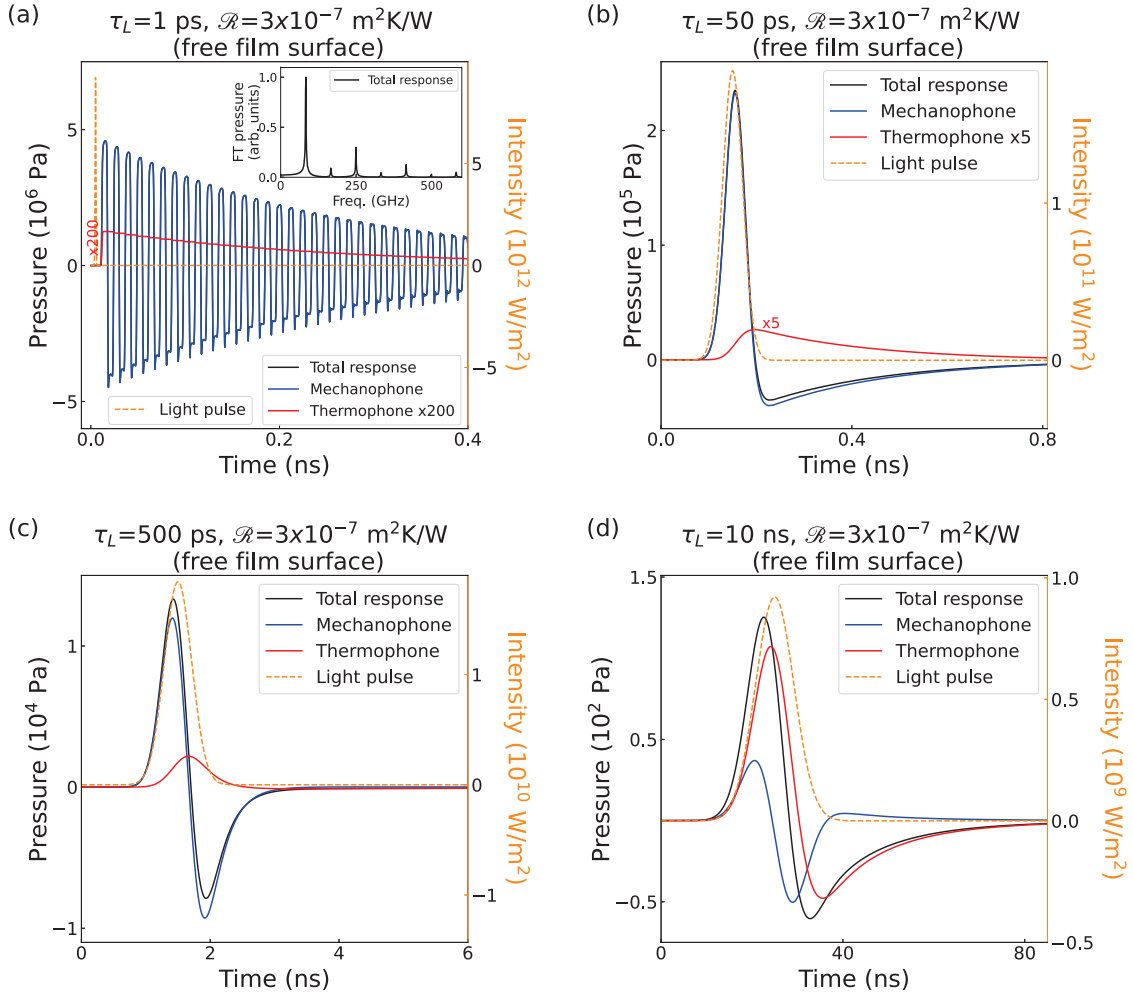


Figure 47. Case of a film with a free surface at  $x = 0$ ;  $\mathcal{R} = 3 \times 10^{-7} \text{ m}^2\text{K/W}$  and different light pulse durations:  $\tau_L = 1 \text{ ps}$  (panel a),  $50 \text{ ps}$  (panel b),  $500 \text{ ps}$  (panel c),  $10 \text{ ns}$  (panel d). Left-axis: time evolution of the pressure in water at 10 nm from the nanofilm/water interface: total pressure (black curves), thermophone pressure contribution (red curves) and mechanophone pressure contribution (blue curves). The thermophone is multiplied by a factor 200 in panel a for sake of visualization. Inset of panel a: modulus of FT of the total pressure. Right-axis: light pulse intensity (orange dashed line) as a function of time. The time and pressure scale differs in each panel.

3.5.6), no longer hold. As a matter of fact, the FT in the inset shows resonances also at frequencies corresponding to even  $n$  eigenmodes. Nevertheless, because of the weak non-homogeneity of  $Q(x, t)$ , these latter peaks are lower than the ones corresponding to odd  $n$  eigenvalues. Moving to  $\tau_L = 50 \text{ ps}$ , which BW includes all frequencies up to the “high frequency” range (Figure 46, panel b), the main contribution is provided by the mechanophone effect. The situation changes in panel c, where  $\tau_L = 500 \text{ ps}$  implies a BW reaching up to the threshold frequency ( $\omega \approx 3 \times 10^9 \text{ rad/s}$ , see Figure 42). In this case, the thermophone and the mechanophone have very similar amplitudes, the total pressure being generated from both mechanisms. Finally, the thermophone prevails over the mechanophone for  $\tau_L = 10 \text{ ns}$  (panel d), where the light pulse BW overlaps only the

“low frequency” region. Here the thermophone effect dominates.

Summarizing, for the case of  $\mathcal{R} = 3 \times 10^{-8} \text{ m}^2\text{K/W}$ , the salient features match the

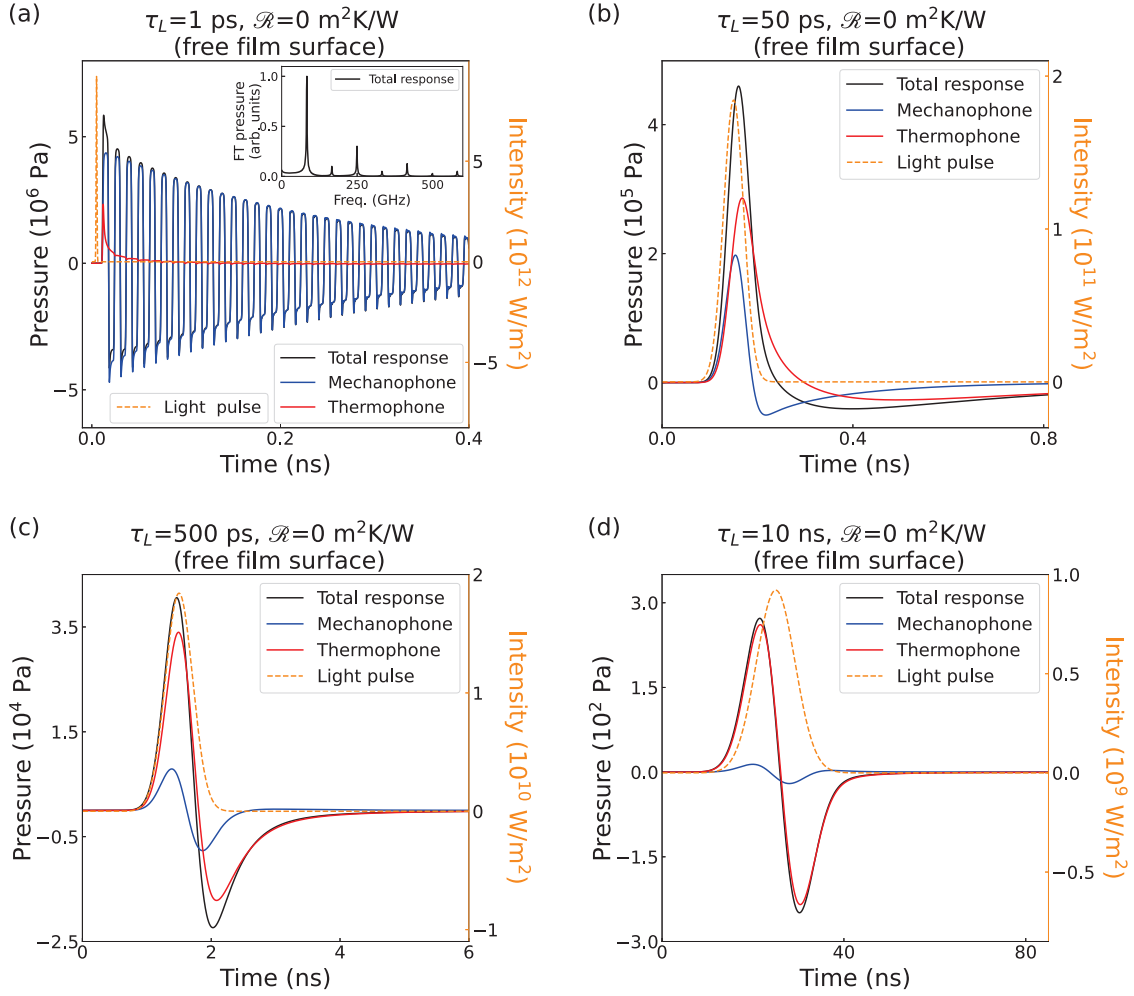


Figure 48. Case of a film with a free surface at  $x = 0$ ;  $\mathcal{R} = 0 \text{ m}^2\text{K/W}$  and different light pulse durations:  $\tau_L = 1 \text{ ps}$  (panel a),  $50 \text{ ps}$  (panel b),  $500 \text{ ps}$  (panel c),  $10 \text{ ns}$  (panel d). Left-axis: time evolution of the pressure in water at  $10 \text{ nm}$  from the nanofilm/water interface: total pressure (black curves), thermophone pressure contribution (red curves) and mechanophone pressure contribution (blue curves). Inset of panel a: modulus of FT of the total pressure. Right-axis: light pulse intensity (orange dashed line) as a function of time. The time and pressure scale differs in each panel.

predictions of the frequency-sweep analysis.

We now explore the role of the TBR in the frame of the pulsed excitation scheme. For  $\mathcal{R} = 3 \times 10^{-7} \text{ m}^2\text{K/W}$ , reported in Figure 47 (same color code as Figure 46), the frequency threshold is shifted towards smaller values (see panel c), where the mechanophone contribution exceeds by far the thermophone one. This is at variance to what happens for  $\mathcal{R} = 3 \times 10^{-8} \text{ m}^2\text{K/W}$  (Figure 46, panel c), where, for the same  $\tau_L = 500 \text{ ps}$ , the thermophone and mechanophone contributions are comparable. The fact that the mechanophone prevails at high TBR is appreciated also for  $\tau_L = 1 \text{ ps}$  (Figure 47, panel a) and  $\tau_L = 50 \text{ ps}$  (panel b). For sake of visualization we had to multiply the thermophone contribution by

a factors of 200 and 5 respectively. For  $\tau_L = 10$  ns, corresponding to the low frequency region, the thermophone contribution exceeds the mechanophone one, but to a lesser extent than for the  $\mathcal{R} = 3 \times 10^{-8}$  m<sup>2</sup>K/W case (Figure 46, panel d).

Finally, the case for a vanishing TBR,  $\mathcal{R} = 0$ , is reported in Figure 48 (same color code as Figure 46). The  $\tau_L = 50$  ps case (panel b) demonstrates the threshold frequency shift towards higher values for a vanishing TBR. Indeed, the thermophone contribution is higher than the mechanophone one, at variance with the finite TBR cases discussed in the previous figures, where the major contribution was provided by the mechanophone. The dominance of the thermophone is, of course, even more remarkable for  $\tau_L = 500$  ps (panel c) and  $\tau_L = 10$  ns (panel d). Nevertheless, the  $\tau_L = 1$  ps case (panel a) shows a prevailing mechanophone contribution. This result, qualitatively anticipated during the discussion of Equation 3.104, proofs that, also for the case of an impulsive excitation, there exist a frequency threshold beyond which the mechanophone rules even in the most disadvantageous scenario for the mechanophone, i.e. vanishing TBR.

### 3.7 Conclusions on the gold nanofilm in water

In this section, we addressed the photoacoustics of a solid nanofilm with a surface in contact with water. This system was chosen because it allows, at least in the frequency domain, an analytical solution in relatively simple terms (exponential rather than Bessel's functions, as in the case of the a cylindrical system). We developed a fully analytical model in the frequency domain, describing the acoustic response in the liquid upon excitation with a spatially homogeneous, sinusoidally time varying heating source for the nanofilm. We examined both the cases of stress-free and zero-displacement boundary conditions for the nanofilm surface not in contact with the fluid. We were able to extract in explicit analytical form the pressure in the liquid both for the thermophone and the mechanophone effects. The thermophone efficiency decreases with frequency, whereas the mechanophone has the opposite behaviour, becoming important at high frequency. Approximating the exact solutions, it was possible to extract simple equations for the thermophone at low frequency and the mechanophone at high frequency. Intersecting the respective curves, we found the expression for the threshold frequency, i.e. the frequency above which the mechanophone becomes the predominant mechanism.

Subsequently, we analyzed the role of the TBR in the thermophone vs mechanophone competition in the frequency domain. We proved analytically that the threshold frequency decreases as the TBR increases. In fact, the efficiency of the thermophone decreases with increasing TBR. Moreover, even in the case of vanishing TBR, we showed that it exists a threshold frequency beyond which the mechanophone is still the predominant mechanism. Finally, we addressed the same problem but assuming an impulsive heating source. This description is closer to the experimental situations that might be encountered [231]. It

is in fact not feasible to sinusoidally modulating an otherwise continuous source up to modulations frequencies of  $\sim 100$  GHz, which would be the scenario accounted by the frequency sweep analysis.

We selected four different durations of the excitation light pulse, so as to compare the pressures with the ones obtained in different spectral regions with the frequency sweep analysis. Moreover, the role of the TBR was also considered. We proved the down shifting of the threshold frequency when increasing the TBR value. The mechanophone may then become the dominant mechanism even for relatively long laser pulses. Also the vanishing TBR case was taken into account. In this case, we showed that the thermophone is enhanced, being the dominant mechanisms also for shorter light pulses (large BW). Nevertheless, for a light impulse of duration 1 ps, the mechanophone effect dominates even for a vanishing TBR. This results extends what found in Section 3.4, where the mechanophone was the predominant mechanism only at relatively large TBR values.

In the next chapter, we will consider the photoacoustic effect generated in two realistic and rather involved systems: a single-wall carbon nanotube (SWCNT) and a multi-walls carbon nanotube (MWCNT) immersed in water. We will inspect the thermophone vs mechanophone competition for a realistic value of the TBR —retrieved by atomistic simulations— and different nano-object size/light pulse combinations. We will then focus on the activation of few nanometers wavelength sound waves in water, matching the acoustic frequencies of the oscillating nano-object.

## 4. Photoacoustic effect: carbon nanotubes in water

This chapter presents the investigation of the photoacoustic effect triggered by short laser pulses on carbon nanotubes immersed in water, which was published under the title *Ultrafast nano generation of acoustic waves in water via a single carbon nanotube*, *Photoacoustics* **28**, 100407 (2022), of which I am first author.

My contribution consisted in contextualizing the problem and developing the model in the frame of continuum mechanics. I performed the numerical simulations, extracting the thermal boundary resistance from thermal data and the relevant physics of the thermo-mechanical dynamics. This was also the first article I redacted in first person.

Molecular dynamics simulations, necessary for the extraction of the thermal boundary resistance between the nanotube and water, were carried out by colleagues at Politecnico di Torino, Italy. The analytical model of the elastic constants of the single wall carbon nanotube was carried out in collaboration with Prof. Stefano Roddaro at Istituto Nanoscienze and Scuola Normale Superiore in Pisa, Italy.

### 4.1 Introduction

In this chapter we will investigate photoacoustic generation of pressure waves in water for the case of a single water immersed Carbon nanotube (CNT). We will account for the effect of the system size and light pulse duration, demonstrating that, upon a suitable combination of these two parameters, the CNT can act as a thermophone or a mechanophone, as pictured in Figure 49.

Our study will focus on two paradigmatic sizes, a single wall (SW) and a multi wall (MW) CNT, and two pulse durations, 5 ns and 1 ps. Light pulses of ps duration, not only enhance the mechanophone effect, perhaps as the leading launching mechanism, but can also excite CNT vibrational modes, provided a certain minimum size of the CNT. Activation of these vibrational modes launches few nanometers wavelength pressure waves in water, a desirable feature for a variety of applications. Guided by these considerations, we will inspect the spatio-temporal profile of the pressure wave in water for the four parameters combination.

In respect to the systems studied in Chapter 3, the CNT presents a higher complexity. The purpose of Chapter 3 was to clarify the physics of the thermophone vs mechanophone competition, therefore adopting simplest context possible. The water immersed CNT, instead, represents a highly complicated system, exhibiting high anisotropy [247, 248], thermal and mechanical properties dependency on the number of walls [249, 250]. Furthermore

the literature lacks of a definitive and consistent description of the CNT elastic properties [248, 250, 251].

To address the CNT immersed in water system, we adopt a multi-physics, multi-scale approach, a strategy that has been shown very effective in addressing ultrafast opto-thermal [252, 208] and opto-acoustic [253, 254] transients in nano to mesoscale systems. Possible water infiltration in the CNTs and the TBR at the CNT/water interface are obtained from atomistic simulations [255, 256]. The impulsive opto-thermo-mechanical dynamics is then cast in the frame of a continuum model, but upon insertion of the geometrical and thermal microscopic parameters, and finally solved via Finite Element Methods (FEM).

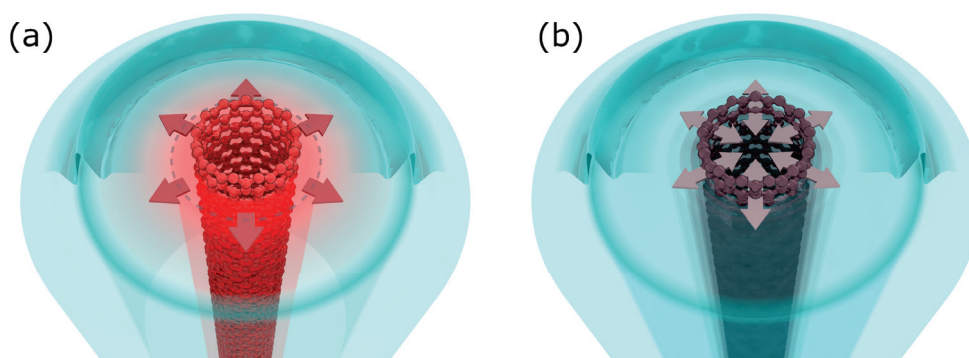


Figure 49. Thermophone (panel a) and mechanophone (panel b) effects. The acoustic wave in water is generated in the thermophone case (panel a) from the thermal expansion of water, the CNT acting as a nanoheater; in the mechanophone case (panel b) from the thermal expansion of the CNT, the latter acting as a nanopiston. Image taken from [5].

## 4.2 Theoretical model

The theoretical frame, conceived to address the transient photothermal-acoustic response of water-immersed individual CNTs triggered by an ultrafast laser pulse, is inherently multi-physics. Similarly to the gold nanosystems, it involves optics (absorption of the laser pulse by the system), thermics and acoustics. The difference is that here the macro-physics approach, based on continuum equations, relies on insertion of the TBR at the CNT/water interface retrieved from dedicated Molecular dynamics (MD) simulations.

The following assumptions apply: (i) cylindrical symmetry: the CNT height/diameter ratio is large enough to neglect border effects close to the top/bottom of the CNT; (ii) materials thermal and mechanical parameters are temperature independent, the variations being exiguous: their values are taken as the average over the temperature span resulting from simulations; (iii) linear elasticity: the resulting displacement and pressure fields are small enough to justify this assumption; (iv) negligible thermo-acoustic feedback: the thermal dynamics affects the mechanical one, but the opposite effect is negligible (v); the thermal and mechanical parameters are frequency independent; (vi) non viscous water is

assumed: intrinsic dissipation in water is hence not present. This last assumption is an idealization at high frequencies, nevertheless (a) it allows to understand the physics behind the generation mechanism; (b) it provides results based on solid basis, the dissipation mechanism in water in the hypersonic frequency range being yet a debated issue.

### 4.2.1 CNT modelling

Two paradigmatic cases are addressed in this work: the case of a single, water-immersed, (5,5)<sup>1</sup> SWCNT and that of a MWCNT composed of  $N = 24$  walls. To use continuum equations, however, we need to convert the CNTs from an atomistic view to a continuum model. The time and lengths scales involved in the photoacoustic dynamics are too extended to be addressed in the frame of atomistic simulations, thus requiring a continuum approach. To this end, the atomistic view of a CNT has to be replaced by a continuum one.

**Continuum framework.** It is well known that CNTs are composed of one or multiple concentric walls made by rolling up graphite sheets. When modelling a CNT in a continuum framework, two main strategies are possible: considering the walls as distant thin layers of 0.066 nm thickness [257] interacting by van der Waals force [258], or considering the walls as layers of thickness  $h$  corresponding to the interlayer distance between graphite's sheets ( $h = 0.34$  nm) [248, 259].

In this work we followed the second strategy, by considering the CNT walls as adjoining hollow cylinders of thickness  $h$ , where the  $i$ -th wall has a central  $i$ -th radius given by  $R_i = R_1 + (i - 1) \times 0.34$  nm (where  $R_1$  is the radius of the first wall and  $i = 1, \dots, N$ ), see Figure 50. In this way the entire  $N$ -walls-CNT results in a continuous hollow cylinder with internal radius  $R_{int} = R_1 - h/2$  and external radius  $R_{ext} = R_N + h/2$ .

In our case, since the nominal central radius for a (5,5) SWNCT is 0.34 nm, its internal and external radii are given by  $0.34$  nm  $\pm h/2$ , i.e.  $R_{int}^{sw}=0.17$  nm,  $R_{ext}^{sw} = 0.51$  nm. In parallel, we take  $R_{int}^{mw}=7.3$  nm and  $R_{ext}^{mw} = 15.5$  nm for the MWCNT with 24 walls. Along the axial direction,  $z$ , both CNTs are assumed infinitely extended.

**Water infiltration.** Another issue, that has to be considered when describing the CNTs, is the eventual presence of water within their internal volume. MD simulations show that water does not infiltrate the (5,5) SWCNT, so we will consider it empty. However, repeating the simulations for a larger system, (10,10) SWCNT, spontaneous water infiltration is observed, the internal diameter of the CNT being extremely important for the infiltration phenomena. This is seen in Figure 51, reporting two frames of the MD simulations, for the (5,5) SWCNT (panel a) and the (10,10) SWCNT (panel b), both water

<sup>1</sup>(5,5) determines the chirality of the SWCNT and fixes its size.

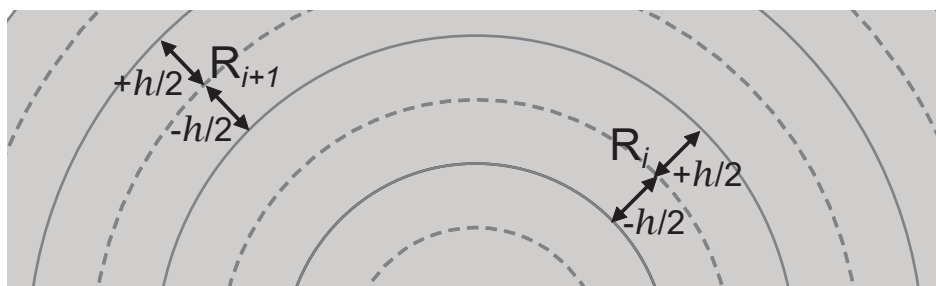


Figure 50. Scheme for the CNT walls. The  $(i + 1)$ -th wall has a central  $(i + 1)$ -th radius given by  $R_{i+1} = R_i + h$  nm and a thickness  $\pm h/2$ .

immersed. In this picture, grey spheres represents C atoms, red ones Oxygen (O) atoms and white ones Hydrogen (H) atoms.

MD simulations were not performed on the MWCNT (due to the prohibitive computational burden). However, regarding the MWCNT investigated in this thesis work, its internal diameter exceeds by far that of a (10,10) SWCNT; thus, water infiltration is expected. For these reasons, the (5,5) SWCNT simulated in the continuum model is considered hydrophobic, while the MWCNT is water infiltrated. Further supporting this scenario is the fact that water entrance in MWCNT of similar dimensions has been observed by several techniques such as neutron [260] and X-ray scattering [261].

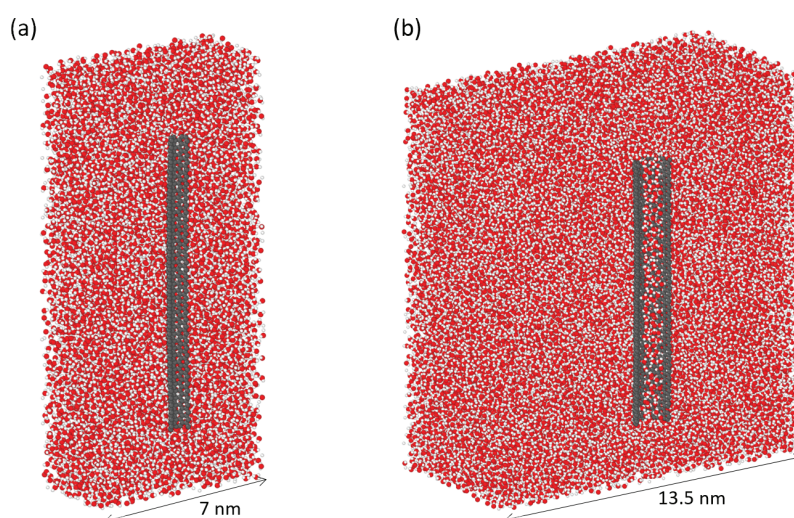


Figure 51. MD images of (5,5) SWCNT (panel a) and (10,10) SWCNT (panel b) immersed in water. Grey sphere represents C atoms, red ones O atoms and white ones H atoms. Note the presence of water inside the CNT only in the (10,10) SWCNT (panel b).

Summarising, the external water is modeled as a coaxial cylindrical shell domain of external radius  $R_{wt}$  much greater the CNT external radius. A cross-sectional view of the two modelled continuum CNTs in water is reported in Figure 52. Materials properties of CNTs and water, such as thermal conductivity  $k$  (W/mK), heat capacity  $c_p$  (J/kgK), density  $\rho$  (kg/m<sup>3</sup>), elastic coefficients and thermal expansion coefficients  $\alpha$  (1/K) are summarized in Table 6 and will be discussed as they appear in the following sections.

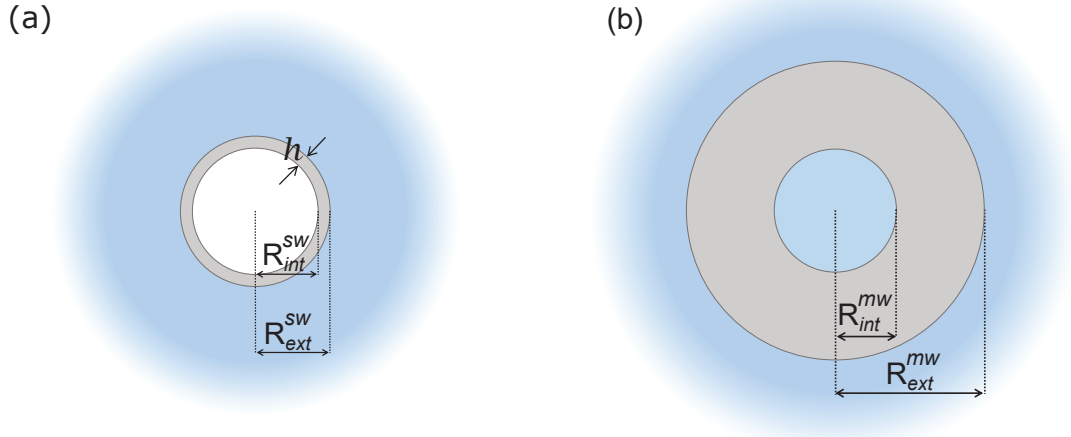


Figure 52. Cross-sectional view at constant  $z$  of the continuum model for the water-immersed SWCNT (panel a):  $R_{int}^{sw}=0.17$  nm and  $R_{ext}^{sw} = 0.51$  nm; MWCNT (panel b):  $R_{int}^{mw}=7.3$  nm and  $R_{ext}^{mw} = 15.5$  nm. The MWCNT is water filled, at variance with the SWCNT. The figures are not to scale. Image adapted from [5].

Table 6. Materials properties used in the continuum model.

Material property	SWCNT	MWCNT	Water
Radial thermal conductivity (W/(m K))	6 (see text)	6	0.6
Heat capacity (J/(kg K))	650	650	$4.2 \times 10^3$
Density (kg/m <sup>3</sup> )	$2.3 \times 10^3$	$2.3 \times 10^3$	$1 \times 10^3$
First Lamé coefficient (GPa)	/	/	2.25
Second Lamé coefficient (GPa)	/	/	0
Young modulus (GPa)	$1 \times 10^3$	30	/
Poisson ratio	0.15	0.28	/
Linear thermal expansion coefficient (K <sup>-1</sup> )	$3 \times 10^{-7}$	$2.5 \times 10^{-5}$	$7 \times 10^{-5}$
Internal radius (nm)	0.17	7.3	/
External radius (nm)	0.51	15.5	/
Number of walls	1	24	/

## 4.2.2 Optics

The photoacoustic dynamics is triggered by a light pulse impinging on the CNT-water system. We assume the light intensity to be spatially homogeneous and gaussian in time:

$$I(t) = 2\sqrt{\frac{\ln(2)}{\pi}} \frac{\Phi}{\tau_L} \exp\left(-4 \ln(2) \frac{(t-t_0)^2}{\tau_L^2}\right), \quad (4.1)$$

where  $I(t)$  is in W/m<sup>2</sup>,  $\tau_L$  is the pulse temporal full width half maximum (fwhm),  $t_0$  the time at which the pulse intensity is at its maximum (in this chapter we take  $t_0 = 0$ ) and  $\Phi$  is the light fluence (J/m<sup>2</sup>). All simulations have  $\Phi=5$  J/m<sup>2</sup>, which means that the total energy carried by the light pulse remains constant, independently on the pulse temporal width  $\tau_L$ .

The laser wavelength is chosen in the visible range and in the water transparency window, 400-700 nm, which corresponds to the therapeutic spectral window in theranostic applications. In this way the water temperature rise is only due to the heat dissipated from the CNT.

The power density  $Q_{cnt}$  (W/m<sup>3</sup>), absorbed by the CNT, reads:

$$Q_{cnt}(t) = \frac{\sigma_{cnt}^{abs} I(t)}{V_{cnt}}, \quad (4.2)$$

where  $V_{cnt}$  (m<sup>3</sup>) and  $\sigma_{cnt}^{abs}$  (m<sup>2</sup>) represent the CNT volume and absorption cross section, respectively.  $I(t)$ , and consequently  $Q_{cnt}(t)$ , are assumed spatially uniform, even if in a real experiment the laser pulse impinges on the CNT from one side (assuming the pulse propagating with normal incidence to the  $z$ -axis). However, the high thermal conductivity within the CNT walls, and the small CNT radial dimension and absorption cross-section, imply a spatially uniform  $Q_{cnt}(t)$  on a short timescale, inferior to the characteristic times involved in heat propagation to water and the mechanical response of the system.

Regarding the cross section, the quantity  $\sigma_{cnt}^{abs}$  is calculated summing the contributions of every C-atoms in the CNT, assuming all of them possess an equal absorption cross section,  $\sigma_C^{abs} = 6 \times 10^{-22}$  m<sup>2</sup>, independently of the wall to which they belong. The latter is a mean value, corresponding to the cross section for individual C atoms in a flat graphene sheet [262, 263]. Specifically, let us estimate  $\sigma_{cnt}^{abs}$  for a generic SWCNT (in our model, from a purely optical perspective, a MWCNT is just the sum of many co-axial SWCNTs with different radius). The structure of the wall is the result of rolling up a graphene sheet with a honeycomb lattice in which the C-C atoms distance is  $s = 1.42$  Å. The area of each hexagon in the lattice is  $A_{hex} = 3\sqrt{3}s^2/2$  and it contains two C atoms (more precisely 1/3 of a C atom at each of the 6 corners). This means that the absorption cross section of one hexagon is  $2\sigma_C^{abs}$ . Thus, instead of counting the C-atoms in the sheet, we can count the number of hexagons. If we consider a SWCNT of diameter  $d$  and length  $H$ , its area will be  $A_{swcnt} = \pi dH$  and the number of hexagons in the SWCNT will read  $A_{swcnt}/A_{hex}$ . We are finally ready to calculate the absorption cross section:

$$\sigma_{swcnt}^{abs} = \frac{A_{swcnt}}{A_{hex}} 2\sigma_C^{abs} \quad (4.3)$$

$$= \frac{\pi dH}{3\sqrt{3}s^2/2} 2\sigma_C^{abs} \quad (4.4)$$

$$= \frac{\pi dH}{3\sqrt{3}s^2/2} 2 \times 6 \times 10^{-22} \quad (4.5)$$

$$= 2.3 \times 10^{-22} \pi dH. \quad (4.6)$$

For a MWCNT, then, we just need to sum  $\sigma_{swcnt}^{abs}$  over the number of walls  $N$ , choosing the correct  $d_i$  accordingly to the  $i$ -th wall we are taking into account:

$$\sigma_{mwcnt}^{abs} = \sum_{i=1}^N \sigma_{swcnt}^{abs}(d_i) = \sum_{i=1}^N 2.3 \times 10^{-2} \pi d_i H. \quad (4.7)$$

Note that both  $\sigma_{cnt}^{abs}$  and  $V_{cnt}$  are proportional to the CNT length  $H$ ,  $Q_{cnt}(t)$  is then independent on length.

Recapitulating and explicating the volume of the CNT, we finally obtain the absorbed power density throughout the system as

$$Q(t) = \begin{cases} Q_{cnt}(t) = \sum_{i=1}^N 2.3 \times 10^{-2} d_i \frac{4I(t)}{(d_N^2 - d_1^2)}, & \text{in the CNT} \\ 0 & \text{in water.} \end{cases} \quad (4.8)$$

### 4.2.3 Thermal dynamics

The thermal dynamics of the system, initiated by the absorbed power density,  $Q(t)$ , is addressed via Fourier's law and the continuity equation in cylindrical coordinates, exactly as in the case of the gold nanocylinder (see Equations 3.5 and 3.6, Chapter 3). The only difference between the two systems is the presence of three domains (water/CNT/water for the MWCNT and vacuum/CNT/water for the SWCNT) instead of two (gold/water). We report directly the radial component (being the only non null one):

$$q_r = -k \frac{\partial T}{\partial r} \quad (4.9)$$

$$\rho c_p \frac{\partial T}{\partial t} = -\frac{1}{r} q_r - \frac{\partial q_r}{\partial r} + Q(t), \quad (4.10)$$

where  $T$  is the temperature (K),  $q_r$  the radial heat flux (W/m<sup>2</sup>) and the material parameters  $k$ ,  $\rho$  and  $c_p$  are the radial thermal conductivity (W/(mK)), mass density (kg/m<sup>3</sup>) and specific heat (J/(kgK)) of the CNT and water in their respective domains.

We assume that the radial thermal conductivity of the MWCNT closely matches the out-of-plane thermal conductivity of graphite [264], whose value is 6 W/(mK). Regarding the SWCNT, the concept of radial thermal conductivity does not apply, since it is made of a single carbon layer. However, modeling the SWCNT as a cylindrical shell of finite thickness  $h$  requires the introduction of an artificial radial thermal conductivity, in order for Equation 4.9 to be meaningful. The  $k$  value should then be taken high enough to avoid any temperature gradient across the CNT thickness on the timescales of interest. Given the small value of  $h$ , this is achieved even adopting the same  $k$  value of the MWCNT. We actually tested values ranging from 6 W/(mK) up to 6 orders of magnitude larger with

no appreciable differences in the simulations results. For the CNT specific heat of both SWCNT and MWCNT, we consider 650 J/(kgK) as for graphite [265, 266]. The values of the adopted materials parameters are summarized in Table 6.

The heat flux at the CNT/water interface, i.e. for  $r=R$ , is regulated via the usual equations describing the continuity of the heat flux and accounting for the TBR:

$$q_r(R^-) = q_r(R^+) = q_r(R) \quad (4.11)$$

$$q_r(R) = \frac{1}{\mathcal{R}}(T(R^-) - T(R^+)), \quad (4.12)$$

where  $R^-$  and  $R^+$  refer to the inner and outer side of the interface respectively, and  $\mathcal{R}$  is the value of the TBR (which will be discussed later). For the case of the SWCNT,  $R=R_{ext}^{sw}$ , with the only CNT/water interface being at the SWCNT external radius; a thermal insulating boundary condition,  $q_r=0$ , is taken at the internal CNT/vacuum boundary  $r=R_{int}^{sw}$ , see Figure 52 (panel a). For the case of the MWCNT, instead,  $R=R_{int}^{mw}$  at the internal, and  $R=R_{ext}^{mw}$  at the external CNT/water interface, respectively, see Figure 52 (panel b). For both cases, a thermal insulating boundary condition is enforced at the water domain outer boundary,  $q_r(R_{wt}) = 0$ . However,  $R_{wt}$  is taken large enough to avoid any non-physical heat accumulation at the boundary of the system during the simulations timescale. Before the laser pulse strikes, the system is at the ambient temperature  $T_0=293$  K.

**TBR retrieval.** The value of  $\mathcal{R}$  was retrieved from dedicated approach to Equilibrium Molecular Dynamics (EMD) simulations for the SWCNT. First, we obtain, from MD simulations, the temperature time evolution for the water-immersed SWCNT,  $T_{cnt}^{md}(t)$ , whose initial temperature is set at 360 K, while in the surrounding water  $T = 290$  K. We then fit  $T_{cnt}^{md}(t)$  with the numerical solution of the continuum model described in this section,  $T(r, t; \mathcal{R})$ , calculated for a coordinate  $r$  inside the SWCNT wall and with  $\mathcal{R}$  set as the fitting parameter.

Molecular dynamics simulations are implemented using the LAMMPS package [267] while the initial set-up is created with the software Moltemplate [268] and VMD [269]. A Verlet integration scheme is used to integrate the equation of motions every fs for all simulations. Long-range electrostatic interactions are simulated with a particle-particle particle-mesh solver (PPPM) [270]. Carbon-carbon interactions are simulated by means of the reactive Tersoff force-field [271, 272]. Water molecules interactions are simulated with the extended version of the single point charge (SPC/E) force-field [273]. The rigid model for water bonds and angle is implemented in LAMMPS via the SHAKE algorithm [274]. Carbon-oxygen interactions are simulated with a 12-6 Lennard-Jones potential with a cut-off radius of 1 nm. Lennard-Jones parameters are taken with respect to the experimental contact angle of water and graphite, namely  $86^\circ$  [275].

A 10 nm long (5,5) SWCNT is placed in a 8.14 nm x 8.14 nm x 10.4 nm simulation box, with water molecules outside the cylindrical CNT cavity. The system is first brought to

equilibrium by means of an energy minimization with conjugate gradient method; it is then simulated at 290 K and 1 bar in a NPT ensemble with a Nose-Hoover thermostat and barostat for 1 ns. Subsequently, another equilibration is performed in NVT with a Nose-Hoover thermostat at 290 K. The temperature of the CNT only is then set at 360 K, while water is kept at 290 K for 200 ps with two different Nose-Hoover thermostats. Finally, in a NVE ensemble, the temperature of the carbon nanotube (which is now let free to evolve),  $T_{cnt}^{md}(t)$ , and throughout water are monitored for 500 ps, which corresponds to the time needed to reach thermal equilibrium in the simulation domain.

Finally, we fit  $T_{cnt}^{md}(t)$  with the numerical solution of the continuum thermal model, obtaining  $\mathcal{R}=3.5 \times 10^{-7} \text{ m}^2\text{K/W}$ . This value is also used in our model for the TBR value at the interface between MWCNT and water. Only a small difference in the  $\mathcal{R}$  value at the interface with water is indeed expected between SWCNT and MWCNT, as reported in the case of graphene with single and multi-sheets [276, 277].

#### 4.2.4 Mechanical response

With the spatio-temporal temperature field obtained in the previous section, we can now calculate the stress fields throughout the entire system and, ultimately, the pressure dynamics in water. The procedure follows that outlined in Chapter 3, with the constitutive equations being:

$$\rho \frac{\partial^2 \vec{u}}{\partial t^2} = \nabla \cdot \boldsymbol{\sigma} \quad (4.13)$$

$$\boldsymbol{\sigma} = \mathbf{C} \cdot (\nabla_s \vec{u} - \alpha \Delta T), \quad (4.14)$$

where  $\vec{u}$  is the displacement field (m),  $\boldsymbol{\sigma}$  the stress tensor (Pa),  $\nabla_s \vec{u}$  the symmetric part of the displacement gradient tensor operator and  $\Delta T$  the temperature difference  $T - T_0$ . The material parameters  $\mathbf{C}$  and  $\alpha$  are the stiffness tensor (Pa) and the linear thermal expansion tensor (1/K) of the CNT and water in the respective domains. Anticipating that the thermal expansion can be here taken as a scalar,  $\alpha$ , and exploiting cylindrical symmetry, Equations 4.13 and 4.14 may be re-cast in cylindrical components  $(r, \phi, z)$ , as for the gold nanocylinder (Equations 3.15). Also in this case we use the tensor  $\mathbf{C}$  in Voigt notation, with cylindrical symmetry, but, at variance with Equation 3.13, here we use the generic  $c_{ij}$

coefficients ( $i, j = 1, \dots, 6$ ):

$$\mathbf{C} = \begin{pmatrix} c_{11} & c_{12} & c_{13} & 0 & 0 & 0 \\ c_{21} & c_{11} & c_{13} & 0 & 0 & 0 \\ c_{13} & c_{13} & c_{33} & 0 & 0 & 0 \\ 0 & 0 & 0 & c_{44} & 0 & 0 \\ 0 & 0 & 0 & 0 & c_{44} & 0 \\ 0 & 0 & 0 & 0 & 0 & c_{66} \end{pmatrix}. \quad (4.15)$$

Using the same notation adopted in Equations 3.11, 3.12 and 3.13 with the only exception of  $\mathbf{C}$  (which is taken as in Equation 4.15), we obtain:

$$\begin{aligned} \rho \frac{\partial v_r}{\partial t} &= \frac{\partial \sigma_{rr}}{\partial r} + \frac{1}{r} (\sigma_{rr} - \sigma_{\phi\phi}) \\ \frac{\partial \sigma_{rr}}{\partial t} &= c_{11} \frac{\partial v_r}{\partial r} + c_{12} \frac{v_r}{r} - \alpha (c_{11} + c_{12} + c_{13}) \frac{\partial T}{\partial t} \\ \frac{\partial \sigma_{\phi\phi}}{\partial t} &= c_{12} \frac{\partial v_r}{\partial r} + c_{11} \frac{v_r}{r} - \alpha (c_{11} + c_{12} + c_{13}) \frac{\partial T}{\partial t} \\ \frac{\partial \sigma_{zz}}{\partial t} &= c_{13} \frac{\partial v_r}{\partial r} + c_{13} \frac{v_r}{r} - \alpha (2c_{13} + c_{33}) \frac{\partial T}{\partial t}, \end{aligned} \quad (4.16)$$

where  $v_r = \partial u_r / \partial t$ . Note that the equation for  $\sigma_{zz}$  is useless for our scopes, since it doesn't affect the dynamics in the radial direction. The reason why we kept  $\mathbf{C}$  with generic  $c_{ij}$  coefficients is that we will use different elastic parameters for CNTs and water. In the latter, we will make use of the first Lamé parameter  $\lambda$  (Pa) (the second,  $\mu$ , being null in water), retrieving Equations 3.15. In the CNTs, instead, we will see in the next section that it is more practical to use the Young modulus  $E_Y$  (Pa) and Poisson ratio  $\nu$ .

At the CNT/water interface, we assume the continuity of  $v_r$  and of  $\sigma_{rr}$ :

$$v_r(R^-) = v_r(R^+) \quad (4.17)$$

$$\sigma_{rr}(R^-) = \sigma_{rr}(R^+). \quad (4.18)$$

In particular, for the case of the SWCNT,  $R=R_{ext}^{sw}$ , there being only the external CNT/water interface, whereas a stress-free boundary condition is set at the internal CNT-vacuum boundary,  $\sigma_{rr}(R_{int}^{sw})=0$ , see Figure 52 (panel a). For the case of the MWCNT instead,  $R=R_{int}^{mw}$  at the internal, and  $R=R_{ext}^{mw}$  at the external CNT/water interface, respectively, see Figure 52 (panel b). For both cases, a stress-free boundary condition is set at the water domain outer boundary,  $\sigma_{rr}(R_{wt}) = 0$ . However, the water outer boundary is taken far enough that it is never reached by the propagating pressure wave on the timescale of our simulations. Before the light pulse strikes, the system is at rest and stress free, with initial conditions  $u_r = 0$ ,  $v_r = 0$  and  $\sigma_{rr} = 0$ .

A crucial, yet unsolved, issue concerns the elastic constants to be adopted when

describing the CNTs. Developing a model for CNTs elasticity is not straightforward. CNTs are built of an highly anisotropic material, graphite, which is rolled up and even radially deformed to accommodate for the correct matching of the single atomic cylinders. For all these reasons, the literature lacks an ultimate and unanimous model for the  $c_{ij}$  coefficients of CNTs [248, 251, 278].

In this thesis, we proceeded as follows. We modeled the CNT as a hollow cylindrical shell, assuming it is made out of a *homogeneous* and *isotropic* material with Young modulus  $E_Y$  and Poisson ratio  $\nu$ . The chosen values for such parameters will correctly predict the CNT behaviour only with respect to the radial direction, which is enough for our purpose.

Specifically, for the SWCNT case, we developed a simple analytical model, for  $E_Y$  and  $\nu$  starting from the known 2D elastic properties of graphene. Notably, using of the calculated values in a continuum mechanics model, we correctly predict the experimentally observed frequency of the radial breathing modes reported in the literature [279]. For the more complex MWCNT case, instead, we rely on experimental values that can be found in the literature [250]. Both these methods are detailed in Section 4.2.5. The actual values of  $E_Y$  and  $\nu$  are reported in Table 6. We highlight that this approach can lead to imprecise estimates for vibrational modes different from those in radial direction (as for instance a lateral bending). Our choice, however, serves for our scope, correctly describing elasticity in the radial direction and retaining the symmetries of the problem. Furthermore, its simplicity allows for a straightforward understanding of the physics involved.

Once obtained  $E_Y$  and  $\nu$ , we calculate the  $c_{ij}$  coefficients for the CNT pertinent to our model [280]:

$$\begin{aligned} c_{11} &= \frac{E_Y}{1 + \nu} \left( 1 + \frac{\nu}{1 - 2\nu} \right) \\ c_{12} &= \frac{E_Y}{1 + \nu} \left( \frac{\nu}{1 - 2\nu} \right) \\ c_{13} &= c_{12}, \end{aligned} \tag{4.19}$$

whereas, for the water domain, the elastic coefficients are expressed as  $c_{11}=c_{12}=c_{13}=\lambda$ . These values, together with the linear thermal expansion of water, and the radial thermal expansion coefficients of the SWCNT [249] and MWCNT<sup>2</sup> are reported in Table 6. After solving numerically Equations 4.16, we can extract the pressure wave launched in the water surrounding the CNT, which is obtained as  $p = -\sigma_{rr} = -\sigma_{\phi\phi}$ .

As in Chapter 3, the strategy to discriminate between thermophone and mechanophone contributions consists in setting to zero the thermal expansion coefficient  $\alpha$  in the CNT or external water domain, respectively.

<sup>2</sup>For the MWCNT,  $\alpha$  closely matches the out-of-plan graphite's one [247, 281, 282].

## 4.2.5 CNT Mechanical properties

### SWCNT: elastic constants from an analytical model

We consider the SWCNT as a rolled sheet of graphene. For this reason, a possible approach to model its elastic constants is to start from its 2D Young modulus  $E^{2D} = 340 \text{ N/m}$  ( $E^{2D} = 1 \text{ TPa} \times h$ , where 1 TPa is the graphene planar Young modulus and  $h = 0.34 \text{ nm}$  is the nominal thickness of the graphene plane) and Poisson ratio  $\nu = 0.15$ . We underline that graphene is also characterized by a (small) bending modulus, which *cannot* be calculated using the standard bulk elastic formulas for an isotropic material and rather depends on the elastic energy required to bend the atomic graphene network and its in-plane bonds. Such a bending is clearly non-zero in a SWCNT but it does not affect the breathing oscillation, thus we will neglect it in the following.

When the radius of a SWCNT is expanded from its equilibrium value  $r_0$  to  $r = r_0 + \Delta r$ , the circumference  $2\pi r$  of the rolled graphene layer is stretched as well. Since we assumed the SWCNT to be long and unable to experience significant movements/contractions along its axis, we consider the SWCNT as fixed at infinity and neglect any expansion or contraction in the axial direction. In this way, graphene can only stretch along the tangential direction  $\phi$  with a strain  $\epsilon_{\phi\phi} = \Delta r/r_0$ , as shown in Figure 53 (panel a), while  $\epsilon_{zz} = \epsilon_{z\phi} = 0$ . The stress tensor components of the cylindrical surface of the SWCNT can now be calculated using the constitutive strain-stress equations [283]:

$$\begin{aligned}\epsilon_{\phi\phi} E^{2D} &= \sigma_{\phi\phi} - \nu \sigma_{zz} \\ \epsilon_{zz} E^{2D} &= \sigma_{zz} - \nu \sigma_{\phi\phi} = 0 \\ \epsilon_{z\phi} E^{2D} &= (1 + \nu) \sigma_{z\phi} = 0,\end{aligned}\tag{4.20}$$

where we neglected any strain or stress components in the direction perpendicular to the graphene plane, since they are not consistent with the 2D mechanical description (in other words, the thickness of the graphene layer is constant). We note also that the unit of the planar tensor components  $\sigma_{ij}$  is here N/m. From the second and third equations we obtain  $\sigma_{zz} = \nu \sigma_{\phi\phi}$  and  $\sigma_{z\phi} = 0$ . In this way, inserting the obtained results in the first equation, we obtain the stress and strain relation along the tangential directions

$$\epsilon_{\phi\phi} = \frac{1}{E^{2D}} (\sigma_{\phi\phi} - \nu^2 \sigma_{\phi\phi}) = \frac{1 - \nu^2}{E^{2D}} \sigma_{\phi\phi} = \frac{1}{\tilde{E}^{2D}} \sigma_{\phi\phi}\tag{4.21}$$

where  $\tilde{E}$  represents an effective 2D Young modulus  $\tilde{E}^{2D} = E^{2D}/(1 - \nu^2)$ . This result has been extracted just considering a model of the 2D elastic response of a folded graphene layer, which does not take into account any deformation of the graphene sheet in the radial direction: the atomic network is and remains one atom thick regardless the mechanical

configuration of the SWCNT.

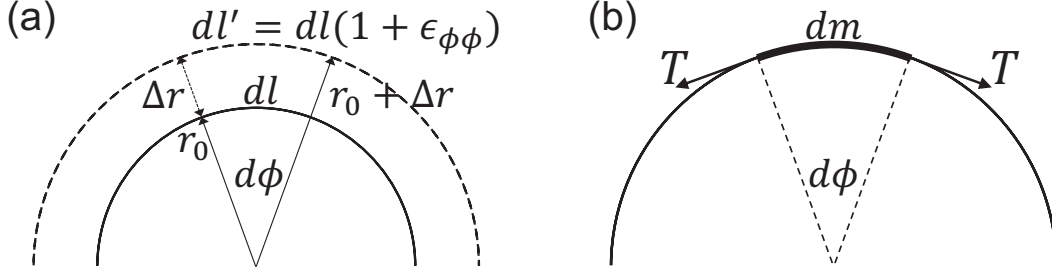


Figure 53. Schematics of the model to extract the elastic constants of the SWCNT. Stretching along the radial tangential direction due to the radial expansion  $\Delta r$  (panel a). Tension acting on an infinitesimal portion of the SWCNT (panel b). Panel b is taken from [5].

### Calculation of the breathing frequency

For the sake of benchmarking, we now calculate the frequency of the breathing modes using the elastic constants obtained by the 2D elastic model just described. Let us consider an infinitesimal portion of the SWCNT surface, of axial size  $dz$  and azimuthal length  $r d\phi$ . The tangential tension acting on the edges of this portion of cylindrical surface is  $T = \sigma_{\phi\phi} dz$  and, given the curvature of the surface, it implies a radial recovery force, as sketched in Figure 53 (panel b),

$$dF = T 2 \sin(d\phi/2) \approx \sigma_{\phi\phi} d\phi dz. \quad (4.22)$$

If we consider the mass of the cylindrical portion  $dm = \rho r d\phi dz$ , where  $\rho = 0.76 \text{ mg/m}^2$ , the radial force will counteract the expansion of the SWCNT, this is:

$$dm \ddot{r} = (\rho r d\phi dz) \ddot{r} = -dF = -\sigma_{\phi\phi} d\phi dz. \quad (4.23)$$

This yields the Ordinary Differential Equation which describes the radial breathing of the SWCNT,  $\rho r \ddot{r} = -\sigma_{\phi\phi}$  or, assuming a small radial expansion  $r \approx r_0$ ,

$$\rho \frac{d^2}{dt^2} (r_0 + \Delta r) = \rho \ddot{\Delta r} = -\frac{\sigma_{\phi\phi}}{r_0} = -\frac{\tilde{E}^{2D}}{r_0^2} \Delta r \quad (4.24)$$

with an expected radial oscillation frequency

$$\omega = \sqrt{\tilde{E}^{2D} / \rho r_0^2}. \quad (4.25)$$

In the (5,5) SWCNT case,  $\omega = 6.28 \times 10^{13}$  rad/s, in very good agreement with values found in the literature [251, 284]. The same breathing frequencies can be reproduced by a bulk model of a  $h$ -thick cylinder shell built of an isotropic material with Young modulus  $E_Y = \tilde{E}^{2D}/h \approx 1$  TPa. Such  $E_Y$  is exactly the Young modulus adopted in the our 3D continuum model to describe the elastic constants of the SWCNT.

### MWCNT: elastic constants from experimental values

We now discuss the MWCNTs. In this case, we take the radial Young modulus  $E_Y$  and Poisson ratio  $\nu$ , from published experimental data [250]. In their work, Palaci *et al.* measured  $E_Y$  for MWCNTs with a fixed ratio of their external and internal radii, taking the external radius twice larger than the internal one. With reference to figure 3 of Palaci *et al.*,  $E_Y$  converges to 30 GPa for  $R_{ext} > 4$  nm.

We chose the MWCNT to follow the  $R_{ext}/R_{int} = 2$  prescription and with  $R_{ext} = 15.5 > 4$  nm. We then conclude that, for our MWCNT, we can take  $E_Y = 30$  GPa and  $\nu = 0.28$  as reported in Palaci *et al.*

Remarkable for the sake of consistency, again by looking at figure 3 of Palaci *et al.*, the Young modulus measurements for the number of walls decreasing towards one converges, upon extrapolation, to the Young modulus value found from our SWCNT model. Inserting  $E_Y$  and  $\nu$  in equation 4.19 we then obtain the  $c_{ij}$  coefficients for the CNT (both SW and MW). We underline once more that this result brings to a stiffness tensor  $\mathbf{C}$  of a homogeneous and isotropic material (automatically implying cylindrical symmetry), which matches the real CNTs Young modulus and Poisson ratio in the radial direction.

## 4.3 Results

### 4.3.1 Thermal dynamics

In this section, we report simulations results for the thermal dynamics upon excitation by a laser pulse of duration  $\tau_L=1$  ps (first column of Figure 54) and  $\tau_L=5$  ns (second column) in the SWCNT (first row) and MWCNT (second row) systems. Each panel reports, on the left axis, the temperature increase  $\Delta T=T(t)-T_0$  calculated at the mid point of the CNT thickness (blue curve and dot), at a point of the external water positioned 5 nm away from the external CNT/water interface (green curve and dot) and, only in the case of the MW, inside the internal water at  $r = 0$  (magenta curve and dot). The right axis reports the light pulse intensity time evolution (red dashed curve).

In a general description of all cases, the CNT temperature increases due to absorption of the laser pulse and then cools down, delivering heat to the proximal water, also rising its temperature. Finally, the CNT and the proximal water relax to the initial temperature, heat

being diffused towards the water bulk.

In the *SW/ps pulse case* (Figure 54, panel a), the relative CNT temperature rises up

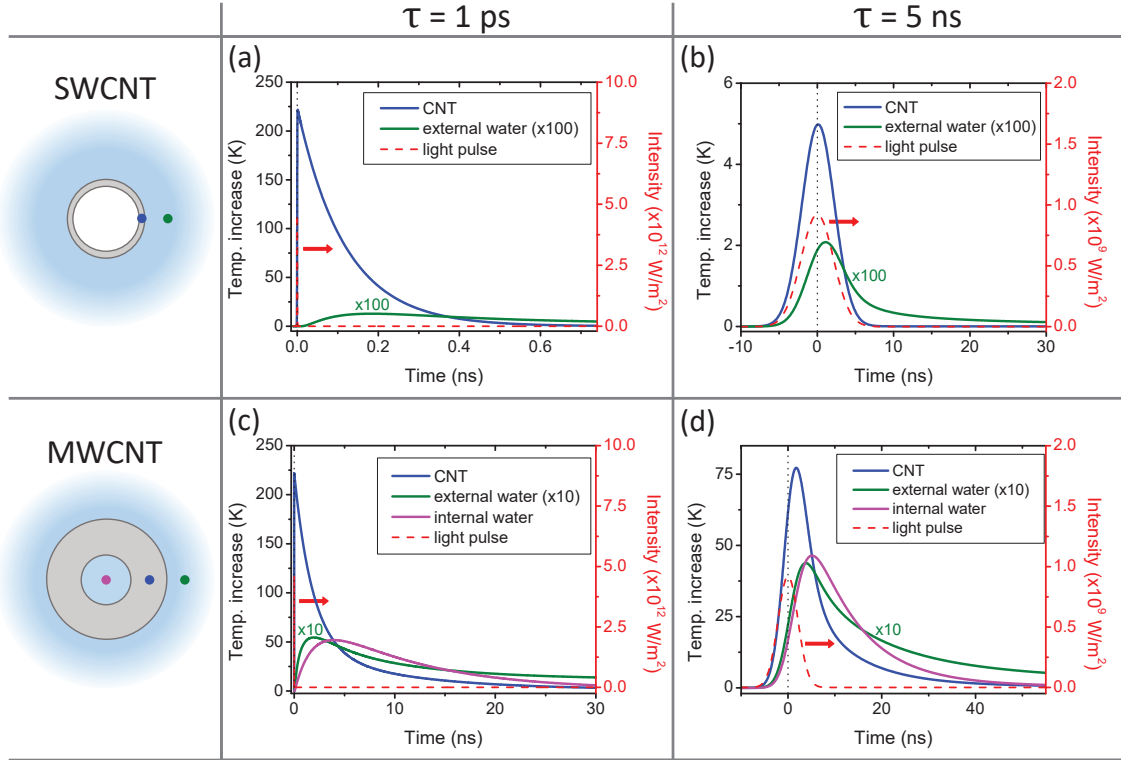


Figure 54. Time evolution of the temperature increase in the different CNTs/light pulse duration cases for incident pump fluence  $\Phi = 5 \text{ J/m}^2$ : SW/ps (panel a), SW/ns (panel b), MW/ps (panel c) and MW/ns (panel d). Left axis: CNT temperature increase in the middle of the CNT radius (blue curve and dot), at a point in the external water 5 nm away from the external CNT/water interface (green curve and dot) and, only for the MWCNT case, the internal water temperature increase at the radial coordinate  $r = 0$  (magenta curve and dot). The external water temperature increase curves are multiplied by a factor 100 for the SWCNT case (a,b) and 10 for the MWCNT case (c, d) to ease readability. Right-axis: light pulse intensity (red dashed curve) as a function of time. Maximum intensity in panels a and c is  $\approx 5 \times 10^{12} \text{ W/m}^2$ . The vertical black dotted curve labels the instant at which the peak pulse intensity occurs. The timescale differs in each panel. Image taken from [5].

to  $\Delta T \approx 225 \text{ K}$  on the timescale of the laser pulse duration  $\tau_L = 1 \text{ ps}$ .

As we have seen in Chapter 3 for the gold nanocylinder, when the cooling dynamics is limited by the TBR, we can define a characteristic time  $\tau_{Th}$  for the temperature decay of a nano-object in contact with an isothermal medium. In the case of the SWCNT,  $\tau_{Th}$  assumes a more complex form, due to the hollow cylinder shape:

$$\tau_{Th} = \frac{\mathcal{R} \rho c_p R_{ext}^{sw}}{2} \left( 1 - \left( \frac{R_{int}^{sw}}{R_{ext}^{sw}} \right)^2 \right) = 118 \text{ ps}. \quad (4.26)$$

The validity of the formula is assured by a Biot number  $Bi = R_{ext}^{sw} (1 - (R_{int}^{sw}/R_{ext}^{sw})^2) / 2k\mathcal{R} \ll 1$  and an essentially isothermal water (in respect to the CNT temperature excursion, see

Figure 54). This value perfectly matches the value of  $\tau_{Th}$  obtained fitting the numerical curve. Thus the SWCNT dissipates heat into water, which  $\Delta T$  reaches a maximum of a fraction of a degree. The important message to retain here is that the SWCNT is heated up on a timescale  $\tau_L$  and remains hot and thermally decoupled from water on a much longer timescale,  $\tau_{Th}$ , ruled by the TBR. Under these circumstances, arising for  $\tau_{Th}/\tau_L \gg 1$ , we expect the mechanophone effect to play a significant role, as demonstrated in Chapter 3.

In the *SW/ns pulse case* (Figure 54, panel b) the situation is the opposite, i.e.  $\tau_{Th}/\tau_L \ll 1$ . The light pulse temporal width, now  $\tau_L=5$  ns, exceeds by far  $\tau_{Th}=118$  ps, implying that the heat dissipation rate from the CNT to water matches, on the ns time-scale, the rate at which the CNT absorbs energy from the light pulse. This is clearly visible in panel b of Figure 54, where the CNT  $\Delta T$  temporal evolution precisely matches the light pulse temporal one,  $I(t)$ , releasing heat fast enough to the external water, and ending with  $\Delta T \approx 0$  at the instant in which also the light pulse is concluded, i.e.  $t \approx 5$  ns. The water  $\Delta T$  temporal evolution, at a point 5 nm out of the CNT/water boundary, matches almost as well the CNT's one (delay between the two curves  $\approx 1$  ns). In other words, for  $\tau_L=5$  ns, the thermal behaviour of the system is that of a steady state heat transfer under continuum illumination with a slowly (with respect to the thermal transient time from the CNT to water, i.e.  $\tau_{Th}$ ) modulated heat source (the modulation being the Gaussian pulse profile lasting  $\sim \tau_L$ ). This scenario is the one commonly encountered in nanofluids under irradiation with ns pulses [145] and described in Chapter 3 for  $\tau_{Th}/\tau_L \ll 1$ , thus we expect the thermophone effect being the predominant photoacoustic launching mechanism.

In the *MW/ps case* (Figure 54, panel c), we need to consider two new aspects: an increased CNT volume and the presence of the internal water. Both these aspects imply an overall longer thermal relaxation time of the CNT  $\Delta T$ , also characterized by a non-exponential temperature decay, the internal water being a new dissipation channel. We still maintain the concept of  $\tau_{Th}$  as the timescale over which the CNT relaxes heat to the external water, even though, in this case, due to the more complex thermalization dynamics,  $\tau_{Th}$  is not anymore an exponential decay. We then propose an operative way to estimate  $\tau_{Th}$ , defining it as the time it takes for the CNT  $\Delta T$  to fall to 1/e of its maximum value, resulting in  $\tau_{Th} \approx 5$  ns. With such definition, although somewhat arbitrary, we are able to provide an estimate for the CNT thermal relaxation time to the external water. The reasons for the increased  $\tau_{Th}$  in the MWCNT case stand in the augmented thermal mass of the CNT and the added contribution of the internal water thermal inertia.

We are now in the position to discuss the details of the thermal dynamics and to substantiate the above-mentioned concepts. Again with reference to Figure 54 (panel c), the CNT has two heat thermal pathways in parallel, namely the internal and the external water. The CNT initially cools rapidly, delivering heat to both water domains. The internal water  $\Delta T$  becomes, however, rapidly higher than the external water one and, after  $t \approx 5$  ns, attains the same value as that of the CNT. Starting from this instant, the heat flux between the

CNT and the internal water is reversed, flowing from the internal water domain towards the CNT. This heat absorption by the CNT clearly slows down its cooling rate, since the dissipated heat towards the external water is partially counterbalanced from heat received by the internal one. This explains why, starting from 5 ns, the internal water temperature overshoots the CNT's one. Summing up, the important message for our proposes is that, for the MW/ps case,  $\tau_{Th}/\tau_L \gg 1$ , thus indicating that the mechanophone should contribute significantly.

In the *MW/ns case* (Figure 54, panel d) the laser pulse duration  $\tau_L = 5 \text{ ns} \approx \tau_{Th}$ . This situation is a cross-over between the SW/ns and the MW/ps case. The mechanophone effect could potentially be active, but to a lesser extent with respect to the MW/ps. Consistently with the above discussion, and contrary to the SW/ns case, the situation is not that of steady state heat flow, and indeed the CNT  $\Delta T$  profile does not match that of laser pulse intensity  $I(t)$ .

To summarize all investigated cases, the solutions to the thermal problem, first, provide the source terms for the mechanics and, second, suggest that the mechanophone effect should not contribute much in the SW/ns case but could be important in the SW/ps and MW/ps cases, and potentially, also in the MW/ns one.

### 4.3.2 Mechanical response

We now report simulations results for the mechanical response triggered by a laser pulse duration  $\tau_L=1 \text{ ps}$  (first column of Figure 55) and 5 ns (second column) in the SWCNT (first row) and MWCNT (second row) systems, with the already retrieved spatio-temporal temperature profile being the source term for the acoustic problem. Each panel reports, on the left axis, the pressure field due solely to the thermophone (cyan curve), solely to the mechanophone effect (orange curve) and the total pressure (black dotted curve) calculated at a point in the external water 5 nm away from the CNT/water interface (black dot). The right axis shows instead the light pulse intensity time-dependence (red dashed curve), with  $t = 0$  being the instant at which the peak pulse intensity occurs (vertical dashed line).

The first striking feature is that, as suggested by the analysis of the thermal behaviour of the different systems, the mechanophone effect contributes significantly to the total pressure in all cases except the SW/ns one. Specifically, comparing the peak pressure 5 nm out of the CNT/water interface, the mechanophone and thermophone similarly contribute in both the SW/ps (Figure 55, panel a) and MW/ns cases (panel d), whereas, for the MW/ps case the mechanophone is the predominant contributing term (panel c).

However, as for Chapter 3, our aim is to quantitatively address the relative contributions of the thermophone and mechanophone effects in terms of the acoustic energy generated.

We first calculate, for each size/pulse duration case and accounting for the thermophone

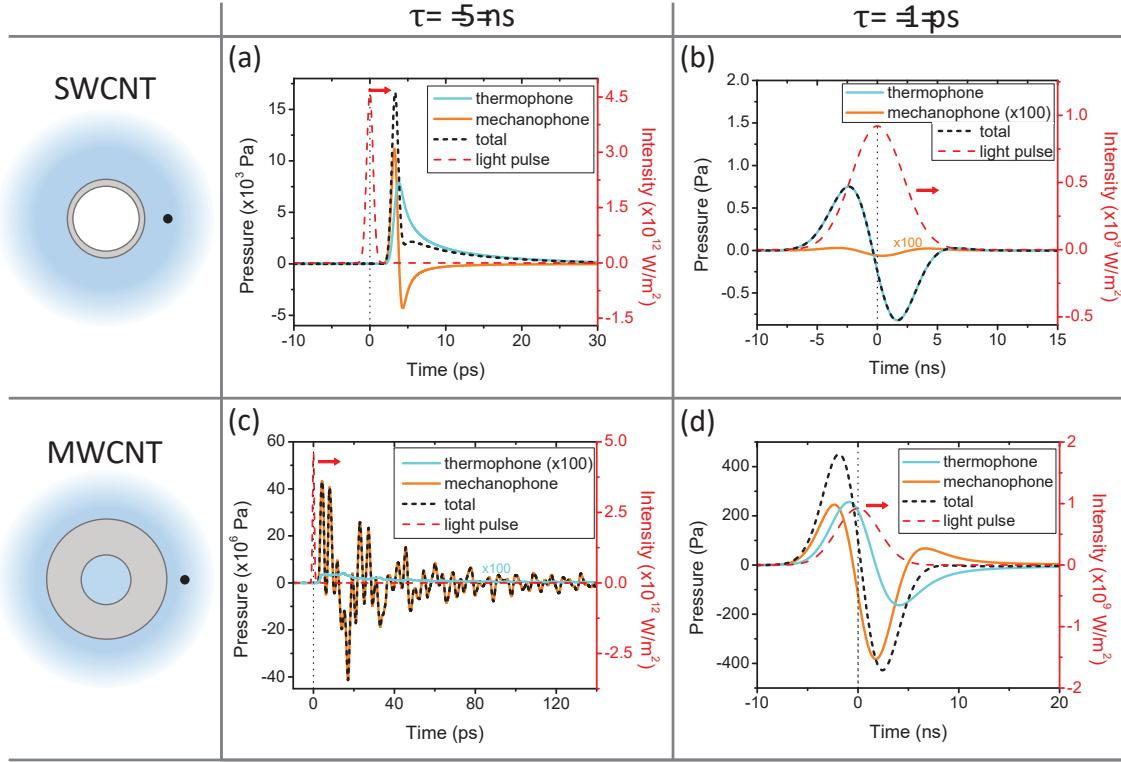


Figure 55. Time evolution of the pressure field for the different CNTs/light pulse cases: SW/ps (panel a), SW/ns (panel b), MW/ps (panel c) and MW/ns (panel d). The pressure is calculated at a point in the external water 5 nm from the CNT/water interface (black dot). Left axis: thermophone pressure contribution (cyan blue curve), mechanophone pressure contribution (orange curve) and total pressure (black dotted curve). The pressure curves are multiplied by a factor 100 for the mechanophone contribution in the SW/ns case (panel b) and for the thermophone contribution in the MW/ps case (panel c) to ease readability. Right-axis: light pulse intensity (red dashed curve) as a function of time. The vertical black dotted line labels the instant at which the peak pulse intensity occurs. The time and pressure scale differs in each panel. Image taken from [5].

and mechanophone effects separately, the acoustic Poynting vector ( $\text{W/m}^2$ ):

$$\vec{P} = -v_r \sigma_{rr} \hat{r}, \quad (4.27)$$

where  $\hat{r}$  is the radial versor. Subsequently, we evaluate the total mechanical energy transported by the acoustic wave in the external water, calculating the flux of  $\vec{P}$  across a generic cylindrical closed surface  $S$  coaxial to and encapsulating the CNT. Finally, to obtain the energy, we integrate the flux in time:

$$U = \int_t \oint_S \vec{P} \cdot \hat{n} \, dS dt, \quad (4.28)$$

where  $\hat{n}$  is the outgoing unit vector perpendicular to the surface  $S$ . As an observation in retrospect, we underline that the  $S$  surface radius has to be chosen long enough so as for the energy  $U$  to attain an asymptotic value.

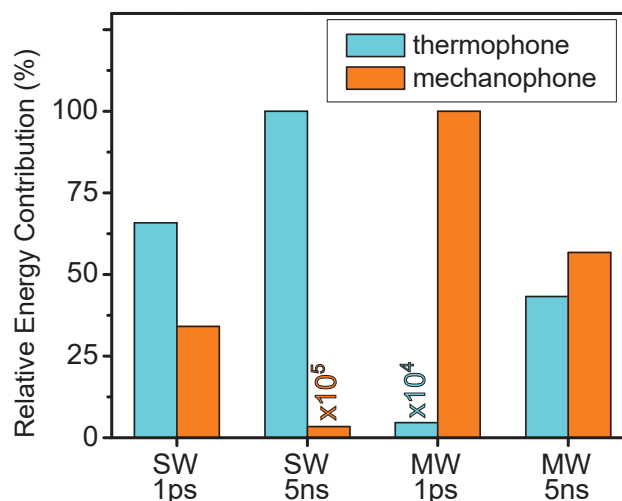


Figure 56. Relative energy contribution, in percentage, of the thermophone (cyan bar) vs mechanophone (orange bar) effects calculated from the acoustic Poynting vector for the different cases SW/ps, SW/ns, MW/ps and MW/ns. For the sake of visualization, in the SW/ns case the mechanophone contribution is multiplied by  $10^5$ , while in the MW/ps case the thermophone contribution is multiplied by  $10^4$ . Image taken from [5].

Figure 56 reports, in histogram form, the comparison between the relative thermophone and mechanophone energy contributions in percentage for the different CNT size/pulse duration cases. For the SW/ps case, the thermophone and the mechanophone contributions are comparable, with the thermophone exceeding the mechanophone by 60% (despite the fact that, in panel a of Figure 55, the thermophone pressure peak is lower than the mechanophone one). For the SW/ns case the thermophone dominates, while for the MW/ps case only the mechanophone contributes. For the MW/ns case the mechanophone contribution is slightly greater than the thermophone's.

The histogram confirms, on a quantitative basis, our predictions, based on the solution of the thermal problem. Specifically, the mechanophone effect starts to become significant, on an equal footing with the thermophone or even as the prevailing contribution, when the pulse duration is comparable or smaller than  $\tau_{Th}$ . We highlight that, as seen in Chapter 3 (Figure 38), for common metallic nanosystems excited with a ns laser pulse, as commonly addressed in the literature, only the thermophone effect plays a role [145, 199, 200]. In our case, instead, the mechanophone effect shows a significant contribution also for the MW/ns case. Contributing to this difference is the fact that the TBR at the CNT/water interface is about one order of magnitude higher than for the typical metal/water interfaces [221, 222, 223]. This increases  $\tau_{Th}$  in the CNT case, making the mechanophone more effective. In other words, the higher TBR value reduces the water peak temperature increase and thermal expansion accordingly, thus weakening the thermophone effect; on the other hand, it brings the CNT to a higher temperature and greater thermal expansion, enhancing the mechanophone contribution in the acoustic wave generation.

We now focus on the shape of the pressure pulse in time and on the possibility, in

the MW/ps case, to launch acoustic waves in water with hypersonic frequency and few nanometers wavelength, matching the CNT mechanical eigenmodes frequencies.

In the two *ns cases* (panels b and d of Figure 55), the total pressure displays the typical profile expected for sound waves generated by liquid-embedded nano-systems excited by ns laser pulses [145, 147, 202, 285], with a positive peak followed in time by a negative one, the pressure profile being roughly proportional to the time derivative of the light pulse intensity [285]. Things are quite different for the case of ps pulse excitation.

In the *SW/ps case* (Figure 55, panel a), the total pressure exhibits a sharp positive peak, followed, on a longer timescale, by a shallow trailing edge. The sharp peak pulse is mainly due to the mechanophone contribution (orange curve), whereas the trailing edge is mostly due to the thermophone effect (cyan curve). This can be rationalized observing the dynamics in the different system domains: after the sharp acoustic pulse is launched, mainly by the CNT expansion, the external water is still rising its temperature, layer by layer as heat propagates radially, resulting in a long lasting pressure tail as a cumulative effect.

In the *MW/ps case* (Figure 55, panel c), water pressure shows damped oscillations in time,

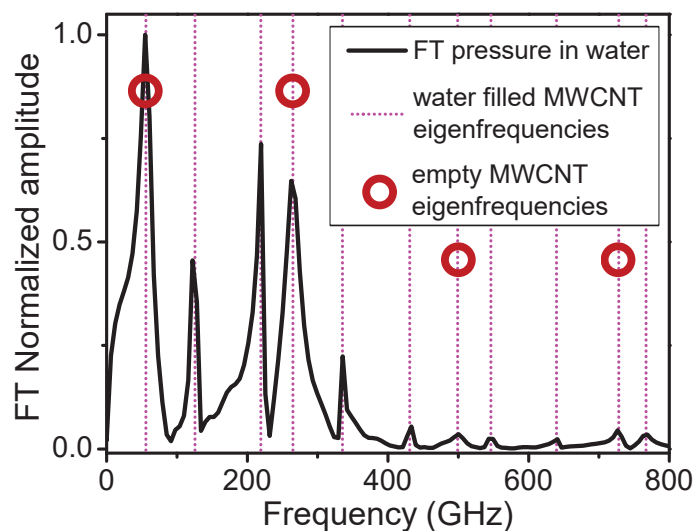


Figure 57. Normalized Fourier transform amplitude of the total pressure time evolution curve in water for the MW/ps case (black curve). Eigenvalues of the radial displacement field for the water-filled MWCNT (vertical dotted magenta lines) and for the empty MWCNT (empty dots). Image taken from [5].

similarly to what we already observed in Figure 46 for the nanofilm. The pressure (Figure 55, panel c) is solely contributed by the mechanophone effect, strongly suggesting that oscillations are related to the eigenmodes of the water-filled MWCNT. The complexity is here twofold: on the one hand, there is the presence of the internal water which, as we will prove, affects the system’s vibrational modes; on the other hand, even an empty MWCNT exhibits two different types of oscillations: the breathing mode, related to the periodic variation of its diameter, and the “walls modes”, related to the periodic variation

of the wall thickness. The contribution of the internal water is demonstrated in Figure 57, showing the amplitude, normalized to its maximum, of the Fourier transform (FT) of the total pressure curve for the MW/ps case (black curve). The FT is peaked at the eigenvalues of the displacement for the water-filled MWCNT system (vertical dotted magenta lines) calculated following Ref. [251]. As can be seen, the radial displacement eigenvalues of the non-infiltrated (empty) MWCNT are only a subset of the water-filled MWCNT ones (magenta dots), thus proving that the infiltrated water play an important role in determining the launched frequencies.

These eigenmodes are activated since their frequencies fall within the laser pulse bandwidth (BW)  $\approx \tau_L^{-1} = 1$  THz. This is not the case for the MW/ns case, where the laser pulse BW  $\approx 0.2$  GHz falls short of the fundamental radial eigenfrequency, nor for the SWCNT cases, the SWCNT breathing mode occurring at 10 THz. The appearance of the water-filled MWCNT oscillations and their relation to the laser pulse duration are well visualized in Figure 58. Here we report the radial displacement time evolution (green curve, left axis) calculated at  $r=13$  nm, i.e. a point inside the MWCNT thickness and close to its external interface with water (green dot in the inset sketch), for the MW/ns case (panel a) and for the MW/ps case (panel b). Note that the time-scales are different in the two graphs for the sake of visualization. In the ns case, the radial displacement increases, due to thermal

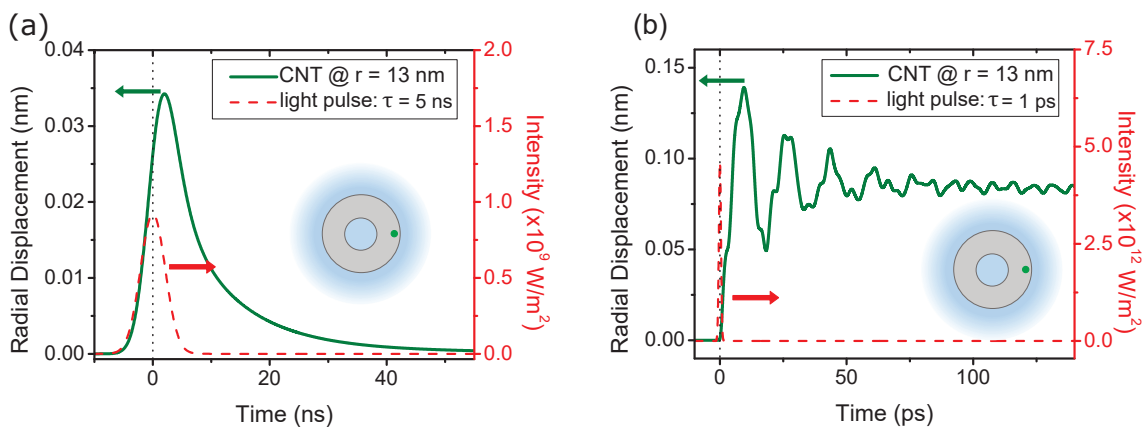


Figure 58. Time evolution of the radial displacement (green curve, left axis) calculated at  $r = 13$  nm (green dot in figure inset) for (panel a) the MW/ns and (panel b) MW/ps cases. Laser pulse intensity time-dependence (red dashed curve, right axis) for the respective cases. Mind the different timescale in each graph. Image adapted from [5].

expansion, as long as the CNT accumulates energy. Then, it returns to its initial value on a ten ns timescale, while the CNT transfers heat to the surrounding water. In the ps case, oscillations of the CNT vibrational modes are activated by the short laser pulse, and superposed on top of the slowly decreasing displacement background. The oscillations are damped via acoustic radiation to the surrounding water on a 100 ps timescale, whereas the average CNT radius relaxes with the temperature decrease, on a 5 ns timescale. The latter relaxation is not appreciable on the present time window but may be seen from the

temperature dynamics of Figure 54 (panel c).

We now address in Figure 59 also the spatio-temporal dynamics of the pressure

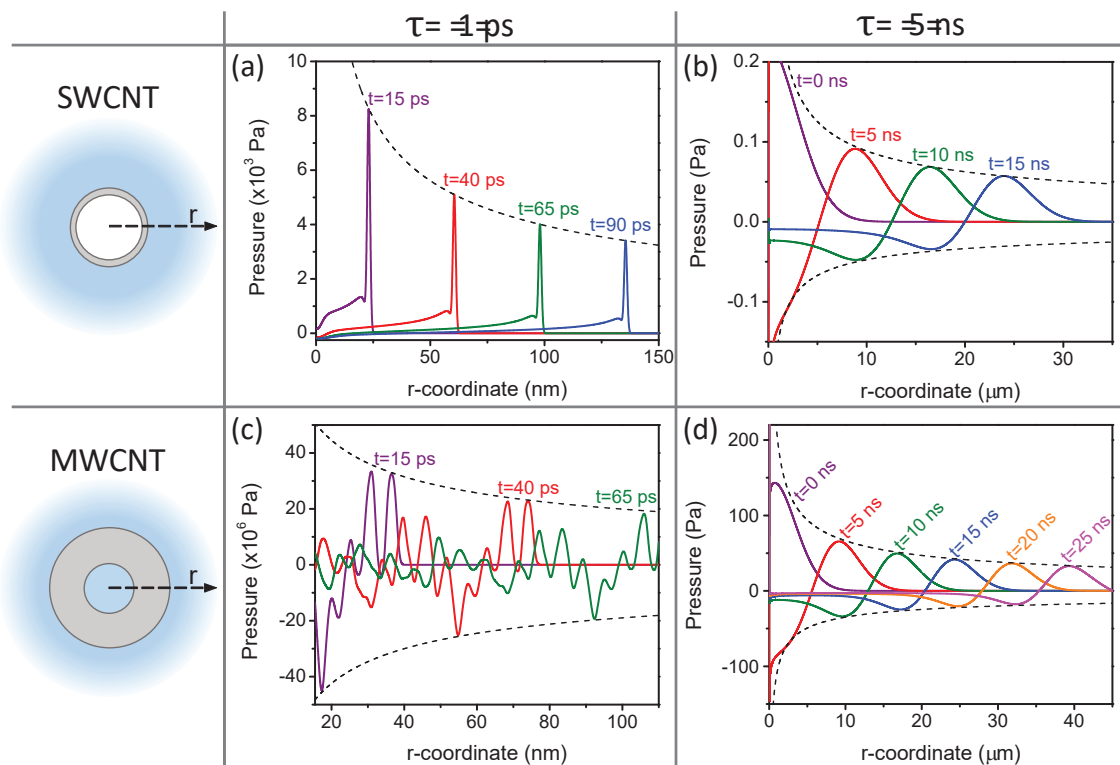


Figure 59. Pressure along the radial coordinate in the external water for the different cases: SW/ps (panel a), SW/ns (panel b), MW/ps (panel c) and MW/ns (panel d). Different colors show different instants in time. The  $\propto 1/\sqrt{r}$  envelope to the peaks maxima and minima is reported as a dashed black curve for each panel. Image taken from [5].

wave. The graphs show the total pressure along the radial coordinate  $r$ , calculated at different time instants, for all the CNT sizes/light pulse cases. The pressure is reported in the external water domain: for the SW/ps (panel a), SW/ns (panel b), and MW/ns (panel d) the CNT radius is negligibly small compared to the plotted radial range and cannot be appreciated. For the MW/ps case (panel c), instead, the CNT radius is comparable to the plotted radial range, the  $r$  axis hence being reported for  $r > 15.5$  nm. The envelopes to the highest (positive) and lowest (negative) peaks (black dotted curves) scale as  $1/\sqrt{r}$ , which, due to energy conservation, is the expected asymptotic behaviour for a cylindrical pressure wave.

For the SW/ns (panel b) and MW/ns (panel d) cases, also in space we observe the typical acoustic wave-like profile, with a positive peak followed by a negative one. Differently, for the SW/ps case (panel a), a positive pressure spike clearly stands out for each time snapshot, followed by a pressure bulge trailing behind (at smaller  $r$  coordinates with respect to the pressure spike). As time evolves, this bulge spreads out and, for radial coordinates closer to the CNT, eventually becomes negative (see Figure 59 for  $r$  coordinates very close to 0). This pressure bulge is continuously fed by the thermophone effect. It arises

as the cumulative effect of a reduced thermal expansion in water shells at smaller  $r$  coordinates, which are cooling down, and an increased thermal expansion in water shells that are being reached by the propagation of heat (larger  $r$ ). Although thermal diffusion continuously contributes to the pressure, we recognize the pressure spike, mostly due to the mechanophone effect, as the pressure pulse of interest for photoacoustics applications. For the MW/ps case, panel c yields a clear representation of the spatially short wavelengths involved in the oscillating pressure generated by the water filled-MWCNT system, here acting as a mechanophone.

At the light of the results, one *a posteriori* remark is due concerning some of the adopted assumptions at the basis of our modeling. As previously explained, in the present work we did not account for intrinsic damping of acoustic waves in water (inviscid water), a yet open issue in the present frequency range. Generally speaking, intrinsic damping is expected to increase with frequency, hence acting as a low pass filter, with minor effects for the case of pressure waves excited with long laser pulses but, in the present case, possibly hampering water oscillations frequencies in excess of the MWCNT fundamental mode at  $\approx 50$  GHz when exciting with ps pulses. For the sake of disentangling the launching mechanisms when exciting with pulses of different temporal width, which is the primary goal of this work, we therefore avoided considering an additional effect, i.e. viscosity, which is yet unclear in the hundreds of GHz frequency range [286, 287].

## 4.4 Conclusions

In this chapter, we applied the knowledge developed throughout the entire thesis work, to design and investigate a realistic model via a multi-scale theoretical approach encompassing atomistic simulations, analytical calculations and FEM simulations in a continuum framework. We investigated the generation mechanism of acoustic waves in water upon excitation of both a single-wall (SW) and a multi-wall (MW) CNT with laser pulses of temporal width ranging from 5 ns down to the ps. First we showed that, depending on the combination of CNT size and laser pulse duration, the CNT can act both as a thermophone and a mechanophone. In the former case the CNT acts as a nanoheater for the surrounding water, which, upon thermal expansion, launches the pressure wave; in the latter case the CNT acts as a nanopiston, its thermal expansion directly triggering the pressure wave in water. Consistently with results from Chapter 3, the mechanophone is shown to play a significant role when the laser pulse duration is much shorter than the CNT characteristic cooling time towards the external water:  $\tau_{Th}/\tau_L \gg 1$ . Second, we proved that the mechanophone can enable the generation of few nanometers wavelength acoustic waves in water, matching the water filled-CNT oscillation frequencies. This is achieved for a laser pulse duration shorter than the fundamental CNT period. These nanometers wavelength sound waves in water are interesting in fields ranging from theranostics [288],

nanoscale acoustic imaging [177, 289, 290, 291] to water dynamics at the nanoscale [292, 286, 287, 231, 293, 294, 295] and in the hypersonic frequency range [296], below the elastic spectral window accessible to Inelastic X-ray, Brillouin inelastic ultraviolet and neutron scattering techniques [297, 298, 299, 230, 300].

Attention was devoted to the role of the infiltrated water within the CNT. Specifically, in the contest of energy exchanges between the nanoparticle and its environment, the case of the photoacoustic effect generated by a CNT immersed in water is a peculiar one. For the SWCNT, atomistic simulations show that no water infiltration is present. In this case, the SWCNT plays the role of the optical nano-absorber, thermal nano-heater and mechanical nano-piston; providing to the external water both the heat that generates the thermophone effect, as well as the mechanical pressure that generates the mechanophone. In this respect, the SWCNT follows the same behaviour as the gold nanoparticles discussed in Chapter 3. The MWCNT case, with water infiltrating its internal volume, is more complex. Initially, only the CNT absorbs the light pulse, with both the internal and external water not contributing to the absorption phenomenon. However, during the heat exchange between the CNT and its surrounding, the internal water rapidly reaches the CNT temperature and then overshoots it. From that moment on, it is the internal water which dissipates heat into the CNT, with the latter now dissipating only in the direction of the external water. In this way, the energy exchange between the nanoparticle and its environment does not occur in a single direction throughout the dynamic, but switches roles at a certain time. Subsequently, also in the mechanical dynamics the internal water plays a key role. For  $\tau_L = 1$  ps, in fact, the oscillation frequencies of the pressure in the external water, generated by the mechanophone effect, can only be understood by considering as the nano-resonator the water-filled-CNT system and not the CNT alone.

Summing up, this chapter shows, for a realistic nanosystem, the importance of the mechanophone effect, suggesting this additional generation pathway on top of the one commonly addressed in the case of water-immersed single nano-objects excited with ns laser pulses, where only the thermophone effect contributes. Furthermore, it points to perspective work to be undertaken to further progress in the field. In particular, the role of intrinsic damping in the propagation of such sound waves, i.e. viscous and viscoelastic damping [231, 301], a yet open issue in the present frequency range, will need to be addressed. Indeed, intrinsic damping could hamper the propagation in water of oscillations with frequencies greater than that of the MWCNT fundamental mode. Finally, upon further shortening the laser pulse duration, water might respond as a solid rather than a liquid, exhibiting a non linear dispersion with the sound velocity increasing to 3200 m/s [230].

## General conclusions and perspectives

In this thesis work, the opto-thermo-mechanics of several nano-systems is investigated in the general framework of energy exchanges at the nanoscale, by means of both experimental and theoretical approaches. Across the chapters, we addressed such different phenomena as electron-electron interaction, electron-lattice thermalization, nanoscale acoustic vibrations and nanoscale thermal dynamics.

In Chapter 1, we reported on time resolved spectroscopy measurements performed on individual gold nanodisks nanopatterned on a sapphire substrate. First we introduced the spatial modulation spectroscopy technique, which allows to measure the optical properties of individual nanoparticles and, together with numerical simulations, retrieve their morphological features. Then we introduced the pump-probe set up, deployed to measure the transient optical properties of single nanodisks upon excitation on two different timescales. At the ns scale, we accessed the absolute temperature time evolution of the nanodisk and retrieved the thermal boundary resistance at the nanoparticle/substrate interface. At the (sub-)ps scale, we investigated electron-electron interactions and electron-lattice thermalization, showing that the transient optical dynamics is sensible to the probe wavelength, thus permitting to selectively access the electronic or the lattice thermal dynamics separately. This work demonstrates the possibility to access single nanoparticles internal thermalization and cooling dynamics. A future development of such an experiment could be the investigation of two nanoparticles in contact, characterized by different localized surface plasmons resonances. In such a system, one could selectively excite and probe only one of the two nanoparticles, by means of different wavelengths of the pump and probe pulses. In this way, energy exchanges between two different nano-objects could be investigated.

In Chapter 2, we addressed a forest of vertically aligned Indium Arsenide (InAs) nanowires grown on an InAs substrate. We focused on the nanowires mechanical vibrations. The study was performed with a multi-technique approach, encompassing electron microscopies, pump-probe measurements and finite element simulations. Particular attention was devoted to the nanowires elastic constants. Then, through numerical simulations in the frequency domain, we found that the oscillations observed with time resolved measurements correspond to the longitudinal modes of the nanowires. The scaling of the longitudinal modes with NWs length, together with numerical modelling, allowed retrieving information on the NWs elastic parameters. Finally, we also modeled the time dependent excitation and thermo-mechanical response of the system in the time domain, in order to understand the origin of such oscillations. Their activation is due to an impulsive

“hammer-like” excitation triggered in the substrate and propagating into the nanowires, rather than from the nanowires expansion itself. This process is the opposite with respect to the one involved in the case of gold nanodisk, where the sapphire substrate only serves to evacuate the energy received from the nanodisk, the latter being responsible for the optical absorption, the heat conversion and for the overall mechanical response of the system (although the discussion on the mechanics goes beyond the purpose of Chapter 1). The scope of the investigation on InAs nanowires is twofold: on the one hand, retrieving the elastic constants, which are fundamental for any device and application based on InAs nanowires; on the other hand, unveiling the mechanism behind the impulsive activation of the vibrational modes. This mechanism bears generality beyond the specific system.

The competition between the nanoparticle and its environment in the generation of acoustic waves is at the core of the next two chapters. In Chapter 3, a theoretical study on the photoacoustic effect generated by gold nanotransducers immersed in water is carried out. Here we systematically investigated the role of the thermal boundary resistance and the pulse excitation duration on the competition between the environment contribution (thermophone effect) and the nanoparticle one (mechanophone effect) in photoacoustic generation. This investigation is performed in the time domain as well as in the frequency domain, exploiting time-resolved numerical simulations and analytical calculations. In particular, for a gold nanocylinder described in the time domain framework, we defined an adimensional quantity,  $\tau_{Th}/\tau_L$ , given by the ratio of the cooling characteristic time (proportional to the thermal boundary resistance, where this effect is the limiting cooling mechanism) and the light pulse temporal width. For a ns light pulse, the thermophone vs mechanophone competition is strongly dependent on  $\tau_{Th}/\tau_L$ , with the mechanophone effect prevailing for  $\tau_{Th}/\tau_L \gg 1$ , and the thermophone for  $\tau_{Th}/\tau_L \ll 1$ . Reducing the light pulse temporal width down to the 10 ps timescale, the mechanophone effect becomes almost independent on  $\tau_{Th}/\tau_L$ . We rationalized these results in terms of the temperature time evolution in the nanoparticle and in the water domains, showing that the mechanophone (thermophone) contributes when the thermal boundary resistance/temporal light pulse width combination results in a slow (fast) heat exchange between the nanoparticle and its surrounding. Furthermore, the case of a realistic gold/water thermal interface was discussed for each light pulse temporal width, showing that the thermophone effect prevails for ns light pulses, whereas the mechanophone effect prevails for 10 ps light pulses. In parallel, similar considerations were carried out in the simpler Au film-on-water system, operating in the frequency domain. This choice allows to formally retrieve the interplay of the parameters ruling the photoacoustic generation in an analytical, explicit form. These results are compared to those obtained in the time domain. This study demonstrates the importance of the mechanophone effect, often not considered in the literature. It also suggests the possibility to exploit photoacoustic systems that make use of liquid-immersed metal nanoparticles characterized by a high thermal boundary resistance to launch acoustic

waves in the liquid while minimizing their temperature increase.

The thermophone vs mechanophone competition is also the topic of Chapter 4. Here we developed a multi-scale model combining molecular dynamics and continuum mechanics simulations to describe the photoacoustic effect triggered by single wall (SW) and multi walls (MW) carbon nanotubes (CNTs) in water. In this study, we add to the thermophone vs mechanophone discussion the effect of the nanoparticle size, showing that for a ns excitation pulse the thermophone effect prevails for the SWCNT, while both the thermophone and the mechanophone contributions are important for the MWCNT. Reducing the light pulse down to the ps, instead, both the two launching mechanisms contribute for the SWCNT case, but now the only effective launching mechanism for the MWCNT is the mechanophone one. Moreover, in this last case, the ps light pulse is short enough to activate the vibrational modes of the MWCNT, thus generating high frequencies ( $\approx 50$ -100 GHz) sound waves propagating in water. These high frequency sound waves bear great interest in such diverse fields as theranostics, nanoscale acoustic imaging, and water dynamics at the nanoscale in the hypersonic frequency range. Our findings suggest the CNTs as an ideal photoacoustic candidate to explore these physics. Nevertheless, our study focus mostly on the launching mechanisms of the acoustic waves.

The present works opens to a variety of perspectives. First of all, in order to make further progress, it would be desirable to extend the model to include the effect of intrinsic damping, i.e. viscous and viscoelastic damping, which is still an open issue at such high frequencies. Another interesting development would be reducing the light pulse to the fs regime, in order to excite also the breathing mode of the SWCNT, increasing the frequencies of the launched sound wave to the THz regime. In this case, water might respond as a solid rather than a liquid, with a non linear dispersion and a higher sound velocity. In addition to this, SWCNTs can also be semiconductors, at variance from the (5,5)SWCNT of Chapter 4, which is a metal. In the semiconducting case, as seen for the InAs nanowires, also the deformation potential launching mechanism could contribute in addition to the thermophone and mechanophone effects. Another interesting perspective would be to investigate metal nanoparticles in environments with different expansion coefficients, as in the case of ice, which has a negative expansion coefficient between -20 and 0 Celsius degrees. In this case, the thermophone effect would result from a contraction of the environment surrounding the nanoparticle, rather than its expansion, creating new photoacoustic effects.

## Bibliography

- [1] Romain Rouxel. “Ultrafast thermo-optical dynamics of single plasmonic nanoparticles”. PhD thesis. Université Claude Bernard Lyon 1, 2020.
- [2] Romain Rouxel et al. “Ultrafast Thermo-Optical Dynamics of a Single Metal Nano-Object”. In: *The Journal of Physical Chemistry C* 124.28 (2020), pp. 15625–15633.
- [3] Romain Rouxel et al. “Electron and Lattice Heating Contributions to the Transient Optical Response of a Single Plasmonic Nano-Object”. In: *The Journal of Physical Chemistry C* 125.42 (2021), pp. 23275–23286.
- [4] Marco Gandolfi et al. “Ultrafast Photoacoustic Nanometrology of InAs Nanowires Mechanical Properties”. In: *The Journal of Physical Chemistry C* 126.14 (2022), pp. 6361–6372.
- [5] Michele Diego et al. “Ultrafast nano generation of acoustic waves in water via a single carbon nanotube”. In: *Photoacoustics* 28 (2022), p. 100407. ISSN: 2213-5979.
- [6] Richard P Feynman. “Plenty of Room at the Bottom”. In: *APS annual meeting*. 1959.
- [7] JE Hulla, SC Sahu, and AW Hayes. “Nanotechnology: History and future”. In: *Human & experimental toxicology* 34.12 (2015), pp. 1318–1321.
- [8] Dwaine F Emerich and Christopher G Thanos. “Nanotechnology and medicine”. In: *Expert opinion on biological therapy* 3.4 (2003), pp. 655–663.
- [9] Mihail C Roco. “Nanotechnology: convergence with modern biology and medicine”. In: *Current opinion in biotechnology* 14.3 (2003), pp. 337–346.
- [10] Anna Pratima Nikalje et al. “Nanotechnology and its applications in medicine”. In: *Med chem* 5.2 (2015), pp. 081–089.
- [11] Rajiv Saini, Santosh Saini, and Sugandha Sharma. “Nanotechnology: the future medicine”. In: *Journal of cutaneous and aesthetic surgery* 3.1 (2010), p. 32.
- [12] DG Rickerby and Mark Morrison. “Nanotechnology and the environment: a European perspective”. In: *Science and Technology of Advanced Materials* 8.1-2 (2007), p. 19.
- [13] Devarajan Thangadurai, Jeyabalan Sangeetha, and Ram Prasad. *Nanotechnology for food, agriculture, and environment*. Springer, 2020.

- 
- [14] Gregory V Lowry, Astrid Avellan, and Leanne M Gilbertson. “Opportunities and challenges for nanotechnology in the agri-tech revolution”. In: *Nature nanotechnology* 14.6 (2019), pp. 517–522.
- [15] Mamadou Diallo and C Jeffrey Brinker. “Nanotechnology for sustainability: environment, water, food, minerals, and climate”. In: *Nanotechnology research directions for societal needs in 2020*. Springer, 2011, pp. 221–259.
- [16] Manijeh Razeghi. *Technology of quantum devices*. Springer, 2010.
- [17] Robert Chau et al. “Integrated nanoelectronics for the future”. In: *Nature materials* 6.11 (2007), pp. 810–812.
- [18] Cheng Cen et al. “Oxide nanoelectronics on demand”. In: *Science* 323.5917 (2009), pp. 1026–1030.
- [19] Avram Bar-Cohen, Peng Wang, and Emil Rahim. “Thermal management of high heat flux nanoelectronic chips”. In: *Microgravity Science and Technology* 19.3 (2007), pp. 48–52.
- [20] Daniel Jaque et al. “Nanoparticles for photothermal therapies”. In: *nanoscale* 6.16 (2014), pp. 9494–9530.
- [21] Xiaohua Huang et al. “Plasmonic photothermal therapy (PPTT) using gold nanoparticles”. In: *Lasers in medical science* 23.3 (2008), pp. 217–228.
- [22] Philippe Sciau. “Nanoparticles in ancient materials: the metallic lustre decorations of medieval ceramics”. In: (2012).
- [23] Philippe Colomban. “The use of metal nanoparticles to produce yellow, red and iridescent colour, from bronze age to present times in lustre pottery and glass: solid state chemistry, spectroscopy and nanostructure”. In: *Journal of Nano Research*. Vol. 8. Trans Tech Publ. 2009, pp. 109–132.
- [24] Ian Freestone et al. “The Lycurgus cup—a roman nanotechnology”. In: *Gold bulletin* 40.4 (2007), pp. 270–277.
- [25] Gustav Mie. “Beiträge zur Optik trüber Medien, speziell kolloidaler Metallösungen”. In: *Annalen der physik* 330.3 (1908), pp. 377–445.
- [26] N Del Fatti and F Vallee. “Ultrafast optical nonlinear properties of metal nanoparticles”. In: *Applied Physics B* 73.4 (2001), pp. 383–390.
- [27] Aurélien Crut et al. “Optical absorption and scattering spectroscopies of single nano-objects”. In: *Chemical Society Reviews* 43.11 (2014), pp. 3921–3956.
- [28] Christophe Voisin et al. *Ultrafast electron dynamics and optical nonlinearities in metal nanoparticles*. 2001.

- [29] Jana Olson et al. “Optical characterization of single plasmonic nanoparticles”. In: *Chemical Society Reviews* 44.1 (2015), pp. 40–57.
- [30] Craig F Bohren and Donald R Huffman. *Absorption and scattering of light by small particles*. John Wiley & Sons, 2008.
- [31] K Lance Kelly et al. *The optical properties of metal nanoparticles: the influence of size, shape, and dielectric environment*. 2003.
- [32] Surbhi Lal et al. “Tailoring plasmonic substrates for surface enhanced spectroscopies”. In: *Chemical Society Reviews* 37.5 (2008), pp. 898–911.
- [33] Eric T Swartz and Robert O Pohl. “Thermal boundary resistance”. In: *Reviews of modern physics* 61.3 (1989), p. 605.
- [34] RJ Stoner and HJ Maris. “Kapitza conductance and heat flow between solids at temperatures from 50 to 300 K”. In: *Physical Review B* 48.22 (1993), p. 16373.
- [35] Orla M Wilson et al. “Colloidal metal particles as probes of nanoscale thermal transport in fluids”. In: *Physical Review B* 66.22 (2002), p. 224301.
- [36] Vincent Juvé et al. “Cooling dynamics and thermal interface resistance of glass-embedded metal nanoparticles”. In: *Physical Review B* 80.19 (2009), p. 195406.
- [37] Claudio Giannetti et al. “Thermomechanical behavior of surface acoustic waves in ordered arrays of nanodisks studied by near-infrared pump-probe diffraction experiments”. In: *Physical Review B* 76.12 (2007), p. 125413.
- [38] Claudio Giannetti et al. “Ultrafast laser pulses to detect and generate fast thermo-mechanical transients in matter”. In: *IEEE Photonics Journal* 1.1 (2009), pp. 21–32.
- [39] Gang Chen. “Nonlocal and nonequilibrium heat conduction in the vicinity of nanoparticles”. In: (1996).
- [40] Mark E Siemens et al. “Quasi-ballistic thermal transport from nanoscale interfaces observed using ultrafast coherent soft X-ray beams”. In: *Nature materials* 9.1 (2010), pp. 26–30.
- [41] Marco Gandolfi et al. “Accessing temperature waves: A dispersion relation perspective”. In: *International Journal of Heat and Mass Transfer* 143 (2019), p. 118553.
- [42] Michele Simoncelli, Nicola Marzari, and Andrea Cepellotti. “Generalization of Fourier’s law into viscous heat equations”. In: *Physical Review X* 10.1 (2020), p. 011019.
- [43] Jose H Hodak, Arnim Henglein, and Gregory V Hartland. “Size dependent properties of Au particles: Coherent excitation and dephasing of acoustic vibrational modes”. In: *The Journal of chemical physics* 111.18 (1999), pp. 8613–8621.

- [44] Fabio Medeghini et al. “Controlling the quality factor of a single acoustic nanoresonator by tuning its morphology”. In: *Nano letters* 18.8 (2018), pp. 5159–5166.
- [45] GM Odegard, TC Clancy, and TS Gates. “Modeling of the mechanical properties of nanoparticle/polymer composites”. In: *Characterization of Nanocomposites*. Jenny Stanford Publishing, 2017, pp. 319–342.
- [46] Dan Guo, Guoxin Xie, and Jianbin Luo. “Mechanical properties of nanoparticles: basics and applications”. In: *Journal of physics D: applied physics* 47.1 (2013), p. 013001.
- [47] Fabien Violla and Natalia Del Fatti. “Time-Domain Investigations of Coherent Phonons in van der Waals Thin Films”. In: *Nanomaterials* 10.12 (2020).
- [48] Begoña Abad et al. “Nondestructive measurements of the mechanical and structural properties of nanostructured metalattices”. In: *Nano letters* 20.5 (2020), pp. 3306–3312.
- [49] Todd A. Major et al. “Time-Resolved Studies of the Acoustic Vibrational Modes of Metal and Semiconductor Nano-objects”. In: *The Journal of Physical Chemistry Letters* 5.5 (2014), pp. 866–874.
- [50] Min Hu et al. “Dark-field microscopy studies of single metal nanoparticles: understanding the factors that influence the linewidth of the localized surface plasmon resonance”. In: *Journal of materials chemistry* 18.17 (2008), pp. 1949–1960.
- [51] H Baida et al. “Ultrafast nonlinear optical response of a single gold nanorod near its surface plasmon resonance”. In: *Physical review letters* 107.5 (2011), p. 057402.
- [52] Paul V Ruijgrok et al. “Damping of acoustic vibrations of single gold nanoparticles optically trapped in water”. In: *Nano letters* 12.2 (2012), pp. 1063–1069.
- [53] Hristina Staleva and Gregory V Hartland. “Vibrational Dynamics of Silver Nanocubes and Nanowires Studied by Single-Particle Transient Absorption Spectroscopy”. In: *Advanced Functional Materials* 18.23 (2008), pp. 3809–3817.
- [54] Aurélien Crut et al. “Acoustic vibrations of metal nano-objects: time-domain investigations”. In: *Physics Reports* 549 (2015), pp. 1–43.
- [55] Arnaud Arbouet et al. “Direct measurement of the single-metal-cluster optical absorption”. In: *Physical review letters* 93.12 (2004), p. 127401.
- [56] William E Moerner and Lothar Kador. “Optical detection and spectroscopy of single molecules in a solid”. In: *Physical review letters* 62.21 (1989), p. 2535.
- [57] Christopher R Carey et al. “Imaging and absolute extinction cross-section measurements of nanorods and nanowires through polarization modulation microscopy”. In: *The Journal of Physical Chemistry C* 114.38 (2010), pp. 16029–16036.

- [58] Otto L Muskens, Natalia Del Fatti, and Fabrice Vallée. “Femtosecond response of a single metal nanoparticle”. In: *Nano letters* 6.3 (2006), pp. 552–556.
- [59] Martin Husnik et al. “Quantitative experimental determination of scattering and absorption cross-section spectra of individual optical metallic nanoantennas”. In: *Physical review letters* 109.23 (2012), p. 233902.
- [60] M Bom and E Wolf. *Principles of optics (3rd edn), Section 4.8*. 1965.
- [61] Fabio Medeghini et al. “Signatures of small morphological anisotropies in the plasmonic and vibrational responses of individual nano-objects”. In: *The Journal of Physical Chemistry Letters* 10.18 (2019), pp. 5372–5380.
- [62] Eliza Hutter and Janos H Fendler. “Exploitation of localized surface plasmon resonance”. In: *Advanced materials* 16.19 (2004), pp. 1685–1706.
- [63] N Goubet et al. “Size and nanocrystallinity controlled gold nanocrystals: synthesis, electronic and mechanical properties”. In: *Nanoscale* 7.7 (2015), pp. 3237–3246.
- [64] Yibin Xu et al. “Measurement of interfacial thermal resistance by periodic heating and a thermo-reflectance technique”. In: *Materials transactions* 48.2 (2007), pp. 148–150.
- [65] Justin P Freedman et al. “Thermal interface conductance across metal alloy–dielectric interfaces”. In: *Physical Review B* 93.3 (2016), p. 035309.
- [66] Maité Blank and Ludger Weber. “Influence of the thickness of a nanometric copper interlayer on Au/dielectric thermal boundary conductance”. In: *Journal of Applied Physics* 124.10 (2018), p. 105304.
- [67] Tatjana Stoll et al. “Time-resolved investigations of the cooling dynamics of metal nanoparticles: impact of environment”. In: *The Journal of Physical Chemistry C* 119.22 (2015), pp. 12757–12764.
- [68] Marco Gandolfi et al. “Ultrafast thermo-optical dynamics of plasmonic nanoparticles”. In: *The Journal of Physical Chemistry C* 122.15 (2018), pp. 8655–8666.
- [69] Michael E Thomas et al. “Frequency and temperature dependence of the refractive index of sapphire”. In: *Infrared physics & technology* 39.4 (1998), pp. 235–249.
- [70] RB Wilson et al. “Thermoreflectance of metal transducers for optical pump-probe studies of thermal properties”. In: *Optics express* 20.27 (2012), pp. 28829–28838.
- [71] Tatjana Stoll et al. “Advances in femto-nano-optics: ultrafast nonlinearity of metal nanoparticles”. In: *The European Physical Journal B* 87.11 (2014), pp. 1–19.
- [72] Jonathan S Weerakkody et al. “Surface plasmon resonance imaging-based optoelectronic nose: fundamental study on the effects of temperature and humidity”. In: *Optical Sensing and Detection VI*. Vol. 11354. SPIE. 2020, pp. 182–194.

- [73] Po-Ting Shen et al. “Temperature-and roughness-dependent permittivity of annealed/unannealed gold films”. In: *Optics Express* 24.17 (2016), pp. 19254–19263.
- [74] Harsha Reddy et al. “Temperature-dependent optical properties of gold thin films”. In: *Optical Materials Express* 6.9 (2016), pp. 2776–2802.
- [75] Shangyu Zhang, Yanbo Pei, and Linhua Liu. “Dielectric function of polycrystalline gold films: Effects of grain boundary and temperature”. In: *Journal of Applied Physics* 124.16 (2018), p. 165301.
- [76] Michele Magnozzi et al. “Plasmonics of Au nanoparticles in a hot thermodynamic bath”. In: *Nanoscale* 11.3 (2019), pp. 1140–1146.
- [77] N Del Fatti et al. “Nonequilibrium electron dynamics in noble metals”. In: *Physical Review B* 61.24 (2000), p. 16956.
- [78] Uwe Kreibig and Michael Vollmer. *Optical properties of metal clusters*. Vol. 25. Springer Science & Business Media, 2013.
- [79] H Hövel et al. “Width of cluster plasmon resonances: Bulk dielectric functions and chemical interface damping”. In: *Physical Review B* 48.24 (1993), p. 18178.
- [80] Peter B Johnson and R-WJPrB Christy. “Optical constants of the noble metals”. In: *Physical review B* 6.12 (1972), p. 4370.
- [81] Tonatiuh Rangel et al. “Band structure of gold from many-body perturbation theory”. In: *Physical Review B* 86.12 (2012), p. 125125.
- [82] RN Gurzhi. “Mutual electron correlations in metal optics”. In: *Sov. Phys. JETP* 8.4 (1959), pp. 673–675.
- [83] Arnaud Arbouet et al. “Electron-phonon scattering in metal clusters”. In: *Physical Review Letters* 90.17 (2003), p. 177401.
- [84] Chuancheng Jia et al. “Nanowire electronics: from nanoscale to macroscale”. In: *Chemical reviews* 119.15 (2019), pp. 9074–9135.
- [85] Li Na Quan et al. “Nanowires for photonics”. In: *Chemical reviews* 119.15 (2019), pp. 9153–9169.
- [86] La Li, Chuqiao Hu, and Guozhen Shen. “Low-Dimensional Nanostructure Based Flexible Photodetectors: Device Configuration, Functional Design, Integration, and Applications”. In: *Accounts of Materials Research* 2.10 (2021), pp. 954–965.
- [87] Enrique Barrigón et al. “Synthesis and applications of III–V nanowires”. In: *Chemical reviews* 119.15 (2019), pp. 9170–9220.
- [88] Miquel Royo et al. “A review on III–V core–multishell nanowires: growth, properties, and applications”. In: *Journal of Physics D: Applied Physics* 50.14 (2017), p. 143001.

- [89] Milo Yaro Swinkels and Ilaria Zardo. “Nanowires for heat conversion”. In: *Journal of Physics D: Applied Physics* 51.35 (2018), p. 353001.
- [90] Domenic Prete et al. “Thermoelectric conversion at 30 K in InAs/InP nanowire quantum dots”. In: *Nano letters* 19.5 (2019), pp. 3033–3039.
- [91] Zahra Sadre Momtaz et al. “Orbital Tuning of Tunnel Coupling in InAs/InP Nanowire Quantum Dots”. In: *Nano letters* 20.3 (2020), pp. 1693–1699.
- [92] Riccardo Rurali. “Colloquium: Structural, electronic, and transport properties of silicon nanowires”. In: *Reviews of Modern Physics* 82.1 (2010), p. 427.
- [93] Shiliang Wang, Zhiwei Shan, and Han Huang. “The Mechanical Properties of Nanowires”. In: *Advanced Science* 4.4 (2017), p. 1600332.
- [94] D Martínez-Gutiérrez and VR Velasco. “Acoustic waves of GaN nitride nanowires”. In: *Surface science* 605.1-2 (2011), pp. 24–31.
- [95] Yong Zhu. “Mechanics of crystalline nanowires: an experimental perspective”. In: *Applied Mechanics Reviews* 69.1 (2017).
- [96] Mohammad Nasr Esfahani and Burhanettin Erdem Alaca. “A Review on Size-Dependent Mechanical Properties of Nanowires”. In: *Advanced Engineering Materials* 21.8 (2019), p. 1900192.
- [97] Yujie Chen, Xianghai An, and Xiaozhou Liao. “Mechanical behaviors of nanowires”. In: *Applied Physics Reviews* 4.3 (2017), p. 031104.
- [98] Erika M. Van Goethem et al. “Observation of Phonon Propagation in Germanium Nanowires Using Femtosecond Pump and Probe Microscopy”. In: *ACS Photonics* 6.9 (2019), pp. 2213–2222.
- [99] Pierre-Adrien Mante, Laurent Belliard, and Bernard Perrin. “Acoustic phonons in nanowires probed by ultrafast pump-probe spectroscopy”. In: *Nanophotonics* 7.11 (2018), pp. 1759–1780.
- [100] Peijun Guo et al. “Gigahertz Acoustic Vibrations of Elastically Anisotropic Indium Tin-Oxide Nanorod Arrays”. In: *Nano Letters* 16.9 (2016), pp. 5639–5646.
- [101] Pierre-Adrien Mante et al. “Nondestructive Complete Mechanical Characterization of Zinc Blende and Wurtzite GaAs Nanowires Using Time-Resolved Pump and Probe Spectroscopy”. In: *Nano Letters* 16.8 (2016), pp. 4792–4798.
- [102] A. Jurgilaitis et al. “Time-Resolved X-ray Diffraction Investigation of the Modified Phonon Dispersion in InSb Nanowires”. In: *Nano Letters* 14.2 (2014), pp. 541–546.
- [103] Yanying Li et al. “Ultrafast Electron and Phonon Response of Oriented and Diameter-Controlled Germanium Nanowire Arrays”. In: *Nano Letters* 14.6 (2014), pp. 3427–3431.

- [104] Hirotaka Sakuma et al. “Vibrational modes of GaAs hexagonal nanopillar arrays studied with ultrashort optical pulses”. In: *Applied Physics Letters* 100.13 (2012), p. 131902.
- [105] Alexandre A. Kolomenskii et al. “Observation of coherent acoustic and optical phonons in bismuth nanowires by a femtosecond pump-probe technique”. In: *Journal of Applied Physics* 104.10 (2008), p. 103110.
- [106] Monica Lexholm et al. “Optical determination of Young modulus of InAs nanowires”. In: *Applied Physics Letters* 95.11 (2009), p. 113103.
- [107] Róbert Erdélyi et al. “In-situ mechanical characterization of wurtzite InAs nanowires”. In: *Solid state communications* 152.19 (2012), pp. 1829–1833.
- [108] X Li et al. “Mechanical properties of individual InAs nanowires studied by tensile tests”. In: *Applied Physics Letters* 104.10 (2014), p. 103110.
- [109] Jinshui Miao et al. “Single InAs nanowire room-temperature near-infrared photodetectors”. In: *ACS nano* 8.4 (2014), pp. 3628–3635.
- [110] VJ Logeeswaran et al. “A perspective on nanowire photodetectors: current status, future challenges, and opportunities”. In: *IEEE Journal of selected topics in quantum electronics* 17.4 (2011), pp. 1002–1032.
- [111] Daya S Dhungana et al. “Insight of surface treatments for CMOS compatibility of InAs nanowires”. In: *Nano Research* 12.3 (2019), pp. 581–586.
- [112] Wei Lu, Ping Xie, and Charles M Lieber. “Nanowire transistor performance limits and applications”. In: *IEEE transactions on Electron Devices* 55.11 (2008), pp. 2859–2876.
- [113] a RS Wagner and s WC Ellis. “Vapor-liquid-solid mechanism of single crystal growth”. In: *Applied physics letters* 4.5 (1964), pp. 89–90.
- [114] UP Gomes et al. “Controlling the diameter distribution and density of InAs nanowires grown by Au-assisted methods”. In: *Semiconductor Science and Technology* 30.11 (2015), p. 115012.
- [115] Philippe Caroff et al. “Controlled polytypic and twin-plane superlattices in III–V nanowires”. In: *Nature nanotechnology* 4.1 (2009), p. 50.
- [116] Damiano Nardi et al. “Impulsively Excited Surface Phononic Crystals: A Route Toward Novel Sensing Schemes”. In: *IEEE Sensors Journal* 15.9 (2015), pp. 5142–5150.
- [117] Andrea Ronchi et al. “Light-Assisted Resistance Collapse in a  $V_2O_3$ -Based Mott-Insulator Device”. In: *Physical Review Applied* 15.4 (2021), p. 044023.
- [118] Gianluca Rizzi et al. “Analytical model of the acoustic response of nanogranular films adhering to a substrate”. In: *Phys. Rev. B* 104 (3 2021), p. 035416.

- [119] Simone Peli et al. “Mechanical properties of Ag nanoparticle thin films synthesized by supersonic cluster beam deposition”. In: *The Journal of Physical Chemistry C* 120.8 (2016), pp. 4673–4681.
- [120] Martin Grossmann et al. “Characterization of thin-film adhesion and phonon lifetimes in Al/Si membranes by picosecond ultrasonics”. In: *New Journal of Physics* 19.5 (2017), p. 053019.
- [121] Mike Hettich et al. “Viscoelastic properties and efficient acoustic damping in confined polymer nano-layers at GHz frequencies”. In: *Scientific reports* 6.1 (2016), pp. 1–9.
- [122] Lev Davidovich Landau and Eugin M Lifshitz. *Course of Theoretical Physics Vol 7: Theory and Elasticity*. Pergamon press, 1959.
- [123] Gregory V Hartland. “Optical studies of dynamics in noble metal nanostructures”. In: *Chemical reviews* 111.6 (2011), pp. 3858–3887.
- [124] Gregory V. Hartland. “Coherent vibrational motion in metal particles: Determination of the vibrational amplitude and excitation mechanism”. In: *The Journal of Chemical Physics* 116.18 (2002), pp. 8048–8055.
- [125] Min Hu et al. “Vibrational response of nanorods to ultrafast laser induced heating: theoretical and experimental analysis”. In: *Journal of the American Chemical Society* 125.48 (2003), pp. 14925–14933.
- [126] Simon O Mariager et al. “Direct observation of acoustic oscillations in InAs nanowires”. In: *Nano letters* 10.7 (2010), pp. 2461–2465.
- [127] Bertram Alexander Auld. *Acoustic fields and waves in solids*. John Wiley & SONS, 1973.
- [128] Bertram Alexander Auld. *Acoustic fields and waves in solids*. John Wiley & SONS, 1973.
- [129] Dominik Kriegner et al. “Unit cell structure of crystal polytypes in InAs and InSb nanowires”. In: *Nano letters* 11.4 (2011), pp. 1483–1489.
- [130] Dominik Kriegner et al. “Unit cell structure of crystal polytypes in InAs and InSb nanowires”. In: *Nano letters* 11.4 (2011), pp. 1483–1489.
- [131] Koichi Momma and Fujio Izumi. “VESTA 3 for three-dimensional visualization of crystal, volumetric and morphology data”. In: *Journal of applied crystallography* 44.6 (2011), pp. 1272–1276.
- [132] Andrea Ronchi et al. “Discrimination of nano-objects via cluster analysis techniques applied to time-resolved thermo-acoustic microscopy”. In: *Ultrasonics* 114 (2021), p. 106403.

- [133] Giulio Benetti et al. “Photoacoustic sensing of trapped fluids in nanoporous thin films: device engineering and sensing scheme”. In: *ACS applied materials & interfaces* 10.33 (2018), pp. 27947–27954.
- [134] ZM Fang et al. “Photoluminescence of InSb, InAs, and InAsSb grown by organometallic vapor phase epitaxy”. In: *Journal of Applied Physics* 67.11 (1990), pp. 7034–7039.
- [135] Michele B Rota et al. “Bandgap energy of wurtzite InAs nanowires”. In: *Nano Letters* 16.8 (2016), pp. 5197–5203.
- [136] Pascal Ruello and Vitalyi E Gusev. “Physical mechanisms of coherent acoustic phonons generation by ultrafast laser action”. In: *Ultrasonics* 56 (2015), pp. 21–35.
- [137] Michele Celebrano et al. “Optical tuning of dielectric nanoantennas for thermo-optically reconfigurable nonlinear metasurfaces”. In: *Optics Letters* 46.10 (2021), pp. 2453–2456.
- [138] Davide Rocco et al. “Opto-thermally controlled beam steering in nonlinear all-dielectric metastructures”. In: *Optics Express* 29.23 (2021), pp. 37128–37139.
- [139] Giuseppe Grosso and Giuseppe Pastori Parravicini, eds. *Solid State Physics*. Second Edition. Amsterdam: Academic Press, 2014. ISBN: 978-0-12-385030-0.
- [140] Blair C Connelly et al. “Direct minority carrier lifetime measurements and recombination mechanisms in long-wave infrared type II superlattices using time-resolved photoluminescence”. In: *Applied physics letters* 97.25 (2010), p. 251117.
- [141] Hannah J Joyce et al. “Electronic properties of GaAs, InAs and InP nanowires studied by terahertz spectroscopy”. In: *Nanotechnology* 24.21 (2013), p. 214006.
- [142] MI Daunov, IK Kamilov, and SF Gabibov. “Experimental determination of the constants of absolute volume deformation potentials at band edges in semiconductors”. In: *Physics of the Solid State* 46.10 (2004), pp. 1825–1829.
- [143] G Le Guillou and HJ Albany. “Phonon conductivity of InAs”. In: *Physical Review B* 5.6 (1972), p. 2301.
- [144] Mirko Rocci et al. “Suspended InAs Nanowire-Based Devices for Thermal Conductivity Measurement Using the  $3\omega$  Method”. In: *Journal of Materials Engineering and Performance* 27.12 (2018), pp. 6299–6305.
- [145] Marco Gandolfi, Francesco Banfi, and Christ Glorieux. “Optical wavelength dependence of photoacoustic signal of gold nanofluid”. In: *Photoacoustics* 20 (2020), p. 100199.

- [146] Y Asadi and Z Nourbakhsh. “First principle characterization of structural, electronic, mechanical, thermodynamic, linear and nonlinear optical properties of zinc blende InAs, InSb and their InAs<sub>x</sub>Sb<sub>1-x</sub> ternary alloys”. In: *Journal of Physics and Chemistry of Solids* 132 (2019), pp. 213–221.
- [147] Amaury Prost, Florian Poisson, and Emmanuel Bossy. “Photoacoustic generation by a gold nanosphere: From linear to nonlinear thermoelastics in the long-pulse illumination regime”. In: *Physical Review B* 92.11 (2015), p. 115450.
- [148] Francesco Floris et al. “Self-assembled InAs nanowires as optical reflectors”. In: *Nanomaterials* 7.11 (2017), p. 400.
- [149] Francesco Floris et al. “Strong Modulations of Optical Reflectance in Tapered Core–Shell Nanowires”. In: *Materials* 12.21 (2019), p. 3572.
- [150] Lucas Güniat, Philippe Caroff, and Anna Fontcuberta i Morral. “Vapor phase growth of semiconductor nanowires: key developments and open questions”. In: *Chemical reviews* 119.15 (2019), pp. 8958–8971.
- [151] E Petronijevic et al. “Photo-acoustic spectroscopy reveals extrinsic optical chirality in GaAs-based nanowires partially covered with gold”. In: *International Journal of Thermophysics* 39.4 (2018), pp. 1–9.
- [152] Emilija Petronijevic et al. “Broadband optical spin dependent reflection in self-assembled GaAs-based nanowires asymmetrically hybridized with Au”. In: *Scientific reports* 11.1 (2021), pp. 1–9.
- [153] Erika M Van Goethem et al. “Observation of Phonon Propagation in Germanium Nanowires Using Femtosecond Pump–Probe Microscopy”. In: *ACS Photonics* 6.9 (2019), pp. 2213–2222.
- [154] Paolo Maioli et al. “Mechanical vibrations of atomically defined metal clusters: From nano-to molecular-size oscillators”. In: *Nano letters* 18.11 (2018), pp. 6842–6849.
- [155] Gary Beane et al. “Ultrafast measurements of the dynamics of single nanostructures: a review”. In: *Reports on Progress in Physics* 82.1 (2018), p. 016401.
- [156] Denis Mongin et al. “Acoustic vibrations of metal-dielectric core–shell nanoparticles”. In: *Nano letters* 11.7 (2011), pp. 3016–3021.
- [157] M Fernanda Cardinal et al. “Acoustic vibrations in bimetallic Au@ Pd core–shell nanorods”. In: *The journal of physical chemistry letters* 3.5 (2012), pp. 613–619.
- [158] Hirotaka Sakuma et al. “Vibrational modes of GaAs hexagonal nanopillar arrays studied with ultrashort optical pulses”. In: *Applied Physics Letters* 100.13 (2012), p. 131902.

- [159] Srirang Manohar and Daniel Razansky. “Photoacoustics: a historical review”. In: *Advances in optics and photonics* 8.4 (2016), pp. 586–617.
- [160] Mario Bertolotti and Roberto Li Voti. “A note on the history of photoacoustic, thermal lensing, and photothermal deflection techniques”. In: *Journal of Applied Physics* 128.23 (2020), p. 230901.
- [161] Alexander Graham Bell. *Upon the production of sound by radiant energy*. Gibson Brothers, printers, 1881.
- [162] ME Mercadier. “On radiophony”. In: *The London, Edinburgh, and Dublin Philosophical Magazine and Journal of Science* 11.65 (1881), pp. 78–80.
- [163] William Henry Preece. “I. On the conversion of radiant energy into sonorous vibrations”. In: *Proceedings of the Royal Society of London* 31.206-211 (1881), pp. 506–520.
- [164] Wilhelm Conrad Röntgen. “Ueber Töne, welche durch intermittirende Bestrahlung eines Gases entstehen”. In: *Annalen der Physik* 248.1 (1881), pp. 155–159.
- [165] John Tyndall. “III. Action of an intermittent beam of radiant heat upon gaseous matter”. In: *Proceedings of the Royal Society of London* 31.206-211 (1881), pp. 307–317.
- [166] ML Veingerov. “Eine methode der gasanalyse beruhend auf dem optisch-akustischen Tyndall-Röntgeneffekt”. In: *Dokl. Akad. Nauk SSSR*. Vol. 19. 1938, p. 687.
- [167] AH Pfund. “Atmospheric contamination”. In: *Science* 90.2336 (1939), pp. 326–327.
- [168] ML Veingerov. “Spectrophone-an instrument for investigation of infrared absorption spectra of gases and for quantitative and qualitative spectrum analysis of multicomponent gas mixtures”. In: *Dokl. Akad. Nauk SSSR*. Vol. 46. 1945, p. 182.
- [169] G Gorelik. “On a possible method of studying energy exchange times between the different degrees of freedom of molecules in a gas”. In: *Dokl. Akad. Nauk SSSR*. Vol. 54. 1946, p. 779.
- [170] TL Cottrell et al. “Measurement of vibrational relaxation times by the spectrophone. Application to CH<sub>4</sub>, CO<sub>2</sub>, N<sub>2</sub>O, COS, NH<sub>3</sub> and HCN”. In: *Transactions of the Faraday Society* 62 (1966), pp. 2655–2666.
- [171] Allan Rosenwaig. “Photoacoustic spectroscopy of solids”. In: *Optics Communications* 7.4 (1973), pp. 305–308.
- [172] William R Harshbarger and Melvin B Robin. “Opto-acoustic effect. Revival of an old technique for molecular spectroscopy”. In: *Accounts of chemical research* 6.10 (1973), pp. 329–334.

- [173] Stanislav Y Emelianov, Pai-Chi Li, and Matthew O'Donnell. "Photoacoustics for molecular imaging and therapy". In: *Physics today* 62.8 (2009), p. 34.
- [174] Minghua Xu and Lihong V Wang. "Photoacoustic imaging in biomedicine". In: *Review of scientific instruments* 77.4 (2006), p. 041101.
- [175] Changhui Li and Lihong V Wang. "Photoacoustic tomography and sensing in biomedicine". In: *Physics in Medicine & Biology* 54.19 (2009), R59.
- [176] Lihong V Wang. *Photoacoustic imaging and spectroscopy*. CRC press, 2017.
- [177] Wanwan Li and Xiaoyuan Chen. "Gold nanoparticles for photoacoustic imaging". In: *Nanomedicine* 10.2 (2015), pp. 299–320.
- [178] Xinmai Yang et al. "Nanoparticles for photoacoustic imaging". In: *Wiley interdisciplinary reviews: nanomedicine and nanobiotechnology* 1.4 (2009), pp. 360–368.
- [179] Yash Mantri and Jesse V Jokerst. "Engineering plasmonic nanoparticles for enhanced photoacoustic imaging". In: *ACS nano* 14.8 (2020), pp. 9408–9422.
- [180] Geoffrey P Luke, Doug Yeager, and Stanislav Y Emelianov. "Biomedical applications of photoacoustic imaging with exogenous contrast agents". In: *Annals of biomedical engineering* 40.2 (2012), pp. 422–437.
- [181] Ravi Shukla et al. "Biocompatibility of gold nanoparticles and their endocytotic fate inside the cellular compartment: a microscopic overview". In: *Langmuir* 21.23 (2005), pp. 10644–10654.
- [182] Ana Maria Craciun et al. "Surface plasmon resonance or biocompatibility—key properties for determining the applicability of noble metal nanoparticles". In: *Materials* 10.7 (2017), p. 836.
- [183] Pierre Guiraud et al. "Thermoacoustic wave generation in multilayered thermophones with cylindrical and spherical geometries". In: *Journal of Applied Physics* 129.11 (2021), p. 115103.
- [184] Pierre Guiraud et al. "Multilayer modeling of thermoacoustic sound generation for thermophone analysis and design". In: *Journal of Sound and Vibration* 455 (2019), pp. 275–298.
- [185] Ali E Aliev et al. "Alternative nanostructures for thermophones". In: *ACS nano* 9.5 (2015), pp. 4743–4756.
- [186] Paolo La Torraca et al. "On the frequency response of nanostructured thermoacoustic loudspeakers". In: *Nanomaterials* 8.10 (2018), p. 833.
- [187] Antti O Niskanen et al. "Suspended metal wire array as a thermoacoustic sound source". In: *Applied Physics Letters* 95.16 (2009), p. 163102.

- [188] Rajen Dutta et al. “Gold nanowire thermophones”. In: *The Journal of Physical Chemistry C* 118.50 (2014), pp. 29101–29107.
- [189] He Tian et al. “Flexible, ultrathin, and transparent sound-emitting devices using silver nanowires film”. In: *Applied Physics Letters* 99.25 (2011), p. 253507.
- [190] He Tian et al. “Graphene-on-paper sound source devices”. In: *ACS nano* 5.6 (2011), pp. 4878–4885.
- [191] Wenwen Fei, Jianxin Zhou, and Wanlin Guo. “Low-voltage Driven Graphene Foam Thermoacoustic Speaker”. In: *Small* 11.19 (2015), pp. 2252–2256.
- [192] Choong Sun Kim et al. “Free-Standing Graphene Thermophone on a Polymer-Mesh Substrate”. In: *Small* 12.2 (2016), pp. 185–189.
- [193] Lu-Qi Tao et al. “Flexible graphene sound device based on laser reduced graphene”. In: *Applied Physics Letters* 111.10 (2017), p. 103104.
- [194] Zhi Lin Ngoh et al. “Experimental characterization of three-dimensional Graphene’s thermoacoustic response and its theoretical modelling”. In: *Carbon* 169 (2020), pp. 382–394.
- [195] Manuela Loeblein et al. “Configurable Three-Dimensional Boron Nitride–Carbon Architecture and Its Tunable Electronic Behavior with Stable Thermal Performances”. In: *Small* 10.15 (2014), pp. 2992–2999.
- [196] Taylor S Ashton and Arden L Moore. “Three-dimensional foam-like hexagonal boron nitride nanomaterials via atmospheric pressure chemical vapor deposition”. In: *Journal of materials science* 50.18 (2015), pp. 6220–6226.
- [197] Ali Hatef et al. “Analysis of photoacoustic response from gold–silver alloy nanoparticles irradiated by short pulsed laser in water”. In: *The Journal of Physical Chemistry C* 119.42 (2015), pp. 24075–24080.
- [198] Deepak Kumar, Devinder Pal Ghai, and RK Soni. “Simulation studies of photoacoustic response from gold-silica core-shell nanoparticles”. In: *Plasmonics* 13.6 (2018), pp. 1833–1841.
- [199] Yun-Sheng Chen et al. “Environment-dependent generation of photoacoustic waves from plasmonic nanoparticles”. In: *Small* 8.1 (2012), pp. 47–52.
- [200] Khosro Shahbazi et al. “Photoacoustics of core–shell nanospheres using comprehensive modeling and analytical solution approach”. In: *Communications Physics* 2.1 (2019), pp. 1–11.
- [201] Yujiao Shi, Sihua Yang, and Da Xing. “Quantifying the plasmonic nanoparticle size effect on photoacoustic conversion efficiency”. In: *The Journal of Physical Chemistry C* 121.10 (2017), pp. 5805–5811.

- [202] Genny A Pang et al. “Theoretical and experimental study of photoacoustic excitation of silica-coated gold nanospheres in water”. In: *The Journal of Physical Chemistry C* 124.1 (2019), pp. 1088–1098.
- [203] Lucia Cavigli et al. “Impact of Kapitza resistance on the stability and efficiency of photoacoustic conversion from gold nanorods”. In: *Journal of Colloid and Interface Science* 578 (2020), pp. 358–365.
- [204] Haoxue Han, Samy Mérabia, and Florian Müller-Plathe. “Thermal transport at solid–liquid interfaces: High pressure facilitates heat flow through nonlocal liquid structuring”. In: *The journal of physical chemistry letters* 8.9 (2017), pp. 1946–1951.
- [205] An Pham, Murat Barisik, and BoHung Kim. “Pressure dependence of Kapitza resistance at gold/water and silicon/water interfaces”. In: *The Journal of chemical physics* 139.24 (2013), p. 244702.
- [206] Murat Barisik and Ali Beskok. “Temperature dependence of thermal resistance at the water/silicon interface”. In: *International Journal of Thermal Sciences* 77 (2014), pp. 47–54.
- [207] Jerry Vera and Yildiz Bayazitoglu. “Temperature and heat flux dependence of thermal resistance of water/metal nanoparticle interfaces at sub-boiling temperatures”. In: *International Journal of Heat and Mass Transfer* 86 (2015), pp. 433–442.
- [208] F Banfi et al. “Ab initio thermodynamics calculation of all-optical time-resolved calorimetry of nanosize systems: Evidence of nanosecond decoupling of electron and phonon temperatures”. In: *Physical Review B* 81.15 (2010), p. 155426.
- [209] Francesco Banfi et al. “Temperature dependence of the thermal boundary resistivity of glass-embedded metal nanoparticles”. In: *Applied Physics Letters* 100.1 (2012), p. 011902.
- [210] Xuewang Wu et al. “Thermal transport across surfactant layers on gold nanorods in aqueous solution”. In: *ACS applied materials & interfaces* 8.16 (2016), pp. 10581–10589.
- [211] Matthew E Caplan, Ashutosh Giri, and Patrick E Hopkins. “Analytical model for the effects of wetting on thermal boundary conductance across solid/classical liquid interfaces”. In: *The Journal of Chemical Physics* 140.15 (2014), p. 154701.
- [212] Bladimir Ramos-Alvarado, Satish Kumar, and GP Peterson. “Solid–liquid thermal transport and its relationship with wettability and the interfacial liquid structure”. In: *The journal of physical chemistry letters* 7.17 (2016), pp. 3497–3501.

- [213] Bo Hung Kim, Ali Beskok, and Tahir Cagin. “Molecular dynamics simulations of thermal resistance at the liquid-solid interface”. In: *The Journal of chemical physics* 129.17 (2008), p. 174701.
- [214] Truong Quoc Vo et al. “Nano-scale liquid film sheared between strong wetting surfaces: Effects of interface region on the flow”. In: *Journal of Mechanical Science and Technology* 29.4 (2015), pp. 1681–1688.
- [215] Jean-Louis Barrat and François Chiaruttini. “Kapitza resistance at the liquid–solid interface”. In: *Molecular Physics* 101.11 (2003), pp. 1605–1610.
- [216] Han Hu and Ying Sun. “Effect of nanopatterns on Kapitza resistance at a water-gold interface during boiling: A molecular dynamics study”. In: *Journal of Applied Physics* 112.5 (2012), p. 053508.
- [217] Y Wang and P Keblinski. “Role of wetting and nanoscale roughness on thermal conductance at liquid-solid interface”. In: *Applied Physics Letters* 99.7 (2011), p. 073112.
- [218] Mohammad Rashedul Hasan, Truong Quoc Vo, and BoHung Kim. “Manipulating thermal resistance at the solid–fluid interface through monolayer deposition”. In: *RSC advances* 9.9 (2019), pp. 4948–4956.
- [219] Onur Yenigun and Murat Barisik. “Effect of nano-film thickness on thermal resistance at water/silicon interface”. In: *International Journal of Heat and Mass Transfer* 134 (2019), pp. 634–640.
- [220] Cecilia Herrero, Laurent Joly, and Samy Merabia. “Ultra-high liquid–solid thermal resistance using nanostructured gold surfaces coated with graphene”. In: *Applied Physics Letters* 120.17 (2022), p. 171601.
- [221] Zhenbin Ge, David G Cahill, and Paul V Braun. “AuPd metal nanoparticles as probes of nanoscale thermal transport in aqueous solution”. In: *The Journal of Physical Chemistry B* 108.49 (2004), pp. 18870–18875.
- [222] Samy Merabia et al. “Heat transfer from nanoparticles: A corresponding state analysis”. In: *Proceedings of the National Academy of Sciences* 106.36 (2009), pp. 15113–15118.
- [223] Jie Chen et al. “Interfacial thermal resistance: Past, present, and future”. In: *Reviews of Modern Physics* 94.2 (2022), p. 025002.
- [224] N Del Fatti, Arnaud Arbouet, and F Vallée. “Femtosecond optical investigation of electron–lattice interactions in an ensemble and a single metal nanoparticle”. In: *Applied Physics B* 84.1 (2006), pp. 175–181.

- [225] Etienne Pertreux. “Spectroscopie optique de nano-objets individuels : effets d’environnement, de forme et d’orientation”. PhD thesis. Université Claude Bernard Lyon 1, 2015.
- [226] Jay Giblin et al. “Experimental determination of single CdSe nanowire absorption cross sections through photothermal imaging”. In: *Acs Nano* 4.1 (2010), pp. 358–364.
- [227] Craig F Bohren and Donald R Huffman. “Absorption and scattering by a sphere”. In: *Absorption and scattering of light by small particles* 4 (1983), pp. 82–129.
- [228] Lev Davidovich Landau. *Course of Theoretical Physics Vol 5*. Pergamon Press, 1958.
- [229] LD Landau. “EM Lifshitz Theory of elasticity”. In: *Course of theoretical physics* 7 (1986).
- [230] G Ruocco and F Sette. “The history of the "fast sound" in liquid water”. In: *Condensed Matter Physics* (2008).
- [231] Kuai Yu et al. “Nanoparticle–fluid interactions at ultrahigh acoustic vibration frequencies studied by femtosecond time-resolved microscopy”. In: *ACS Nano* 15.1 (2021), pp. 1833–1840.
- [232] Eduardo Gil-Santos et al. “High-frequency nano-optomechanical disk resonators in liquids”. In: *Nature nanotechnology* 10.9 (2015), pp. 810–816.
- [233] Eduardo Gil-Santos et al. “Optomechanical detection of vibration modes of a single bacterium”. In: *Nature nanotechnology* 15.6 (2020), pp. 469–474.
- [234] Benoît Dacosta Fernandes et al. “Acoustic vibrations of Au nano-bipyramids and their modification under Ag deposition: a perspective for the development of nanobalances”. In: *ACS nano* 7.9 (2013), pp. 7630–7639.
- [235] Kuai Yu et al. “Probing silver deposition on single gold nanorods by their acoustic vibrations”. In: *Nano letters* 14.2 (2014), pp. 915–922.
- [236] Matthew Pelton et al. “Viscoelastic flows in simple liquids generated by vibrating nanostructures”. In: *Physical Review Letters* 111.24 (2013), p. 244502.
- [237] Kuai Yu et al. “Compressible viscoelastic liquid effects generated by the breathing modes of isolated metal nanowires”. In: *Nano letters* 15.6 (2015), pp. 3964–3970.
- [238] Vahe Galstyan, On Shun Pak, and Howard A Stone. “A note on the breathing mode of an elastic sphere in Newtonian and complex fluids”. In: *Physics of Fluids* 27.3 (2015), p. 032001.
- [239] Debadi Chakraborty and John E Sader. “Constitutive models for linear compressible viscoelastic flows of simple liquids at nanometer length scales”. In: *Physics of Fluids* 27.5 (2015), p. 052002.

- [240] Renaud Marty et al. “Damping of the acoustic vibrations of individual gold nanoparticles”. In: *Nano letters* 11.8 (2011), pp. 3301–3306.
- [241] Petr Leonidovitch Kapitsa. *Collected Papers*. Pergamon Press, 1964.
- [242] S Torquato and MD Rintoul. “Effect of the interface on the properties of composite media”. In: *Physical review letters* 75.22 (1995), p. 4067.
- [243] Fabio Pavanello et al. “Generalized interface models for transport phenomena: Unusual scale effects in composite nanomaterials”. In: *Journal of Applied Physics* 112.8 (2012), p. 084306.
- [244] Fabio Pavanello and Stefano Giordano. “How imperfect interfaces affect the non-linear transport properties in composite nanomaterials”. In: *Journal of Applied Physics* 113.15 (2013), p. 154310.
- [245] Simone Peli et al. “Discrimination of molecular thin films by surface-sensitive time-resolved optical spectroscopy”. In: *Applied Physics Letters* 107.16 (2015), p. 163107.
- [246] Gilad Rosenblatt et al. “Nonmodal plasmonics: Controlling the forced optical response of nanostructures”. In: *Physical Review X* 10.1 (2020), p. 011071.
- [247] Shunji Bandow. “Radial thermal expansion of purified multiwall carbon nanotubes measured by X-ray diffraction”. In: *Japanese Journal of Applied Physics* 36.10B (1997), p. L1403.
- [248] Jian Ping Lu. “Elastic properties of carbon nanotubes and nanoropes”. In: *Physical Review Letters* 79.7 (1997), p. 1297.
- [249] Chunyu Li and Tsu-Wei Chou. “Axial and radial thermal expansions of single-walled carbon nanotubes”. In: *Physical Review B* 71.23 (2005), p. 235414.
- [250] Ismael Palaci et al. “Radial elasticity of multiwalled carbon nanotubes”. In: *Physical Review Letters* 94.17 (2005), p. 175502.
- [251] VR Velasco and MC Muñoz. “Vibrations in cylindrical shells with transverse elastic isotropy: Application to III–V nitride nanotubes”. In: *Surface science* 603.19 (2009), pp. 2950–2957.
- [252] Claudia Caddeo et al. “Thermal boundary resistance from transient nanocalorimetry: a multiscale modeling approach”. In: *Physical Review B* 95.8 (2017), p. 085306.
- [253] Gianluca Rizzi et al. “Analytical model of the acoustic response of nanogranular films adhering to a substrate”. In: *Physical Review B* 104.3 (2021), p. 035416.
- [254] Giulio Benetti et al. “Bottom-up mechanical nanometrology of granular Ag nanoparticles thin films”. In: *The Journal of Physical Chemistry C* 121.40 (2017), pp. 22434–22441.

- [255] Shahin Mohammad Nejad et al. “Heat transfer at the interface of graphene nanoribbons with different relative orientations and gaps”. In: *Energies* 12.5 (2019), p. 796.
- [256] Anna Sofia Tascini et al. “Thermal transport across nanoparticle–fluid interfaces: The interplay of interfacial curvature and nanoparticle–fluid interactions”. In: *Physical Chemistry Chemical Physics* 19.4 (2017), pp. 3244–3253.
- [257] Boris I Yakobson, CJ Brabec, and Jerzy Bernholc. “Nanomechanics of carbon tubes: instabilities beyond linear response”. In: *Physical Review Letters* 76.14 (1996), p. 2511.
- [258] XB Dai, H Merlitz, and CX Wu. “Transverse elasticity of multi-walled carbon nanotubes”. In: *The European Physical Journal B-Condensed Matter and Complex Systems* 54.1 (2006), pp. 109–112.
- [259] Zhan-chun Tu and Zhong-can Ou-Yang. “Single-walled and multiwalled carbon nanotubes viewed as elastic tubes with the effective Young’s moduli dependent on layer number”. In: *Physical Review B* 65.23 (2002), p. 233407.
- [260] Yutaka Maniwa et al. “Ordered water inside carbon nanotubes: Formation of pentagonal to octagonal ice-nanotubes”. In: *Chemical Physics Letters* (2005). ISSN: 00092614.
- [261] Alexander I. Kolesnikov et al. “Anomalously soft dynamics of water in a nanotube: A revelation of nanoscale confinement”. In: *Physical Review Letters* (2004). ISSN: 00319007.
- [262] Jean-Christophe Blancon et al. “Direct measurement of the absolute absorption spectrum of individual semiconducting single-wall carbon nanotubes”. In: *Nature communications* 4.1 (2013), pp. 1–8.
- [263] Fabien Violla et al. “Universal nonresonant absorption in carbon nanotubes”. In: *Physical Review B* 90.15 (2014), p. 155401.
- [264] Jianwei Che, Tahir Cagin, and William A Goddard III. “Thermal conductivity of carbon nanotubes”. In: *Nanotechnology* 11.2 (2000), p. 65.
- [265] J Hone et al. “Thermal properties of carbon nanotubes and nanotube-based materials”. In: *Applied Physics A* 74.3 (2002), pp. 339–343.
- [266] NR Pradhan et al. “The specific heat and effective thermal conductivity of composites containing single-wall and multi-wall carbon nanotubes”. In: *Nanotechnology* 20.24 (2009), p. 245705.
- [267] A. P. Thompson et al. “LAMMPS - a flexible simulation tool for particle-based materials modeling at the atomic, meso, and continuum scales”. In: *Comp. Phys. Comm.* 271 (2022), p. 108171.

- [268] Andrew I. Jewett et al. “Moltemplate: A Tool for Coarse-Grained Modeling of Complex Biological Matter and Soft Condensed Matter Physics”. In: *Journal of Molecular Biology* (2021). ISSN: 10898638.
- [269] William Humphrey, Andrew Dalke, and Klaus Schulten. “VMD – Visual Molecular Dynamics”. In: *Journal of Molecular Graphics* 14 (1996), pp. 33–38.
- [270] R W Hockney and J W Eastwood. *Computer Simulation Using Particles*. 1988.
- [271] J. Tersoff. “New empirical approach for the structure and energy of covalent systems”. In: *Physical Review B* (1988). ISSN: 01631829.
- [272] Francesco Maria Bellussi et al. “Anisotropic Electrostatic Interactions in Coarse-Grained Water Models to Enhance the Accuracy and Speed-Up Factor of Mesoscopic Simulations”. In: *The Journal of Physical Chemistry B* 125.43 (2021), pp. 12020–12027.
- [273] H. J.C. Berendsen, J. R. Grigera, and T. P. Straatsma. “The missing term in effective pair potentials”. In: *Journal of Physical Chemistry* (1987). ISSN: 00223654.
- [274] Jean-Paul Ryckaert, Giovanni Ciccotti, and Herman J.C Berendsen. “Numerical integration of the cartesian equations of motion of a system with constraints: molecular dynamics of n-alkanes”. In: *Journal of Computational Physics* 23.3 (1977), pp. 327–341. ISSN: 0021-9991.
- [275] T. Werder et al. “On the water-carbon interaction for use in molecular dynamics simulations of graphite and carbon nanotubes”. In: *Journal of Physical Chemistry B* (2003). ISSN: 10895647.
- [276] Sobin Alosious et al. “Kapitza resistance at water–graphene interfaces”. In: *The Journal of chemical physics* 152.22 (2020), p. 224703.
- [277] Dmitry Alexeev et al. “Kapitza resistance between few-layer graphene and water: liquid layering effects”. In: *Nano letters* 15.9 (2015), pp. 5744–5749.
- [278] MM Zaeri, S Ziaei-Rad, and AR Shahidi. “On the elastic constants of single walled carbon nanotubes”. In: *Procedia Materials Science* 11 (2015), pp. 666–671.
- [279] J Maultzsch et al. “Radial breathing mode of single-walled carbon nanotubes: Optical transition energies and chiral-index assignment”. In: *Physical Review B* 72.20 (2005), p. 205438.
- [280] Robert B Leighton and Matthew Sands. *The Feynman lectures on physics*. Addison-Wesley Boston, MA, USA, 1965.
- [281] Yutaka Maniwa et al. “Multiwalled carbon nanotubes grown in hydrogen atmosphere: An x-ray diffraction study”. In: *Physical Review B* 64.7 (2001), p. 073105.

- [282] Barry Marsden, Andrew Mummery, and Paul Mummery. “Modelling the coefficient of thermal expansion in graphite crystals: implications of lattice strain due to irradiation and pressure”. In: *Proceedings of the Royal Society A: Mathematical, Physical and Engineering Sciences* 474.2218 (2018), p. 20180075.
- [283] G Thomas Mase, Ronald E Smelser, and George E Mase. *Continuum mechanics for engineers*. CRC press, 2009.
- [284] Hadley Mark Lawler et al. “Radial-breathing mode frequencies for single-walled carbon nanotubes of arbitrary chirality: First-principles calculations”. In: *MRS Online Proceedings Library (OPL)* 899 (2005).
- [285] Irio G. Calasso, Walter Craig, and Gerald J. Diebold. “Photoacoustic Point Source”. In: *Phys. Rev. Lett.* 86 (16 2001), pp. 3550–3553.
- [286] Debadi Chakraborty et al. “When can the elastic properties of simple liquids be probed using high-frequency nanoparticle vibrations?” In: *The Journal of Physical Chemistry C* 122.25 (2017), pp. 13347–13353.
- [287] Chi-Kuang Sun et al. “Observation of Femtosecond Acoustic Anomaly in a Solid Liquid Interface”. In: *The Journal of Physical Chemistry C* 124.5 (2020), pp. 2987–2993.
- [288] Colman Moore and Jesse V Jokerst. “Strategies for image-guided therapy, surgery, and drug delivery using photoacoustic imaging”. In: *Theranostics* 9.6 (2019), p. 1550.
- [289] Taehwa Lee et al. “Efficient photoacoustic conversion in optical nanomaterials and composites”. In: *Advanced Optical Materials* 6.24 (2018), p. 1800491.
- [290] Srivalleesha Mallidi et al. “Multiwavelength photoacoustic imaging and plasmon resonance coupling of gold nanoparticles for selective detection of cancer”. In: *Nano Letters* 9.8 (2009), pp. 2825–2831.
- [291] Fang Chen et al. “Gold nanoparticles to enhance ophthalmic imaging”. In: *Biomaterials Science* 9.2 (2021), pp. 367–390.
- [292] Pierre-Adrien Mante et al. “Probing hydrophilic interface of solid/liquid-water by nanoultrasonics”. In: *Scientific Reports* 4.1 (2014), pp. 1–6.
- [293] Daisuke Ishikawa and Alfred Q.R. Baron. “Interaction of Acoustic and Quasi-Elastic Modes in Liquid Water on Nanometer Length Scales”. In: *Journal of the Physical Society of Japan* 90.8 (2021), p. 083602.
- [294] VE Zakhvataev and LA Kompaniets. “On the existence of soliton-like collective modes in liquid water at the viscoelastic crossover”. In: *Scientific Reports* 11.5417 (2021), pp. 1–12.

- 
- [295] Matteo Fasano et al. “Thermally triggered nanorocket from double-walled carbon nanotube in water”. In: *Molecular Simulation* 45.4-5 (2019), pp. 417–424.
- [296] Chi-Kuang Sun. “Femtosecond Acoustics and Terahertz Ultrasonics”. In: *EPJ Web of Conferences*. Vol. 195. EDP Sciences. 2018, p. 00005.
- [297] F Sette et al. “Collective dynamics in water by high energy resolution inelastic x-ray scattering”. In: *Physical Review Letters* 75.5 (1995), p. 850.
- [298] Giancarlo Ruocco and Francesco Sette. “The high-frequency dynamics of liquid water”. In: *Journal of Physics: Condensed Matter* 11.24 (1999), R259.
- [299] F Bencivenga et al. “High-frequency dynamics of liquid and supercritical water”. In: *Physical Review E* 75.5 (2007), p. 051202.
- [300] F Bencivenga et al. “Temperature and density dependence of the structural relaxation time in water by inelastic ultraviolet scattering”. In: *The Journal of chemical physics* 131.14 (2009), p. 144502.
- [301] Kuai Yu et al. “Energy Dissipation for Nanometer Sized Acoustic Oscillators”. In: *The Journal of Physical Chemistry C* 126.8 (2022), pp. 3811–3819.